# Sustainable energy cycles based on liquid oxygenates as carbon-neutral hydrogen carriers: A holistic vision

James Highfield, Agnieszka Ruppert, Nicolas Keller

# Sustainable energy cycles based on liquid oxygenates as carbon-neutral hydrogen carriers: a holistic vision

**James G. Highfield,[†,2] Agnieszka M. Ruppert,[*,3] and Nicolas Keller[*,1]**

1. Institut de Chimie et Procédés pour l'Energie, l'Environnement et la Santé (ICPEES), CNRS, Université de Strasbourg, 25 rue Becquerel 67087 Strasbourg, France.
2. Independent consultant, Singapore.
3. Institute of General and Ecological Chemistry, Faculty of Chemistry, Łódź University of Technology, ul. Żeromskiego 116, 90-924 Łódź, Poland.

* Corresponding author : nkeller@unistra.fr ; aruppert@p.lodz.pl

† This monograph is dedicated to the memory of James G. Highfield, who passed away during the revision of this work. We hope that this publication, in its own way, will continue to carry forward his legacy and stand as a testament to our profound respect and gratitude. James was the initiator of this work, and this monograph is a tribute to his memory, as well as to his unwavering intellectual commitment.

## Abstract

Simple energy-dense liquid oxygenates obtained directly from biomass e.g., fermentation ethanol, or "solar methanol", synthesised from renewable hydrogen (via PV-driven water electrolysis) and recycled carbon dioxide, could provide the basis of an energy cycle that is climate-neutral and promotes long-term sustainability in industrial chemical processing. The development of new earth-abundant heterogeneous (photo-)catalysts and associated reaction

engineering promoting hydrogen release (by steam-reforming) and insertion (by $CO_2$ hydro-deoxygenation) under mild conditions will be pivotal to its success. This review anticipates the key methodologies involved in future bio-refineries and forecasts the increasing role therein of modular and portable low-power solar concentrators as renewable (photonic and thermal) resources. The techno-economic prospects for oxygenates like acetaldehyde, ethylene glycol, and glycerol, are also considered based on their reactivity ($C_2$) and/or a pre-existent supply glut in need of valorisation ($C_3$). Many examples highlighting the growing importance of computational (DFT and microkinetic) modelling in catalyst development are presented.

Keywords : Oxygenates reforming; catalytic upgrading; $CO_2$ valorisation; solar hydrogen; renewable fuels; sustainable energy cycles; carbon-neutral hydrogen carriers

# 1. Introduction

The 3rd Millennium has so far been notable for conspicuous and alarming meteorological trends that do not augur well for the future. The marked increase in frequency and degree of climate extremes and related natural disasters can almost surely be attributed to anthropogenic climate change driven mainly by accumulating levels of atmospheric carbon dioxide [1-3]. Notably there is high confidence that humans are the main drivers responsible for more intense heat waves, melting glaciers, and warmer oceans. Levels of methane largely caused by agricultural farming and oil and gas operations, are also implicated.

An urgent transition must be made away from fossil fuels towards a renewable energy cycle based on carbon-neutral alternatives or "net-zero" emitters, and at a global scale [4]. While it chimes with common sense, there is a solid scientific foundation that *resource depletion* caused by the ever-increasing demand must ultimately come to govern the prevailing economics [5,6]. The ideal system should offer the clean-burning properties of hydrogen coupled with the storage and handling of a high-energy-dense liquid fuel or gasoline equivalent. While hydrocarbons ($C_xH_{x+y}$) *per se* are ruled out for this purpose due to their lack of reactivity in dehydrogenation except at very high temperature, a similar group, carbon-based oxygenates ($C_xH_yO_z$), a sub-class of *organic hydrides* comprising mono- and polyhydric alcohols, aldehydes, ketones, ethers, carboxylic acids, esters, carbohydrates (sugars), etc., may be eminently suitable as discussed in the following *Thematic Overview*.

The sustainable energy cycle under consideration is shown schematically in Fig. 1. This review covers recent advances in fundamental and applied catalytic processes and materials that are pivotal to its ultimate success. These are the central H-cycling reactions, viz., oxygenate synthesis (H-insertion) from renewable syngas and/or biomass, and oxygenates reforming (H-release) in the vapour and/or liquid state. Catalytic aspects of renewable $H_2$ generation,

indirectly via PV-driven water electrolysis or directly via photonic (photocatalytic or photoelectrochemical) water splitting, are briefly covered. In view of its importance to renewable syngas supply, advances in carbon capture and utilisation (CCU) are also summarised. The rationale and outlook for 2nd generation bio-refineries based on lignocellulosic biomass feedstock sets the scene for this review on oxygenates as H-carriers. *Ethanol* occupies a key position as it can now be made from renewable syngas, a strategic alternative to the traditional route from sugar fermentation. Assessment of its wider importance as a valuable platform chemical is beyond the scope of this review. Nevertheless, the feasibility and potential synergies in operation from integrating future solar- and bio-refineries are briefly outlined. Regrettably, there is not enough scope for related topics, e.g., fuel cells based on $H_2$ (in reformate) or direct alcohol fuel cells, electro-oxidative processing of biomass, electro-reduction of $CO_2$, or lignin valorisation.

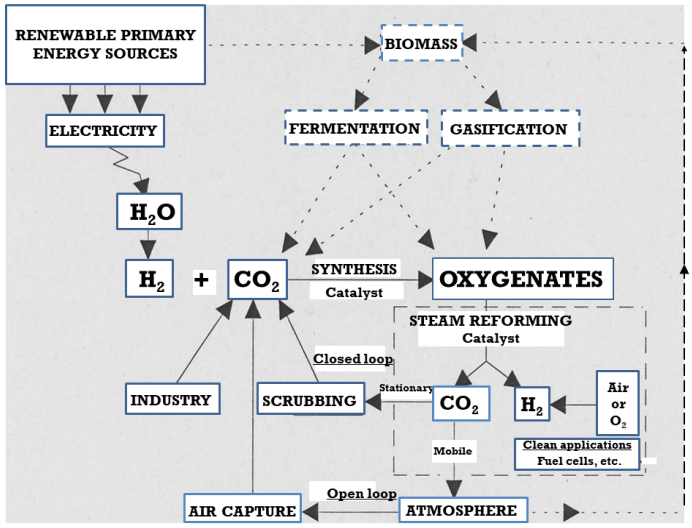


**Fig. 1** Energy scheme for renewable $H_2$ storage in liquid oxygenates

## 2. Thematic overview

## 2.1. Background – benefits and limitations of hydrogen fuel

Pure hydrogen generated from water electrolysis by renewable primary sources like solar, wind and hydro-power would provide stable long-term (chemical) storage of electrical energy in an ultra-clean fuel but in impractical (high-volume) form [7,8]. Unfortunately, physical storage methods, e.g., adsorption, pressurisation, liquefaction, etc., are inefficient and lead to impracticably low energy densities, as shown in Fig. 2A. In addition, decades of intensive research into chemical storage forms e.g., metal hydrides, have yet to identify a compound having workable (fixed and reversible) mass-specific energy density [9,10]. Fig. 2B shows the corresponding plot in gravimetric (wt.% H) terms.

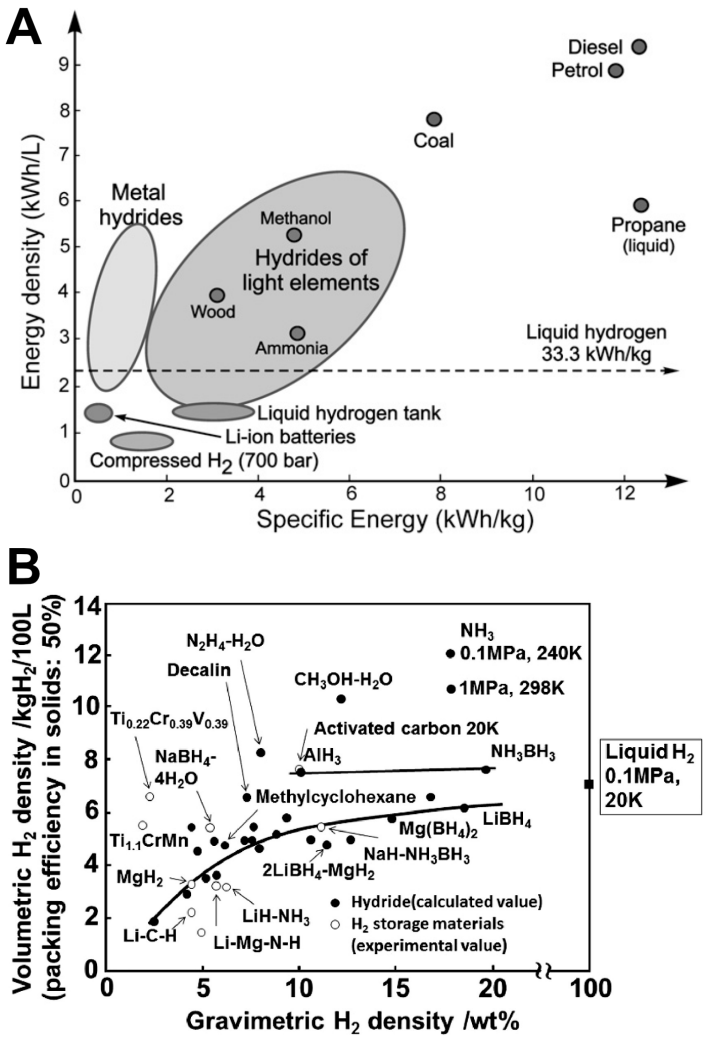

**Fig. 2 (A)** Energy densities of hydrogen storage forms vs. fossil fuels. [Taken with permission from ref. 9 ; **(B)** Gravimetric (wt.%) H-levels in metallic, organic & inorganic hydrides. [Taken with permission from ref. 10]

In 2012, the US DOE (Department of Energy) set the target at 5.5% H by 2020 for on-board storage in mobile applications, e.g., fuel cells. Effective H-cycling also needs good energetics, kinetics, and mechanical stability in solid storage forms, i.e., avoidance of particle decrepitation [11]. The ideal energy cycle should have net zero- emissions and couple the advantages of $H_2$ as a clean-burning fuel with the practical storage and handling properties of a liquid fuel. Hydrogenated N-based inorganic compounds like ammonia are attracting interest as high-density storage forms (17.6 wt% H) as they are carbon-free energy vectors [9]. However, $NH_3$ becomes liquid only at sub-zero temperatures, while its stability disfavours $H_2$ release, needing quite severe treatment ($T > 450°C$) over a precious metal catalyst like Ru [12]. Elsewhere, progress in lowering the enthalpy and process temperature associated with hydrogenation/dehydrogenation cycling in liquid organic H-carriers (LOHCs), e.g., hetero-atom-based aromatics like N-ethylcarbazole and hydrogenated analogues, have been notable [13]. However, while the H-density range (5-6 wt% H) is just adequate, the scheme seems unsustainable in the long-term, with major concerns over the availability of such (non-renewable) carriers at a global scale and their limited recyclability [14]. Just as in the case of ammonia, LOHCs have safety issues and are also dependent on the use of expensive precious metal catalysts like platinum.

### 2.2. Reactive and reversible storage of hydrogen in liquid oxygenates

The incipient H-content of liquid oxygenates is typically in the range 10-15 wt%, slightly lower than their (saturated) hydrocarbon counterparts, but oxygenates offer more realistic

prospects as sustainable hydrogen carriers because the catalytic release proceeds under far milder conditions In the storage step, gaseous $H_2$ is "reactively liquefied" with carbon dioxide to yield methanol:

$$CO_2 + 3\ H_2 \leftrightarrow CH_3OH_{(g)} + H_2O_{(g)} \qquad (\Delta H^0 = -50\ kJ.mol^{-1}) \qquad (1)$$

Methanol synthesis is a well-known industrial process for converting CO-rich syngas ($CO/CO_2/H_2$) into a valuable commodity chemical. However, with only modest adjustment of the process and catalyst (to overcome deleterious effects of water co-product) it also works on renewable syngas in a slightly exothermic reaction proceeding over supported Cu under mild conditions. Renewable syngas consists of $H_2$ and $CO_2$ but is a net "zero emission" fuel because the $CO_2$ is recycled from process off-gases or, in the longer-term, will be recovered by direct air capture [15]. Renewable $H_2$ is obtained by solar PV-driven electrolysis or photoelectrochemical splitting of water [16]. These are then reacted in stoichiometric proportions to obtain the desired product, e.g., $3H_2$:$1CO_2$ for methanol synthesis (1).

Reaction (1) has already been demonstrated at pilot scale (230°C/50 bar) [17]. It is also an excellent example of a process running under kinetic control, hydrocarbons being the products favoured by thermodynamics. In the H-release step, it is useful to compare methanol with its $C_1$ hydrocarbon analogue methane. H-release from methanol is readily achieved by steam-reforming (SR) (2).

$$CH_3OH_{(l)} + H_2O_{(l)} \leftrightarrow CO_2 + 3\ H_2 \qquad (\Delta H^0 = +130\ kJ.mol^{-1}) \qquad (2)$$

$$CH_4 + H_2O_{(l)} \leftrightarrow CO + 3\ H_2 \qquad (\Delta H^0 = +250\ kJ.mol^{-1}) \qquad (3)$$

Methanol SR is a highly endothermic process that proceeds over Cu-based catalysts already at 250°C [18] because the thermodynamics are made favourable ($\Delta G \leq 0$) by the entropy

146 factor, i.e., the molar volume increase. In contrast, methane SR has the same molecularity as
147 Reaction (2) but suffers from both kinetic and thermodynamic limitations. The stable C-H bond
148 in $CH_4$ needs activation by an aggressive dehydrogenation catalyst (supported Ni) above 400°C,
149 and acceptable syngas yields are only achieved above 700°C due to the higher endothermicity
150 of Reaction (3) [19].
151
152 **2.3. Benefits of oxygenates pre-reforming**
153 Direct combustion of oxygenates like methanol and ethanol, e.g., as fuel additives in
154 gasoline as practised currently, is far from ideal. Oxygenates pre-reforming, as in the case of
155 methanol (Reaction 2), offers two key benefits. Firstly, it features thermochemical recuperation
156 [20], an energy increase due to production of $H_2$, one third of which comes from water via the
157 Water-Gas Shift (WGS) reaction (4).
158
159 $CO + H_2O \leftrightarrow CO_2 + H_2$ $(\Delta H^0 = -40\ kJ.mol^{-1})$ (4)
160
161 In fact, for the stoichiometry of ethanol SR ($C_2H_5OH{:}3H_2O$), the recuperation factor
162 (32%) is double that for methanol and raises the volumetric energy density of the pure alcohol,
163 in terms of H-enthalpy (~30 $MJ.l^{-1}$) close to that of gasoline (~33 $MJ.l^{-1}$ as C + H) [21].
164 Secondly, pre-reforming develops the ultra-clean (and lean-) burning properties of the resulting
165 $H_2$-rich gas mixture. The value of on-board (catalytic) reformers for internal combustion
166 engines in the transportation sector has been reviewed recently [22].
167
168 **2.4. The methanol economy and beyond**
169 Historically, interest in $CO_2$ as a recyclable substrate in renewable fuel alcohol schemes
170 gained impetus in the late ‘80s [24-26] after the discovery that it was the more reactive C-source
171 (vs. CO) in syngas conversion to methanol [23]. Olah et al. have since proclaimed the advent

of the "methanol economy" [17,26,27]. Extension of the principle to ethanol anticipates the growing importance of the $C_2$ alcohol as carbon- neutral biofuel (H-carrier) and platform chemical in future biorefineries. Unfortunately, selectivity in ethanol synthesis by thermal heterogeneous catalysis remains poor, although indirect routes from methanol, e.g., dehydration to dimethyl ether (DME) followed by isomerization to ethanol offer some prospects [28]. Ethanol SR (the corresponding reverse process) suffers from ineffective C-C bond activation below 400°C, leading to coking and catalyst deactivation [29]. Extension to oxygenates as a broad class is justified by the pioneering work of the Dumesic group [30]. They reported substantial $H_2$ release from biomass-related sugars and polyols using aqueous-phase reforming (APR) over Pt/©-$Al_2O_3$ in liquid water at 220°C and 30 bar. For $C_6$ ring compounds glucose and sorbitol, $H_2$ and $CO_2$ made up > 90 mol% of the product. This implies effective C-C bond cleavage, a possible benefit of working in a large excess of water. Selectivities to $H_2$ increased from 50% in glucose to nearly 100% for the short chain polyols glycerol ($C_3$) and ethylene glycol ($C_2$).

**2.5. Contingent supply of oxygenates from biorefinery processing**

The generic equation for oxygenates reforming is as follows:

$$C_nH_mO_k + (2n-k)\ H_2O \leftrightarrow n\ CO_2 + (2n + m/2 - k)\ H_2 \quad (5)$$

A particularly encouraging feature of Reaction (5) is that it can be driven by thermal- and/or photo-excitation [31]. This raises prospects of using solar energy for such endergonic (uphill) processes [32,33]. It also provides an opportunity to explore photo-/thermal catalytic synergies [34,35]. Formic acid is a special case (2n-k = 0) where $H_2$ is released by direct dehydrogenation. Despite its low H content (4.4 wt.%), its prospects as a H-carrier are attracting interest due to its very high reactivity in the liquid state in the presence of homogeneous [36]

198 or heterogeneous [37,38] catalysts. The high purity ("CO-free") $H_2$ obtained enables link-up
199 with polymer electrolyte membrane (PEM) fuel cells [39]. Alternatively, it may provide a
200 valuable source of on-site hydrogen for bio-refinery processing. Insofar as many lower
201 oxygenates may be sourced efficiently from biomass, including formic acid [40], biomass
202 processing serves as a vital supply route when industrial synthesis catalysts are either non-
203 existent or not optimised to work on renewable syngas.

204 Apart from encouraging signs that methanol may eventually be obtained from glycerol
205 [41], a versatile by-product from bio- diesel production [42], this C1 alcohol along with its
206 derivatives formaldehyde and dimethyl ether (DME) are not readily obtainable from biomass
207 [43]. However, it is also recognized that renewable methanol installations would benefit from
208 integration into biorefineries based on ethanol fermentation by exploiting the high-quality $CO_2$
209 co-product as feedstock [44]. One important caveat must be made at this point. In any
210 commercial venture where product value-add is crucial, the role of oxygenates as commodity
211 chemicals must take priority over H-storage (fuel-related) applications, unless there is a supply
212 glut as in the case of glycerol [45].

213

214 ## 3. Biomass resources and 2nd generation biorefineries

215

216 Biomass is a generic term for all carbon-based materials derived from photosynthesis
217 [46]. This is Nature's ingenious means of solar energy harvesting and chemical storage, in
218 which H radicals are abstracted from water by absorption of photons in the visible and near
219 infrared region of the electromagnetic spectrum. These reduce carbon dioxide into
220 carbohydrates, oxygenated biopolymers containing energetic C-C and C-H bonds. Insofar as
221 crude oil is the residue of plant matter degraded in a reducing atmosphere over geological aeons,
222 it can be thought of as "fossilised biomass".

While fresh (terrestrial) and ancient (submerged) variants have the same origin, only combustion of the intact vegetative form is considered strictly carbon-neutral. Carbon neutrality is taken to mean that $CO_2$ emissions from vegetative decay are naturally recycled back into terrestrial biota in a short time, thereby restoring the net balance. One credible estimate of the mean residence time of $CO_2$ in the atmosphere is as low as 5 years [47], with positive implications for real-time evaluation of emission reduction strategies. The Intergovernmental Panel on Climate Change of the United Nations sets the rate of the global carbon cycle more conservatively as occurring over "tens to hundreds of years" [48].

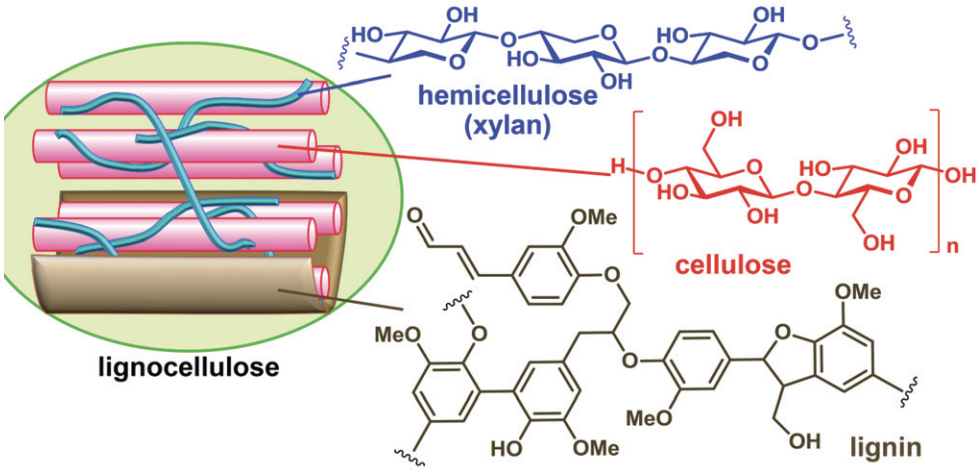


**Fig. 3** Composition of plant biomass (lignocellulose) (Reproduced with permission from ref. 49).

In terms of chemical composition, cellulose, a high-molecular weight crystalline polysaccharide [$(C_6H_{12}O_6)_n$] comprised of D-glucose ($C_6$) units linked by β-1,4-glycosidic bonds, is predominant (see Fig. 3). The other two main forms, hemicellulose [a lower polymer of D-xylose ($C_5$) units] and lignin [an aromatic 3D-network of linked phenylpropane sub-units], are amorphous structures found in plant cell walls [46]. The highly variable level of lignin [10-

242 50 wt%, as nominally $C_9H_{10}O_3$] gives rise to practical issues linked to feedstock inhomogeneity
243 [49,50] and a greater degree of intractability in pre-treatment due to its aromatic (hydrophobic)
244 qualities. The importance of lignocellulose to early Man was recognized after the invention of
245 fire from dry brush-wood, which served as a source of heat and social protection over past
246 millennia. Indeed, biomass as an energy source remains central to its future advancement
247 despite the fact that it contains only half the calorific value of fuel oil (21 vs. 42 $MJ.kg^{-1}$) due
248 to its high oxygen content, ranging from 35 to 50 wt.% O. Biomass has an extremely wide range
249 in elemental composition depending on the source type (woody, herbaceous, aquatic, etc.).
250 Representative values are 50 wt.% C, 6 wt.% H, 42 wt.% O, 2 wt.% others (mainly, S, N and
251 ash) [50]. For combustion purposes, an empirical formula of $CH_{1.44}O_{0.66}$ can be assumed [46].
252 By the same token, the intrinsic hydrophilicity of the cellulose fraction, after hydrolytic
253 depolymerization of the crystalline form into soluble monomers (sugars), renders it amenable
254 to green (aqueous-phase) processing [51]. Applied catalysis in future bio-processing will see a
255 major re-orientation towards *hydrodeoxygenation* and *hydrogenolysis* [52,53]. However,
256 sourcing of sufficient process $H_2$ on-site is problematic as the H-level in raw biomass is
257 typically just 6 wt.%, a substantial fraction of which is associated with O as elements of water.
258 Bio-ethanol ($C_2H_6O$, 30 $MJ.kg^{-1}$) and bio-diesel ($C_{19}H_{34}O_2$, 37 $MJ.kg^{-1}$) are H-enriched liquid
259 products of biomass and established transportation fuels with a revenue forecast of USD 24
260 billion by 2020. The transition to a sustainable fuels & chemicals economy will hinge on the
261 judicious harnessing and management of biomass resources and drastic (x7) scale-up thereof
262 [54].
263 It can be taken as axiomatic that during the transitional phase away from industrial
264 dependence on a dwindling supply of oil, any new energy source must offer better routes to the
265 same base chemicals, viz., methanol, ethylene, propylene, butadiene, benzene, toluene, and
266 xylenes, etc. These base chemicals should be obtained from renewable feedstock via green and

sustainable practices and on a competitive economic basis. However, despite agreed plans for price reform over the last decade fossil fuel subsidies rose again to over USD 400 billion in 2018, vastly exceeding those on renewables [55,56]. Realistic costing of any energy source should be based on internalisation of the "price" of environmental damage caused by its usage, as measured in ecological (planetary)- and human- health terms. A suitably adjusted estimate of the International Monetary Fund for 2017 is USD 5.2 trillion [57], substantiating fears of a veritable "cost iceberg".

Without such holistic and necessarily long-term analyses helping to drive a natural market re-orientation, the outlook for human progress in the 3rd Millennium has little cause for optimism. Substitution of oil as primary feedstock by biomass leads to a multitude of techno-economic challenges from the very outset. These are to some extent familiar to the agriculturalist but are also highly interdisciplinary issues. Depending on the target product or platform chemical (process intermediate) under consideration, good decisions need to be made on crop selection, scale of cultivation, logistics of harvesting, drying, and pre-treatment, e.g., mechanical (comminution), hydrothermal (steaming), chemical (hydrolysis), biochemical (enzymatic saccharification), and/or combinations thereof. This complexity leads to the concept of a versatile centralised installation dealing holistically with sourcing, pre- processing and refining of biomass towards a select range of products that offer synergies in technical operation and resilience (flexibility in response) to market forces. Income security is best achieved by a judicious choice of independent revenue streams in the "portfolio". This means balancing the scale of operations between (low-value high-volume) fuels production and a few (high-value low-volume) specialty chemicals.

For economic viability in a mature industry in which feedstock scarcity is an ever-present threat due to the vagaries of agriculture, i.e., long growing cycles and unpredictable yields, the installation must prioritise the *minimisation* and/or *valorisation* of waste [58]. The modern

292 petrochemical refinery has been optimised to do this heuristically over many decades. Hence
293 the timely inception of the *integrated biorefinery* at the beginning of the 3rd Millennium [59].
294 The principles and current perspectives on biorefineries can be found in reference sources
295 [60,61]. The International Energy Agency definition should read: "*Biorefining is the*
296 *sustainable processing of biomass into a spectrum of marketable products and energy"*. The
297 keyword here is "sustainable" and candidate processes only qualify after rigorous evaluation
298 by Life Cycle Sustainability Assessment (LCSA) [62] in three categories - environmental,
299 economic, and social.

300 The most useful classification of biorefineries is on the basis of the *product* (biofuel,
301 bulk/specialty chemical, material, etc.) or *platform* (biogas, biosyngas, $C_5$-$C_6$ sugars, etc). These
302 depend on the main regional variety of cultivable biomass and/or assimilable carbon-based
303 resources, which can include municipal solid waste, etc. Historically, the main bio-based
304 product has been fuel ethanol derived from edible crops, corn and sugarcane. Whereas the
305 benefits from corn, grown mainly in the USA, are considered marginal at best [63], ethanol
306 from sugarcane as practised in Brazil under the *Pro-Alcool* (now *RenovaBio*) government
307 initiative has demonstrable energetic and environmental benefits and remains a genuine market
308 competitor [64]. This is partly due to the remarkably high yield of sugarcane plantations, which
309 has effectively doubled (from 40 to 80 ton/ha) since 1975. Indeed, *Pro-Alcool* has been so
310 successful that a major question is now posed as to the re-invention/adaptation of over 400
311 biorefineries of the 1st *generation* type, i.e., those based on *edible* crops, in Brazil alone [65].
312 The country's commitment at COP-21 (21th Conférence de Paris, Paris, 2015) was to double its
313 output from today's level to 50 billion litres per annum by 2030 [66].

314 Emerging *2nd generation* bio-refineries are designed to process *lignocellulosic* or
315 woody/herbaceous biomass, the most abundant and globally ubiquitous renewable feedstock
316 [67]. Being non-edible, it also satisfies a key sustainability premise by avoiding issues of

competition (for cultivable land) with food/feed agriculture. However, it is an intractable material and highly resistant to physicochemical pre-treatment to separate the hydrolysable cellulose and hemicellulose from lignin for downstream processing. The most obvious development for sugarcane bioethanol is to valorise the bagasse and straw wastes, normally burned for heat and electrical power [68]. Constituting one half of the total sugarcane by dry mass, its processing would lead to a substantial increase in alcohol yield [69]. This merging of 1st and 2nd generation (1G-2G) processing strategies into a single biorefinery is a natural evolution for existing facilities and may provide a seamless transition for the industry [70]. It seems unquestionable that the *sugar platform* will continue in 2G biorefineries in view of the intrinsic efficiency of the natural process of fermentation, its high level of technical development [71], and the versatility of the ethanol product, now being considered as a prospective platform chemical for production of butadiene, ethylene, acetic acid, etc [72].

From a green chemistry viewpoint, enzymatic anaerobic fermentation of glucose [$C_6(H_2O)_6$], in which all the hydrogen is present as the elements of water (H/C=0), to ethanol containing 4 "free" paraffinic C-H bonds (H/C=2.0), is virtually ideal.

$$C_6H_{12}O_6 \leftrightarrow 2\ C_2H_5OH + 2\ CO_2 \qquad (6)$$

Driven by the combined (negative) enthalpy and (positive) entropy of $CO_2$ gas formation, Reaction (6) proceeds in high selectivity at ambient temperature in aqueous medium and transmutes two thirds of the hydrogen from O-H into C-H bonds. It is energetically remarkable insofar as 95% of the enthalpy from the original feedstock is assimilated into the product ($\otimes H^0$ = -2805 kJ $mol^{-1}$ for glucose vs. -2734 kJ for 2 moles of ethanol). The disadvantage of Reaction (6) is that it is slow and limited by product intolerance in the yeast (enzyme catalyst), terminating under natural constraints at ≈15 vol.% ethanol. This imposes a significant energy

342 penalty in work-up by distillation or other separation processes. It is not as serious for steam-
343 reforming (SR) since the reaction stoichiometry corresponds to just 40 vol.% ethanol (7).
344
345 $C_2H_5OH_{(g)} + 3\ H_2O_{(g)} \leftrightarrow 6\ H_2 + 2\ CO_2$ $(\Delta H^0 = +175\ kJ.mol^{-1})$ (7)
346
347 The ethanol fermentation/SR route is a mild and green alternative for obtaining bio-
348 hydrogen that is otherwise in short supply from biomass. The composition of renewable syngas
349 obtained by steam gasification of whole biomass, a highly energy-intensive process, is typically
350 $H_2/(CO+CO_2) \approx 1$ [73] whereas the idealised two-stage conversion of the cellulosics (60-70%
351 of biomass on a carbon basis) remaining after alkaline delignification [74] in a 2G refinery can
352 be written as the sum of Reaction (6) and twice Reaction (7) (for chemical balance) (8).
353
354 $C_6H_{12}O_6 + 6\ H_2O_{(g)} \leftrightarrow 12\ H_2 + 6\ CO_2$ (8)
355
356 Such a hydrogen-rich bio-syngas ($H_2/CO_2=2$) is well-suited kinetically for renewable
357 methanol or Fischer-Tropsch (hydrocarbons) syntheses. However, ethanol SR (Reaction 6) as
358 written is idealised and awaits the development of more active and selective catalysts (see the
359 appropriate section [29]). Meanwhile, alternative (non-biomass) sources of renewable $H_2$ are
360 urgently needed.
361

## 362 4. Renewable hydrogen from water electrolysis

363

### 364 4.1. State-of-the-art water splitting devices and prospects for scale-up

365 Renewable hydrogen will be generated in the near term by solar (photon)-driven PV
366 electrolysis (acid/alkali) and photoelectrochemical (PEC) splitting of water [75,76]. Recent
367 cost analysis for an electrical power-to-gas installation indicates that today's $H_2$ price of € 3.2
368 $kg^{-1}$ (USD 3.50 $kg^{-1}$) is already competitive in niche applications and forecasts to drop to €

2.50 $kg^{-1}$ within the next decade [77]. At a time when laboratory-based PV/PEC hybrid systems regularly exceed the US DOE target solar-to-hydrogen conversion efficiency ($\eta_{STH}$ = 10%), the technical challenges of scale-up are becoming an urgent priority.

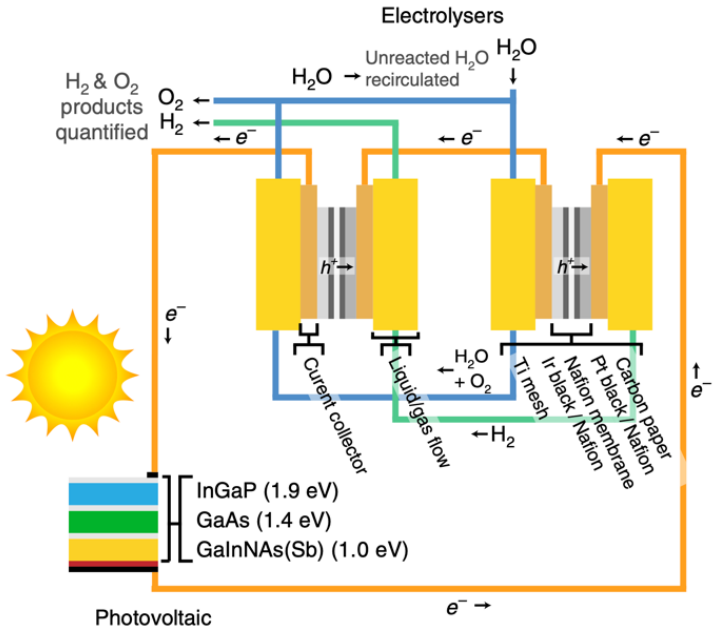


**Fig. 4** PV-E system based on triple-junction solar cell and two PEM electrolysers in series achieved the highest solar-to-hydrogen efficiency in 2016: $\eta_{STH}$ = 30%. (Reproduced with permission from ref. 79)

In an in-depth review, Liu et al. [78] compared PV-electrolyser (PV-E), PEC, and hybrid PV-PEC systems with other emerging technologies for water splitting, including particulate photocatalysis, solar-thermal cycling, etc. It revealed the sobering fact that none of these attain "best laboratory performance" at pilot scale. The highest laboratory efficiency ($\eta_{STH}$= 30%) was recently achieved in a PV-E device with a triple junction InGaP/GaAs/GaInN/AsSb solar cell (electrode area = 0.32 $cm^2$) irradiated by a Xe arc lamp and driving two polymer electrolyte membrane (PEM) electrolysers in series (Fig. 4) [93]. A similar device with an InGaP/GaAs/Ge triple-junction cell (0.57 $cm^2$) reached 24.4% in an optimised (3/5 PV/E) series modular configuration [80].

However, when 13 double-junction Si-based cells (0.5 $cm^2$, $\eta_{STH}$ = 9.5%) of extended length (8 cm) were laid out in a rectangular array of active area 52.8 $cm^2$ (a 100-fold upscaling factor) the efficiencies were only modest ($\eta_{STH}$= 4.7% [81]; 5.1% [82]), almost certainly due to excessive ohmic losses in current collection over a wide area. Sheet resistance losses in transparent conductive oxides (TCO) increase linearly with electrode dimension but become catastrophic upon optical power intensification. For a single absorber device (L = 10 cm), current losses may exceed 50% at 5 suns irradiation, as shown in Fig. 5 [83]. The same issue in thin-film PV technology is mitigated by laser scribing closely-spaced and narrow metal grid lines along the entire length of the high-aspect ratio (1 m x 1 cm) cell [84]. Increasing TCO layer thickness in order to lower sheet resistance is restricted by two factors: material cost, as for In-doped tin oxide (ITO), and the trade-off with needing to maintain high (> 80%) optical transparency. Substitution of ITO by cheaper earth-abundant n-doped oxides of similar conductivity, e.g., Al:ZnO (AZO), is a major goal in TCO development [85].

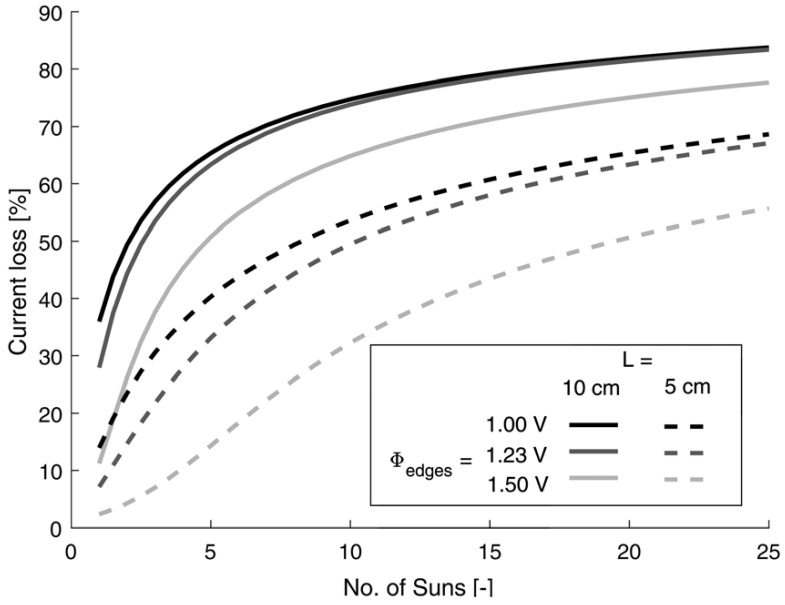


**Fig. 5** Efficiency (sheet resistance) losses for a single absorber at varying dimension and solar intensity (suns) (Reproduced with permission from ref. [83]).

## 4.2.Sustainable absorbers and photo-(electro)catalysts

### 4.2.1. PV-E devices

Sustainability issues are driving materials research for alternative PV absorbers and electrolyzer catalysts in PV-E devices. These are crucial to performance in terms of efficiency, stability and cost. The organic/inorganic hybrid perovskite halide system, for which the model performer is methyl ammonium lead triiodide [$CH_3NH_3PbI_3$, MAPI), is fulfilling its early promise as an alternative to Si in PV cells [86]. These are inexpensive solution-processed materials offering tunable direct (high extinction coefficient) band-gaps, high carrier diffusion lengths and mobilities. Nevertheless, practical devices have a central perovskite layer sandwiched between thin layers for electron transport (typically mesoporous $TiO_2$) and hole transport (usually spiro-based triphenylamine derivatives). Certified efficiencies have doubled in the last 7 years [87,88] to 25.5% (or 20% in high-area form, i.e. > 1$cm^2$) and outperform all other single absorber systems, including amorphous Si:H, polycrystalline Si, and dye-sensitised $TiO_2$, except in terms of stability. These problems relate mainly to sensitivity to ambient water, for which encapsulation methods have been developed, and intrinsic issues, e.g., migration of ionic defects to the layer interfaces that hampers charge extraction. The outlook for integrated devices, such as the tandem perovskite/Si cell, is excellent with theoretical efficiencies estimated at over 40% [89]. As earth-abundant materials that may substitute for Pt, $IrO_2$, and $RuO_2$ in water electrolyzers, Ni-based alloys, oxides, nitrides, and phosphides look promising but mainly for use in alkali [90]. These include Ni/Mo in metallic or partially oxidised forms as cathodes for the $H_2$ evolution reaction (HER) [91,92]. As prospective anodes for the more problematic $O_2$ evolution reaction (OER), Ni-Fe layered double hydroxides (LDH) and Co/Fe/Ni oxides lead the field [93,94].

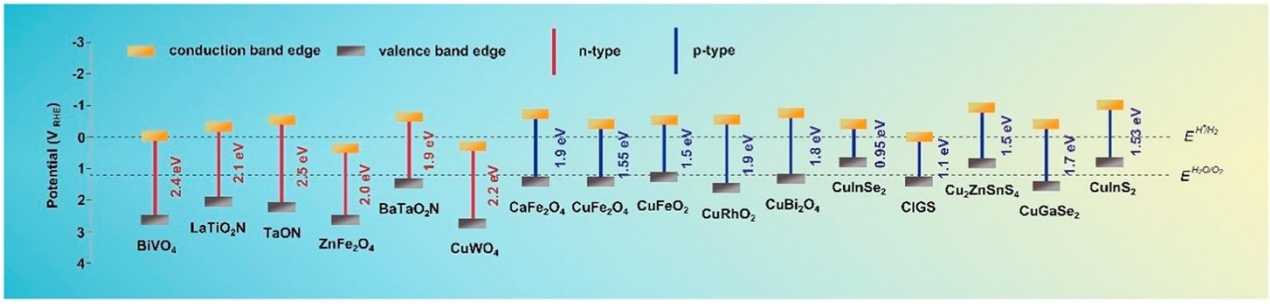


**Fig. 6** Band structure of emerging n- and p-type multinary semiconductor compounds. The bandgap energy is shown with respect to the reversible hydrogen electrode and the water redox energy levels (Reproduced with permission from ref. 107).

### 4.2.2. PEC and hybrid devices

The search for new semiconductor photoelectrode materials that are efficient, stable, earth-abundant, having broad (solar spectral) absorption and suitable energetics to drive solar fuel generation is an exacting but urgent task [95]. So much so that the use of *ab-initio* catalyst design [96,97] and combinatorial screening [98] are gaining in popularity due to advances in computational power, machine learning and robotics. New multinary oxides identified as candidate photoanodes include alkali-stable copper vanadates of suitable bandgap (Eg < 2 eV) based on the $CuO\text{-}V_2O_5$ system [99]. Elsewhere, two plumbates ($Ca_2PbO_4$, $Cu_2PbO_2$), a cobaltate ($NaCoO_2$), a bismuthate ($NaBiO_3$) and two silver compounds ($AgGaO_2$, $AgInO_2$) have been proposed [100]. While an automated high-throughput (statistical) strategy is a powerful tool at the "discovery" stage, revealing beneficial (synergistic) interactions between elements in materials of increasing complexity, it should be coupled with a "rational" approach to early development. Dealing directly with known limitations in established (promising) materials is vital. For example, good progress has been made in overcoming stability issues in cuprous oxide ($Cu_2O$) and countering the deleterious consequences of short carrier diffusion lengths in hematite (⟨-$Fe_2O_3$) and bismuth vanadate ($BiVO_4$). Grätzel *et al.*

450 have prepared a $TiO_2$-coated coaxial nanowire $Cu_2O$ photocathode with a $Cu_2O/Ga_2O_3$ buried
451 p-n junction and Ni/Mo as electrocatalyst, stable in alkali for >100 h [101]. A tandem device
452 with $BiVO_4$ as photoanode reached a solar-to-$H_2$ efficiency ($\eta_{STH}$) of 3.0%. This has now been
453 raised to 4.6% by using CuSCN as a hole transport material in a hybrid PEC-PV setup with a
454 perovskite solar cell [102].

455 Recent advances in the hematite (⟨-$Fe_2O_3$) photoanode have been summarised by
456 Tamirat *et al.* [103]. Allaying earlier concerns as to how PEC cells respond to solar light
457 intensity, a thin (50 nm) polycrystalline hematite film made by pulsed-laser deposition showed
458 a linear increase of photocurrent (and $O_2$ evolution rate) with incident flux. The photo-voltage
459 onset also shifted to lower potentials by 100-220 mV for a x10 increase in flux [104]. This
460 gain in performance for hematite has positive ramifications for practical devices linked to solar
461 concentrators (*vide infra*). Photoelectro-deposited ultra-thin (< 1 nm) transparent layers of
462 $CoFeO_x$ on hematite "nano-cauliflowers" resulted in a 7-fold increase in photocurrent in 1M
463 KOH [105], ascribed to a genuine catalytic effect raising charge injection efficiency at the
464 semiconductor/electrolyte interface. Bismuth vanadate ($BiVO_4$, Eg ~ 2.4 eV) suffers from
465 similar limitations to hematite [106,107], but nano-texturing mitigates issues to do with its
466 short carrier (hole) diffusion length and improves light trapping. A core-shell $WO_3$-$BiVO_4$
467 nanorod photoanode (with cobalt-phosphate CoPi as co-catalyst) reached a photocurrent of
468 6.7 mA $cm^{-2}$ ($\eta_{STH}$ = 8.1%) under 1 sun at 1.23 $V_{RHE}$, corresponding to ~90% of the
469 theoretical value [108]. However, there are stability concerns in alkali [109] and problems
470 with surface charge recombination [110].

471 New copper-based (p-type) multinary oxides $Cu_xM_yO_z$ (M = V, Ta, Fe, etc.) are
472 attracting interest as inexpensive photocathodes amenable to sol-gel processing [111].
473 Delafossite ($CuFeO_2$) appears an especially promising earth-abundant material with a low
474 bandgap (Eg ~1.5 eV) and a high conduction band position (-0.4 $V_{RHE}$) suitable to drive $H_2$

475 evolution [107,112]. Its main limitation is poor charge separation but this is being dealt with
476 at the preparative stage, e.g., by nano-scaffolding [113]. Other p-type oxides under study are
477 copper bismuthite ($CuBi_2O_4$) and calcium ferrite ($CaFe_2O_4$) spinels. With band-gaps of ~1.75
478 eV [107,112] and ~1.9 eV [107] respectively, either would be ideal as the top layer in a tandem
479 absorber. Their high conduction band edges at -0.8 $V_{RHE}$ [114] and −0.6 $V_{RHE}$ [107] make
480 them promising photocathodes [115,116]. However, poor charge transport and stability need
481 attention [117,118], and more facile and scalable preparative routes must be sought [119].
482 In view of their success in solar cells, perovskite halides (methyl ammonium lead
483 halides, $MAPX_3$) are being explored as photo-electrocatalysts [120]. Simple halide
484 substitution allows wide adjustment in the band-gap [121], e.g., from 1.5 eV in MAPI up to
485 2.2 eV in MAPBr, and 2.9 eV in MAPCl, as shown in Fig. 7. Related shifts in the valence
486 band edge position lead to better matching with the energetics of important interfacial redox
487 processes, e.g., water photo-splitting, although they are most suited for the reduction half-cell
488 ($H_2$ evolution). The main obstacle is their instability in liquids, and especially aqueous
489 environments. Most success has come by working in saturated halide solution, developing all-
490 inorganic systems of higher intrinsic stability, or using an encapsulation approach. While
491 MAPI has already been used in a tandem PV-E cell to drive water electrolysis at high
492 efficiency (12.3%), it was not immersed in the electrolyte [122]. A promising candidate for
493 direct use in PEC cells is the all-inorganic $CsPbBr_3$, which was tested as a photoanode in $O_2$
494 evolution in aqueous electrolyte [123]. Contact with a mesoporous carbon layer acting as hole
495 transporter improved electrode kinetics and enabled operation at thermodynamically
496 reversible potential (1.23 $V_{RHE}$). Encapsulation by a hydrophobic graphite sheet resulted in a
497 workable current density (> 2 $mA.cm^{-2}$) stable over 30 h in alkaline electrolyte (pH = 12.5).
498 Protection of perovskites as suspended particulate photocatalysts is a more severe challenge,
499 although a core-shell approach shows early promise. A $TiO_2$ shell on a $CsPbBr_3$ core is

suitably transparent to visible light and mediates charge transfer. In addition, its UV absorption shields the core material from photo-instability [124]. However, pristine $TiO_2$ is a poor water-splitting catalyst and co-catalysts are needed in further development work.

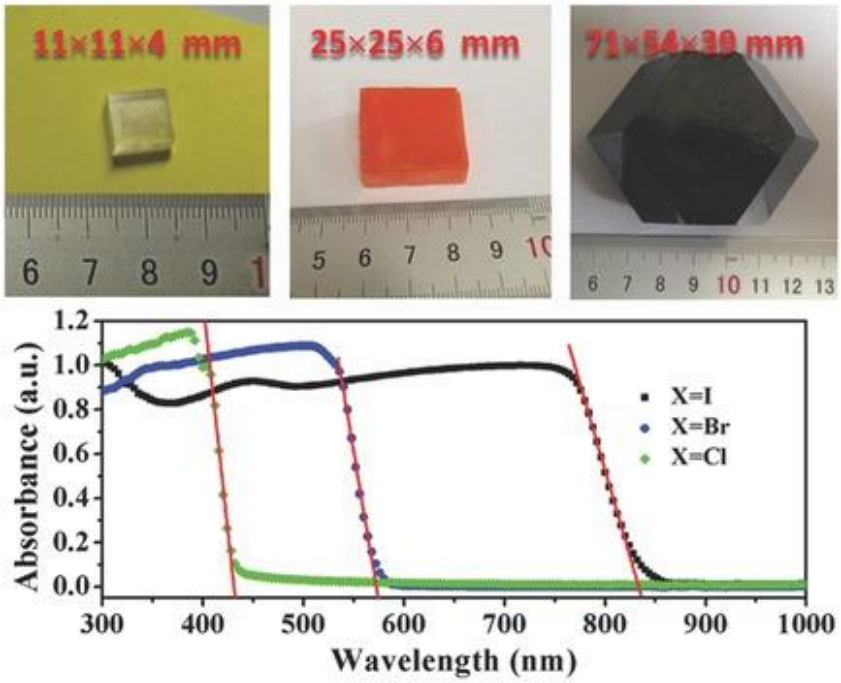


**Fig. 9.** Typical single crystals of $CH_3NH_3PbX_3$ (X = I, Br, Cl) and their wide-ranging band edges (reproduced with permission from ref. 121)

### 4.2.3. Particulate photocatalysts

Much current research on "self-biasing" particulate photocatalysts is concerned with new semiconductor materials, e.g., metal- and carbon nitrides [125], multinary oxides [126], phosphors [127], etc., that are better at solar light harvesting [128]. Apparent quantum efficiencies (AQE) achieved under visible light are continuously increasing [129-131]. Nevertheless, boosting efficiencies by visible-light sensitization of established wide bandgap oxide materials is still a promising strategy [132]. In this regard, a key role for $TiO_2$ is in hierarchical (e.g., core-shell heterojunction) structures due to its protective action and visible-

light transparency [133]. In their benchmark techno-economic assessment, Pinaud et al. [75] concluded that *photocatalytic* water splitting (type I case, with co-generation of $H_2$ and $O_2$ in the same collection space) would offer the lowest levelized cost of $H_2$ (USD 1.60 $kg^{-1}$), based on a solar-to-hydrogen efficiency of 10%. Unfortunately, the highest efficiencies reported fall short of this US DOE target value. Liao et al. reported a peak efficiency of $\eta_{STH}$ = 5.0% for nanoparticulate CoO, an encouraging result for a single-phase material in the absence of co-catalysts or sacrificial agents [134]. This has recently been exceeded by Tian et al. [135], achieving $\eta_{STH}$= 5.45% in black phosphorus by working at 80°C (to exploit strong thermal enhancement) and utilising cobalt phosphide as $H_2$ evolution co-catalyst [136]. In contrast, energy conversion efficiencies in scaled-up testing have not yet exceeded 0.5% for any material [137,138]. This is an order of magnitude lower than those obtained for "wired" (PV-E and PEC) devices. Whereas CoO was unstable, deactivating after one hour, the black phosphorus system showed good stability during 40 h of $H_2$ evolution cycling. Evidence was also found for $H_2O_2$ and peroxy species, potentially valuable co-products from water photo-oxidation. As regards long-term stability testing, a carbon dot/$C_3N_4$ composite ($\eta_{STH}$ = 2.0%) leads the way with stable $H_2$ evolution cycling demonstrated over 200 h, albeit in the Laboratory [130].

Despite this mixed outlook, there remains a financial incentive to explore particulate photocatalyst systems of type II, including separate compartments for $H_2$ and $O_2$ evolution (from safety concerns) and ideally in a vertically-stacked tandem absorber layout. Porous connectors between compartments enable charge-transfer via solution chemical redox shuttles in a so-called Z-scheme [139]. Follow-up work on particle suspension reactors, including theoretical design, efficiency metrics, transport and kinetic modelling, etc., has been reported by the Ardo group [140].

## 5. Carbon capture utilisation and sequestration

Substantial levels of high-purity $CO_2$ being available on-site in a biorefinery, e.g. from starch/sugar fermentation, bio-gas, etc., the outlook is thereby extended to emerging technologies such as bioenergy with carbon capture and sequestration (BECCS) and direct air capture and sequestration (DACS), in which the role of absorbers, solvents, adsorbents, membranes and related processes (electro-swing, chemical looping, etc.) will be pivotal. Advances in carbon capture and utilisation at laboratory and technical scale are in consequence summarised in that section, when underpinning the role of carbon dioxide as recyclable substrate.

### 5.1. 21st Century climate management

Global concerns about climate change have led to a policy framework, designed and endorsed by the Intergovernmental Panel on Climate Change (IPCC) at COP 21 (Paris, 2015), to limit 21st Century global warming to below 2°C, or to a maximum permissible atmospheric $CO_2$ level of 450 ppm. This is an ambitious mitigation strategy with an explicit target of achieving "net zero-emissions" by 2050 [141]. In the transition to a renewables-based economy, if progress in decarbonization, deintensification, and electrification of the energy sector appears insufficient or too slow, more direct means of lowering atmospheric $CO_2$ levels must be implemented [142].

#### 5.1.1. Negative Emission Technologies (NETs).

The solution proposed by IPCC is deployment of carbon capture and sequestration (CCS) and "negative emission technologies" (NETs) on a massive scale [143,144]. Neither strategy is yet proven even at a $Mt_{CO2}$/year scale, or 0.1% of the scale ultimately envisaged [141]. The entire policy and its tacit assumptions have provoked scepticism and controversy [145-147],

not least over the geopolitical and moral imperatives of reaching a fair distribution of costs, making a clear demarcation between subsistence and luxury emissions [148,149]. Implicit is an obligation by the "top emitter" countries (responsible for >80% of global emissions [150]) to reign in their lifestyle ambitions so that United Nations programs can proceed unimpeded, e.g., sustainable development and poverty alleviation in the 3rd world. A key determinant in this socio-political arena will be the fortitude of governments to impose more severe measures, e.g., *pro rata* energy consumption taxes, on its most profligate corporations and citizenry. Integrated assessment models (IAMs) classify several processes involving carbon dioxide removal (CDR) as negative emissions technologies (NETs).

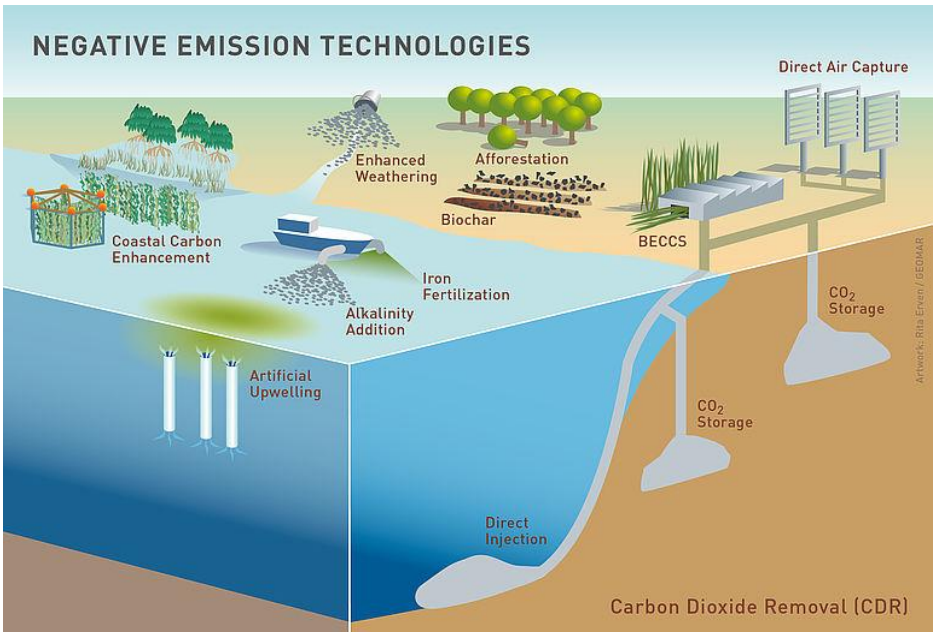


**Fig. 8** Scheme illustrating the range of Negative Emissions Technologies (NETs) (Reproduced with permission from ref. 151) (©) Rita Erven/Geomar.

The two main technical processes are bioenergy with carbon capture and sequestration (BECCS) [152] and direct air capture (DACS) [153,154]. In either case, the $CO_2$ disposal option under consideration is *physical*, i.e., liquefaction and injection into subterranean aquifers or

583 deep ocean beds, as shown in Fig. 8, taken from Ref. 151. Permanent storage of $CO_2$ is an
584 expensive process, difficult to monitor, and prone to leaks and reversibility on a geological
585 timescale [155]. It is increasingly recognized that reservoirs offering in-situ *chemical* fixation,
586 e.g., carbonate formation in porous basalts and alkaline peridotites [156], should be prioritised
587 as more effective in mitigating risk.
588
589 **Bioenergy with carbon capture and sequestration (BECCS).**
590 A bioenergy facility is a power station that combusts biomass to provide renewable heat
591 and power. If $CO_2$ in the vent stream is trapped by carbon capture and sequestration (CCS), the
592 "avoided" emissions qualify as *indirect* negative emissions since this biogenic $CO_2$ was
593 originally sourced from the atmosphere by natural photosynthesis. The largest BECCS utility
594 (50 MW, 500 $t_{CO2}$/day) in operation is the Mikawa power plant (Toshiba ESS [157]) running
595 on palm kernel shell. The CCS component is post combustion capture [143] based on
596 proprietary amine solvents in a 50 m absorber tower. The much larger (2.4 GW) DRAX plant
597 in the UK, adapted for biomass fuel, will not be "carbon-negative" until 2030 [158].
598 Nevertheless, the huge scale implicit in the 2°C warming limit implies thousands of such
599 utilities operating at today's maximum capacity (1 $Mt_{CO2}$/y) by 2050. The general consensus is
600 that the key limitation of BECCS will be that of sustainable biomass supply, currently estimated
601 at ~100 EJ/y, based on 500 Mha land area to grow dedicated energy crops. This represents
602 ~15% of primary energy supply as projected to 2050 [159]. Curiously, from a human cultural
603 perspective a global change in food agriculture away from livestock towards vegetarianism
604 could free up just such an area [143], equivalent to ~10% of agricultural land, or that dedicated
605 to cereals. Such is the resource-intensive inefficiency of today's agro-industry oriented towards
606 meat, eggs and dairy produce, occupying 70% of cultivable land and responsible for ~15% of
607 GHG emissions [160].

608

609 **Direct air capture with carbon sequestration (DACCS).**

610 Direct air capture (DAC) refers to a utility that traps atmospheric $CO_2$ by prolonged air
611 contact or circulation over basic solid adsorbents or liquid alkali absorbents. Depending on the
612 system operating cycle, periodic or continuous regeneration, i.e., $CO_2$ release with
613 pressurisation and storage, is the main heat energy demand stage [143]. However, unlike
614 BECCS no power is generated and this "strategy of last resort" for climate mitigation is
615 expensive due to the high dilution factor (2500:1), requiring ~20 kJ/mol $CO_2$ (vs. 7.5 kJ/mol
616 ex. natural gas combustion) [146]. The techno-economics of DACCS is also more precarious
617 [161] and can only become viable in a market scenario with universal carbon pricing and
618 specific incentives for permanent storage/disposal (CCS), e.g., via government tax credits or
619 tradeable "green bonds". DAC proponents find motivation based on a few key drivers. In the
620 present era of transportation fuel usage, especially in the aviation sector, it's the only means of
621 emissions mitigation since on-board trapping is impracticable [162].

622 Alternatively, the same problem (mobile emissions) can be tackled at source by recycling
623 the $CO_2$ and producing zero-emission synthetic fuels from renewable syngas. However, this
624 carbon capture and utilisation (CCU) approach effectively disqualifies DAC as a negative
625 emissions technology unless it is used to build up a massive "strategic fuel reserve" over an
626 extended period. Finally, it can be argued that DAC acts as an insurance policy ("techno-fix")
627 against accidental leakage from geological storage sites.

628

629 **5.2.Fundamental and technical progress**

630 **5.2.1. CCU – Indirect contributor to climate change mitigation**

631 Although the science behind $CO_2$ capture makes no distinction on the basis of carbon
632 sourcing or end use, this review will focus on recovery methods offering technical synergies in
633 CCU scenarios, e.g. $CO_2$ utilisation as a "reactive liquefier" for $H_2$ in renewable syngas

conversion to sustainable fuels [21]. Combustion of liquid fuels causes the emission of ~10 $Gt_{CO2}$/y, or 25% of the global total (42 $Gt_{CO2}$/y [141]). While biofuels satisfy a low but increasing fraction of transportation demand (3% in 2018), growth is lagging behind the IEA target rate in many countries (ASEAN excepted) aimed at reaching 9% market penetration by 2030 [163]. To achieve defossilisation of the transportation sector by 2050, biofuels need to be bolstered by synthetic routes to zero-emission fuels based on recycled $CO_2$ and electrolytic $H_2$ (e-fuels). These so-called power-to- liquids (PtL) catalytic technologies are not yet economically competitive due to the high price of e-$H_2$ [164]. While modelling studies show that CCU (via synthetic fuels) *per se* is a poor strategy for *direct* mitigation of climate change, providing only a temporary period of $CO_2$ removal [165,166], it has a major role to play *indirectly* by easing the load on natural sinks to slowly recover the "excess". The combined action of land (15 Gt) and ocean (9 Gt) sinks captures ~24 Gt annually [167]. Curiously, a state of net negative imbalance in atmospheric $CO_2$ (emissions rate < trapping rate) is rarely considered in climate mitigation modelling [168] even though it is a highly symbolic landmark and achievable earlier than zero emissions under the more ambitious 2°C scenario. Allowing for inertia (feedback) in the global carbon cycle, evidence for any positive impact might be expected some 10-15 years after passing the "break-even" point. In any event, major progress in decarbonization of the energy sector by mid-century is essential [169]. An early landmark is to go beyond "peak emissions" (a turning point now unlikely to occur by 2020 as forecast [170]), and then maintain a sustained fall in emissions rate of 1.6% per year over the next 3 decades. There are no "quick fixes" to global warming, but then it was, after all, the unremitting burning of fossil fuels for over a century that landed us in this predicament.

### 5.2.2. Scientific advances

The scheme in Fig. 9, taken from a recent CCU review [171], provides a good overview of scientific advances in materials and processes covered in this section.

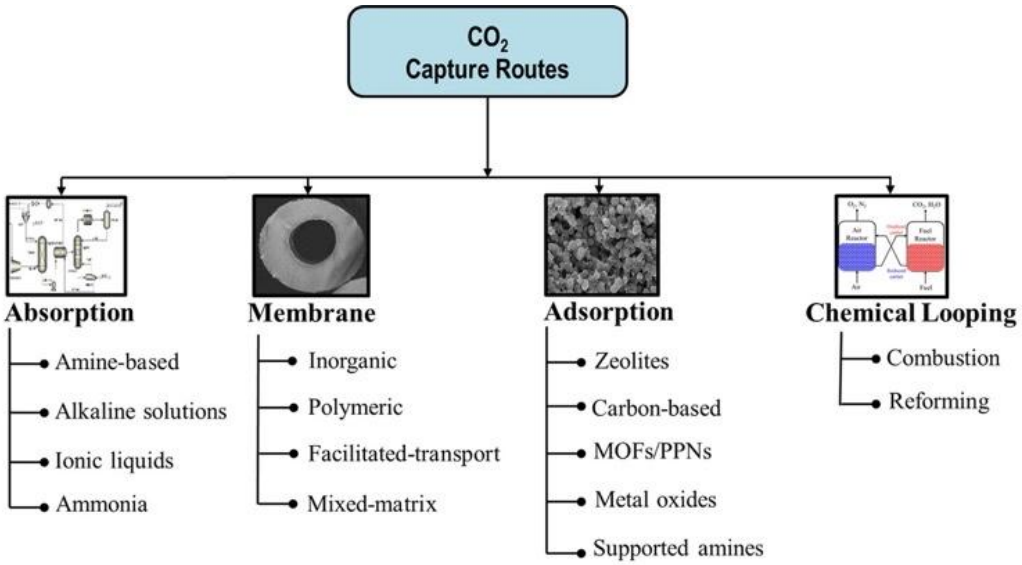


**Fig. 9** Materials and processes for $CO_2$ capture. [Adapted with permission from ref. 171]

- **Absorbers/solvents**

Aqueous monoethanolamine (MEA) remains the benchmark absorber or solvent for $CO_2$ capture at industrial scale in spite of recognized limitations, i.e., high energetics of regeneration (~4 GJ/$t_{CO2}$) and degradation in use. Due to these concerns, multi-component amine blends containing piperazine (PZ) to promote mass transfer, and the sterically hindered 2-amino-2-methyl-1-propanol (AMP) - favouring $CO_2$ desorption via the more labile bicarbonate intermediate -, are superior in some respects [172]. However, blend compositions are limited to $\leq$ 10 wt% PZ to avoid the switch to a complex (multi-phase) absorber system via precipitation of ammonium carbamate/bicarbonate. The same effect was heralded as a benefit in the main rival system, the chilled ammonia process (CAP) originally developed by Alstom (now GE), but this was eschewed in scale-up work [173]. Regeneration is less-demanding at < 3 GJ/$t_{CO2}$, with energy estimates falling to 2.2 GJ/$t_{CO2}$. While there is no solvent degradation, the high volatility of $NH_3$ risks fugitive toxic emissions. A merging of solvent systems based on a synergy between piperazine and aqueous ammonia has recently been explored with encouraging results [174]. Addition of a low level of piperazine ($NH_3$:PZ = 16:1) promotes the

679 low intrinsic rate of the $NH_3/CO_2$ interaction and also lowers the $NH_3$ regeneration heat demand
680 to < 2 GJ/$t_{CO2}$ in a simulated advance flash stripper process.
681

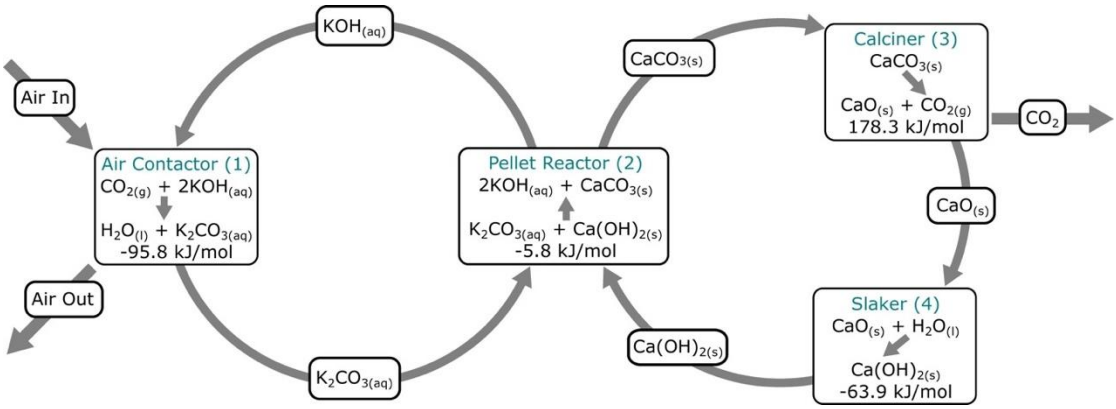

682

683 **Fig. 10** The chemical and thermodynamic of DAC based on Ca and K loop exchange
684 (Reproduced with permission from ref. 153).
685

686 Another notable absorber worthy of mention is aqueous KOH. In one variant of direct air
687 capture technology (GE Eng.) based on connected chemical (K, Ca) loops (see Fig. 10), a 50
688 μm film of KOH fed into a structured plastic bed forms soluble $K_2CO_3$ (air contact in cross-
689 flow) that exchanges with $Ca(OH)_2$ in counterflow to replenish the alkali and precipitate $CaCO_3$
690 for isolation and regeneration by calcination and slaking. Despite the high temperature in the
691 calciner (900°C), the process energy demand is just 8.8 GJ/$t_{CO2}$, leading to levelized costs
692 ranging from USD 94-232/$t_{CO2}$. An emerging class of materials with good prospects as green
693 solvents for carbon capture are ionic liquids (ILs) [175]. Their negligible vapour pressures and
694 high thermal stabilities facilitate regeneration (pressure-, temperature-swing, etc.) over a wide
695 range of conditions in which evaporative and degradative losses are minimal. Their solvent
696 properties are tunable by composition, with the tetracyanoborate [$B(CN)_4^-$] anion conferring a
697 high $CO_2$ capacity of ~0.15 mol $L^{-1}$ $atm^{-1}$ to the 1-ethyl-3-methylimidazolium [emim] salt. This
698 is attributed to a reduced cation/anion interaction [176]. Their disadvantages are high cost, high

699 viscosity and reactivity with water [177]. Most recently, amine-functionalized ILs are under
700 study as components in hybrid sorbents, e.g., in micro-encapsulated or supported forms, to
701 improve mass transfer [175,178,179].
702
703 - **Adsorbents**
704 Nanoporous solids are almost ideal materials for post- combustion (flue gas) $CO_2$ capture
705 at low temperature (< 200°C) [180,181], and come in a burgeoning variety of classes, e.g.,
706 base-functionalized zeolites (ZIFs), silicas, aluminas [182], metal-organic frameworks (MOFs
707 [183]), porous organic polymers (POPs [184]), carbonaceous materials [185,186], alkaline
708 earth oxides [187], and hybrids of the above [188]. Their adsorptive, structural, and textural
709 properties are readily tunable for low-cost (reversible adsorption) energetics, high
710 capacity/selectivity, fast kinetics, stability in recycling, and compatibility with "parameter
711 swing" processes (vacuum/pressure-, temperature-, etc.). $CO_2$ capacities reach or exceed 5
712 mmol/g under conditions typical for flue gas ($P_{CO2}$ < 1 bar, T < 50°C), although working
713 capacities under practical (time-restricted) cycling are somewhat lower.
714 The immense scope for new formulations based on rational design, along with high-
715 throughput screening, is spearheading combinatorial research strategies, particularly in MOFs
716 [189,190], zeolites [191], and a relatively new class - covalent organic frameworks (COFs)
717 [192]. The Cambridge Structural Database has been expanding at an exponential rate with
718 doubling times of less than 5 years in the case of MOFs [193]. The key strategy in
719 computational materials discovery is to find suitable chemical and/or textural (pore-related)
720 "descriptors" for the search algorithm that underpin the desired properties. Topological data
721 analysis (TDA), which deals with pore shape, is a purely structural approach that has
722 impressive predictive power, ranking quite accurately the known high-performing zeolites
723 among a wide virtual range [191]. A wider geometric landscape in materials discovery,
724 obtained via energy-structure-function (ESF) maps [194], is proving valuable in pre-screening

porous molecular crystals as practical adsorbents. These are a new class having only weak intermolecular interactions [195], unlike 3D- reticulated MOFs and COFs [196]. Despite the impressive rate of prediction (and successful syntheses) of promising new materials, the best candidates need to be rapidly carried forward into practical testing (and engineering) at scale. For example, methodologies to formulate fine-powder MOFs into gels and monoliths for adsorption columns has just been reported [197].

The main limitation of adsorbents for $CO_2$ capture from flue gas and other point-source industrial emissions, is interference due to competitive adsorption by water. This almost invariably suppresses the $CO_2$ capacity, especially in non-functionalized physisorbents. However, a recent paper describes a cyclic diamine-modified Mg-MOF that works better in humid $CO_2$ [198]. This problem is also amenable to solution by computational screening. The search for MOFs bearing hydrophobic "absorbaphores" has led to the synthesis of several new candidates that work well in humid conditions [199]. Sorbents for direct air capture (DAC) are under even greater constraints as water is present in excess. Indeed, systems based on adsorptive synergies in $CO_2/H_2O$ also offer good prospects. Emerging as a sub-branch of amine-functionalization strategies [200], the Lackner group has developed ion exchange resins (IERs) with appended highly-basic quaternary ammonium ($NR_3^+$) groups [154,201]. The $CO_2$ uptake and anion chemistry are switchable depending on the presence or absence of water as shown in Fig. 11. In state 1, the carbonate ($CO_3^{2-}$) ion is stabilised by coordinated water [$n_{H2O}$ (n=6-8)]. Upon drying, a water molecule dissociates [202], protonating carbonate and leaving a hydroxyl group (state 2) that adsorbs $CO_2$ to form a 2$^{nd}$ bicarbonate ion ($HCO_3^-$, state 3). Upon humidification, the bicarbonates are destabilised, releasing $H_2O$ and $CO_2$ (state 4) but one $CO_2$ moiety is retained as carbonate ion stabilised in excess water (state 1, cycle closure). The humidity swing principle has since been extended to phosphate-based ion exchange resins [203] and polymeric ILs [204].

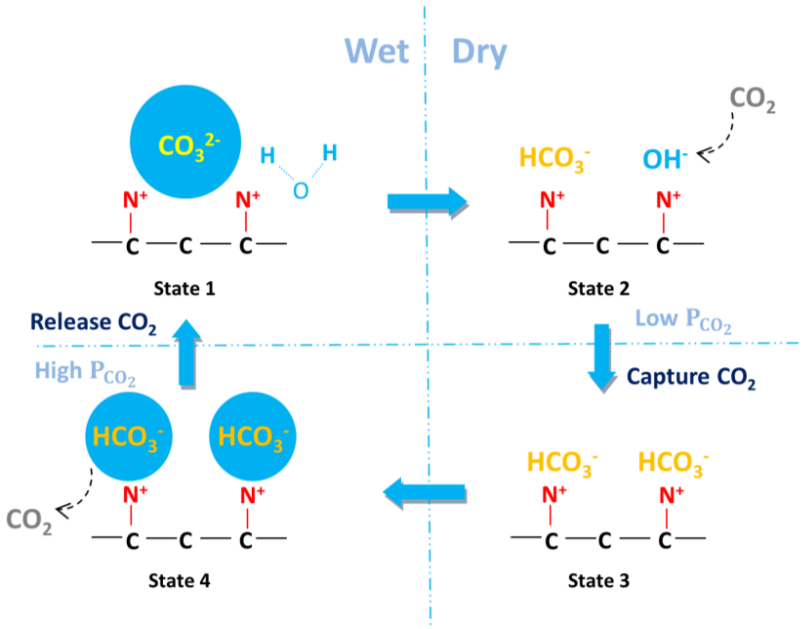


**Fig. 11** Likely mechanism of $CO_2$ capture from air over quaternary ammonium-based anionic resins. (adapted with permission from ref. 154)

- **Membranes**

Membranes separate gas mixtures via selective permeation of one component ($CO_2$) across a thin (50-150 ⌈m) film offering minimal mass transfer resistance (high permeance). A great deal of materials research has been directed at improving the inevitable trade-off between selectivity and permeability, or breaking through the so-called *Robeson upper bound* [205]. Typically made from cheap organic polymer or inorganic materials, they are potentially low cost, low-energy demand alternatives to amine absorption [206]. Polymers are easily processed but have low permeability and limited physico-chemical stability. In contrast, inorganic sorbents like zeolites, silica, carbon, etc., combine high permeability and selectivity with robustness (high T/P stability) but are difficult to fabricate in thin defect-free layers due to brittleness. Thus, the recent trend is towards hybrid or *mixed-matrix* membranes (MMMs), i.e., polymers filled with inorganic phases, ideally to couple the benefits of each component. These are homogeneous films with interdispersed phases or structured multilayer composites with directional functionalities [207].

Polar groups such as the ether O in polyethylene oxide (PEO) act as solvating species promoting hydrophilicity and $CO_2/N_2$ selectivity [208,209]. Permeability can be raised by increasing porosity, aiming for a specific (and uniform) cavity size by judicious selection of the polyimide precursor, followed by thermal rearrangement (TR).

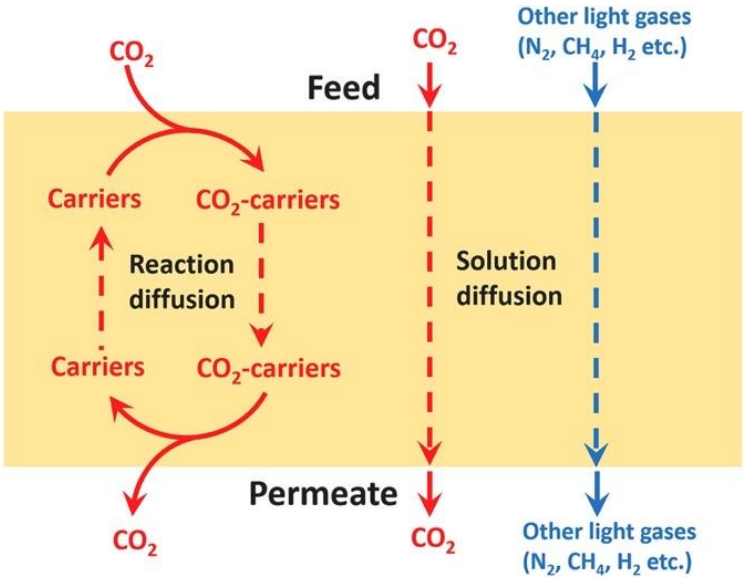


**Fig. 12** Gas permeation mechanism in a facilitated transport membrane (FTM) (Taken with permission from ref. 207).

A special class of polymers showing promise are *facilitated transport* membranes (FTMs). These efficiently separate $CO_2/X$ (X = $N_2$, $H_2$, $CH_4$) mixtures via reactive carrier species that selectively (but reversibly) bind to $CO_2$ (see Fig. 12 -left side). This active mode of transport augments regular diffusion (Fig. 12 - centre/right) and is faster by an order of magnitude. Primary/secondary amino, tertiary amines, and carboxylates are common pendant groups. Amino groups form metastable carbamates in the dry state but the process occurs much faster in the presence of water. Tertiary amine/carboxylates catalyse hydration of $CO_2$ to bi-carbonate ($HCO_3^-$) ion that migrates via an ionic diffusion mechanism [207]. However, control of the hydration state of the membrane for reproducible transport is problematic although some

progress has been made by doping with Ca salts [209]. Recent interest is also being shown in ionic liquids where the anions act as $CO_2$ carriers [210,211]. The Robeson plot shown in Fig. 13 highlights the exceptional performance of FTMs, along with *polymers of intrinsic microporosity* (PIMs) [212] and non-polymer types, mostly self- supporting zeolites [213].

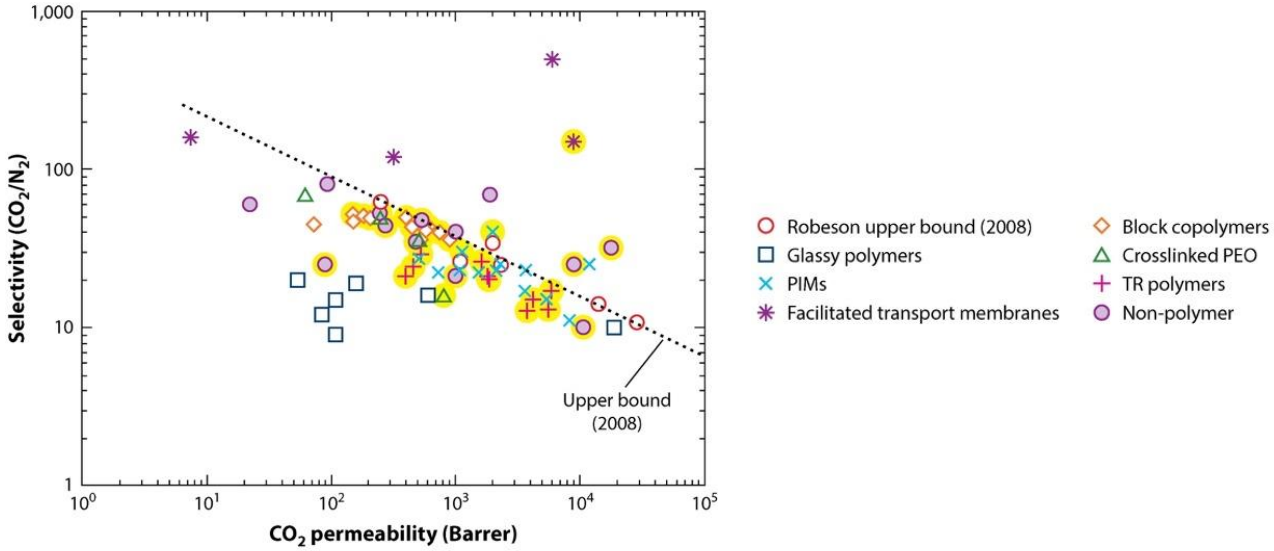


**Fig. 13** Robeson plot ($CO_2/N_2$ selectivity vs. $CO_2$ permeability. Data shaded in yellow is the most recent (2010-2014) (Taken with permission from ref. 212)

### 5.2.3. Process technical advances

- **Electric-/electro-Swing**

Trapping and release of $CO_2$ over adsorbents involves a parameter-swing cycle that suffers from lower energy penalties and negligible material losses (by volatility and degradation) as compared to MEA solvent scrubbing. However, pressure-swing adsorption is not suited for post-combustion $CO_2$ recovery (flue gas at 1 bar), whereas temperature-swing adsorption (TSA) suffers from the large thermal inertia of packed solid beds. This leads to long cycle times (hours) and restricts throughput, marginalising the techno-economics at scale [214]. A promising variant offering rapid and efficient cycling via localised heat delivery is electrical- or electric-swing adsorption (ESA) although its basis in the Joule effect restricts the choice of

adsorbent to electrical conductors, e.g., carbon monoliths, or C-rich zeolite 13X composites [215,216]. The specific energy demand of ESA is slightly higher than TSA, viz., 5.6 MJ/$kg_{CO2}$ vs. 4.0 MJ/$kg_{CO2}$ [215], arising mainly from inefficient electrodes typically responsible for up to 50% power losses by high contact resistance.

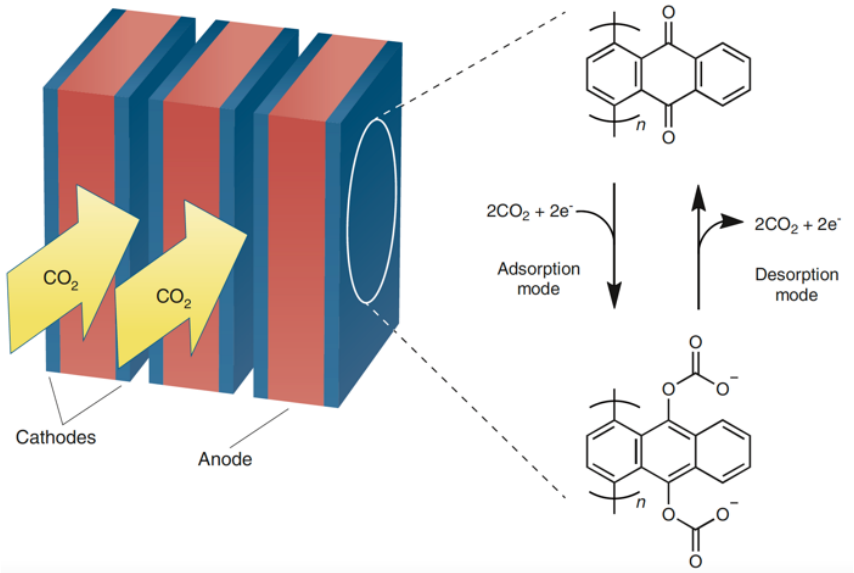


**Fig. 14** Electro-swing principle based on quinone redox cycling (Reproduced with permission from ref. 217)

Specialised methods based on electrochemical principles are now emerging that may open up major new directions in carbon capture. These are classified under the collective term *electro-swing* technologies [217] but are not to be confused with the foregoing electro-thermal approach to $CO_2$ desorption as no heating steps are involved. As shown in Fig. 14, the key process in the "Faradaic electro-swing reactive adsorber" [218] is the electrochemical conversion of two molecules of $CO_2$ to adsorbed carboxylate:

$$2\ CO_2 + 2\ e^- \rightarrow 2\ COO^-_{ad} \quad (9)$$

825 The cathode material, a solid polymer of 1,4-anthraquinone (PAQ), is made conductive
826 by compositing with multi-walled carbon nanotubes (CNT). The cell is laid out in sandwich
827 form, a polyvinylferrocene-CNT anode serving as filler, with the entire electrode assembly
828 mounted on a carbon fibre mat. This acts as a porous matrix to optimise contact area for flow
829 access (via a gas-saturated IL electrolyte) and confers high conductivity via π-π PAQ/CNT
830 interactions. It responds to $CO_2$ levels as low as 0.6% although maximum capacity (1.7 mmol/g
831 sorbent) is only achieved in a pure stream. As regards chemical interference, humidity is largely
832 excluded by the hydrophobic IL electrolyte but is relatively benign. Molecular oxygen may
833 potentially form the superoxide radical anion ($O_2^{\circ -}$) but this can be suppressed by limiting the
834 voltage of the cathodic swing. Rapid and efficient cycling are key benefits of ESA along with
835 an almost ideal working capacity (rectangular isotherm), unlike PSA or TSA as shown in Fig.
836 15. A state of full "charge" (>1.5 $CO_2$/mol AQ or 0.9 mmol/g at 15% $CO_2$) is attained in just
837 15 min at > 90% Faradaic efficiency. $CO_2$ desorption is activated by simple reversal of polarity.
838 Its quasi-instantaneous response should enable direct coupling to intermittent renewable
839 energies, providing a valuable diversion for curtailed (grid-excess) power [219]. The energetics
840 (40-90 kJ/mol $CO_2$ or 0.9-2 MJ/$kg_{CO2}$) are highly favourable, ranging from 20-40 % of values
841 for solvent scrubbing. The durability is good, recording a gradual loss in capacity of just 30%
842 after 7000 cycles. The modularity and compactness of cell design offers flexibility in scale-up,
843 qualifying ESA as a potential technology-disruptive advance. The main drawbacks are $O_2$
844 sensitivity of the anthraquinone and the current high cost of the electrode materials [217].
845

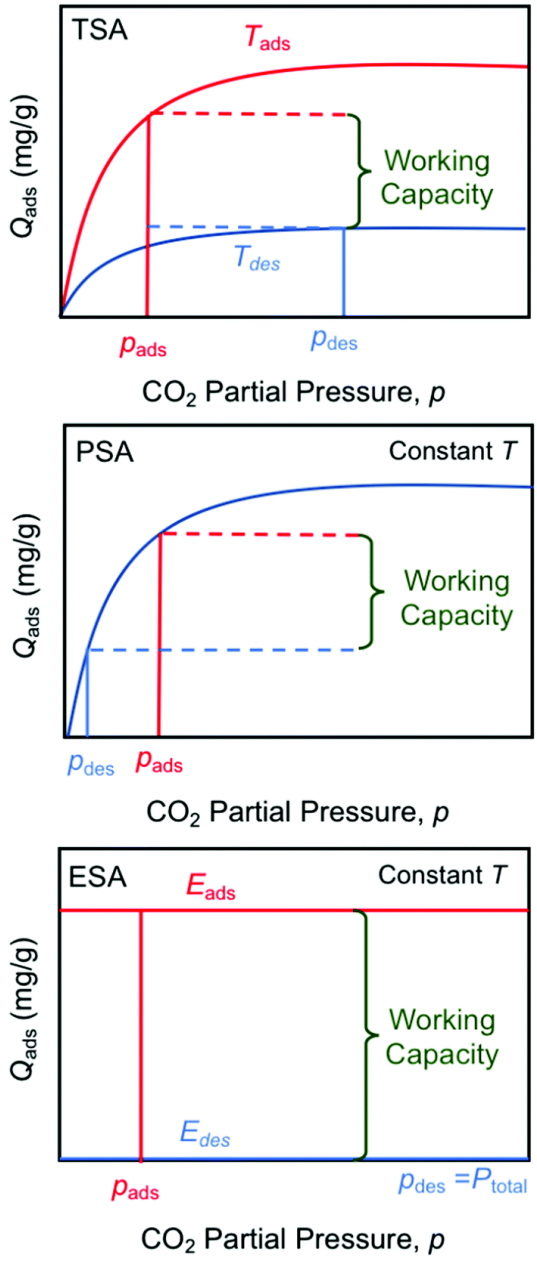


**Fig. 15** Working capacities of various parameter-swing schemes (Reproduced with permission from ref. 217)

Inspired by similar work from Legrand et al. [220] on solvent-free $CO_2$ trapping by membrane capacitive deionization (MCDI), the Hatton group at MIT report a novel electrochemical pH-swing approach to capture $CO_2$ as bicarbonate and carbonate (at high pH) and release it (at low pH) via reversible de-intercalation of protons in a supercapacitive $MnO_2$

electrode [221]. The working principle of the proton concentration process (PCP) is illustrated in Fig. 16.

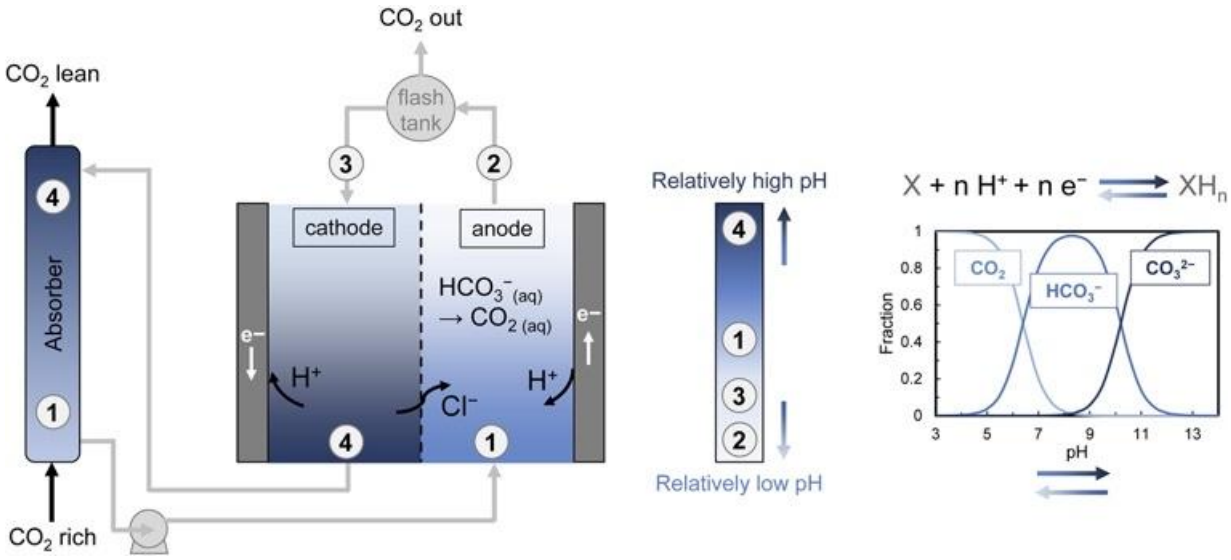


**Fig. 16** $CO_2$ trapping cycle based on pH-modulated hydration chemistry with intercalation/de-intercalation of protons in a supercapacitive $MnO_2$ electrode. (Reproduced with permission from ref. 221).

A $CO_2$-rich stream is fed into an absorber tank containing 1M $K_2CO_3$ (pH 11) for rapid $CO_2$ trapping via the bicarbonate/carbonate couple:

$$CO_{2\,(aq)} + H_2O + K_2CO_3 \rightarrow 2\ KHCO_3\ (aq) \quad (10)$$

$$HCO_3^-{}_{(aq)} \rightarrow CO_3^{2-}{}_{(aq)} + H^+{}_{(aq)} \quad (11)$$

As the level of absorbed $CO_2$ nears saturation [thermodynamic equilibrium curve – Fig. 16 (r)], the electrolyte is pumped into the anode compartment of an electrochemical cell [state (1)], where protons are released from an intercalated $MnO_2$ electrode charged from the previous cycle. This raises the acidity (pH $\leq$ 6.5) and dissolved (bi)-carbonates are de-stabilised [state

874 (1) → state (2)]. $CO_2$ is vented in a flash tank [state (2) → state (3)] during electrolyte transfer
875 into the cathode space, where intercalation proceeds in a twin $MnO_2$ electrode, likely forming
876 a metastable birnessite or manganese bronze ($H_xMn^{IV}_{1-x}Mn^{III}_xO_2$). Thus, the electrolyte is made
877 alkaline [pH $\geq$ 8, state (3) → state (4)], the regenerated solution is returned to the absorber
878 tank, and the polarity reversed (±1 V) to re-charge the anode for the next de-intercalation stage.
879 $MnO_2$ is a low-cost, earth-abundant, and eco-friendly material with a high theoretical
880 capacitance (1100 F $g^{-1}$). Based on an intercalation (Faradaic) efficiency of 0.7, and allowing
881 for modest surface and transport overpotentials (~25 mV), the energetics is conservatively
882 estimated at 33 $kJ_e/mol_{CO2}$. This is even below the range for the anthraquinone system. The
883 actual range of pH (swing) was restricted to 3 units even for the best case ($MnO_2$ mounted on
884 carbon felt) due to the non-ideal electrode capacitance (~100 F $g^{-1}$; 200 mF.$cm^{-2}$). Nevertheless,
885 the authors have succeeded in demonstrating proof-of-principle.
886
887 - **Chemical looping**
888 Chemical looping technology has grown in popularity due to its inherent ability to
889 facilitate carbon capture although its versatility in the use of redox (O) carriers in industrial
890 processing "beyond combustion" gives impetus for further exploration [222]. In its simplest
891 form, a cheap and abundant solid absorbs flue gas emissions and is regenerated periodically by
892 relocation on- stream, e.g., as a fluidized particle bed, to a reactor driven by diverted combustion
893 heat. This yields nearly pure $CO_2$ for downstream processing or permanent sequestration. The
894 most popular absorbent materials are alkaline earth metal oxides CaO [223] and CaO/MgO
895 [224], obtained from limestone ($CaCO_3$) or dolomite [$CaMg(CO_3)_2$], respectively. In Ca-
896 looping (CaL), $CO_2$ is absorbed at 600-700°C (see Fig. 17). where the exergy is more efficiently
897 recovered (for power co-generation), e.g., by using an organic Rankine cycle. However,
898 regeneration of the sorbents at high temperature (T > 900°C), mechanical attrition as brittle

solid in suspension, and poisoning by traces of $SO_2$ cause gradual but irreversible deactivation via sintering (shrinkage of porosity, surface area, etc.), decrepitation (particle fragmentation and elutriation), and loss of surface reactivity. These effects compound together such that sorbent performance deteriorates progressively from cycle to cycle. Advances have been made over all stages in the adsorbent development cycle, starting with precursor capacities in the range 4-15 $mmol.g^{-1}$ (bulk theoretical: 17.8 $mmol.g^{-1}$) have been attained, the highest from a calcium gluconate precursor [225]. Better sintering resistance has been obtained by loading CaO on refractory ceramic supports like $Ca_{12}Al_{14}O_{33}$, $CaTiO_3$, $CaZrO_3$, and $SiO_2$ [226]. A new report of robust $CO_2$ cycling over hierarchical porous Al-stabilized CaO prepared by microfluidic droplet templating also looks encouraging [227].

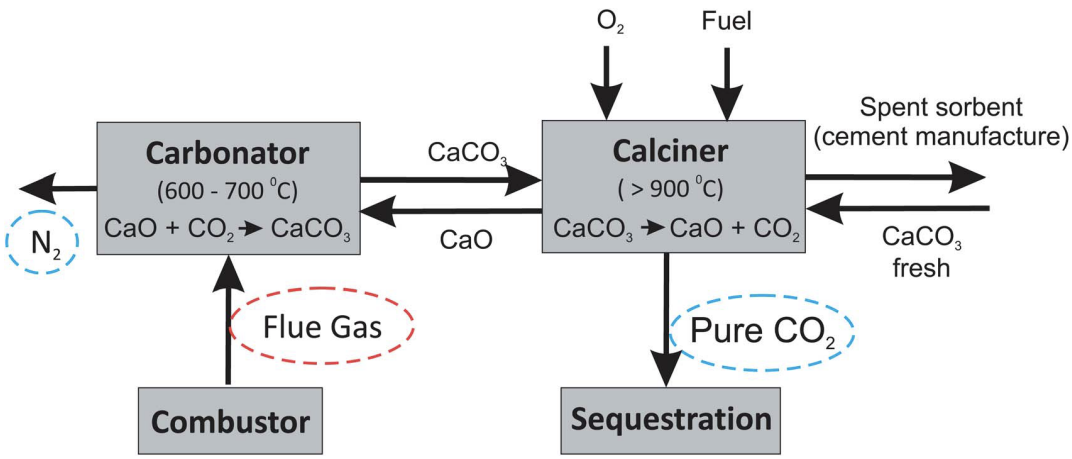


**Fig. 17** Schematic layout and material flows for $CO_2$ capture by Ca-looping (CaL) (Reproduced with permission from ref. 223)

Chemical looping combustion (CLC) is a popular alternative route with inherent $CO_2$ capture. Here, the fuel reacts separately with oxygen (O) atoms from reducible metal oxides like CuO, $Fe_2O_3$, etc [228]. This yields a nearly pure stream of products if the stoichiometry and reactor temperature are well-regulated to restrict carbon laydown, CO formation, and/or

unreacted fuel breakthrough. The CLC principle and typical metal oxide capacities are shown in Figs. 18A and 18B, respectively. Its recent adaptation to *solid* carbonaceous fuels, e.g., *via* oxygen uncoupling (CLOU – spontaneous release of $O_2$ gas), over CuO ($\rightarrow Cu_2O$) and $Mn_2O_3$ ($\rightarrow Mn_3O_4$) [229] should also promote the development of bio-based negative emissions technologies [230]. Materials and catalysts for advanced CL processes in CCU scenarios have been reviewed [231].

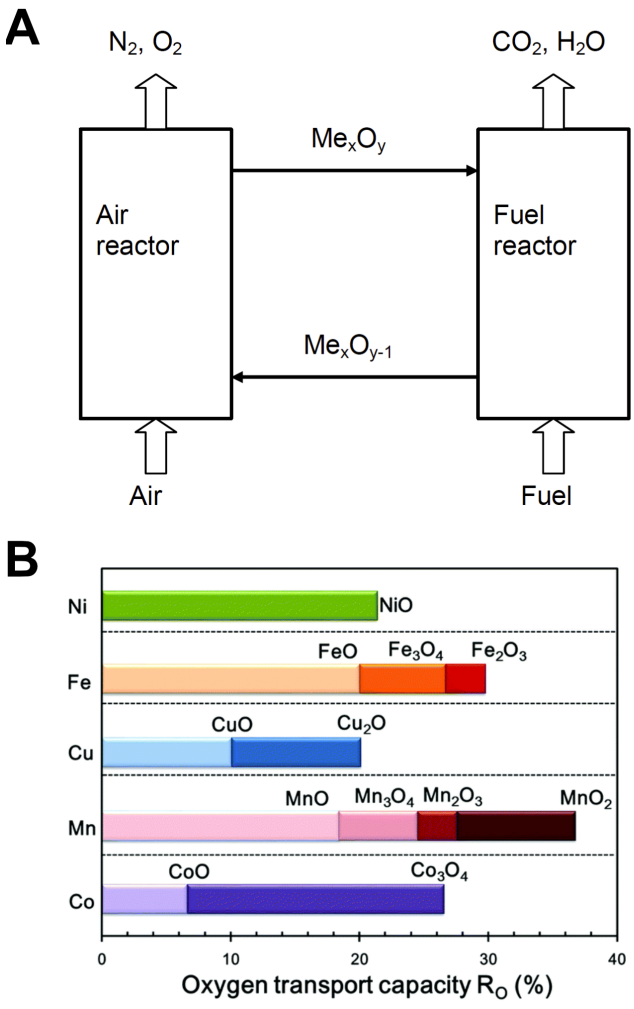


**Fig. 18 (A)** The chemical looping combustion principle (adapted and reproduced with permission from ref. 274). **(B)** O-capacities for typical redox metal/oxide couples

### 5.2.4. Technical synergies

There is growing interest in exploiting recycled $CO_2$ as sustainable carbon source for green fuels and chemicals production [232]. Unlike the storage/disposal (CCS) option, linking of the recovery stage with downstream conversion (CCU) may offer technical synergy avoiding or reducing the principal energy demands of storage *per se*. As shown in Fig. 19, these are $CO_2$ release (desorption) after trapping, purification to >99% and compression at 150 bar for liquefaction and transport [233,234]. Ingenious routes based on multi-functionality in trapping chemicals have been reported, e.g., where amine or alkali absorber doubles as reactant/catalyst to enable $CO_2$ conversion to (alkyl)-ammonium formates and methanol by homogeneous catalytic hydrogenation [235].

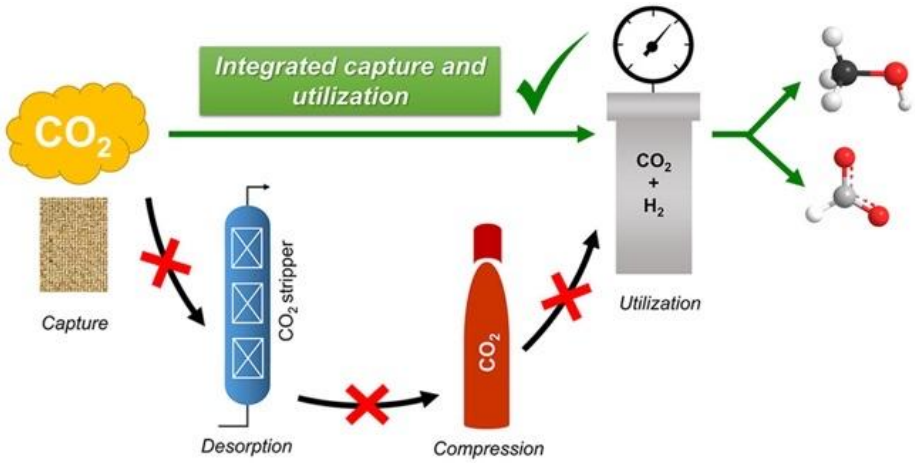

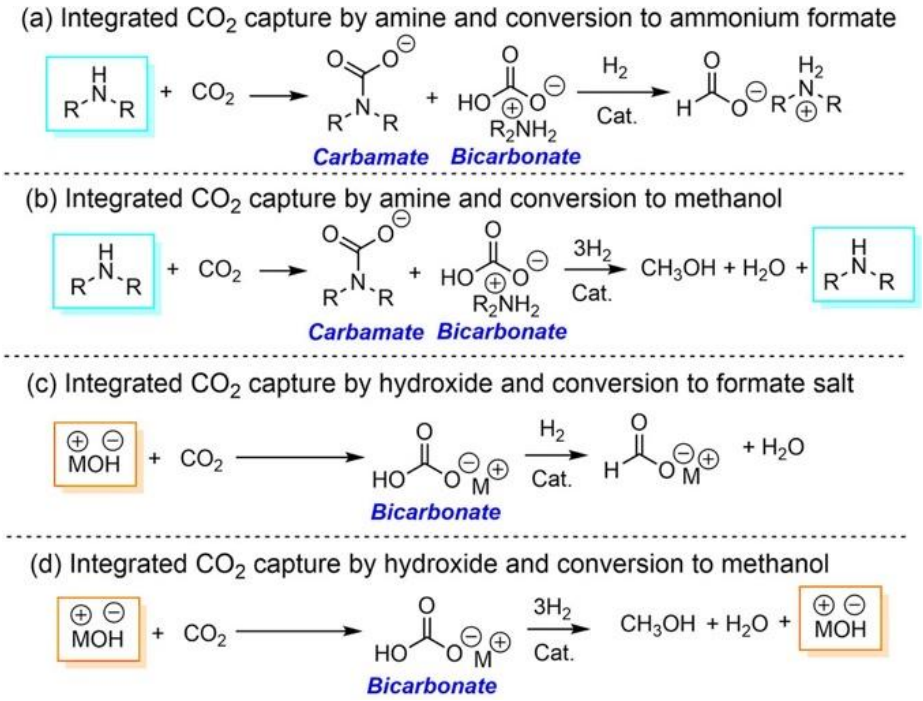


**Fig. 19** The advantage of integrated capture and conversion of $CO_2$ (ICCU) to formats and methanol [Reproduced with permission from ref. 235]

While catalytic hydrogenation of $CO_2$ may become a valuable direct source of formic acid (FA) [236] and a strategic alternative to biomass, the indirect industrial route via methyl formate (MF) is itself a green process of recent provenance [237]. The new sustainable (ICCU) variant eschews methanol carbonylation (using fossil CO) but is based on renewable syngas where methanol doubles as solvent for $CO_2$ and as co-reactant, a process favoured by thermodynamics (Reaction 12).

$$CO_2 + H_2 + CH_3OH \rightarrow HCOOCH_3 + H_2O \qquad (\Delta G^0 = -5.3\ kJ.mol^{-1}) \qquad (12)$$

However, a recent techno-economic/LCA analysis has concluded that, although the environmental benefits are clear, energy savings are not automatic but predicated on an acceptably high $CO_2/CH_3OH$ ratio in the feed. A suitable source is raw natural gas, which

typically contains 30 mol% $CO_2$ at 50 bar [238]. Although not specified in this modelling work, it points to the Rectisol® process, an established scrubbing technology based on chilled methanol [239]. Related laboratory work on $CO_2$ hydrogenation by the Leitner group has extended the use of biphasic systems to separate formate:amine adducts (in the aqueous phase) from the homogeneous Ru-based catalyst [240]. Being also quite soluble in methanol, the same formate:amine adducts were then cascaded into MF synthesis, which was isolated in > 90% purity by reactive distillation below 80°C [241].

## 6. Solar refineries and hydrogen storage

A hypothetical stand-alone solar refinery based on renewable $H_2$ gas would have a precarious techno-economic outlook being confronted with non-trivial storage and distribution issues for the gaseous product. Alternatively, a solar fuel like renewable methanol (RM) offers a practical high energy-density liquid storage form for compressed $H_2$ and its catalytic synthesis from renewable syngas is already demonstrated at pilot scale [17]. However, sourcing of $CO_2$ becomes increasingly energy-intensive depending on its dilution factor at the point of origin. As an instructive example, Herron et al. [242] conceived of a transitional solar refinery (with fossil- and renewable energy components) for renewable methanol synthesis where $CO_2$ is sourced from a fossil fuel power plant, as shown schematically in Fig. 20. Even when all of the $H_2$ was generated by renewables, the energy incorporation efficiency only became positive (renewable methanol energy output > fossil fuel energy input) when solar heat was used for $CO_2$ desorption (5.5 MJ $kg_{CO2}^{-1}$) after amine scrubbing. The key message is that pre-concentrated sources of $CO_2$ are *de rigueur* and the refinery must approach 100% energy self-sufficiency, with all sub-systems powered by renewables. Methanol is the most viable solar fuel as it is produced *indirectly* via pre-formed $H_2$ in a well-established and efficient industrial process.

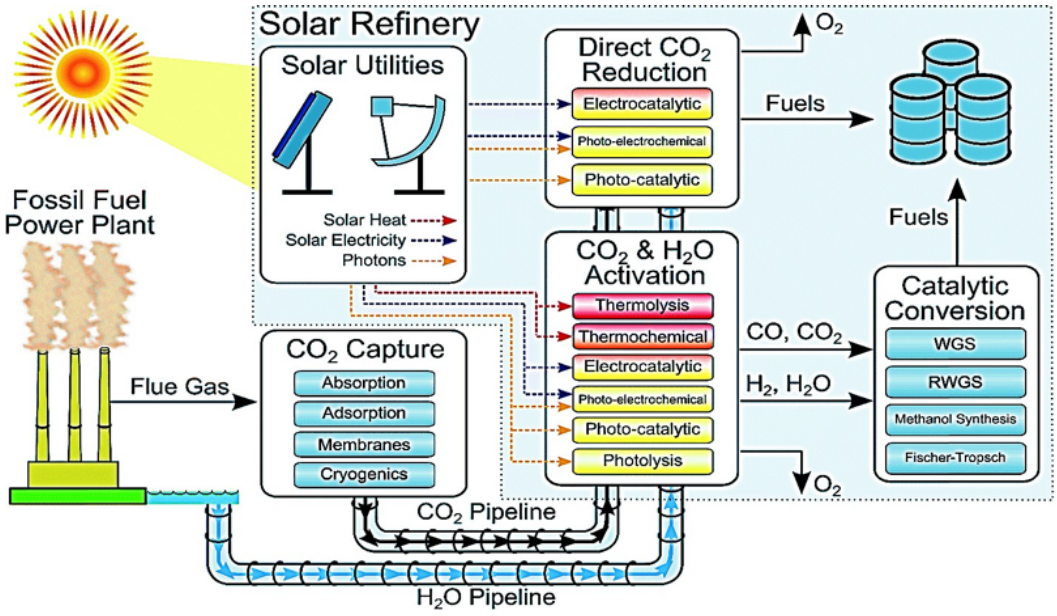


**Fig. 20** Scheme of a solar refinery based on $CO_2$ reduction to methanol: *indirectly* by renewable $H_2$ (ex solar photons, thermochemistry, electrolysis, etc.); or *directly* by $CO_2/H_2O$ co-activation using solar-electricity (PEC) and/or solar photons (photocatalysis). (reproduced from ref [242] with permission).

The highly ambitious target of *direct* routes to solar fuels, e.g., artificial photosynthesis from $CO_2/H_2O$ via electro- or photo-reduction to CO, formic acid, methanol, ethanol, ethylene, etc., where H atoms are abstracted from water, are also under long-term investigation [243-246]. However, offering more immediate prospects is the exploitation of dual-mode synergistic optical/thermal excitation, especially to promote greener and more sustainable industrial catalytic processing.

Topical examples are light-driven $C_1$ chemistry [247] and photo-assisted methanol synthesis over $Cu/ZnO/Al_2O_3$ [248]. A *photo-thermo* catalyst is typically a pan-spectral or "black" absorber, often plasmonic, designed to harness solar light and heat to overcome multiple sequential activation energy barriers. The aim is to achieve a drastic increase in

conversion and/or attain a technical rate (from prior art) but under far milder conditions. Full details of this burgeoning field are available in a separate review by the authors [249].

### 6.1.Tomorrow's solar-biorefinery

#### 6.1.1. Synergies from coupling solar and biomass resources

Integration of solar resources offers advantages based mainly on the reactive coupling of solar $H_2$ to sustainable "pools" of concentrated $CO_2$ from biorefinery processes, e.g., the high-purity (97-99%) off-gas from ethanol fermentation whose recovery in technical (non-food) grade is estimated to be as low as USD 10 per ton [250]. Substantial levels of $CO_2$ (30-50 vol %) are also available in biogas [251] and readily separated using novel adsorbents and membranes [252]. The bio-methane co-product is an ideal fuel for renewable heat and power generation vital in the transition to site-wide carbon- neutral energy self-sufficiency. According to Abate et al. [44,253], an industrial symbiosis underpins the transition to a low carbon bio-economy based on integrating solar energy and $CO_2$ valorisation (ideally renewable methanol synthesis) in 2$^{nd}$ generation (2G) ethanol biorefineries, as depicted schematically in Fig 21. Apart from a reduction in carbon footprint by 50%, co-production of $C_1$ and $C_2$ alcohols, biofuels and complementary platform chemicals, would be an invaluable diversification. It also results in a major increase in carbon (atom) efficiency in biomass utilisation (from 55% to 73%), and a rise in thermal efficiency (from 66% to over 80%) based on synergistic heat recycling from methanol synthesis at ~280°C to a solar-assisted steam generator for low-temperature pre-treatment of cellulosic feedstock (to the bio-ethanol unit). This could drive down the cost of renewable methanol, which is highly-sensitive to the method of carbon sourcing. The most competitive price currently is via biomass gasification at ~USD 400 per ton, i.e., still 2-3x more expensive than fossil fuel-derived methanol.

1026 The growing prospect of fuel interconversion, viz., methanol-to-ethanol [28], would be
1027 of strategic value in terms of operational flexibility. In view of the recent discovery of a "green"
1028 (non-syngas) route to renewable methanol from aqueous glycerol (GtM) over basic oxide
1029 catalysts [41,255], inclusion of the $C_3$ oxygenate ($C_3H_8O_3$) in the alcohol platform would further
1030 consolidate operations. This by-product from the biodiesel (fatty acid methyl ester, FAME)
1031 process, using methanol as feedstock, is among the US DOE "Top 10" bio- products for
1032 upgrading [45,256]. Closing the transesterification cycle by GtM should lead to lower prices
1033 for both biofuels [257]. A report of selective production of ethanol from glycerol has also
1034 appeared [258]. Future schemes centred on renewable fuels are bio-syngas fermentation (under
1035 development by LanzaTech) as a strategic source of ethanol [259] Microbial (acetogenic
1036 bacterial) processes offer excellent (even single product) selectivity, a feature currently lacking
1037 in thermal heterogeneous catalysis based on restricted chain growth, e.g., higher alcohols
1038 synthesis [260]. Interest is also growing in microbial conversion of $CO_2$-rich syngas [261].
1039 Dimethyl ether (DME) is a clean diesel substitute derived from renewable methanol
1040 dehydration [262] and can be classified as a "solar fuel" as depicted in Fig. 21. Aviation (jet)
1041 fuel is a future example of a biofuel derivable from ethanol [263].
1042

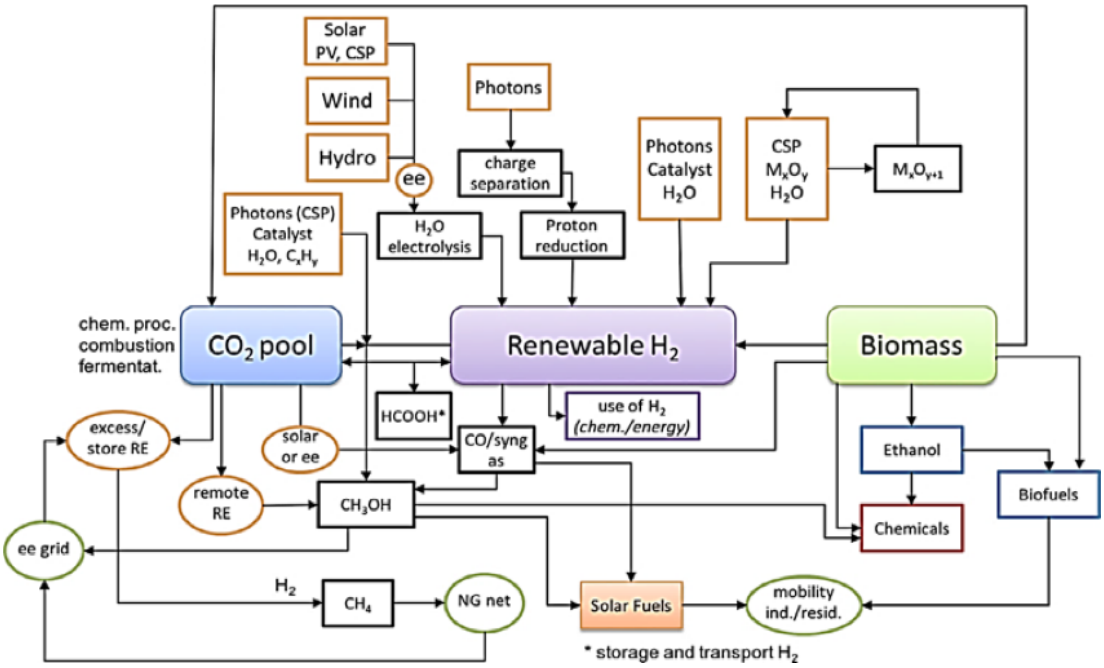


**Fig. 21** The solar-biorefinery concept for energy storage as fuels and platform chemicals – modified from the original presented by Schlögl in Ref. 254 (reproduced with permission from ref. 44).

### 6.1.2. Key role for low-power solar concentrators

Inspection of Fig. 21 reveals the versatility of solar photonic energies in the generation of renewable $H_2$. From upper left, photons incident on single (PV) or tandem (PEC) absorber/catalyst cells drive water electrolysis at efficiencies close to technical implementation. Direct light-to-chemical energy conversion over suspended photocatalysts (upper centre) has future prospects although efficiencies are currently too low. The term CSP features in several places and stands for "concentrating solar power". While the CPS terminology usually refers to solar power plants with heat and steam generation and further electricity production, it can also refer by analogy to high temperature (HT) solar-thermal energy in central receivers that can drive thermodynamically uphill reactions, eg. like the direct thermolysis of water into $H_2$ and $O_2$. However, co-production of such combustible gas mixtures is potentially dangerous and

requires operating temperatures > 2000°C where efficiency (solar-to-chemical conversion) is already falling due to re-radiation and heat transfer losses, and materials durability problems become prohibitive. CSPs are characterised notably by their optical concentration factor (C), defined as the mean solar radiative power flux over the focused area, normalised to the Direct Normal Incident power from the sun (DNI ~1000 W $m^{-2}$) [264].

As depicted in Fig. 21 (upper right), solar-thermal $H_2$ is best produced in water-mediated two-stage metal ($M_xO_y$) redox cycling at efficiencies of 20-40 % [265,266]. This can be viewed as a *renewable* case of "chemical looping for hydrogen" (CLH), which is designed for easier $CO_2$ sequestration from the use of fossil fuels [267]. The solar variant avoids the use of a fuel in the reduction half-cycle as it is based on spontaneous O-vacancy creation in a thermally reducible metal oxide at the high temperatures (HT) readily attainable by concentrators. HT-CSP can easily drive biomass gasification at or above 800°C [268] but the use of central receivers is limited to regions of high direct insolation (clear skies). Co-location in the tropics or other humid regions that promote vegetative growth even at high latitudes is questionable. It is also doubtful that HT-CSP would be sufficiently adaptable (scalable) to the multiple (parallel) processing operations expected in future biorefineries. In contrast, cheap and modular, even portable, devices that offer modest concentration of solar power will probably become ubiquitous. According to Pinaud et al. [75], 10x solar concentrators offer 60-70% savings in capital expenditure (for plant installation) even in an optical tracking configuration by enabling a drastic reduction in the number of photoreactors, along with the cost of associated materials, fabrication, and ancillary equipment. There is no loss in productivity on a fixed areal basis. The estimated cost of $H_2$ (USD 4.00 $kg^{-1}$), as against a fixed-panel array operating in direct sunlight (USD 10.40 $kg^{-1}$), is much lower and reaches the US DOE target price for commercial viability. The non-imaging compound parabolic concentrator (CPC) is one such device which is capable of collecting *diffuse* radiation and directing it to the receiver along with direct (sun disk)

radiation [269]. This is a unique quality among concentrator types and to some extent accounts for its popularity, as the diffuse component of sunlight in the visible/near infrared range can amount to over half the annual total of terrestrial insolation depending on latitude and humidity level [270].

A 2D CPC conveniently focusses the rays onto a simple tubular flow reactor/receiver of commensurate length [271]. It offers low (1-5x) optical power intensification (C) in non-tracking configuration but this can be raised to x10 by daily manual tilt adjustment (quasi-static operation). A field-scale CPC-coupled photocatalytic reactor for water splitting (C = 4x; $\eta_{STH}$ = 1.0%; $H_2$ evolution rate = 4 L $h^{-1}$) has been designed and evaluated [272]. Although $H_2$ generation efficiencies in PV-E cells are well maintained even at 100 suns, as shown in Laboratory tests using a Xe lamp/focusing lens combination [273], low-power (10x) CPCs are considered the most realistic option for PECs from a fundamental viewpoint. Apart from any cell performance gain from (photonic) process intensification, passive heating may have an additional benefit. For example, a 5-fold increase in exchange current density for $H_2$ evolution over Pt is predicted if ambient temperature rises to 80°C [274]. This is the electrochemical equivalent of the Arrhenius (activation energy) factor governing all chemical kinetics and is clearly to be distinguished from concentrator PV technologies where an energy penalty, i.e., active cooling, is necessary to avoid electrical power losses [275]. Thus, by supplying an intensified solar photon beam and localised solar heat together, low-power concentrators promote any synergies arising from this dual (photo-/thermal) mode of excitation (*vide infra*).

The main practical issue to be faced is whereas the incident photon intensity can be quite easily regulated, the heat (temperature) gradient under steady-state illumination will be a complex function of sample optical properties (the wavelengths absorbed and thermalized locally to form a “hot layer”), thermal diffusivity of the suspending fluid, and its flow rate (set to achieve a target conversion). In addition, operation at implicitly higher current densities

(>100 mA.cm$^{-2}$) is accompanied by rapid $H_2/O_2$ (gas bubble) evolution. Issues concern notably optical obscuration (loss of incident power) [276] and mass transfer inhibition (sluggish kinetics) at the 3-phase boundary [277]. Nevertheless, advances in optofluidic technologies may provide solutions. Microchannel photo-reactors are already exploited in solar synthesis [278] and are now being considered for use in solar energy devices [279].

As regards solar-thermal technologies, a low-power CPC (C = 5x) can heat a well-designed receiver to 240°C [271]. However, it should be noted that such *mid-temperature* operation is only attainable under conditions of full light-to-heat energy degradation, i.e., with no luminescence or photochemistry, and in a configuration optimised for high heat-transfer efficiency. These conditions are well met by an annular device consisting of a transparent evacuated tubular jacket with an inner surface absorber coating, designed for high (solar spectral) absorption but low infrared emittance [280]. Heat is efficiently supplied via conductive fins to the central tube holding a thermal fluid of high chemical stability [281]. This is usually water (pressurised for operation above 100°C), due to its low cost, high heat capacity and conductivity [282].

A recent advance is to dispense with the coating and generate heat volumetrically in the thermal fluid by suspending nanoparticle absorbers, e.g., plasmonic metals like Cu or Au. This so-called *direct* optical mode based on "nanofluids" is beneficial in terms of heat delivery and a popular topic in solar-thermal research [283]. For example, alternatives are now being sought to traditional "black" absorbers like nanocarbons due to their high emissivity [284]. A low-power CPC/tubular reactor is compatible with various heat-demand processes in hydrothermal pre-treatment of biomass feedstocks, e.g., pre- extraction of hemicellulose at 150-170°C, and fractionation (to cellulose, hemicellulose and lignin) by steam explosion at 200-250°C [285]. A forerunner (batch-type) system, using gold nanofluids to drive a steam generator for pre-extraction of cellulosic feedstock (at 136°C/4 bar) and energy-intensive ethanol distillation, has

been demonstrated, albeit using a parabolic trough collector restricted to clear sky operation [286].

### 6.1.3 Outlook for solar-driven endothermic ('uphill') processing

As compared to water photo-splitting, more practical and less explored endothermic ('uphill') reactions are oxygenates reforming (*vide infra*) and various dehydrogenation reactions. In photo-/thermal work, the photocatalyst must serve as sole absorber, i.e., as an optimised visible light-responsive nanoparticulate in free (stable) suspension or rigidized on a porous tubular framework. Solar photons offer the prospect of light energy storage in chemical bonds but these endergonic processes need not be restricted to "dream topics" as practised heretofore. While acknowledging their obvious attraction and importance, water photo-splitting and photo-(electro-) catalytic reduction of $CO_2$ are immensely challenging and mechanistically complex processes that suffer from drastic kinetic limitations. Thanks to intensive research expended on these topics over the last four decades, much has been learned at the fundamental level but progress has been incremental and technical efficiencies still appear to lie on a distant time horizon, e.g., ethanol → acetaldehyde → butadiene. A recent report of photocatalytic conversion of biomass (after pretreatment of cellulose or wood sawdust to a mixture of sugars and polyols), to methanol and CO-rich syngas at ambient conditions under UV-light over $Cu/TiO_2$ nanorods looks particularly encouraging [287]. The glycerol-to-methanol (GtM) reaction is also worthy of investigation as the overall chemistry, involving multiple H abstraction and partial re-distribution from low-energy O-H bonds into high energy C-H bonds, is almost certainly endothermic. Recent mechanistic studies by the *Hutchings group* implicate ethylene glycol (EG) and formaldehyde as intermediates [288]. Ethylene glycol is a known product of glycerol hydrogenolysis in the presence [41,289] or absence of external supply of $H_2$. It can be converted to methanol by hydrogenolysis [291] but, with the exception of Raney

Ni [290], expensive precious metals like Ru or Pd are needed to promote C-C bond cleavage. In principle, a cheap semiconductor photocatalyst may serve the same purpose. Ethylene glycol decomposes under UV illumination over $TiO_2$, yielding two moles of formaldehyde by photo-scission of the C-C bond [292]:

$$CH_2(OH)CH_2(OH) \rightarrow 2\ H_2C{=}O + H_2 \quad (13)$$

Formaldehyde is highly reactive and known to undergo Cannizzaro disproportionation in the presence of water to methanol and formic acid over basic catalysts [21,293,294]. The simplest (balanced) global reaction that satisfies these criteria is that consisting in the reaction between glycerol and water to give methanol and formic acid as in reaction 14:

$$C_3H_8O_3 + H_2O \rightarrow 2\ CH_3OH + HCOOH \quad (14)$$

which is endothermic by +96 kJ. $mol^{-1}$. It is unsurprising that formic acid has not been reported as a product as it readily forms methyl formate in the presence of methanol. Indeed, analytical detection of formic acid as its methyl ester is established practice. However, this derivatization method is ruled out for determination of methanol and formic acid in the same analyte [295].

### 6.2.Renewable hydrogen from biomass

The generation of $H_2$ from biomass has recently been reviewed [296]. Although thermal methods have been most popular (summarised below), biological (microbial fermentation) processes should also be considered. These are already established and/or promising in, e.g., renewable fuels generation despite their slow operation at scale. The analogous processes for $H_2$ generation, viz., bio-photolysis, dark and photo-fermentation, CO-gas fermentation, microbial electrolytic cells, etc., offer interesting low-temperature prospects.

### 6.2.1. Established high-temperature processes

The two main thermochemical routes to bio-hydrogen are steam gasification to bio-syngas and/or two-stage conversion via fast pyrolysis to bio-oil and steam reforming, as depicted in Fig. 22. In gasification (800-1000°C) part of the biomass is combusted in oxygen to supply heat to drive this highly endothermic process [297,298]. Based on mean product gas yield and a typical residual char level of 5-10 wt% [299], gasification can be represented empirically as in Reaction 15.

$$\underset{\text{woody biomass}}{C_6H_9O_4} + \underset{\text{steam}}{2\,H_2O} \xrightarrow{catalyst/800°C} \underset{\text{char}}{C[O_{0.1}H]} + \underset{\{\sim 40 \pm 10\}}{4\,H_2} + \underset{\{\sim 30 \pm 10\}.}{3\,CO} + \underset{\{\sim 15 \pm 5\}}{1.5\,CO_2} + \underset{\{\sim 10 \pm 5\}}{CH_4} \quad \{\text{vol.\%}\} \qquad (15)$$

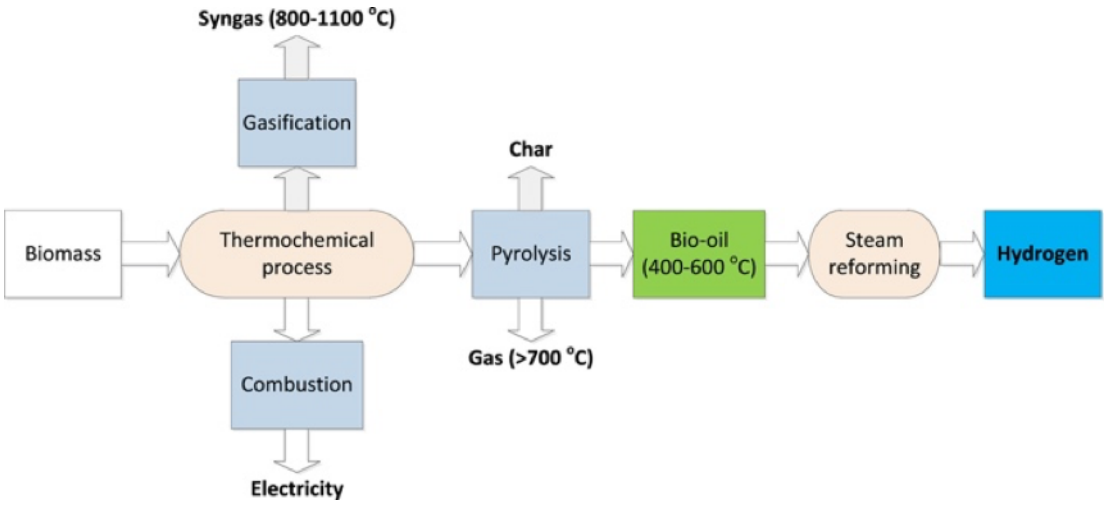


**Fig. 22** Scheme of the two main thermochemical routes to renewable hydrogen from biomass; directly (top) via gasification to biosyngas, or indirectly (right) via fast pyrolysis to bio-oil for steam reforming. [taken from ref. 299 with permission]

The char is subsequently gasified to improve process and atom efficiency. The CO-rich syngas composition is non-ideal, needing $H_2$-enrichment [$(H_2/(CO+CO_2) \geq 2$] for downstream processing, e.g., in the synthesis of methanol [17,50,301] or Fischer-Tropsch [73,302] hydrocarbons. This is achieved in various ways, including high-temperature water-gas shift at 350-450°C over iron-based catalysts [303]:

$$CO + H_2O \leftrightarrow H_2 + CO_2 \quad (16)$$

or steam methane reforming at 700-800°C over supported nickel [18,304]:

$$CH_4 + H_2O \leftrightarrow 3\ H_2 + CO \quad (17)$$

Despite these process complexities, the $H_2$ yields and energy/exergy efficiency profiles for steam gasification are quite good, ranging typically from 20-50 mol $H_2$/kg at thermal efficiencies of 20-70%, depending largely on process optimisation and the use of suitable heterogeneous catalysts. These are typically ZSM-5 zeolites with alkali promoters, and/or Ni, Fe, Co supported on basic oxides like $ZrO_2$, $CeO_2$, CaO, etc., to suppress coking by enhancing steam activation [298,305,306].

Biomass conversion by catalytic fast pyrolysis performed briefly at moderate temperatures (400-600°C) optimises the yield of condensable vapours, typically reaching 45-65 wt.% [308], while restricting gas and char formation. However, catalysts are needed that are less-susceptible to coking and deactivation [304,308-310]. The liquid pyrolysate is known as *bio-oil* despite the fact that water is present in substantial amounts (20-30 %). It is a highly complex mixture of typically over 300 oxygenated $C_2$-$C_{10}$ organic compounds. Major

components (> 5 mol.%) serving as model compounds include formic acid, levoglucosan, acetic acid, hydroxyacetaldehyde, 1-hydroxy 2- propanone, glucose, various phenolics, furfural and derivatives. Handling issues linked to its acidic properties and related instability, along with a low energy content (~16 MJ/l), makes it unsuitable for direct use, e.g., as a renewable fuel oil. Thus, optimisation of the pyrolysis process and the valorisation of bio-oil, typically by catalytic steam reforming, is a research field of high importance. Unfortunately, in view of its aforementioned ill-defined or generic properties, this review offers insufficient scope to consider bio-oil SR in detail.

### 6.2.2. Hydrogen release by reforming of bio-oxygenates: thermodynamics and kinetics

There are now a wide variety of sustainable processes effective in $H_2$ production via reforming of biomass-derived oxygenates. These are briefly introduced here and their advantages and disadvantages are summarised. They are listed in order of increasingly mild (high- to low-temperature) operation. The stoichiometric expression for conversion of oxygenates to gaseous products $H_2$ and $CO_2$ by reaction with water can be written as:

$$C_nH_mO_k + (2n - k)\ H_2O \rightarrow n\ CO_2 + (2n + m/2 - k)\ H_2 \quad (18)$$

#### 6.2.2.1 Steam-reforming (SR)

Inspection of Reaction 18 reveals that, despite their endothermicity for reactants already in the vapour state (e.g., $\Delta H^0 \approx +50$, +90, 128, 135, 175, and 245 kJ/mol for methanol [311], ethylene glycol [312], glycerol [313], acetic acid [312], ethanol [315] and acetone [312] respectively), the entropy term ($-T\Delta S$) soon starts to dominate the thermodynamics due to a doubling (at minimum) in gas volume. For methanol, close to full $H_2$ yield (3 mol/mol alcohol) is theoretically possible already at 120°C [314]. However, even the best catalysts, e.g., $Cu/ZnO/Al_2O_3$ and/or supported Pd are effective only by 250°C due to kinetic limitations [311].

Similarly, for ethanol the standard free energy ($\Delta G^0$) is already negative above ~200 °C [315], but substantial $H_2$ yields (50-80%) have only been measured above 400°C, e.g., over a highly-selective $Ni/CeO_2$-$ZrO_2$ catalyst that restricts production of $CH_4$, a common by-product of exothermic side-reactions in $C_{2+}$ oxygenates conversion over many catalysts [31,316]. Once produced, $CH_4$ can only be reformed at considerably higher temperature (T > 600°C). This introduces the extra complication of catalyst deactivation by coking, which is more severe in higher oxygenates conversion [29,317], including bio-oil due to its $C_5$-$C_6$ sugars and $C_{6+}$ aromatics content [299,318].

Reforming any liquid fuel to $H_2$-rich gas mixtures results in *chemical recuperation* [20-22]. This is an increase in calorific value, measured as the difference between the summed heats of combustion of the (multi-molar amounts of) $H_2$ product and that of 1 mole of the oxygenate according to the SR reaction stoichiometry. This beneficial effect remains fairly constant (+20 to +30%) across a wide range of $C_1$-$C_6$ compounds and so it naturally applies to complex mixtures such as bio-oil. Just as for steam reforming, it also applies regardless of the reforming technology utilised (SCWR, APR, NTPR, SPR - see below in the further sub-sections).

#### 6.2.2.2 Supercritical water reforming (SCWR)

The supercritical condition in water occurs above the critical point, viz., T ≥ 374°C, P ≥ 220 bar. The resulting lower dielectric constant enables dissolution of a wider range of biomass components and shifts the selectivity towards gaseous products [319]. As an alternative to gasification, hydrothermal processing in the sub-critical range, typically from 250-350°C, and P = 100-200 bar, yields an intermediate liquid product analogous to bio-oil (*vide supra*) whilst restricting formation of partially carbonised residues (biotar, biochar) more typical of pyrolysis [320]. The thermal efficiencies in SCWR are quite high at 30-60% while the kinetics are favourably influenced by the high effective fugacity coefficient of water [321,322].

#### 6.2.2.3 Aqueous-phase reforming (APR)

Since the pioneering work of the Dumesic group in the early 2000s [30,323], *aqueous-phase reforming (APR)* for $H_2$ production is now well-established [324] as a viable alternative to conventional (vapour-phase) oxygenates SR, and has more recently been extended to multi-stage processing of biomass for renewable (hydrocarbon) fuels [325] and platform chemicals [326]. The advantages of catalytic APR, conducted in liquid water under pressure (to prevent vaporisation and related energy losses), are manifold. High conversions are achieved at lower reaction temperature (175-275°C, 10-55 bar), probably by raising water fugacity to overcome kinetic limitations. For instance, steam activation over $ZrO_2$ and/or rare earth oxides is a vital function in SR/APR catalyst formulations. Operation under such mild conditions, utilising liquid water as both reactant and solvent, extends the range of feedstocks to include soluble higher oxygenates, e.g., $C_5$-$C_6$ sugars [327] and even cellulose. These compounds are incompatible with steam reforming due to low volatility and/or thermal instability. For cellulose [324,328,329], either in suspension or in a one-pot acid hydrolysis/APR set-up, $H_2$ yields from 30-70% have been achieved over Ni supported on Mg/Al layered double hydroxides (LDHs) at 260°C. Nevertheless, catalyst deactivation remains an issue but via mechanisms other than coking. The typically acid hydrothermal environment causes primarily metal sintering, support oxide dissolution and re-deposition of hydroxylated phases leading to encapsulation of active surface sites [31,330].

#### 6.2.2.4 Non-thermal plasma reforming (NTPR)

In a non-thermal plasma [331], a gaseous substrate is subjected to an electrical discharge supplying a high-energy stream of particles from a partially ionised carrier gas, consisting of neutral species (molecules, radicals, excited states), ions, photons and electrons, which directly impacts adsorbates at the catalytic surface. The electron temperature is in the range $10^4$-$10^5$ K – a non-thermal distribution of energy that offers to overcome kinetic and thermodynamic

limitations on chemical transformations of reactants into desired products. Insofar as its main value is in the conversion of gases difficult to activate, e.g., $CO_2$, $CH_4$ or $N_2$ (as in $NH_3$ synthesis), non-thermal plasma reforming may be thought of as a modest-scale and ubiquitous adjunct to hydrothermal processing of biomass, especially if the $CO_2$ and $CH_4$ is bio-derived, as in biogas deposits, and/or as a valorisation stage for reformate(s) with excess $C_1$ gases. A dielectric barrier discharge reactor (DBR) with a water electrode has been found to produce formaldehyde, methanol, ethanol, and acetic acid at high selectivity [50-60% oxygenates, 40% acetic acid] in a reaction with ideal (100%) atom economy] under ambient conditions [332]. Elsewhere, $H_2$ generation from alcohol vapours has been explored by non-thermal plasma reforming even in the absence of a catalyst [333,334].

**6.2.2.5 (Solar) photo-reforming (SPR)**

Solar photons, the ultimate renewable energy source, can be harnessed through optical absorption by heterogeneous semiconductor photocatalysts of suitable bandgap. In view of known limitations of stable wide-bandgap oxides like $TiO_2$ ($E_g$ ~3.2 eV), responding only to the UV component of sunlight (just 4% of the solar power spectrum), visible and near-IR photo-sensitization based on new semiconductors of narrow band-gap (Eg < 2.5 eV), often in tandem configuration for higher efficiency, has been intensively studied in the last 3 decades but with limited success due to the intrinsically greater instability of these materials [128-131]. The primary function of a photocatalyst is to use electronic (photon) energy to redirect the desired reaction via an alternative low-energy transition state (activation energy barrier – Arrhenius principle), thereby improving its sustainability, viz., increasing exponentially its rate while maintaining conditions close to ambient. More challenging is to use solar photons to drive endergonic (thermodynamically uphill, $\Delta G>0$) processes via surface redox equivalents or charge carriers, electrons (e-) and holes ($h^+$) [31]. As depicted in Fig. 23, any endergonic process increases the energy barrier to reaction, being now the sum of (thermodynamic) light-to-

chemical bond energy storage along with the (kinetic) activation energy barrier. Solar photo-reforming of methanol as sacrificial agent (electron donor) in a deaerated aqueous environment involves 6 successive proton reduction steps and generates 3 moles of hydrogen, as shown in Reaction 19:

$$CH_3OH + H_2O \rightarrow CO_2 + 3\ H_2 \qquad (19)$$

The half-cell potential for photo-oxidation of methanol to carbon dioxide can be written as Reaction 20, taken in reverse from ref. 391:

$$CH_3OH_{(l)} + H_2O_{(l)} \rightarrow CO_{2(g)} + 6\ H^+ + 6\ e^- \qquad [E^0\ (pH\ 0) = -\ 0.03V] \qquad (20)$$

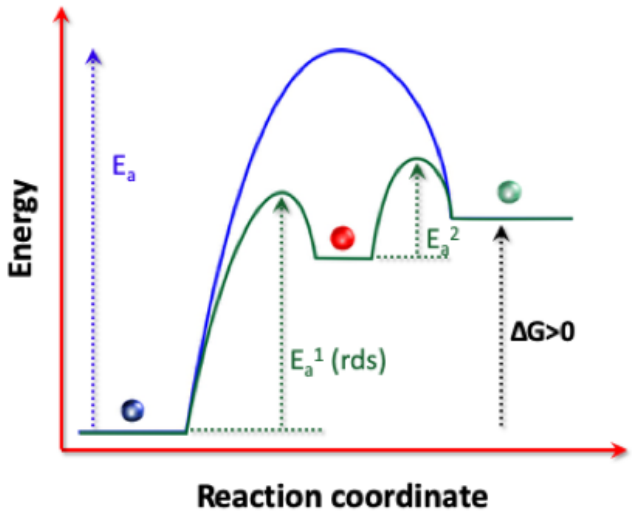


**Fig. 23** Arrhenius diagram of a multiple (two-step, $E_a^1$ and $E_a^2$) activation energy barrier to an endergonic (uphill, energy-storing) process. rds : rate-determining step. (reproduced with permission from ref. 249)

According to the Nernst relation ($\Delta G^0 = -nFE^0$) photo-reforming of aqueous methanol at ambient is marginally uphill ($-6$ x 96.5 x $-0.030$) ≈ +17.4 kJ/mol [335]. Standard free energy

changes ($\Delta G_0$) for higher oxygenates are generally more endergonic: aq. acetic acid (−8 x 96.5 x −0.11) ≈ +85 kJ/mol [335]; aq. ethanol (−12 x 96.5 x −0.085) ≈ +98 kJ/mol. [33,335]; aq. n-propanol (−18 x 96.5 x −0.10) ≈ +173 kJ/mol [335]; etc. In contrast, $\Delta G^0$ for reforming of more hydroxylated compounds (polyols, sugars, etc) approach thermo-neutrality; viz., aq. ethylene glycol (−10 x 96.5 x −0.01) ≈ +10 kJ/mol [336]; aq. glycerol (−14 x 96.5 x −0.004) ≈ +5 kJ/mol [33,336]; and aq. glucose (−24 x 96.5 x −0.001) ≈ +2.3 kJ/mol [337]. This favourable thermodynamic trend underpins serious interest in the direct photo-reforming of raw biomass, i.e., lignocellulose and biowastes [338-341]. While these multiple charge-transfer events render the mechanism more complex, they also lower the threshold photon energy, i.e. effecting a red-shift in the threshold wavelength, and thereby raising the solar-to-hydrogen photoefficiency ($\eta_{STH}$) from ~10 % for a single photon event to ~30 % for coupled processes [342,343]. A pan-spectral absorber with a low-energy bandgap in the near-IR (~1.5 eV) can supply high-energy (UV-vis) quanta *via* "extra-band gap" absorption while offering good solar power spectral matching. Absorption even at the band edge ($\lambda$ = 826 nm) provides energetic quanta (> 145 kJ/E, where 1 mole of photons is denominated as 1 Einstein, E), sufficient to exceed apparent activation energy ($E_a$) barriers in oxygenate reforming in the literature: e.g. methanol [$E_a$ (photo-) ≈ 20-40 kJ/mol [31,344,345]; $E_a$ (thermo-) ≈ 55-85 kJ/mol] [346,347]; ethanol ($E_a$ ≈ 25-95 kJ/mol) [348-350]; ethylene glycol ($E_a$ ≈ 80-150 kJ/mol) [351,352]; selected $C_2$-$C_6$ aldehydes & ketones ($E_a$ ≈ 5-20 kJ/mol) [353]; acetic acid ($E_a$ ≈ 35-45 kJ/mol) [354,355]; glycerol ($E_a$ ≈ 35-135 kJ/mol) [356,357]; bio-oil ($E_a$ ≈ 85-105 kJ/mol) [358,359]; and sugars ($E_a$ ≈ 35-110 kJ/mol) [354,360].

A recent review of photocatalytic hydrogen production [361] stresses the importance of biomass-derived oxygenates as sacrificial agents. These offer a practical interim solution or "bridge" to a future renewable hydrogen-based economy ultimately driven by solar water splitting and artificial photosynthesis. The same authors have also provided a timely update to

the photocatalytic science and technology roadmap [362], itemising key steps in progress towards scientific maturity. These include scrupulous practices in materials preparation (purity and characterization), standardised testing (including inter-laboratory photoactivity benchmarking), and more rigorous reporting of photocatalytic "figures of merit", e.g., rates in *catalyst mass*-specific and/or *irradiated area*-specific units (mmol $H_2$ $g_{cat}^{-1}$ $h^{-1}$ or mmol $H_2$ $m^{-2}$ $h^{-1}$), apparent quantum yields (AQYs), solar-to-hydrogen conversion efficiencies ($\eta_{STH}$), etc., evaluated on a proper statistical footing, i.e. with experimental reproducibility. To reach a consensus on the definition of terms is urgent in view of the recent advent of dual mode photo-thermal activation, e.g., the use of plasmonic metals to extend spectral (photonic) response to the visible region and simultaneously generate localised heat upon non-radiative relaxation. There has been a prolific growth in reports of photo-/thermo synergies, especially under multiple (x5-x10) sun power, which is driving a paradigm shift in applied heterogeneous catalysis [247-249,363,364].

# 7. Scientific and technical advances in the hydrogen release by aqueous reforming of bio-oxygenates

For clarity, recent progress is summarised for the reforming of promising individual oxygenates up to bio-oil, listed in order of increasing complexity.

## 7.1 Methanol

Historically, methanol was recognized in the early 1980's as a potential hydrogen carrier due to its molecular simplicity (absence of C-C bonds) and access to effective formulations based on the $Cu/ZnO/Al_2O_3$ synthesis catalyst. These offer high conversions at low temperature and low yields of CO compatible with on-board reformer links to polymer electrolyte membrane (PEM) fuel cell electric vehicles. Its strategic significance has grown since Olah's

popular concept of the "methanol economy" [26] has inspired more recent advances [17,365,366], along with the recognition of its future role as a solar fuel [242,367]. In recent trends, Cu remains the most popular metal (ahead of Pd and Ni) due to its high natural abundance, low price (sustainability), good catalytic activity at ~250°C, high selectivity (low CO, low $CH_4$), and workable stability below 300°C. Deactivation (by coking, sintering, etc.) is restricted by the selection of suitable supports and promoters [311,368,369]. The close parallel between activity trends (vs. catalyst composition) for both the synthesis (MS) and reforming (MR) suggests that the principle of *microscopic reversibility* holds. As seen in Fig. 24, this offers the potential advantage of a simplified (low capital expenditure/CAPEX) plant for H-cycling via methanol (with closed $CO_2$ loop) based on a single reactor and catalyst for on-site $H_2$ production (Fig. 24b), instead of two separate facilities with a transport/storage stage, e.g., for mobile usage (Fig. 24a).

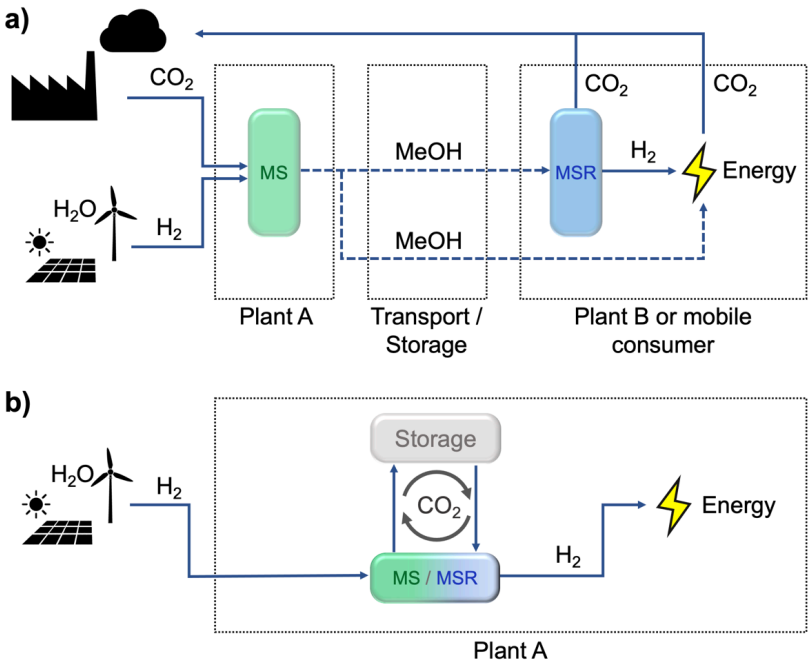


**Fig. 24** Potential scenarios for the application of methanol as an energy carrier within a closed $CO_2$ loop. Methanol is produced from renewables-derived reactants: a) for transportation and

storage to a different end point where it is reformed to release $H_2$; and b) for on-site $H_2$ or energy storage. In the second scenario, the same converter could be used to drive both reactions. (reproduced with permission from ref. 365)

Much recent research has been aimed at improving activity in methanol reforming to achieve viable operation at or below 200°C (the lower limit for full conversion according to thermodynamics is 120°C [314]). This eases the thermal burden on the reformer unit and better matches the working range of high-temperature PEM fuel cells, now reaching 160-180°C based on polybenzimidazole (PBI) membranes [366,370]. It also facilitates greater compatibility in the MR/FC link-up by introducing two reinforcing mechanisms to tackle the CO problem (FC anode poisoning). Apart from the lower level of CO produced due to equilibrium restriction of the (reverse) water gas shift reaction, the high-temperature PEM fuel cell has a greater tolerance to CO (~2 vol%) [371].

In thermal catalysis, a major advance in methanol reforming activity has been achieved with a 2%Pt/α-MoC catalyst, reaching a remarkable $H_2$ evolution rate of ≈ 470 mmol/$g_{cat}$/h at 190°C [346], or an order of magnitude higher than over oxide-supported Pt. Among molybdenum carbides, e.g., (hcp, tetragonal) β- $Mo_2C$, the (fcc) α-MoC structure is unique in promoting atomic dispersion of Pt, as verified by high-resolution STEM-Z contrast and high Pt-Mo coordination number (up to 7 for 0.2% Pt) by EXAFS. DFT calculation shows that the strong metal-support interaction creates electron-deficient Pt, which has a lower affinity for CO, traditionally a catalyst poison. The Pt/MoC interface also serves as a good promoter of water dissociation (vital for Water Gas Shift activity,) with an estimated energy barrier of 0.91 eV, consistent with the measured activation energy ($E_a = 83 \pm 5$ kJ/mol) in methanol reforming. The importance of MoC has been corroborated by similar work showing that Au/MoC has good low-temperature Water Gas Shift activity starting at 40°C [372]. These reports are stimulating

great interest in carbides as catalyst supports (2D MXenes, etc.) [373] and single-atom transition metal catalysts [374]. For example, a 0.5% Zn-modified Pt/MoC catalyst gave good conversions of 17-100 % (up to 160 mmol $H_2/g_{cat}/h$) over the range 120-200°C but deactivated after a few hours at the higher temperature due to irreversible hydrothermal sintering of Pt [375]. A reaction mechanism via methyl formate intermediate was proposed as shown in Fig. 25.

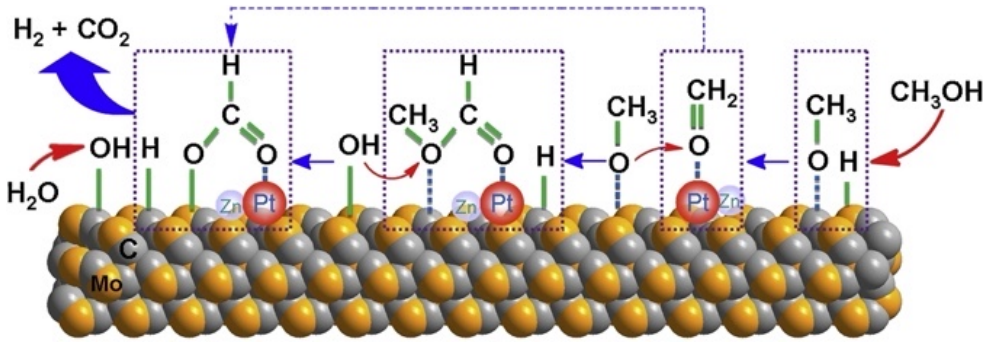


**Fig. 25** Proposed reaction pathway for methanol steam-reforming over 0.5Zn-Pt/MoC catalyst (reproduced with permission from ref. 375)

Yu et al. [376] found a modest activity in MAPR (~20 μmol/$g_{cat}$/h) already at just 80°C over metal-free carbon dot/$C_3N_4$ composites, with an activation energy ($E_a$) of 53.5 kJ/mol. Unfortunately, tests at higher temperature to attain the necessary conversion for practical application (mmol/$g_{cat}$/h range) were not conducted. Ribeirinha et al. [377] reported that their CuO/ZnO/$Ga_2O_3$ catalyst gave nearly twice the conversion (~80%) of commercial CuO/ZnO/$Al_2O_3$ controls in methanol reforming at 180°C after 80 h on-stream, albeit at high space-time ratio (~400 kg.s/mol). Wang et al. [378] have reported a micro-reformer link-up with a low-temperature phosphoric acid fuel cell (LTPAFC) operated from 130-180°C. The reformer was charged with 30-40 mg of a Cu/Mn/Zn oxide nanocomposite (obtained by deposition-precipitation), applied by multiple wash-coat methods and finally calcined at 400°C

for 2h. It was operated as a partial-oxidation methanol reforming (POMR) catalyst with a low flow of air, giving rise to the following reactions proceeding in parallel:

Decomposition (MD):

$$CH_3OH \rightarrow CO + 2\,H_2 \qquad (\Delta H^0 = +92\ \text{kJ/mol}) \qquad (21)$$

Reforming (MR):

$$CH_3OH + H_2O \rightarrow CO_2 + 3\,H_2 \qquad (\Delta H^0 = +49\ \text{kJ/mol}) \qquad (22)$$

Partial oxidation (POM):

$$CH_3OH + 0.5\,O_2 \rightarrow CO_2 + 2\,H_2 \qquad (\Delta H^0 = -192\ \text{kJ/mol}) \qquad (23)$$

in which the exothermicity of POM (Reaction 23) supplies heat to drive the two endothermic processes - methanol decomposition (MD - Reaction 21) and methanol reforming (MR - Reaction 22). The only sacrifice is in terms of the $H_2$ yield, being reduced to ~80% of theoretical for MR. Methanol conversion reached nearly 80% at 130°C and the $H_2$ production rate was remarkable at ~1 mol/$g_{cat}$/h at a space-time ratio of 4.3 kg.s/mol. CO levels were quite good, staying below 25 ppm up to 200°C. This was surprising because the literature often reports a breakthrough of CO (up to several %) in this temperature range [379], due to the onset of methanol decomposition (MD, Reaction 21) along with inadequate WGS activity.

Photocatalytic generation of hydrogen, *ie.* that deriving solely from illumination without deliberate simultaneous heating [249], has been reviewed both as a general topic [361], and in relation to bio-derived renewable oxygenates and alcohols in particular [33,380,381]. While fundamental studies over pristine $TiO_2$ are of key mechanistic importance [382], most reports deal with photo-reforming of methanol (MPR) over the "benchmark" photocatalyst Pt (or Pd)/$TiO_2$, including modelling of charge trapping kinetics and mechanisms of deactivation. Advances have also been made in the use of earth-abundant metal co-catalysts for better sustainability.

Mills et al. [383] presented a kinetic modelling scheme for the rate of $H_2$ evolution in MPR as a function of metal (Pt, Pd) catalyst loading in the gas and liquid phase. The expanding photocatalytic area and overlap (EPAO) kinetic model is a refinement of their earlier metal support interface (MSI) model [384] that only considered the *perimeter* around (assumed) hemispherical metal (close-packed) nanocrystallites of Pt (Pd) of 1-2 nm radius, evenly distributed across a $TiO_2$ support of known surface area. It was already clear from the MSI model that the popular interpretation of the sudden fall in activity (in $H_2$ evolution) with metal loading (beyond ~1 wt%) in terms of an optical "inner filter" effect (obscuration of UV light from access by $TiO_2$) was untenable.

The EPAO model defines an annular "extended zone" surrounding the metal particle, as shown by the red hatching in Fig. 26A. Its existence has been amply demonstrated on a macro- (mm) scale in photo-oxidation studies (visible bleaching/ removal) of a coloured deposit, e.g., ultra-fine porous carbon (soot) distributed widely over a narrow band of Pt [385]. With increasing loading, these zones eventually touch, a condition of maximum active area and concomitant activity in $H_2$ evolution. Beyond this point, the zones start to overlap (grey hatching), introducing a deactivation factor associated with competitive (self-cancelling) electric fields. The polarisation scheme for charge carrier separation and redox chemistry associated with a single metal particle and its peripheral zone of $TiO_2$ is depicted in Fig. 26B. While the metal particle acts as a "sink" for photogenerated electrons, promoting successive proton discharge and $H_2$ evolution, the surrounding $TiO_2$ preferentially adsorbs methanol and facilitates hole-based photo-oxidation and ultimately evolution of $CO_2$. Plots (predictions) of the EPAO model in relation to data points in photocatalyzed $H_2$ evolution from methanol in both the liquid and vapour state(s) are shown in Figs 26C and 26D, respectively. Although the fitting and trends in these plots are qualitatively similar there are certain differences, especially in the metal loading corresponding to maximum activity, viz., 0.25 wt% (liquid) and 0.01 wt%

(vapour), respectively. This derives from a proportionate (x 2.7) increase in extended zone radius with increasing particle radius in the gas phase experiments, the reasons for which remain unclear. A small "dark" contribution to activity at 100°C was also noted.

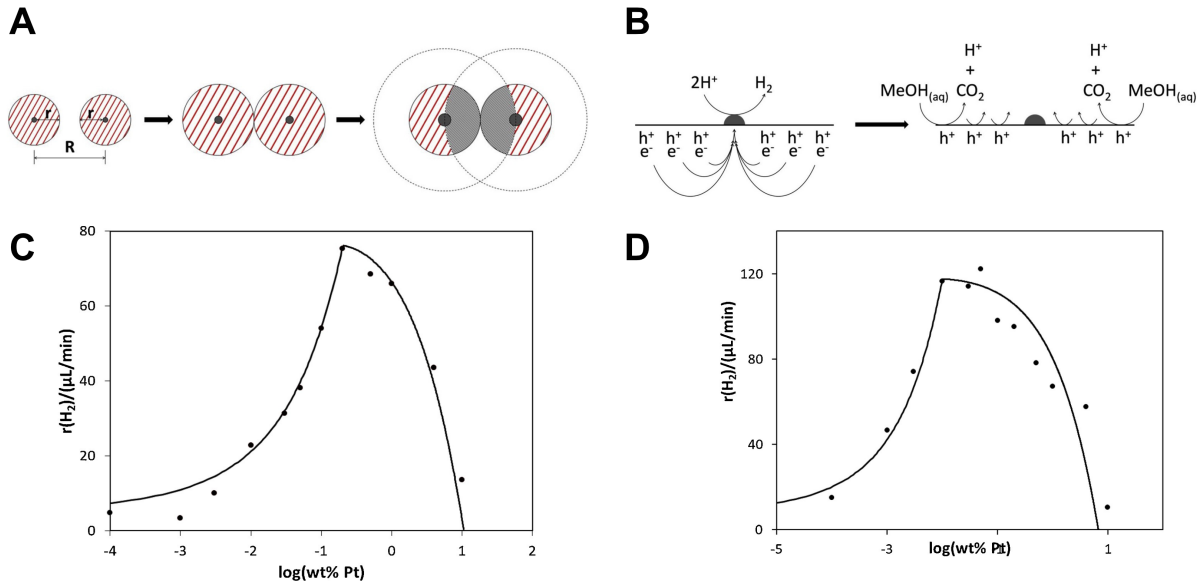


**Fig. 26 A.** The EPAO concept of Mills et al. illustrating the extended zone of influence of adjacent metal particles (red hatched areas) reaching an optimum (touching zones), beyond which overlap (grey areas) leads to lower specific activity. **B.** Polarisation scheme at a single metal particle. By attracting electrons and effecting proton discharge and $H_2$ evolution, the metal particle exerts a peripheral (areal) influence favouring hole interaction with methanol leading to photo-oxidation, ultimately evolving $CO_2$. **C.** EPAO model (solid line) in relation to data points of activity in $H_2$ evolution from methanol aqueous solution vs. log (wt%) Pt loading on P25 $TiO_2$. **D.** EPAO model (solid line) in relation to data points of activity in $H_2$ evolution from methanol vapour at 100°C vs. log (wt%) Pt loading on P25 $TiO_2$. [Reproduced with permission from ref. 383.]

In contrast, Walenta and co-workers, taking a surface science approach to methanol reforming on a rutile (110) surface [386,387], have called into question the popular concept of

1539 the metal (Pt) co-catalyst acting as an “electron” sink (to effect proton discharge). They argue
1540 instead for H migration via reverse spillover, probably in a proton-coupled electron transfer
1541 (PCET) mechanism facilitated by reducible $Ti^{4+}$ centres, including those located in sub-surface
1542 regions [388]. In other words, proton discharge occurs on the support and hydrogen reaches Pt
1543 as an ad-atom, H°, already carrying the photogenerated electron. Due to its finely balanced
1544 adsorptive properties, the role of Pt is to accumulate surface H ad-atoms, eventually leading to
1545 dimerization of adjacent $Pt_s$-H groups and $H_2$ evolution. However, it is fair to point out that
1546 only the initial photo-dehydrogenation step (to HCHO) was considered and the effect of co-
1547 dosing with water vapour was not studied. Analysis was based on TPD after UV pre-irradiation,
1548 detecting simultaneous evolution of $H_2$/HD/$D_2$ and $d_2$-formaldehyde from $CD_3$-labelled
1549 methanol at near-ambient temperature. Future work might benefit from *in-situ* vibrational
1550 spectroscopic studies of the adsorbed intermediate species, e.g., by high-resolution electron
1551 energy loss (HREELS) [389], infrared reflection absorption (IRAS) [390], or sum-frequency
1552 generation (SFG) spectroscopy [391].

1553 On the issue of photocatalytic stability, Haselmann and Eder [392] reported on early-
1554 stage deactivation in methanol photo-reforming over platinized $TiO_2$ samples prepared by
1555 photo-deposition. Initially high activities in $H_2$ evolution (~40 mmol/$g_{cat}$/h, AQY ≈ 56%) under
1556 Hg lamp (UV) illumination (30 mW/$cm^2$) were found to decay slowly in the early stage,
1557 followed by a precipitous drop after 10 h. This was correlated with O-vacancy build-up
1558 rendering the $TiO_2$ ineffective in oxidation of gas-phase CO, found to be accumulating on Pt
1559 over the same time period. Stable activity was temporarily extended either by pre-calcination
1560 of $TiO_2$ in air at 400°C and/or using a higher level of Pt (0.5 → 1.5 wt%). Courtois et al. [393]
1561 investigated the origin of poisoning and claimed that it lies in the thermal back-reaction of
1562 formaldehyde to methoxy. This is in contra-distinction to earlier DFT work showing that the
1563 energy barrier to formaldehyde formation from the methoxy radical (~0.2 eV) is much lower

than recombination leading back to the methoxy anion (~0.6 eV) due to upward band-bending and the large structural reorganisation involved [394]. In a deepening investigation into deactivation, the same group reported on the possible use of Ni, an earth-abundant metal, as a potential substitute for the precious metal in $M/TiO_2$ [395]. Under UV irradiation of $Ni/TiO_2$ (110), tapering levels of $H_2$ and formaldehyde evolution were observed in successive dosing with methanol. This was correlated with the growth of a C signal in Auger spectroscopy. Since no evidence was found for oxidation of the Ni clusters and TPD showed a CO desorption peak at ~180°C, it was inferred that deactivation was due to the build-up of a surface nickel carbide. Such a remarkably low activation temperature for CO dissociation has already been reported for these ultra-small size-selected Ni clusters (10-30 atoms) [396]. While this is a striking example of how valuable (novel) catalytic properties can be developed under cluster size-control [397], it is clearly undesirable in photo-reforming. The adsorbed CO must ideally remain intact for subsequent oxidation to $CO_2$ by $H_2O/OH°$ in the Water Gas Shift reaction, thereby closing the cycle. In other words, judicious tempering of the adsorptive properties of potential rare-metal substitutes on a size basis and/or by alloying, etc., is an essential task. Chung et al. [398] reported on a novel one-pot preparation to obtain nanodispersed $Pt/TiO_2$ photocatalysts. Their activities in $H_2$ evolution were quite high, falling in the range 5-12 $mmol/g_{cat}/h$ (365 nm LED irradiation at 4.4 x $10^{-4}$ E/s). Furthermore, after removal of contaminant $Na^+$ ions, the activities were stable over many hours as compared to control samples prepared by photo-deposition, which lost half their activity within 3h.

Regarding advances in earth-abundant co-catalysts as sustainable alternatives, nickel- and copper-based materials, semiconductor- or self-supported, are receiving increasing attention recently [399-401]. As the metallic state of co-catalysts (M) is essential for $H_2$ generation, Bahruji et al. [402] have stressed the importance of metal (oxide) reducibility in the selection of cheaper candidate materials, e.g., Fe, Co, Ni and Cu. Unlike precious metals for which any

superficial oxide is unstable, only CuO is potentially reducible by methanol under anaerobic conditions *in-situ*. For stable oxides of Mn, Fe, Co and Ni, this property must be imparted by high-temperature pre-reduction (under $H_2$ or CO), followed by passivation in a low pressure of air at near ambient temperature. On the other hand, controlled (partial) reduction to a mixed $M/MO_x$ state is very interesting because the residual oxide, e.g., $Fe_2O_3$, CoO, NiO, CuO and $Cu_2O$, is typically a semiconductor and, depending on its band-edge positions in relation to $TiO_2$ may promote potential synergies in charge carrier separation at heterojunctions. A revised mechanism in water splitting over $Ni/NiO/SrTiO_3$, implicates NiO as a hole acceptor [403]. Furthermore, those with narrow band gaps offer prospects for visible-light sensitization [404,405].

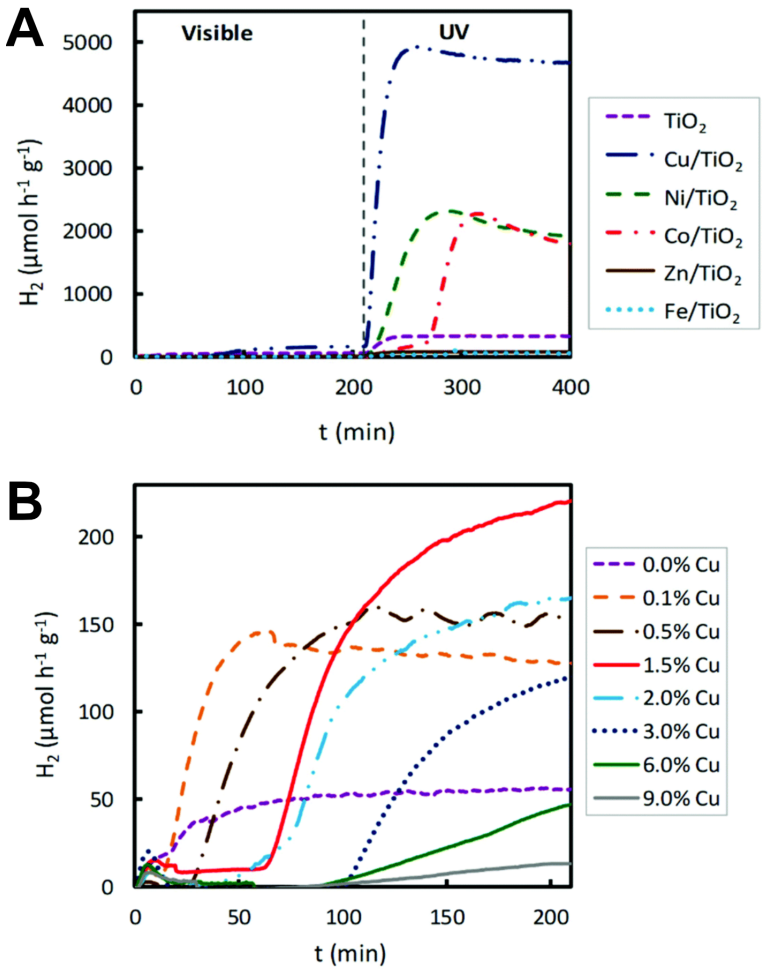

**Fig. 27 (A)** $H_2$ production from aq. methanol over $M/TiO_2$ photocatalysts (M = Fe, Co, Ni, Cu, Zn) at 2 wt% under visible and UV light irradiation. **(B)** Cu loading-dependent induction time in $H_2$ evolution under visible light irradiation. [reproduced with permission from ref. 406]

Díaz et al. [406] compared $TiO_2$-supported metals decorated by Fe, Co, Ni, Cu and Zn in 25% aqueous methanol photo-reforming at 20°C under ambient pressure ($N_2$ bubbling). As shown in Fig. 27A, the most active photocatalyst was 2 wt% $Cu/TiO_2$ (P25), evolving 5 mmol $H_2$ $g_{cat}^{-1}h^{-1}$ under UV irradiation and 0.22 $mmol.g_{cat}^{-1}h^{-1}$ under visible light. The $Pt/TiO_2$ control was only 20% more active than $Cu/TiO_2$ under UV irradiation. Ni and Co samples were also quite active, giving rates exceeding 2 $mmol.g_{cat}^{-1}h^{-1}$. Characterization of $Cu/TiO_2$ by TEM and XPS showed that the copper was well-dispersed and co-existing in reduced ($Cu^0$, $Cu^+$) and oxidised ($Cu^{2+}$) forms. As shown in Fig. 27B, a progressive increase in induction time with Cu loading prior to the onset of detectable $H_2$ under visible light was attributed to *in-situ* sensitization via photo-reduction of $Cu^{2+}$ to other photo-active states, $Cu^+$ and $Cu^0$. Cuprous oxide ($Cu_2O$) is a reddish narrow-bandgap semiconductor ($E_g$ = 2.0 eV, $\lambda_{max} \approx$ 500 nm), while the tawny colour of bulk metallic copper is due to a surface plasmon resonance absorption feature in a similar range ($\lambda_{max} \approx$ 590 nm). While both CuO and $Cu_2O$ are known to have suitable conduction band edges for $H_2$ evolution, activities are generally low in the absence of co-catalysts [407]. The potential of $Cu^0$ photogenerated *in-situ* as a $H_2$ evolution co-catalyst has been confirmed in independent studies on a similar $Cu/TiO_2$ sample [408].

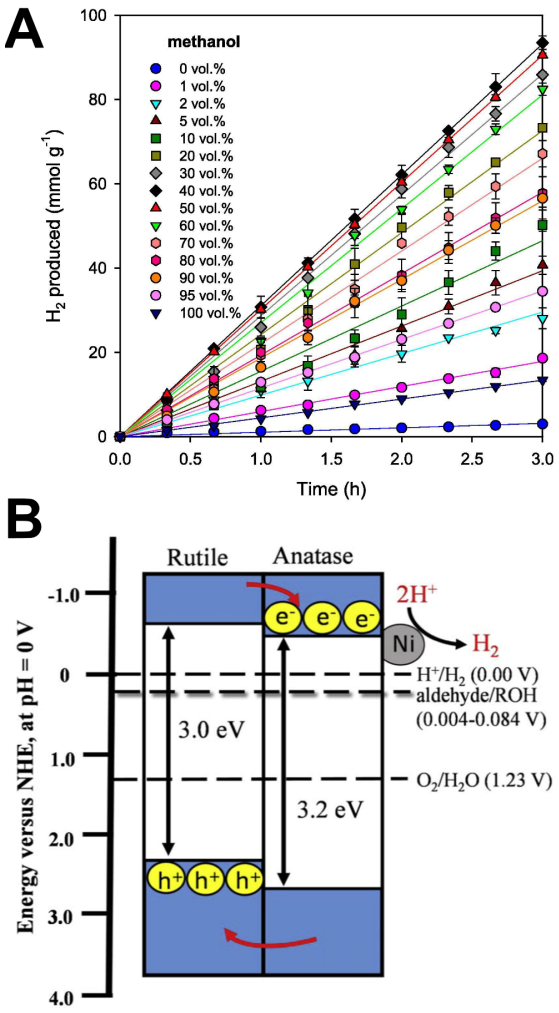


**Fig. 28 (A)** Concentration dependence of $H_2$ evolution from aqueous methanol over 0.5 wt% Ni/$TiO_2$ (P25). **(B)** Energetics and photo-generated charge flow in alcohols photoreforming over Ni/$TiO_2$ (P25). [Reproduced with permission from ref. 409]

Chen et al. [409] explored 0.5 wt% Ni/$TiO_2$ (P25), along with 2% Au/$TiO_2$ (P25) as control, and found high and comparable activities in photo-reforming of a range of alcohols, including methanol. HRTEM, XANES and EXAFS analyses confirmed that the co-catalysts were well-dispersed (5-8 nm) and existing in the metallic state(s). As shown in Fig. 28A, $H_2$ evolution rates were concentration-dependent with the best performance observed (30 mmol.$g_{cat}^{-1}h^{-1}$, AQY ≈ 20%) at ~40 vol% in the case of aqueous methanol. While carbon

products were not analysed, it can be inferred that water assists in $H_2$ generation, implying reforming proper (see Reaction 22). The superior activity of Ni on P25 support (85% anatase, 15% rutile), as compared to Ni on the individual pure $TiO_2$ phases (and their physical mixtures), was attributed to the favourable disposition of heterojunctions, promoting charge carrier separation and directional flow, electrons towards anatase and holes towards rutile. The energetics of the alcohols reforming photo-redox scheme is shown in Fig. 28B. Further examples showing the promise of non-noble elements in methanol photo-reforming will be presented in the following section on photo-thermo synergies.

In *photo-/thermo* catalysis, Sun et al. [410] explored photo-assisted methanol reforming over Cu/Zn/Ti oxide solid solutions and obtained high methanol conversions (20-50%) under largely visible irradiation in the range 200-210°C. High and stable rates of $H_2$ evolution (50-76 $mmol.g_{cat}^{-1}h^{-1}$) were achieved, corresponding to a 4x enhance-ment over the dark rates. A mechanism was proposed to explain the photo-activation effect (colour change grey-green to black) involving *in-situ* photo-reduction of the CuO to $Cu_2O$. No CO was detected in the products. Yu et al. [411] prepared a pan-spectral absorber (sun-weighted absorption = 92%) based on a Cu/Zn/Zr (70/23/7) oxide nanocomposite and investigated the photo/thermos synergism in methanol reforming. Under multiple sun-power irradiation (x5-x16), the reaction temperature rose from 100 to 200°C via a photo-thermal heating mechanism. The $H_2$ evolution rate attained a remarkable 2.4 $mol.g_{cat}^{-1}h^{-1}$ at 200°C ($\eta_{STH} \approx 45\%$), corresponding to 3x the dark rate. Based on IR spectral changes in adsorbed species measured over the relevant temperature range by DRIFT spectroscopy, the mechanism is thought to proceed via methyl formate (known to be promoted by Cu on basic oxide supports) [412], which hydrolyses to formate. The sequence can be represented as:

$$2\ CH_3OH \rightarrow CH_3OCHO + 2\ H_2 \quad (24)$$

$$CH_3OCHO + H_2O \rightarrow HCOOH + CH_3OH \quad (25)$$

1661 $HCOOH \rightarrow CO_2 + H_2$ (26)

1662 (MR) $CH_3OH + H_2O \rightarrow CO_2 + 3\ H_2$ (27)

1663

1664 Fang et al. [413] explored photo/thermo-driven catalysis of MPR in the vapour state from
1665 210 to 310°C over a low-cost $NiO_x$-loaded $TiO_2$ supported on high-light-scattering $SiO_2$. Pure
1666 photocatalysis, i.e., exposure to AM 1.5G sunlight at ambient temperature was ineffective,
1667 resulting in a very low $H_2$ evolution rate (4 $\mu mol.g_{cat}^{-1}h^{-1}$). In contrast, dark (thermal) activity
1668 was already substantial above 200°C, reaching 22 $mmol.g_{cat}^{-1}h^{-1}$ by 260°C. Under dual photo-
1669 thermo excitation at the same temperature, this was raised by a factor of 2.5x (to 54 $mmol.g_{cat}^{-1}h^{-1}$).
1670 As shown in Fig. 29B, the use of a UV-cutoff filter ($\lambda > 420$ nm), revealed that most of
1671 this increase (27 out of 32 $mmol.g_{cat}^{-1}h^{-1}$) derived from irradiation by the visible component,
1672 with estimates of the AQY exceeding 15% up to 500 nm. This was attributed to an absorption
1673 tail in $TiO_2$ due a slightly narrowed band-gap ($E_g$ ~2.88 eV). Visible absorption in the region
1674 420-500 nm is characteristic of F-type centres in $TiO_2$ located at surface O-vacancies [414].
1675 The activity was relatively stable, dropping slowly to 40 $mmol.g_{cat}^{-1}h^{-1}$ over 30h. Isotopic
1676 tracing showed that most of the evolved $H_2$ derived from methanol at 260°C but $D_2O$ became
1677 the primary source at higher temperature. The main carbon product was CO in a 1:2 ratio with
1678 $H_2$, indicating lack of activity in WGS. As shown in Fig. 29A, a mechanistic scheme was
1679 proposed in which the co-catalyst, in the form of a metallic Ni core encapsulated by a thin
1680 porous shell of NiO, promoted both $H_2$ evolution and methanol oxidation, respectively.

1681

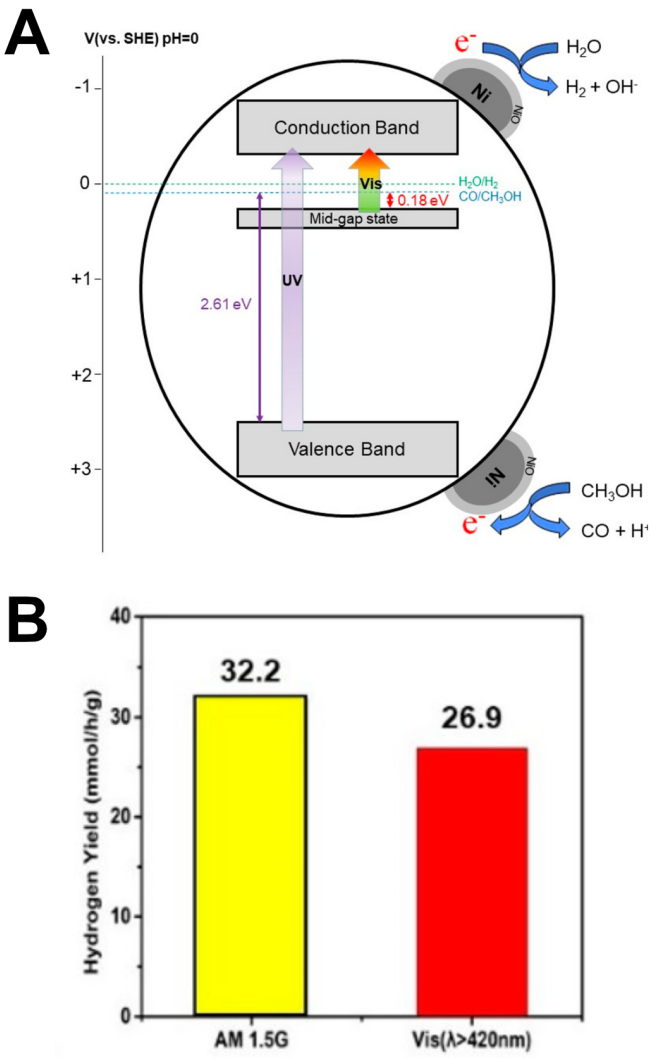


**Fig. 29** Band energy scheme to explain the visible response in photo-/thermo synergistic $H_2$ evolution over $NiO_x$-$TiO_2$ at 260°C under full AM1.5G light (yellow bar) or with UV cut-off at 420 nm (red bar). [Reproduced with permission from ref. 413]

Liu et al. [497] have reported similar $H_2$ evolution rates in photo/thermo-driven reforming of methanol over 10 wt% Cu/$TiO_2$-$CeO_2$ in varying proportions over the same temperature range (200-300°C). The most active catalyst had a $TiO_2/CeO_2$ ratio of 2, achieving a conversion of 84% at 275°C with a $H_2$ production rate of 22 and 50 mmol.$g_{cat}^{-1}h^{-1}$ in the dark and under illumination, respectively. The main difference was the high (> 97%) selectivity to $CO_2$, as expected since supported Cu has excellent Water Gas Shift activity. DRIFTS analysis detected

peaks of methoxy and formate species growing together up to 200°C indicating conversion via a methyl formate intermediate. The mechanism proposed is identical to that of Yu et al. [411] over a Cu/Zn/Zr oxide nanocomposite (Reactions 24-26 – see above).

**7.2 Ethanol**

The balanced expression for ethanol (steam) reforming [E(S)R] is shown below:

$$C_2H_5OH_{(g)} + 3\ H_2O_{(g)} \leftrightarrow 2\ CO_2 + 6\ H_2 \qquad (\Delta H^0 = +175\ kJ.mol^{-1}) \qquad (28)$$

E(S)R is a highly endothermic process that becomes thermodynamically favoured (due to the entropy factor) already at 210°C. In principle, 6 moles of $H_2$ are generated, half of which derive from water conversion via the Water Gas Shift process, a slightly exothermic reaction favoured at low temperature:

$$CO + H_2O \leftrightarrow CO_2 + H_2 \qquad (\Delta H^0 = -40\ kJ.mol^{-1}) \qquad (29)$$

Unfortunately, as compared to methanol, theoretical yields are rarely approached due to the greater complexity of the $C_2$ alcohol, resulting in coking and catalyst deactivation [29]. The catalyst must be highly selective in activating the C-C bond, leading to CO as intermediate. In order to avoid carbon formation via the Boudouard reaction ($2CO \rightarrow C + CO_2$), any CO must be rapidly oxidised via the Water Gas Shift reaction (Reaction 29). Nevertheless, there are competing coking mechanisms that do not require C-C bond rupture. For example, acidic sites at the catalyst surface can promote both ethylene formation by *dehydration* and its subsequent *polymerization* to coke precursors [368]. There is a general consensus that E(S)R proceeds via a preliminary dehydrogenation step to acetaldehyde:

$$C_2H_5OH \rightarrow CH_3CHO + H_2 \qquad (\Delta H^0 = +69\ kJ/mol) \qquad (30)$$

Furthermore, experiments and DFT calculations are consistent in showing that ethanol dehydrogenation (EDH, Reaction 30) is the most probable rate-determining step (rds) with a high apparent activation energy ($E_a \approx$ 50-100 kJ/mol), e.g., over Au/ZSM-5 [416], Ni/Au [417], Ni/Cu [350], Ru, Pd, and Pt [418]. Even for the best EDH catalyst, supported mono-metallic Cu, $E_a$ is still quite high at 70 kJ/mol [419]. The likelihood of such a mechanistic scheme initiating E(S)R is corroborated by the undesirably high methane levels [($CH_4 \approx (CO+CO_2) \approx H_2$] frequently seen in product streams by 300°C [420-422]. Acetaldehyde (AcH) is known to readily decarbonylate on transition metal surfaces [423]:

$$CH_3CHO \rightarrow CO + CH_4 \qquad (\Delta H^0 = -19 \text{ kJ/mol}) \qquad (31)$$

The balance of Reactions 30 and 31 is sometimes termed ethanol "decomposition":

$$C_2H_5OH_{(g)} \rightarrow CO + H_2 + CH_4 \qquad (\Delta H^0 = +50 \text{ kJ/mol}) \qquad (32)$$

Even allowing for full conversion of CO to $CO_2$ (and more $H_2$) via WGS (Reaction 29), the $H_2$ yield rarely exceeds 50% for non-precious metals Co and Ni [421]. $H_2$ levels can only be raised further via steam reforming of $CH_4$ (see Reactions 3 or 17), a very endothermic process with high kinetic barriers. This rationalises the high operating temperature range (400-550°C) typically reported in E(S)R. Apart from the extra heat demand, a deleterious consequence is the acceleration of coking and catalyst deactivation. Cu is the only mono-metallic catalyst with high activity and selectivity in ethanol dehydrogenation (Reaction 30) and Water Gas Shift (Reaction 29), but inactive in decarbonylation (Reaction 31). Future investigations should focus on this earth-abundant metal as one important active-phase component, e.g., in the form of stable (Ni/Cu) [424,425], or metastable (Co/Cu, Fe/Cu) bimetallic alloys [424,426,427]. Atomically dispersed Ni in Cu lowers the activation energy for ethanol dehydrogenation from

~70 to 45 kJ/mol [428]. Cu has been used as a promoter in the Lebedev process (ethanol-to-butadiene, ETB) [429]. While its presence may also moderate coking, the main disadvantage of Cu, at least in mono-metallic form, is its quite high sintering rate above 300°C [430]. The rational design of sinter-resistant forms based on a mechanistic understanding has been emphasised recently [431], as has the exploitation of novel methods such as encapsulation [432], etc., to improve the hydrothermal stability of supported metal catalysts in biomass conversion [433]. The limited data available on Cu-containing catalysts in E(S)R show that it confers several benefits in terms of high activity (> 60% conversion at 350°C), good $H_2$ yields (> 50 %) and low (< 5%) selectivities to CO and $CH_4$ [434-436], as well as stable operation due to low coking rates [434].

A practical reforming catalyst for ethanol (and higher oxygenates) needs to be based on earth-abundant metals for techno-economic reasons [422,437]. This explains the intensive level of research into active phases based on 1st-row transition metals Fe, Co, Ni and Cu [31,368,421,438]. Unfortunately, issues of catalyst instability (poor resistance to coking, sintering and other modes of deactivation) are frequently encountered with these base metals [368,439,440]. For example, Montero et al. [440] have reported on the origin and nature of coke and its relationship with deactivation in E(S)R over $Ni/La_2O_3$-$\alpha Al_2O_3$ in a fluidized-bed reactor at 500 to 650°C in a range of space-time (0.02-0.35 $g_{cat}h.g_{EtOH}^{-1}$) and steam-to-carbon (S/C) ratios of 3-9. The features of the deactivated catalysts and the nature and morphology of the coke deposited were analysed by temperature-programmed oxidation (TPO), X-ray diffraction (XRD), scanning electron microscopy (SEM), and Raman spectroscopy. A typical activity/time curve at low temperature (500°C) and low space time (0.02 $g_{cat}.h.g_{EtOH}^{-1}$) is shown in Fig. 30A.

Ethanol conversion ($X_{EtOH}$) was initially quite low (~0.14) but dropped by 80%, or a factor of 5 (to 0.03), over the next 10h. The only products in significant amounts were acetaldehyde (AcH) and $H_2$, their levels also falling along with $X_{EtOH}$. This yielded a strongly deactivated

1773 catalyst whose carbon level was surprisingly low (0.7 wt%) as measured by TPO (see Fig. 30B).
1774 The deposit was highly reactive in showing an evolution peak below 400°C (black trace),
1775 typical of coke in close contact with the metal (encapsulation). Studies at higher temperature
1776 resulted in only a limited build-up of carbon (< 2 wt%) and less-dramatic deactivation, e.g.,
1777 $X_{EtOH}$ fell from 0.8 to a stable value of 0.4 at 650°C, a drop of 50%. Ethylene ($C_2H_4$) was the
1778 next most abundant product after AcH. The coke (1.8 wt%) was still quite reactive, giving a
1779 peak evolution at 450°C (Fig. 30B - blue trace). At higher space-time (0.18 $g_{cat}.h.g_{EtOH}^{-1}$), i.e.,
1780 a longer contact time, full ethanol conversion ($X_{EtOH} \approx 1$) was observed at all temperatures.
1781

1782

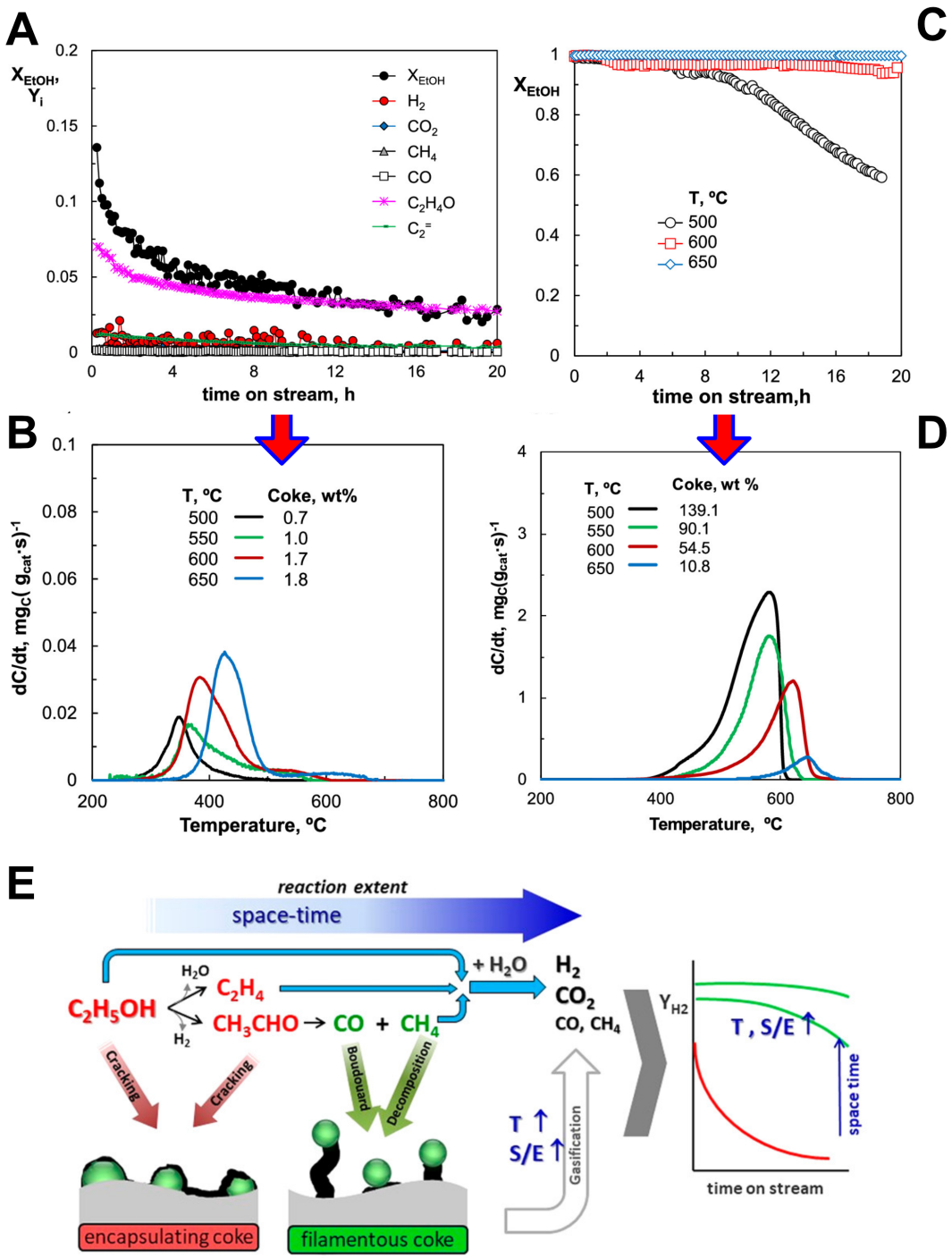


1783

1784 **Fig. 30 (A)** Ethanol conversion and product yields at 500°C and low space-time (0.02 $g_{cat}$

1785 h.$g_{EtOH}^{-1}$; S/E = 6) over 10 wt% Ni/$La_2O_3$-α$Al_2O_3$. **(B)** Coke level and reactivity by TPO

1786 (black trace) on the catalyst deactivated in (A). **(C)** Ethanol conversion at 500-650°C and high

space-time (0.18 $g_{cat}$ $h.g_{EtOH}^{-1}$; S/E = 3). **(D)** Coke level and reactivity by TPO on the catalyst deactivated in (B). **(E)** Overall reaction scheme distinguishing the source of encapsulating (pernicious) coke by $C_2$ cracking (red trace), filamentous (more benign) coke by $C_1$ decomposition (green trace), and gasification (promoted at higher temperature and S/E ratio) leading to more stable performance. [Adapted and reproduced from ref. 440]

However, at 500°C deactivation was progressively evident after 8h on-stream, $X_{EtOH}$ falling to ~0.6, or a drop of 40% relative, over the next 12h (see Fig. 30C). That this rate was lower than at low space-time at the same temperature (Fig. 30A) shows that deactivation is most aggressive during exposure of the catalyst to significant vapour levels of $C_2$ compounds, including ethanol (ethoxy) itself. Separate studies of AcH SR found deactivation rates similar to those for ethanol. [Raising the steam-to-carbon ratio from 3 (stoichiometric - Reaction 26) to 9 at 500 °C almost completely suppressed deactivation via surface carbon gasification]. Product yields of $H_2$ and $C_1$ gases (CO, $CO_2$, $CH_4$) fell from their starting levels (~0.4) while AcH reappeared.

As shown in Fig. 30D, coke levels were raised dramatically, reaching 139.1 wt% at 500 °C and 10.8 wt% at 650°C, i.e., one or two orders of magnitude higher than at low space-time. This coke was much less reactive with a peak evolution near 600°C, although the most abundant variety (deposited at 500°C) showed an onset of reaction in TPO at a lower temperature (T ≈ 400°C), suggesting the presence of a small fraction of the encapsulating form responsible for deactivation. The low-reactivity coke was found to be of the filamentous type by SEM. Its benign nature is well-exemplified by the fact that when full ethanol conversion was maintained by operating at a higher S/E (= 9), the catalyst nevertheless accumulated 24.6 wt% carbon.

A summary of the main features of coking and deactivation in E(S)R over Ni/ $La_2O_3$-$\alpha Al_2O_3$ is depicted schematically in Fig. 30E. The most pernicious variety of coke is the so-

called metal-encapsulating type, deposited at low-temperature from cracking reactions of ethanol itself and $C_2$ intermediates, mainly ethylene, acetaldehyde and acetic acid. At higher temperature and higher space-time, a more benign filamentous coke results from cracking reactions of $C_1$ products CO and $CH_4$.

It is already clear that any oxide support, a key catalyst component, must have basic surface chemical properties to promote dehydrogenation over dehydration, otherwise coking proceeds via $C_2H_4$ intermediate. This precludes $Al_2O_3$ and alumino-silicate supports in favour of alkaline earths MgO, CaO, ZnO, layered double hydroxides (LDH), etc. In the foregoing example [440], $La_2O_3$ (9 wt%) was used to counteract the Brönsted acidity ($H^+$) of the alumina, deemed necessary to confer structural and hydrothermal stability for working in high steam atmospheres. While the gasification properties of the mixed-oxide support were impressive, the beneficial effect of $La_2O_3$ was somewhat limited, as judged by the modest resistance to coking and presence of $C_2H_4$ under certain conditions. With the exception of some rare-earths, basic oxides generally manifest poor hydrothermal stability.

In contrast, there is growing interest in catalytic applications of ceria ($CeO_2$), a basic and thermally stable material, that is the most abundant and affordable of the rare earths priced in bulk quantities. $CeO_2$ is readily prepared in high surface-area/porous nano-forms, and only starts to sinter in steam above 700°C [441,442]. In E(S)R, its perceived role is to protect the active metal from coking by promoting water activation and OH-group migration to the surface carbon to effect gasification. Alternatively, it can divert the coking mechanism from the more aggressive mode, i.e., metal encapsulation by graphitic carbon, to more innocuous types. There is a recent report of deactivation-free E(S)R where filamentous carbon growth can be sustained almost indefinitely with no loss in activity [443]. From intensive characterization and *in-situ* spectroscopic studies of Ni/$CeO_2$ model catalysts [444-446], this special ability of ceria is attributed to its unique O-storage capacity, i.e., reversible redox properties involving the

1837 $Ce^{4+}/Ce^{3+}$ couple. This can be extended by judicious doping with low-valent ions, e.g., $Mg^{2+}$
1838 [447]. A related strong metal-support interaction (SMSI) is claimed to stabilise electron
1839 deficient forms of nickel ($Ni^{™+} \rightarrow Ni^{2+}$) in a reducing environment, imparting high activity in
1840 WGS and greater sintering resistance to the active metal [448].

1841 Relatively few reports have appeared on ethanol aqueous-phase reforming (APR),
1842 conducted below 300°C. This seems surprising in view of clear operational advantages
1843 compared to gas-phase (steam) reforming [449]. A bimetallic Pd/Zn catalyst [420], supported
1844 on carbon nanotubes (for hydrothermal stability), achieved only 30% conversion at 250°C and
1845 65 bar, generating 1.9 mol $H_2$/mol ethanol (30% yield). The carbon product distribution
1846 consisted of 35% $CO_2$, 37% acetic acid (AcOH), 24% $CH_4$, 5% alkanes and traces (< 1%) of
1847 AcH, methanol, and acetone. This distribution was rationalised by a reaction network involving
1848 initial dehydrogenation (Reaction 30) and subsequent decomposition of AcH in two evenly
1849 balanced routes, namely hydrolysis/dismutation (Reaction 33) and decarbonylation/WGS
1850 (Reaction 34, issued from Reactions 31 and 29):

1851

1852 $$2\ CH_3CHO + H_2O \rightarrow CH_3COOH + C_2H_5OH \quad (33)$$

1853 $$CH_3CHO + H_2O \rightarrow CO_2 + CH_4 + H_2 \quad (34)$$

1854

1855 The overall chemical balance can be written as:

1856

1857 $$2\ C_2H_5OH + 2\ H_2O \rightarrow CO_2 + CH_4 + CH_3COOH + 4\ H_2 \quad (35)$$

1858

1859 where Reaction 35 also satisfies the often reported 2:1 molar yield in $H_2$. There are two recent
1860 reports of APR on the components of Fischer-Tropsch water effluent consisting in large part of
1861 $C_1$-$C_3$ alcohols at low (< 1%) levels. Coronado et al. [450] found that a 10% Ni/$CeO_2$-$ZrO_2$

catalyst was weakly active, achieving just 20% conversion (and 40% $H_2$ yield) at 230°C, possibly due to metal sintering, being most pronounced in tests on ethanol ($d_{Ni}$ 20→70 nm). In related work, Zoppi et al. [451] explored APR of Fischer-Tropsch effluent at 230-270°C over a 5% Pt/C catalyst. Conversion of the ethanol component after 2h was in the range 80-95% with a carbon-to-gas efficiency up to 60%. The $H_2/CO_2$ ratio was 2.3 suggestive of incomplete reforming (Reaction 28), while selectivity to $CH_4$ was quite high at 25%. The only observed liquid by-product was acetic acid, increasing from 630-730 ppm. This was attributed to Cannizzaro/Tischenko-type reactions (Reaction 33). Roy and Leclerc [452] studied the effect of preparation/pre-activation and operational variables (feed rate, pressure) on a 10%Ni/$CeO_2$ catalyst in APR at low conversion (~5%) and low temperature (145-175°C). The main influence on activity/selectivity was found to be Ni particle size and not the metal oxidation state(s). Selectivities to gas-phase products $H_2$ and $CO_2$ increased with temperature from 75-95% and 65-80%, respectively, while $CH_4$ dropped from 30 to 15%. Increased pressure and/or feed rate resulted in higher selectivity to $CH_4$. In the liquid products, AcH selectivity was raised from 70 - 85%, at the expense of AcOH (25→10%). XPS analysis of the spent catalyst showed that the support was largely reduced to $Ce_2O_3$, which was inferred to stabilize the $Ni^0$ state.

Nozawa et al. [453] reported that addition of 5% Re as promoter to 5% Ru, Rh, Ir, and Pt on $TiO_2$ led in all cases to higher activity in ethanol conversion (and $H_2$ production) at 200°C. Most notable was the effect of Re on Rh/$TiO_2$ and Ir/$TiO_2$, increasing conversions from 14→36% and 6→15%, respectively. The highest conversion among single metal controls was for Ru (30→36%) after 10h but the selectivity to $CH_4$ was high (12.4 mmol.$g_{cat}^{-1}$) with a $H_2/CH_4$ mole ratio of ~0.3. This increased to ~0.8 upon Re addition, due mainly to enhanced $H_2$ generation. The value was better for Rh (1.4) but unchanged upon Re addition, the productivity of both gases increasing proportionately (see Fig. 31A). Another effect of Re was on selectivity to AcOH reaching 24, 25, and 30 mmol.$g_{cat}^{-1}$ over Rh, Ru and Ir, respectively. A reaction

network similar to that inferred by Xiong et al. [420] (Reactions 30, 33, 34 – see above) was proposed, as shown in Fig. 31B. This involves initial dehydrogenation to AcH and its subsequent decomposition by two competing routes; type I - decarbonylation/WGS, and/or type II - "hydrolysis" to AcOH and $H_2$, a highly endothermic process:

$$CH_3CHO_{(l)} + H_2O_{(l)} \rightarrow CH_3COOH_{(l)} + H_2 \qquad (\Delta H^0 = +230\ kJ/mol) \qquad (36)$$

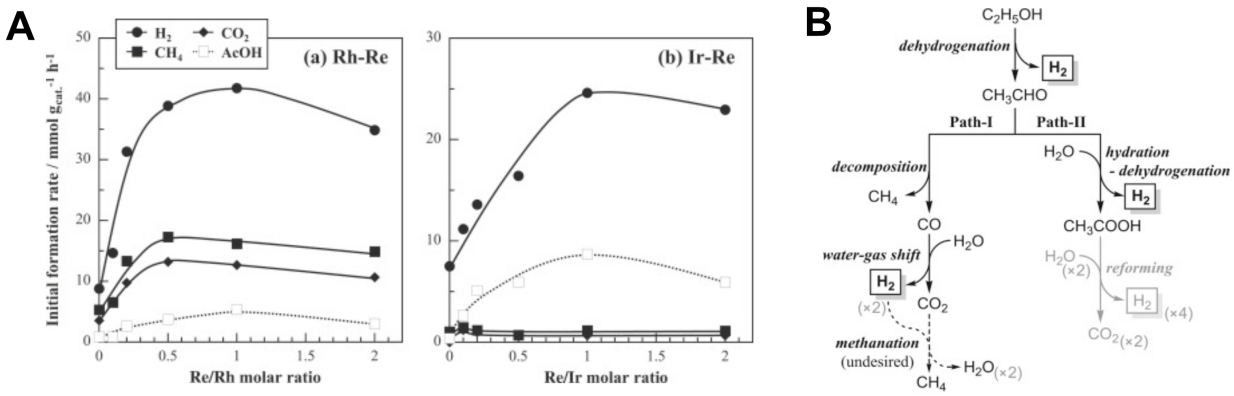


**Fig. 31 (A)** Effect of Re addition on initial rate in ethanol APR over $Rh/TiO_2$ and $Ir/TiO_2$ at 200°C. **(B)** Reaction scheme showing the two main pathways for acetaldehyde: I – decarbonylation; II – hydrolysis/dehydrogenation. [Reproduced with permission from ref. 453]

In the case of Ir/Re, the $H_2$/AcOH ratio (~2.5 after adjustment for the minor $CH_4$ and $CO_2$ levels assumed to be formed by decarboxylation) suggests an almost purely type II reaction and an overall reaction balance as below:

$$C_2H_5OH + H_2O \rightarrow CH_3COOH + 2\ H_2 \qquad (37)$$

Zhao et al. [454] have reported a synergism in Ru/Pt bimetallic catalysts supported on carbon or titania for EAPR at 250°C. Conversions for all bimetallic catalysts and single-metal controls were quite low at ~10%. While Pt is itself ineffective in C-C bond cleavage leading to limited $H_2$ production, its presence was found to stabilise smaller particles of Ru (d ≈ 2 nm) that have higher selectivity in $H_2$ production but lower $CH_4$ selectivity. The $TiO_2$-supported bimetallics were 2.5x and 1.5x more active than the best single metal controls, 0.5% Ru/$TiO_2$ and 2% Pt/$TiO_2$, respectively. Consistent with this trend, the bimetallic catalyst most selective for $H_2$ (0.5%Ru/2%Pt/$TiO_2$) gave a $H_2/CH_4$ mole ratio of 10, a factor of 4 higher than for 0.5%Ru/$TiO_2$ (2.5). However, in terms of overall performance 1%Ru/2%Pt/$TiO_2$ had the highest $H_2$ production rate at 44 mmol (≡ 300 mmol.$g_{cat}^{-1}h^{-1}$) along with high activity in C-C bond cleavage, as indicated by the low level of $C_2$ products; acetaldehyde (1.8 mmol), acetic acid (0), diethyl ether (0.19 mmol), and ethane (2.75 mmol), summing to 4.74 mmol. Corresponding values for 0.5% Ru/2% Pt/$TiO_2$ and 2%Pt/0.5%Ru/$TiO_2$ were 10.1 and 11.7 mmol, respectively, the most striking difference being the presence of significant levels of acetic acid (~4 mmol) in both.

In summary, conversion levels in EAPR are generally quite low (10-30%) except when the ethanol is highly dilute. This is probably due to the associated low-temperature regime under which the experiments must be conducted (T ≈250°C). The mechanistic chemistry is not dissimilar to that in ESR except there is stronger evidence for acetic acid as intermediate. Its importance as a potential source, along with acetaldehyde, of undesirable $CH_4$ needs further evaluation.

Ethanol supercritical water reforming, (ESCWR), has been reviewed recently [455,456], but most of the cited literature is from the past decade. Despite offering direct processing of dilute aqueous bio-based effluents, avoiding costly vaporisation/distillation, the dearth of research activities in this field may be attributed to its highly-specialised and ruggedized

(expensive) equipment and the need to work above 374°C and 220 bar. In practice, working conditions are even more severe, with the temperature necessary to achieve significant ethanol conversion lying above 500°C. Therdthianwong et al. [457] explored SCWR of 5 % bioethanol at 500°C and 250 bar (50 s residence time) over $Ni/Al_2O_3$ and $Ni/CeZrO_2/Al_2O_3$ catalysts. Ethanol conversion exceeded 80 and 100%, respectively, or 4-5x higher than the value obtained in the absence of catalyst (20%), probably due to adventitious activation on the reactor wall. The product distribution over Ce-promoted Ni consisted of $H_2$ in low (1 mol/mol ethanol) yield (35%), $CO_2$ (20%), and $CH_4$ (40%) along with small amounts of $C_2$ gases and liquids, i.e., the familiar pattern observed in other water-based treatments, ESR and EAPR, as summarised above. However, unlike steam-reforming where coking is problematic, activities were stable with a much lower C deposition rate (0.14 vs. 2.08 $mmol.g_{cat}^{-1}h^{-1}$).

Ethanol photo-reforming at ambient temperature, EPR, encompasses two distinct classes of photocatalysts - those effecting initial photodehydrogenation (PDH) to acetaldehyde (AcH) in the absence of water (Reaction 30) and those designed for full reforming in the presence of water to obtain potentially higher $H_2$ yields along with $CO_x$ co-products (Reaction 28). Despite its higher endothermicity ($\Delta(\Delta H^0)$ = 175 - 69 = + 106 $kJ.mol^{-1}$), the energetics favours the 2nd reaction (full reforming) over the 1st (PDH) from free-energy considerations ($E^0_{vs\ NHE}$ = +0.084 V vs. +0.19 V) [458]. On the other hand, full reforming is a 12 $e^-$ process (vs. 2$e^-$ for AcH) and so mechanistically much more complex. Nevertheless, the rate-determining step in ethanol reforming is AcH production (Reaction 30), so that the techno-economics ultimately hinges on the relative value-add of producing the aldehyde over $H_2$, e.g., as a chemical feedstock [419,424,459], and/or as a recycled substrate in which ethanol becomes a liquid organic H-carrier (LOHC) [460].

In terms of recent advances in E(P)R, studies of supported precious-metals Pt, Pd, Au, etc., deal mainly with fundamental aspects, while the development of emerging photocatalysts

based on earth-abundant materials takes a more applied perspective. Al-Azri et al. [458] made a systematic study of the effect of noble metal (M = Pt, Pd, Au) particle size and loading (0.25–4.0 wt%) on hydrogen ion photo-reduction (UV 365 nm, 6 $mW.cm^{-2}$) in 80 vol% aqueous ethanol at 30-35°C. Pt was the most highly-dispersed metal (d $\approx$ 1.0-1.5 nm) on $TiO_2$ (P25), followed by Pd (2-3 nm) and Au (5.0-5.5 nm). The activity vs. loading curves show familiar maxima in the range 0.5-1 wt %, Pt and Pd performing slightly better than Au (45 vs. 32 $mmol.g_{cat}^{-1}h^{-1}$). In contrast, when normalised per particle, rates over Au were higher by one to two orders of magnitude, as shown in Fig. 32. This is despite the higher work functions of Pt and Pd, a provisional measure of electron-trapping power. In the absence of any intrinsic advantage of Au in electronic terms, it must be inferred that for a fixed loading, larger particles that are more widely-spaced perform better than a higher number of smaller particles in closer proximity to each other. Significant levels of $CO_2$ in the products ($H_2/CO_2$ = 3-5), along with minor levels of $CH_4$, $C_2H_4$, $C_2H_6$, traces of AcH, and the absence of CO was strong evidence for full reforming (according to Rx. 26), and possibly photo-assisted WGS activity. Comparing the rate for 2wt% Au with that obtained serving as a control in separate studies under identical conditions [409], respectable QEs for ethanol PR in the range 0.16 (Au) to 0.25 (0.5wt% Pt, 0.5wt% Pd) may be inferred.

| sample | $H_2$ production rate (mmol $g^{-1}$ $h^{-1}$) | molecules of $H_2$ ($M_{atom}$·s) | molecules of $H_2$ ($M_{particle}$·s) |
|---|---|---|---|
| P25 $TiO_2$ | 1.5 ± 0.01 | | |
| 0.25 wt % Pd | 38.7 ± 0.4 | 0.46 | 130 |
| 0.5 wt % Pd | 45.0 ± 2.0 | 0.26 | 75 |
| 1 wt % Pd | 41.1 ± 0.9 | 0.12 | 34 |
| 2 wt % Pd | 32.3 ± 1.6 | 0.05 | 18 |
| 4 wt % Pd | 29.9 ± 3.3 | 0.02 | 8 |
| 0.25 wt % Pt | 34.1 ± 1.5 | 0.74 | 26 |
| 0.5 wt % Pt | 43.5 ± 1.8 | 0.47 | 22 |
| 1 wt % Pt | 33.4 ± 3.4 | 0.18 | 14 |
| 2 wt % Pt | 29.8 ± 1.6 | 0.08 | 6 |
| 4 wt % Pt | 27.2 ± 1.5 | 0.04 | 2 |
| 0.25 wt % Au | 20.8 ± 0.7 | 0.43 | 1552 |
| 0.5 wt % Au | 24.0 ± 1.5 | 0.25 | 1071 |
| 1 wt % Au | 31.2 ± 0.5 | 0.17 | 822 |
| 2 wt % Au | 32.5 ± 0.9 | 0.09 | 525 |
| 4 wt % Au | 25.3 ± 2.3 | 0.03 | 180 |

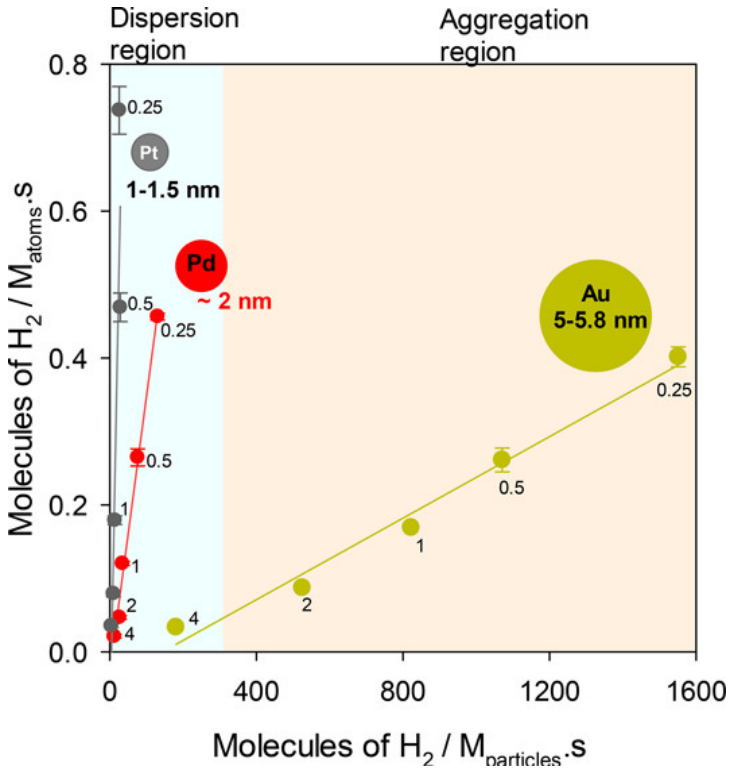


**Fig. 32 (top).** Tabulated data for $H_2$ production activity in ethanol PR, normalised to total catalyst weight (mmol.$g_{cat}^{-1}h^{-1}$), per metal atom (molecules $H_2$ $M_{atom}^{-1}$ $s^{-1}$), or per metal particle (molecules $H_2$ $M_{particle}^{-1}$ $s^{-1}$). **(bottom)** Graph of $H_2$ evolution rate per metal atom vs. rate per metal particle. Data points are rates over a range of metal loadings in wt.%. [Reproduced with permission from ref. 458].

In follow-up work, Katsiev et al. [461] exploited scanning tunnelling microscopy (STM) for accurate dimensional measurements in an ultra-low loading $Au/TiO_2$ [rutile(110)] model sample. Gold was vapour-deposited in UHV onto an $Ar^+$ ion sputter-cleaned $TiO_2$ [rutile (110)] to a deep blue appearance, estimated to have removed 5% of a monolayer of bridging O, and leaving the remainder partially dehydroxylated. For Au coverage ranging from 0.0066 to 0.11 monolayer equivalents (MLE), the cluster number density was found to increase monotonically, resulting in monodisperse (~8 Å) particles with a spacing decreasing progressively from 57 to 21 Å. After pre-dosing ethanol to ~0.3 ML coverage, the surface was exposed to UV light at 10 $mW.cm^{-2}$ [$1.84 \times 10^{16}$ photons $s^{-1}cm^{-2}$], and mass spectroscopy (MS) was used to detect $H_2$ evolution (m/e = 2). A stable signal was observed at each coverage and integrated over 300 s. Saturation was observed already at ~0.06 MLE, as reflected in the coverage-normalised rate in Fig. 33*top*, with a steep decline in mass-specific activity towards an asymptote.

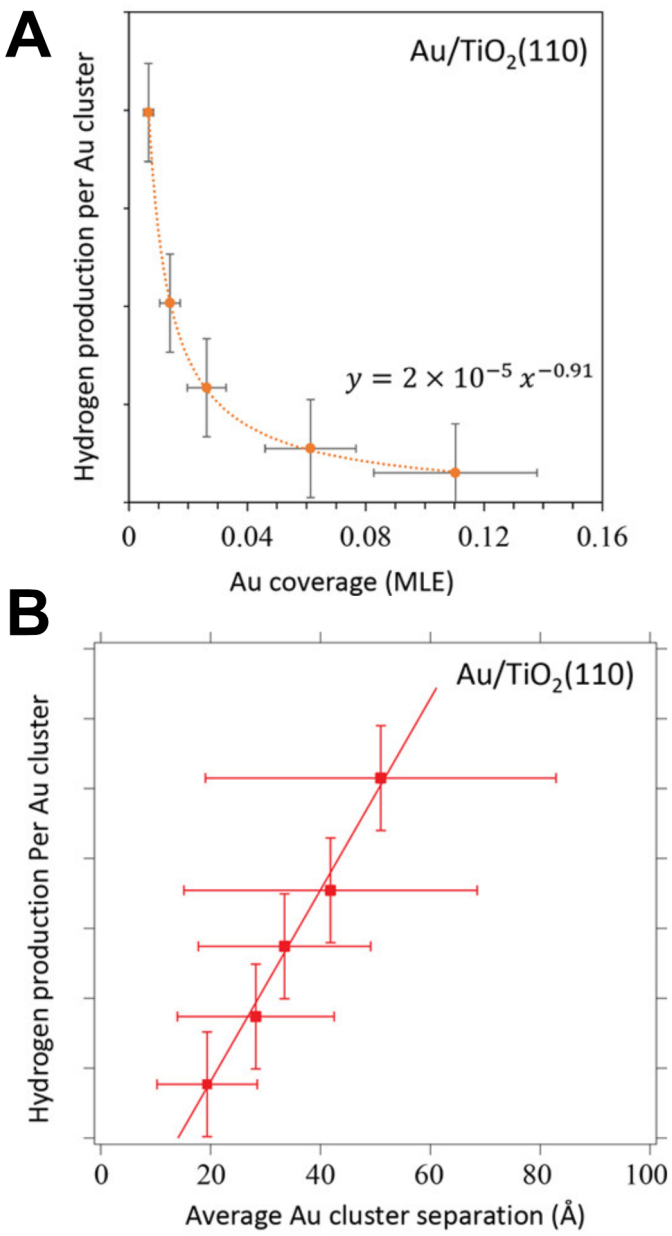


**Fig. 33 (top)** Au coverage-normalised $H_2$ evolution rate vs. coverage (MLE); **(bottom)** Au cluster number-normalised $H_2$ evolution rate vs. cluster spacing (Å) [Reproduced with permission from ref. 461]

The corresponding plot of Au cluster number-normalised evolution rate vs. mean cluster separation was linear, as shown in Fig. 33*bottom*. A plot of photon flux vs. normalised $H_2$ evolution rate (not shown) was linear with a slope of 1.08. This implies that only one photon is

needed to evolve one molecule of $H_2$, nominally a $2e^-$ process. The analogous process in photoelectrochemistry is the so-called *current doubling* effect, in which the first electron is provided by ethanol, forming the adsorbed ethoxy species via H-atom abstraction in a dark exothermic reaction. The minimum spacing between metal particles for optimum performance (~50 Å) is much less than the typical diffusion (Debye) length for photogenerated electrons in $TiO_2$ (10-100 microns) [462]. This action over large distances has been amply demonstrated in macroscopic "ring photocatalytic" studies of soot oxidation over Pt nanodots [385], or optical quenching already at ultra-low (< 0.05 wt%) metal loadings. This confirms that the steep decline in particle density-normalised rate is due to overlapping (self-cancelling) polarisation zones, as concluded from related modelling work in Ref. 383.

In ethanol photo-dehydrogenation aiming specifically for acetaldehyde (AcH), Xing et al. [463] have reported a $Cu_2O/TiO_2$ catalyst based on type II heterojunctions, prepared in a one-pot hydro-thermal method, responsive to visible light and highly active, selective and stable. The highest $H_2$ production rate from 1:9 ethanol/water vapour flow at near-ambient temperature (24.5 mmol.$g_{cat}^{-1}h^{-1}$) was attained over a 1 wt% $Cu_2O$-loaded sample, corresponding to an AQY = 6.4% under 15 Suns UV power equivalent (365 nm, 79 mW.$cm^{-2}$) at nominally 100% selectivity to the aldehyde ($H_2$/AcH $\approx$ 1.00). This is comparable to 41 mmol. $g_{cat}^{-1}h^{-1}$ (> 90% selectivity) obtained over a state-of-the-art thermal catalyst, Cu supported on thin carbon layer-coated porous $SiO_2$, at 260°C [419]. As shown in Fig. 34A, studies at lower UV power (11 mW.$cm^{-2}$) resulted in a 2x-3x increase in rate upon addition of visible light. As this well exceeded the response for “UV+heat” (37°C), an *ad hoc* control for adventitious heating from any visible-induced photothermal effect, it confirmed type II heterojunction behaviour, with visible absorption by the $Cu_2O$ component contributing substantially to the photo-generation of charge (see Fig. 34B).

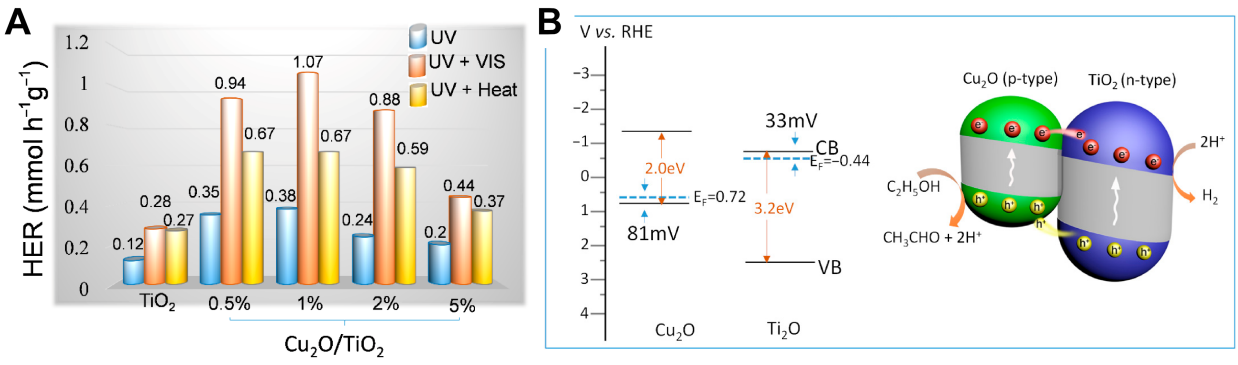


**Fig. 34 (A)** Effect of UV, UV+vis, UV+heat, and Cu loading on $H_2$ evolution rate over $Cu_2O/TiO_2$. **(B)** Relative band edge positions and photo-generated charge flow in $Cu_2O$ and $TiO_2$ (type II heterojunction). [reproduced with permission from ref. 463]

Exploiting a photo-thermo synergy, Luo et al. [464] reported a similar study of solar-driven ethanol dehydrogenation over Ni-promoted $Cu/SiO_2$ at high activity and selectivity (to AcH). As shown in Fig. 35A, the dark $H_2$ production rate from pure ethanol vapour over supported Cu nanoparticles (d ≈ 30 nm) was already ~30 mmol.$g_{cat}^{-1}h^{-1}$ at 210°C. The activation energy measured over the range 170-210°C was $E_a$ = 92.4 kJ. $mol^{-1}$ (see Fig. 35B). Low-level Ni addition (0.04 at.%) raised productivity to 71.5 mmol.$gcat^{-1}$ $h^{-1}$ and lowered significantly the apparent activation energy to $E_a$ = 67.4 kJ.$mol^{-1}$. A similar fall in $E_a$ for atomically-dispersed Ni in Cu, indicative of a new route via a lower energy transition state [249], has been reported elsewhere [428]. Visible irradiation of $Ni_{0.04}Cu$ caused a linear rise in steady-state temperature with optical power input via the plasmon resonance absorption of Cu centred at 575 nm and photo-thermal heating. In contrast, the photo-enhancement of $H_2$ evolution was non-linear with a strong positive curvature towards maximum optical power (5.7 Suns). This further lowered $E_a$ to 41.5 kJ.$mol^{-1}$, and raised the $H_2$ production rate to 176.6 mmol.$g_{cat}^{-1}h^{-1}$, corresponding to a solar-to-$H_2$ efficiency $\eta_{STH}$ = 3.8%.

2049

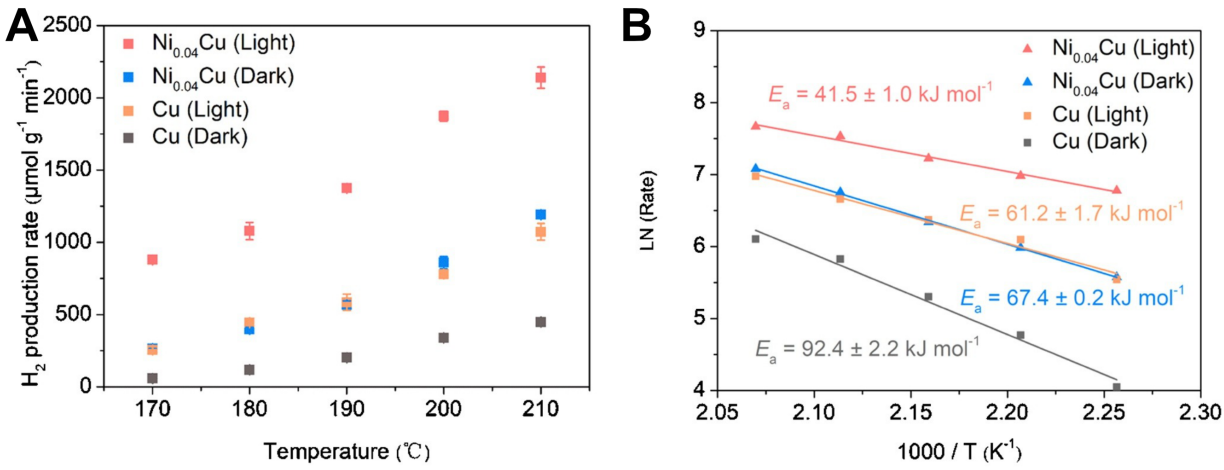


2050

2051 **Fig. 35 (A)** Effect of Ni (4 at%) and visible light (5.7 Suns) on $H_2$ evolution rate over
2052 $Cu/SiO_2$. **(B)** Arrhenius plots of $H_2$ evolution rate for $Cu/SiO_2$ (dark, light) and $Ni_{0.04}Cu/SiO_2$
2053 (dark, light). [Reproduced with permission from ref. 464]

2054

2055 Several groups have made recent studies on $TiO_2$-supported Cu-Ni bimetallic catalysts
2056 for $H_2$ evolution from ethanol. *Lin et al.* [465] prepared 5-7 wt% $Cu_{83}Ni_{17}$, $Cu_{63}Ni_{37}$, $Cu_{54}Ni_{46}$,
2057 $Cu_{41}Ni_{59}$, and $Cu_{22}Ni_{78}$ (along with pure Cu, Ni, and Pt controls) on $TiO_2$ nanorods (NR) by the
2058 method of laser ablation in liquid (LAL). The Cu-Ni particle size range was 15-80 nm and the
2059 lattice spacing by TEM was consistent with homogeneous alloying, as was the systematic
2060 increase in work function with increasing Ni fraction by UPS. In $H_2$ photo-evolution from
2061 ethanol, the bimetallics out-performed both single metal controls and, in the case of $Cu_{63}Ni_{37}$,
2062 surpassed the activity of 1% $Pt/TiO_2$, reaching ~6.2 (vs. 4.7) $mmol.g_{cat}^{-1}\ h^{-1}$.

2063 By first-principles calculations, the adsorption energies for H atoms and $H_2$ molecules
2064 were estimated and compared (see Fig. 36). Whereas the individual components Cu and Ni lie
2065 on opposing sides of the volcano curve for $H_{ads}$ binding (weaker and stronger adsorption than
2066 Pt, respectively), alloying promotes electronic state mixing (adjustment of the d-band centre)

to "tune" the $M_{CuNi}$-$H_{ads}$ bond strength towards the ideal value of Pt close to zero free energy ($\Delta G_{H^*} \approx 0$) [466]. That these co-catalyst interactions are of the dark type is confirmed by a similar report claiming that $CuNi_2$ is a better electro-cathode material than Pt for $H_2$ evolution in alkali [467]. In similar work by Spanu et al. [468] sputter-deposited CuNi films were subjected to controlled thermal dewetting (annealing) at 450°C into nano-dispersed alloys (d = 30-40 nm) on $TiO_2$ (NR).

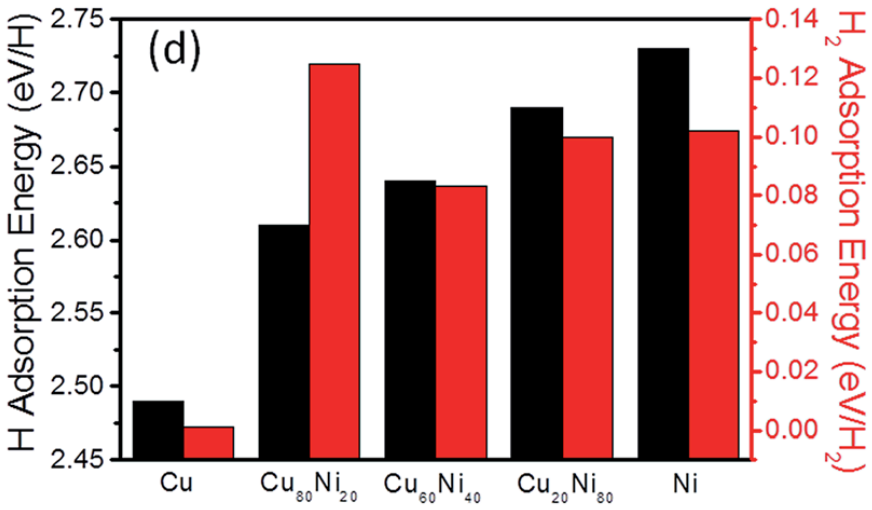


**Fig. 36** Calculated adsorption energies for H* (M-$H_{ads}$) and molecular $H_2$ on CuNi/$TiO_2$ (NR) bimetallic photo-catalysts. [Reproduced with permission from ref. 465]

As shown in Fig. 37, the most active alloy in $H_2$ photo-evolution was $Cu_{50}Ni_{50}$ at 6.04 $\mu L.cm^{-2}h^{-1}$ (AQY = 0.04 %), a stable rate maintained for 30 h. A Pt/$TiO_2$ (NR) control was twice as active at 12 $\mu L.cm^{-2}h^{-1}$. In view of the higher ambient reactivity of non-noble metals, often responsible for irreproducible data, Spanu *et al.* [469] followed up with *operando* X-ray absorption work on the same photocatalysts during $H_2$ photo-evolution activities in aqueous ethanol. While Cu and Ni were partially oxidised in the as-formed bi-metallic co-catalysts and

underwent partial dissolution in the liquid phase under dark conditions, such species were reduced/re-deposited as homogeneous Ni-Cu alloy phases at the $TiO_2$ surface under illumination. Thus, it was unambiguously shown that Cu and Ni, responsible for photo-activity in CuNi/$TiO_2$ (NR), were present in the zero-valent (metallic) state.

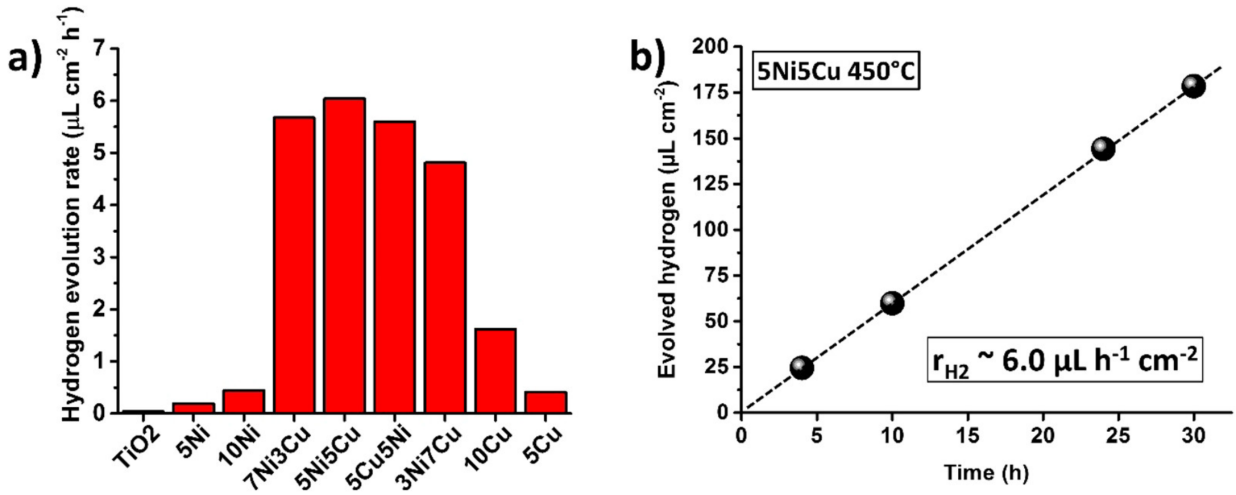


**Fig. 37 (a)** Photo-evolution of $H_2$ from ethanol over de-wetted CuNi alloys on $TiO_2$ (NR). **(b)** Stable $H_2$ photo-evolution from ethanol over the most active alloy $Cu_{50}Ni_{50}$ on $TiO_2$ (NR). [Reproduced with permission from ref. 468]

## 7.3. $C_2$-$C_3$ glycols

### *7.3.1. Ethylene glycol*

Ethylene glycol [$(CH_2OH)_2$, EG] is the simplest (dibasic) polyol and its reforming (EGR) is of interest as a model compound and major component of renewable bio-oil:

$$C_2H_6O_2 + 2\,H_2O \rightarrow 2\,CO_2 + 5\,H_2 \qquad (\Delta H^0 = +90\ kJ.mol^{-1}) \qquad (38)$$

Due to the two oxygenated C atoms, EGR (Reaction 38) is less endothermic than ethanol reforming but the free energy change is close to zero at room temperature ($\Delta G^0_{298K}$ = +10 kJ.mol$^{-1}$) due the high entropy factor (T$\Delta$S). However, despite the favourable thermodynamics, steam-reforming (EGSR) needs to operate under extreme conditions (T > 500°C) more typical of ethanol. This is not surprising since these $C_2$ oxygenates share kinetic and mechanistic decomposition pathways, as shown in Fig. 38. Acetaldehyde is obtainable as a common intermediate either by dehydration (of ethylene glycol) or dehydrogenation (of ethanol). More harmful types of coking and consequent deactivation linked to $C_2$ reactants and by-products have already been demonstrated [440].

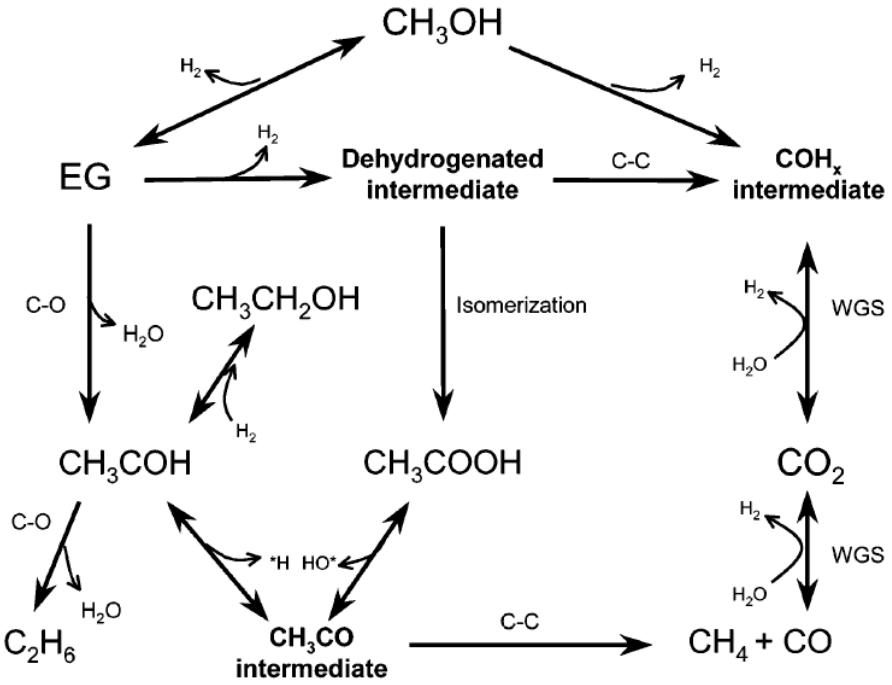


**Fig. 38** Reaction network indicating shared pathways between ethylene glycol and simple alcohols. [Reproduced with permission from ref. 470]

By analogy with ethanol, first principles (DFT) and microkinetic modelling have shown that activation energy barriers for early steps in the dehydrogenation of EG over Pt and Ni are high and probably rate-determining. These typically exceed 100 kJ. $mol^{-1}$ [470,471], although APR is kinetically favoured over SR, being associated with a lower activation energy barrier (1.15 vs. 1.52 eV) [472]. In recent experimental and modelling work in EGSR over Ni, Co, and Rh on $MgAl_2O_4$ spinel at 500°C, Mei et al. [473] found that Co (15 wt%) was the least active metal but most selective to $H_2$, giving just 8% $CH_4$ as compared to the equilibrium level (~24%) over Ni and Rh. All catalysts deactivated during reactant C-feeding up to 40 $mol.g_{cat}^{-1}$ (S/C = 3) with initial conversion falling from 75% to below 30%. This was due mainly to coking, although the Co catalyst maintained a steady conversion (~80%) at higher steam-to-carbon ratio (S/C = 6) suggestive of carbon gasification. In modelling work the energetics of elementary steps in the decomposition of the most likely initial intermediate, dihydroxyethylene [HOCH-HCOH], were evaluated. The predicted order of bond breakage for Ni(111) and Co(0001) was C-H > O-H ≈ C-O > C-C. In numerical terms, apparent activation energies over Ni and Co were estimated as $E_a$ = 41 and 36 $kJ.mol^{-1}$, respectively, while C-C bond cleavage was the most disfavoured process with $E_a$ = 103 $kJ.mol^{-1}$ and 104 $kJ.mol^{-1}$. Such late-stage chain fragmentation may exacerbate coking and deactivation due to the extended presence of $C_2$ intermediates. After C-C bond cleavage, HCOH may undergo consecutive dehydrogenation to 1. COH + H and 2. CO + H (ex. COH) most easily over Co ($E_a^1$ = 10 $kJ.mol^{-1}$, $E_a^2$ = 92 $kJ.mol^{-1}$). Steam activation (to H and OH) is also favoured over Co, preventing the build-up of $CH_x$ (x > 1) fragments that otherwise lead to $CH_4$.

On a similar note, Larimi & Khorasheh reported that addition of Pt conferred greater stability and coking resistance to $Ni/Al_2O_3$ catalysts [474]. The optimum sample consisted of 3.75% Ni and 1.25% Pt, resulting in the highest ethylene glycol conversion (60%), highest $H_2$ selectivity (45%) and yield (27%), and a minimum of 20 h of stability due to the lowest amount

of coke deposited on the catalyst surface. Kinetic modelling gave an estimate for the apparent activation energy of $E_a$ = 103.4 kJ. $mol^{-1}$.

De Vlieger et al. [475] studied ethylene glycol reforming (5-15% EG, WHSV = 18 $h^{-1}$) in supercritical water (450°C, 250 bar) over alumina-supported Pt, Ir, Ni, and multimetallic catalysts. While Pt (≤ 1.5 wt%) was the most active metal (42% conversion), deactivation was evident at lower loadings during 9h on-stream. In the absence of detectable carbon deposition, this was attributed to Pt sintering. Addition of a small amount of Ni (0.10-0.35%) raised the $H_2$ yield from 35 to 70% and stabilised the Pt-based bimetallic catalyst, which maintained high (~80%) conversion, with an 85% carbon-to-gas efficiency and 80% selectivity to $H_2/CO_2$.

The pioneering work on ethylene glycol aqueous-phase reforming [EGAPR] was made by the Dumesic group over Pt/γ-$Al_2O_3$ [476]. In studies at 210-225°C (22-29 bar) with a 10% EG feed, this noble metal was found to be of good initial activity and highly selective for $H_2$, with very low levels of alkanes and CO (300 ppm) produced. The reaction kinetics had a high activation energy ($E_a$ = 100 kJ.$mol^{-1}$), was of low order in EG (0.3-0.5) and slightly inhibited by $H_2$ (rate $\propto P_{H2}^{-0.5}$). A mechanism was proposed involving irreversible dehydrogenation of adsorbed ethylene glycol to form adsorbed $C_2H_xO_2$ species, cleavage of the C-C bond to form $COH_y$, and further dehydrogenation leading to adsorbed CO and its removal by WGS. Deactivation was soon observed due to a combination of hydro-thermal instability in the oxide support, transforming to the more acidic boehmite (γ-$Al_2O_3$ → AlO(OH)], Pt sintering, and laydown of carbonaceous deposits. The effect of additives to improve rate, selectivity, and stability in Pt- and Ni-based catalysts for EGAPR has been reviewed [449]. Concerning prospects for earth-abundant metals, synergies in alloying of Pt (Pt/Ni, Pt/Co and Pt/Fe) on $Al_2O_3$ were discovered in early high-throughput testing [477]. The base metal is understood to suppress the adsorption strength of CO and H intermediates that otherwise act as poisons on monometallic Pt. Subsequent In-situ EXAFS investigations of Pt/Ni/C have shown that the

bimetallic is superior in APR due to surface segregation of Ni, the more active component, and possibly its partial oxidation under reaction conditions. Tao et al. [478] reported on EGAPR at 225°C, and 26 bar over unsupported Ni, Fe, NiFe, and Co-promoted NiFe composite alloy catalysts prepared by a sol-gel method. As shown in Figs. 39, while the mono- and bi-metallics showed low (< 50 %) conversion and high selectivity to alkanes, the tri-metallic NiFeCo alloy catalyst pre-reduced at 660°C achieved 95.1 % conversion, with 99.8 % selectivity to $H_2$ and only 1.3% to alkanes. Upon reduction at intermediate temperatures (400-660°C), Ni and Fe passed via a mixed oxide phase ($NiFe_2O_4$) into a $Ni_{36}Fe_{64}$ alloy, and finally into an iron-rich Ni/Fe alloy, as identified by XRD. The spent NiFeCo catalyst showed evidence for $Fe_2O_3$ formation, an oxide known for its WGS activity.

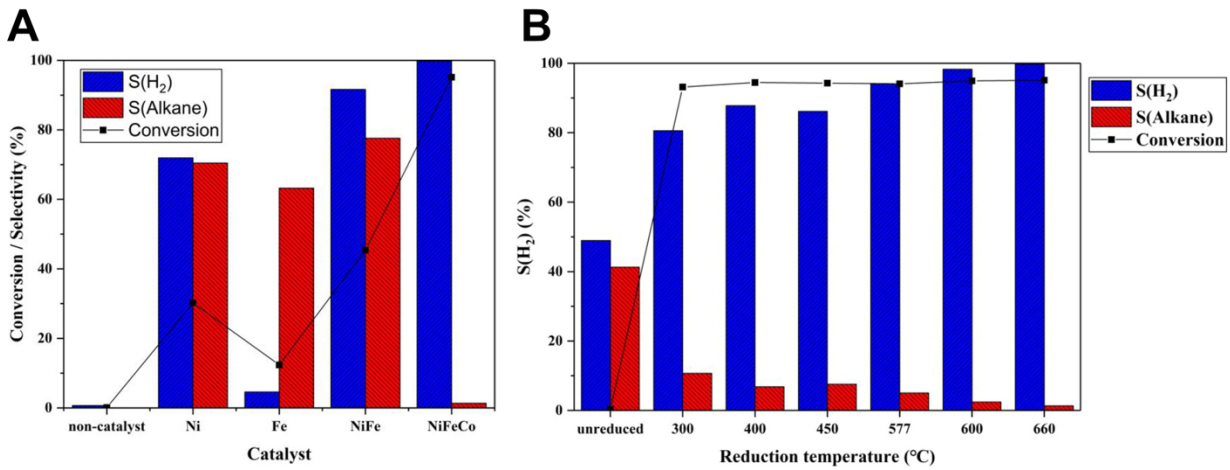


**Fig. 39 (A)** Activity/selectivity in APR of ethylene glycol over mono- (Ni,Fe), bi-(NiFe) and tri- (NiFeCo = 6:20:1) metallic alloy catalysts. **(B)** Activity/selectivity in APR of ethylene glycol over $Ni_6Fe_{20}Co$ alloy catalyst. Effect of pre-reduction temperature.[Reproduced with permission from ref. 478]

The beneficial effect of such a low Co loading may be linked to promotion of an alternative decomposition route via EG dehydrogenation/isomerization to acetic acid (see Fig. 38), based on FTIR evidence for adsorbed acetate, viz., carboxyl bands at 1230 and 1156 $cm^{-1}$.

The decomposition of ethylene glycol (EG) over $TiO_2$ model surfaces [461] is complex and coverage-dependent. Whereas thermal excitation above 300°C tends to yield $C_2$ products (and coke precursors) ethylene and acetaldehyde [479], photoexcitation tends to favour C-C bond scission at or below ambient temperature. Two recent TPD/MS-based investigations of EG reactivity under UV-irradiation (in the absence of water) over rutile (110) agree that the main photo-decomposition pathway at low coverage ($\theta_{EG} < 0.3$) is via formaldehyde ($CH_2O$) and molecular hydrogen [292,480]:

$$EG + 2Ti + 2O_b^{2-}[2V_{Ob}] + h\nu \rightarrow 2CH_2O_{Ti} + 2OH_b^{-}[2HV_{Ob}] \quad (39)$$

$$2OH_b^{-} + 2\,e^{-} \rightarrow 2O_b^{2-} + H_2 \quad (40)$$

where $O_b^{2-}$ are bridging O anions (and/or electrons trapped at $O_b$ vacancies [$V_{Ob}$]) adjacent to EG, chemisorbed at nearest neighbour 5-coordinate surface Ti centres. Although there is evidence that Reactions 39 and 40 can proceed in the dark, it is slow and probably a non-catalytic process [481]. In the study by Jin et al. [292], adsorbed $CH_2O$ grew to saturation coverage according to 1st order kinetics ($k = 0.04\ min^{-1}$), while $H_2$ evolution exhibited zero-order behaviour suggesting Reaction 40 as the rate-determining step. The product ratio ($CH_2O:H_2 = 2:1$ was consistent with the balance of Reactions 39 and 40. At high (multi-layer) coverage, C-C bond scission was almost completely suppressed while Xu *et al.* [480] found a change in selectivity at higher coverage ($\theta_{EG} \geq 0.45$ ML), the reaction now proceeding via EG photo-dehydration, giving rise to $CH_3CHO$ and $H_2O$ evolution peaks at sub-ambient temperatures. Extending their studies to metallized (Pt, Pd, Au) P25, Jin et al. [292] found that

the evolution kinetics of HCHO (FTIR band growing in at 1717 $cm^{-1}$[$\nu_{C=O}$] and progressively weaker bands at 3333 [νOH], 2940 [$\nu_{as}CH_x$] and 2880 $cm^{-1}$ [$\nu_sCH_x$]) and $H_2$ (MS, m/z = 2) were both 1st order with markedly increased (x3-x4) rates in the presence of metal deposits, as shown in Fig. 40. The plateaux reached in product(s) formation, most clearly seen for $CH_2O$ over $Pt/TiO_2$ after 3h UV-irradiation (Fig. 40c) shows that formaldehyde is the genuine end-product. In contrast, studies made in the presence of $H_2O$ over $Rh/TiO_2$ by Berto et al. [482] detected significant amounts of $CO_2$, suggestive of full (aqueous) reforming.

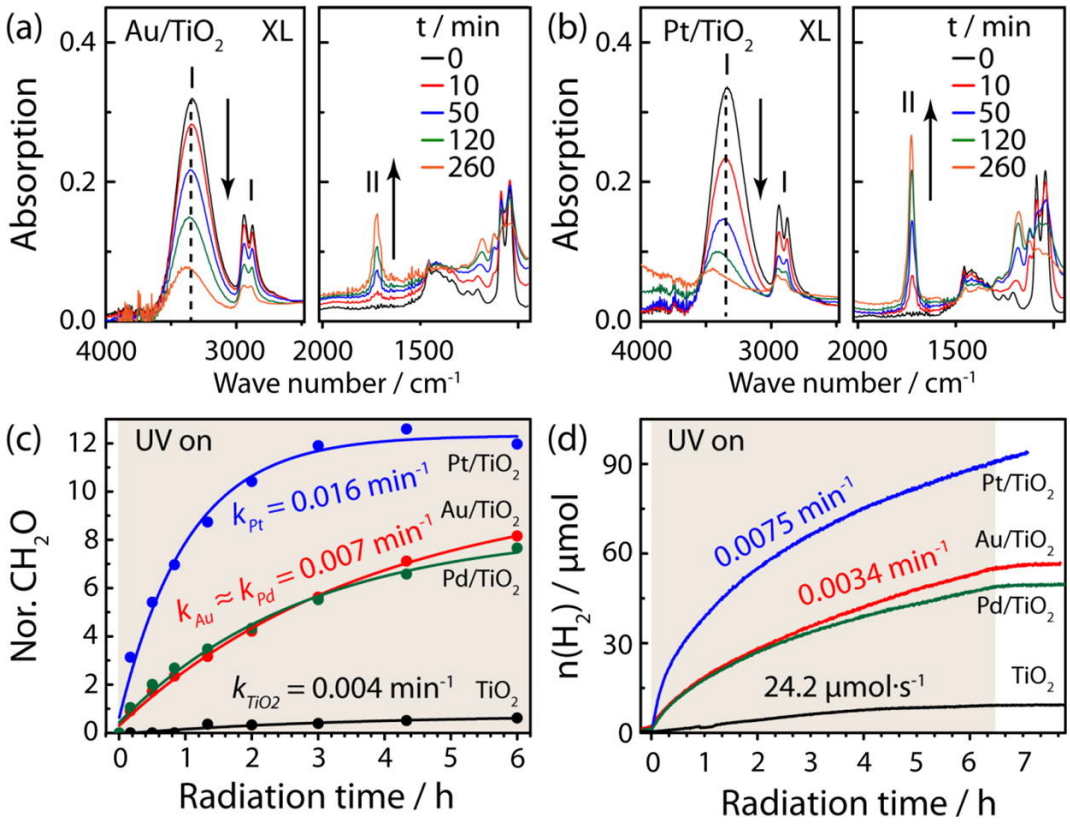


**Fig. 40.** In-situ FTIR band intensity changes during UV irradiation of EG at thin-layer coverage over **(a)** Au, **(b)** Pt, on P25 $TiO_2$. Normalised MS intensities for **(c)** $CH_2O$ (m/z = 30) and **(d)** $H_2$ (m/z = 2), showing markedly increased evolution rates (vs. pristine $TiO_2$) and 1st order kinetics up to saturation coverage. [Reproduced with permission from ref. 292]

Photo-reforming of a wide range of aqueous alcohols (10 vol%) over M/$TiO_2$ (P25) (M = Pt, Pd, Au) have been reported by Al-Azri et al. [336]. EG was the 2nd most reactive sacrificial agent (after glycerol), producing $H_2$ at 44.5 mmol.$g_{cat}^{-1}h^{-1}$ over 1 wt% Pd/$TiO_2$ under UV irradiation (365 nm, 5 mW.$cm^{-2}$). The overall reactivity sequence was the same over all precious metals but rates over Pt and Au were roughly half the Pd values, which are listed below: glycerol (48) > EG (45) > 1,2-propanediol (32) > methanol (31) > ethanol (26) > 2-propanol (17) > tert-butanol (5). Systematic correlations were found with, e.g., decreasing polarity and/or more positive (energetically less favourable) oxidation potential. Tert-butanol and methanol showed anomalously low activities, the first having no α-H atom, implying conversion by a different mechanism, while methanol oxidation kinetics may be dominated by high levels of adsorbed CO (potential metal poison) and/or formate decomposition. Follow-up work by Chen et al. on earth-abundant co-catalysts 0.5 wt% Ni [409] and 1 wt% Cu (each on P25 $TiO_2$) [483] found $H_2$ evolution rates from aqueous EG (10 vol%) that were comparable to a 2 wt% Au control, viz., 21.4 and 15.5 mmol.$g_{cat}^{-1}h^{-1}$ for Ni and Cu, respectively, vs. 25.8 mmol.$g_{cat}^{-1}h^{-1}$ for Au. These correspond to relatively high apparent quantum efficiencies (AQE) of $\varphi_{Ni} \approx 0.30$, $\varphi_{Cu} \approx 0.22$, and $\varphi_{Au} \approx 0.37$. Intensive spectroscopic characterization of the pre-reduced co-catalysts confirmed their presence in the metallic state ($Ni^0$, $Cu^0$), Cu exhibiting its characteristic localised surface plasmon resonance (LSPR) absorption at ~600 nm. This is important as other reports suggest that $Cu^0$ and $Cu^I$ likely co-exist and may have complementary effects [484].

Just such a case is well-exemplified in the work of Praveen Kumar *et al*. [485]. They explored a range of Cu loadings on $TiO_2$ nanotubes (TNT) and various alcohols as sacrificial agents. As shown in Fig. 41*top*, the effect of Cu loading on the $H_2$ evolution rate from 5 vol% aqueous ethylene glycol (EG) was found to be optimal at 1.5 wt% Cu. As compared to simple mono-ols, the superiority of EG as a hole scavenger is shown in Fig. 41*bottom*, reaching a $H_2$ evolution rate of ~80 mmol.$g_{cat}^{-1}h^{-1}$. This was raised to an unprecedentedly-high level of 115

mmol.$g_{cat}^{-1}h^{-1}$ at 10% EG and was stable over several 4h cycles. This was attributed to extended absorption into the visible range by the narrow band-gap semiconductor cuprous oxide ($Cu_2O$, $E_g \approx 2.17$ eV) in combination with effective electron trapping by metallic copper at Schottky junctions on the $TiO_2$ nanotubes. Visible-light sensitization, e.g., by incorporating metal co-catalysts with localised surface plasmon resonance (LSPR), leads to more efficient utilisation of the solar spectrum.

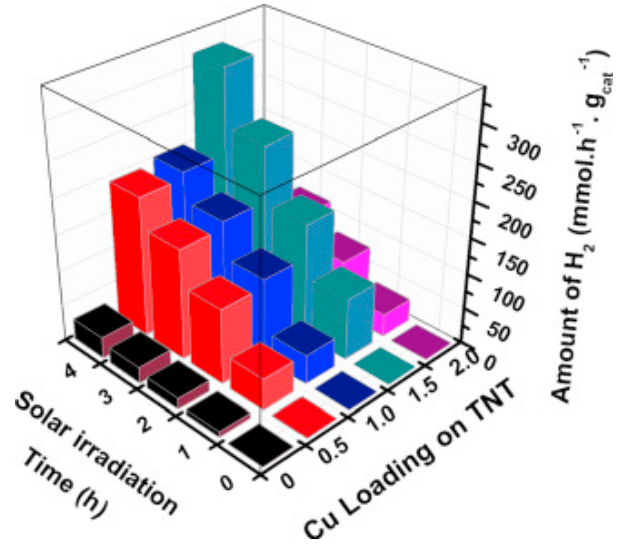


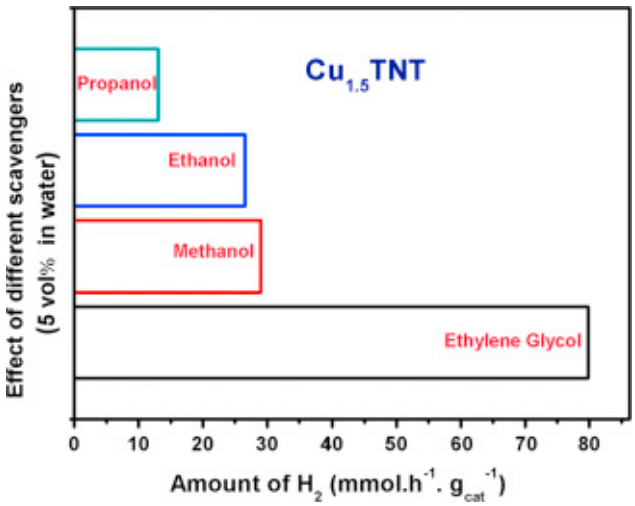

**Fig. 41 (top)** Effect of Cu loading on solar-driven $H_2$ rates from ethylene glycol (5%) over Cu1.5 TNT. **(bottom)** Solar-driven $H_2$ evolution rates from ethylene glycol and $C_1$-$C_3$ monool (5%) over Cu1.5 TNT. [reproduced with permission from ref. 485]

While this is an important objective in photocatalysis, progress is not necessarily straightforward. Nadeem et al. [486] reported on the effect of replacing palladium with silver on biphasic (anatase:rutile = 4:1) $TiO_2$. Of interest was to assess any benefit of displacing metallic Pd, known to work well as a $H_2$ evolution co-catalyst, i.e., a Schottky component, with extended visible response via the Ag LSPR showing a broad absorption from 420-570 nm, i.e. just beyond the band-edge of $TiO_2$. While tests with bandpass filters revealed a slight positive (3%) correlation of LSPR areal intensity with turnover frequency in $H_2$ evolution from EG in the 1%Ag-Pd bimetallics, this was evidently insufficient to compensate for any detrimental effect on Pd, either through its lower loading and/or due to intrinsic electronic effects via alloy formation (Ag/Pd ≈ 3/2 in 10 nm nanocrystallites was found by EDX). Unfortunately, the best bimetallic sample (0.2% Ag-0.8%Pd) was already less active than the 1%Pd control at ~10 mmol. $H_2$ $g_{cat}^{-1}h^{-1}$ (vs. 14 mmol. $g_{cat}^{-1}h^{-1}$) and the performance deteriorated progressively with increasing Ag. As a more practical alternative, a similar study should be considered for Au-Pd/$TiO_2$ bimetallics, another miscible system with two photo-active metals but with Au having a more intense LSPR peaking near the solar spectral power maximum at 600 nm. Previous work has also shown that a synergy exists between Au and Pd in $H_2$ evolution [487].

### *7.3.2. Glycerol*

Glycerol [$C_3H_5(OH)_3$] exists in high reserves as a by-product of biodiesel production via transesterification of triglycerides with methanol, as shown in Fig. 42. As a major bio-resource, its valorisation is potentially an important contributor to commercial viability. In view of recent

interest in fuel interconversion, e.g., the glycerol-to-methanol (GtM) process (see Reaction 14) [41,255,258], such technical consolidation may lead to increased flexibility in biorefinery operations. Glycerol is also a growing source of specialty chemicals such as acrolein, lactic acid, citric acid, and 1,3-propanediol. The cost penalty incurred in the work-up of crude glycerol to the necessary purity as a platform chemical is considered to be largely offset by being a source of renewable energy [489].

As a potential source of process hydrogen, glycerol steam reforming (GSR, reaction 41) can be considered as the sum of two consecutive and mechanistically distinct processes, viz., glycerol decomposition (Reaction 42) and WGS (Reaction 43):

$$C_3H_8O_3 + 3\ H_2O \rightarrow 3\ CO_2 + 7\ H_2 \qquad (\Delta H^0 = +128\ kJ/mol) \qquad (41)$$

$$C_3H_8O_3 \rightarrow 3\ CO + 4\ H_2 \qquad (\Delta H^0 = +251\ kJ/mol) \qquad (42)$$

$$3\ CO + 3\ H_2O \rightarrow 3\ CO_2 + 3\ H_2 \qquad (\Delta H^0 = -41\ kJ/mol) \qquad (43)$$

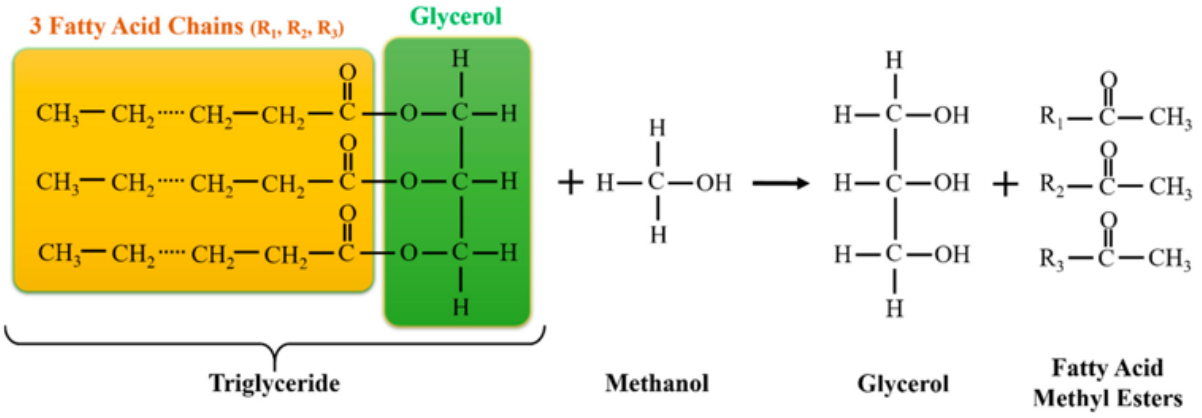

**Fig. 42** Biodiesel (fatty acid methyl esters, FAME) is derived from vegetable oils by transesterification of tri-glycerides with methanol, yielding crude glycerol as by-product. [Reproduced with permission from ref. 488]

Despite the exothermicity of WGS (Reaction 43), the overall reforming process (Reaction 41) is still quite endothermic with a standard enthalpy of +128 kJ.mol$^{-1}$. Nevertheless, the thermodynamics are compensated by the high entropy gain and the free energy change is close to zero at ambient temperature ($\Delta G^0_{298K}$ = + 5 kJ.mol$^{-1}$) [336]. As shown in Fig. 43A, equilibrium calculations by Ismaila *et al*. [490] confirm that full glycerol conversion is achievable already at low temperature (325°C), just 35 degrees above the boiling/decomposition point. Furthermore, the $H_2$ yield can exceed 80% by operating at ~600°C in excess steam, i.e., a steam-to-glycerol molar flow ratio, SGFR = 10. Fig. 43B shows that under the same conditions, the equilibrium level of solid carbon is effectively zero. In practice, just as for ethanol and ethylene glycol, coking and deactivation is the greatest obstacle in GSR as it often involves the same $C_{2+}$ coke precursors if C-C bond scission occurs too early in the mechanistic sequence. This is ideally one of "pure" dehydrogenation (C-H and O-H bond cleavage) to $C_3O_3$ chains, followed by dissociation (C-C bond cleavage) to CO and WGS conversion. Fig. 44A also shows that at lower temperatures $H_2$ yields are restricted mainly by its preferential consumption in methanation ($CO_x$ hydrogenation), a highly exothermic reaction. A key factor in improving both catalyst *selectivity* (away from $CH_4$) and *stability* (against growth of graphitic carbon from ad-atom forms) is to suppress any intrinsic activity in C-O bond cleavage by modification of the active (metal) phase, e.g., by alloying. In addition, the inclusion of basic and reducible supports (with labile O) and alkali promoters that activate water for carbon gasification is important.

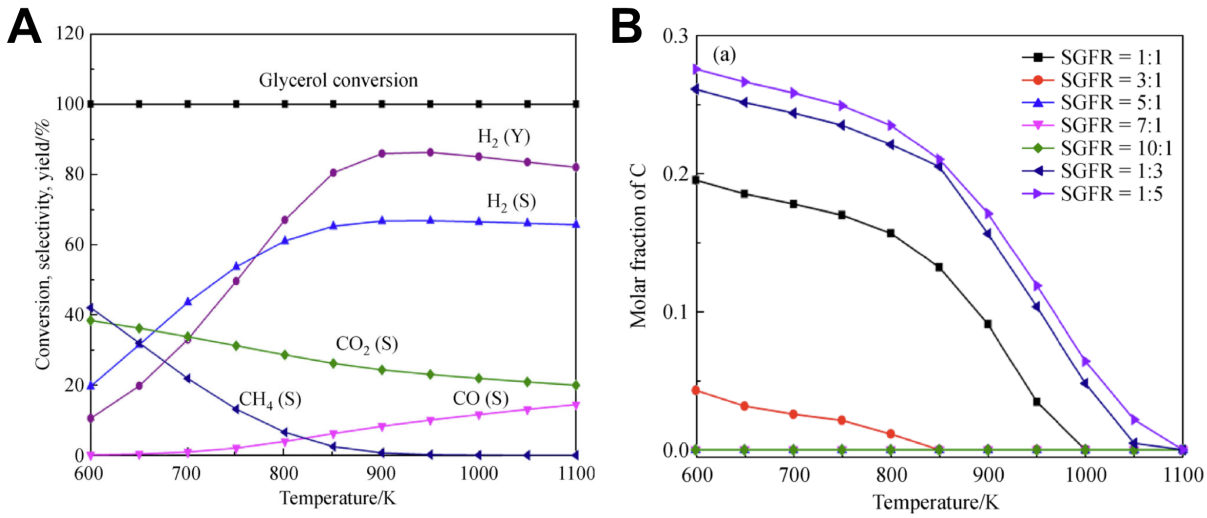


**Fig. 43. (A)** Glycerol conversion, $H_2$ yield, and product gas selectivities (P = 1 bar). **(B)** Effect of SGFR on carbon laydown at indicated temperatures (P = 1 bar). [with permission from ref. 490]

In view of its technical potential as an abundant source of renewable hydrogen, glycerol decomposition and steam reforming over transition metals has been extensively reviewed, with emphasis on promoted Ni-based catalysts and 1st principles (DFT) reaction modelling [356,357,368,418,488,489,491,492]. In view of the broad scope of this review, just a few examples are given that deal with catalyst instability in GSR and offer promising solutions.

Menezes et al. [493] modified a 20 wt%Ni/$Al_2O_3$ (NiAl) control by niobia addition (10 % as $Nb_2O_5$) and the glycerol conversion with time-on-stream (TOS) at 500°C was evaluated. As shown in Fig. 44A, the niobia-modified (NiNbAl) catalyst gave high (> 90%) and stable conversion over 30 h whereas the activity of the NiAl control fell drastically to 30% after 8 h. The superiority of NiNbAl over NiAl was also reflected in the high conversion to gas (80% vs. 20%) and $H_2$ yield (50% vs. 15%). This was attributed to the lower amount and type of coke deposition [more filamentous (benign) and less amorphous (pernicious)], linked to the higher dispersion of metallic Ni. Evidence for improved WGS activity by $Nb_2O_5$ addition was seen in

the high $CO_2$/CO ratio (~7), although NiNbAl also gave the highest $CH_4$ yield (~10%). High space velocities, low glycerol content, and low temperatures (≤ 450°C) favoured liquid products acrolein ($CH_2CHCHO$, 15.5%) and acetol ($CH_3COCH_2OH$, 8.9%).

Wang et al. [494] explored bimetallic Ni-M (M = Co, Cu, Zn) catalysts supported on attapulgite (ATP). This natural clay mineral, a magnesium aluminum silicate $[(H_2O)_4(Mg,Al,Fe)_5(OH)_2Si_8O_{20} \cdot 4H_2O]$, has basic properties and contains iron, which may impart WGS activity. As compared to $Ni/Al_2O_3$, Ni/ATP gives higher $H_2$ and $CO_2$ at the expense of CO, $CH_4$, and liquid products [495]. As shown in Fig. 44B, 10% Ni/ATP was the least stable catalyst as compared to the bi-metallics (5% Ni, 5% M), conversion of glycerol ($X_{gly}$) and fractional conversion to gaseous products ($X_{gas}$) dropping steadily over 30 h at 600°C from 90 to 65% and 70 to 20%, respectively. In contrast, NiZn/ATP and NiCo/ ATP showed good stabilities, $X_{gly}$ and $X_{gas}$ falling only slightly from 90 to 85% and 70 to 65%, respectively. They also gave the highest and most stable yields of $H_2$ ($Y_{H2}$) at ~60% (4 mol/mol - see Reaction 41). The stability and productivity of NiCu/ATP ($X_{gly}$ = 80%, $X_{gas}$ = 50%, $Y_{H2}$ = 40%) after 30h was less impressive but still superior to Ni/ATP. It also gave the highest $CO_2$/CO ratio of all (~4), an unsurprising result as Cu is the most well-known metal for WGS. All bimetallic catalysts had low (≤ 5%) selectivities to $CH_4$ as compared to the monometallic control (10-20%). The level of stability in glycerol conversion appeared to correlate inversely with the level of carbon deposition - NiZn (16%) < NiCo (23%) < NiCu (33%) < Ni (48%). This sequence may have been due to a clear trend in metal particle size: NiZn (11.2 nm) < NiCo (14.3 nm) < NiCu (18.7 nm) < Ni (22.5 nm), in turn a possible consequence of a lower degree of reduction: NiZn (36%) < NiCo (55%) < NiCu (74%) < Ni (86%).

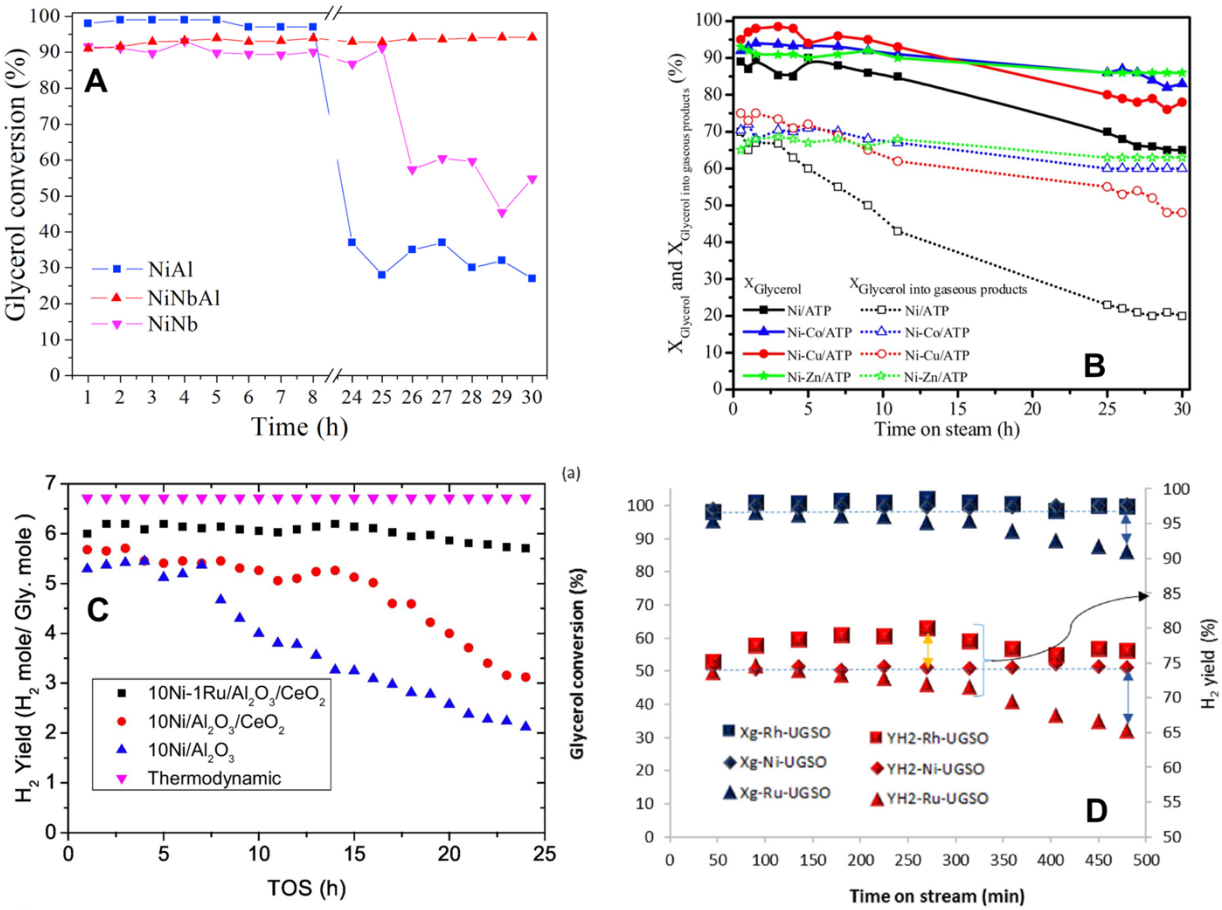


**Fig. 44 (A)** Glycerol conversion with time-on-stream over 20%Ni/$Al_2O_3$ (**blue**), 20%Ni/10%$Nb_2O_5$/$Al_2O_3$ (**red**), and 20%Ni/$Nb_2O_5$ (**pink**) at 500°C. [Reproduced with permission from ref. 493]. ; (B) Glycerol conversion with time-on-stream at 600°C (total: filled symbols; to gas: open symbols) over Ni/ATP (black); Ni/Co/ATP (**blue**), Ni/Cu/ATP (**red**), and Ni/Zn/ATP (**green**) - Reaction conditions: SGFR = 9, GHSV = 9619 $h^{-1}$. [Reproduced with permission from ref. 494] ; (C) $H_2$ yield with time-on-stream over 10%Ni-1%Ru/$Al_2O_3$/5%$CeO_2$, 10%Ni/ 5%$CeO_2$/$Al_2O_3$, and 10%Ni/$Al_2O_3$ at 650°C [Reproduced with permission from ref. 496] ; (D) Glycerol conversion ($X_G$) and $H_2$ yield ($Y_{H2}$) with time-on-stream at 630°C over 1%Rh, 1%Ru, or 5%Ni, supported on upgraded slag oxides (UGSO - MgO/$Mg(Fe,Al)_2O_4$) - Reaction conditions: SGFR = 9 (S/C = 3), GHSV = 10,966 $h^{-1}$. [Reproduced with permission from ref. 499]

Demsash et al. [496] studied co-doping 10%Ni/$Al_2O_3$ with $CeO_2$ (5%) and a low level of precious metal Ru (1%), and its effect on the $H_2$ yield is shown in Fig. 44C. While the Ni/$Al_2O_3$ control showed its characteristic instability, $Y_{H2}$ falling from 5.4 mol/mol (77%) to 2.1 mol/mol (30%), notably between 7 and 25h at 650°C, the Ni/Ru /$CeO_2$/$Al_2O_3$ catalyst gave a very stable $Y_{H2}$, with a slight fall from 6.3 to 5.6 mol/mol (90-85%). The absence of Ru resulted in a less impressive performance by the Ni/$CeO_2$/$Al_2O_3$ control although still superior to Ni/$Al_2O_3$, with $Y_{H2}$ falling from 5.6 (80%) to 3.1 mol/mol (45%). The instability in $Y_{H2}$ correlated mainly with a similar trend in glycerol conversion ($X_{gly}$), Ni/$Al_2O_3$ showing a pronounced drop (starting after ~7h), from 100% to 78% whereas Ni/Ru/$CeO_2$/$Al_2O_3$ maintained virtually full (100%) conversion throughout. The $CeO_2$-doped control was stable for up to 17h before $X_{gly}$ fell slowly to 94.5 %. In the instability regime, a crossover was seen in selectivity with CO growing at the expense of $H_2$ and $CO_2$, implying an inhibition of WGS, a reaction possibly more susceptible to the remarkably low levels of coke deposited, especially over the Ru-$CeO_2$ co-doped sample (< 0.5%), $CeO_2$-only (< 1.5%) and even over Ni/$Al_2O_3$ (< 2.5%). This may have been an advantage of working at high SGFR (12/1 water-to glycerol), although this would raise energy costs for reactant(s) vaporization in any technical process.

In the context of increased sustainability in industrial catalytic processing based on cheap and abundant materials, the group of Iliuta et al. [497-499] have investigated Fe/Mg-containing "upgraded slag oxides" (UGSO) as a catalyst support in GSR. This consists primarily of mixed metal oxides of iron, e.g., $Mg(Fe,Al)_2O_4$, and free magnesia (MgO), conferring the basic properties desired in oxygenates SR catalysts. In their original study [497], 12.5% Ni on USGO was found to out-perform a commercial 30% Ni/$Al_2O_3$ catalyst, giving higher glycerol conversion ($X_{gly}$ = 87%), hydrogen yield ($Y_{H2}$ = 79%), and a $H_2$/CO molar ratio of 5.5. These parameters remained very stable over 48 h TOS at 580°C, probably due to the well-controlled

level of coke deposition, estimated at 2.7 $mg_{coke}g_{cat}^{-1}h^{-1}$ by thermogravimetry (TG) under air flow. The UGSO support itself had significant activity in glycerol cracking ($X_{gly}$ = 23%, $Y_{H2}$ = 14%) and WGS ($CO_2/CO \approx 1$), attributed to co-promotion by $Fe_xO_y$ and MgO acting in synergy. In a follow-up study [498], the Ni loading and preparative methodology were optimised at 5% by solid-state impregnation (causing lower amounts of coke in less-pernicious form) on the basis of maximum gas yield (~100%) and negligible production of liquids during TOS at 630°C.

Most recently [499], a comparative study was made of stability in GSR for UGSO-supported Rh (1%), Ru (1%) and Ni (5%) and the results are shown in Fig. 44D. Glycerol conversion over Ni/UGSO during 8h at 630°C was complete (100%), as was the fractional conversion to gas ($X_{gas} \approx$ 100%). Its remarkable stability was attributed to MgO, creating atomically-dispersed $Ni^{2+}$ [via Mg(Ni)O solid solution formation prior to reduction], imparting good sintering resistance to the Ni nanoparticles [$d_{Ni}$ increasing only slightly from 19.6 to 23.9 nm after TOS], thus favouring low coking rates (< 0.01 $g_{coke}.g_{cat}^{-1}h^{-1}$). Its overall catalytic performance was comparable to that of Rh, giving a slightly lower $H_2$ yield, $Y_{H2}$ = 74% (vs. 78%), and a less-favourable $CO_2/CO$ ratio of 2.1 (vs. 2.4). In contrast, Ru/UGSO was clearly unstable with $X_{gly}$ and $X_{gas}$ falling to 85% and 65%, respectively, trends attributed to metal diffusion into the sub-surface region as seen by XPS. A mechanism for GSR was proposed involving cooperation between the incorporated metal (Rh, Ru, Ni) and the Fe/Mg bearing species on the surface of the reduced UGSO. As shown in Fig. 45, associative and regenerative (redox) mechanisms were proposed, in which MgO and (reducible) $Fe_xO_y$ combine to play key roles in water activation and WGS.

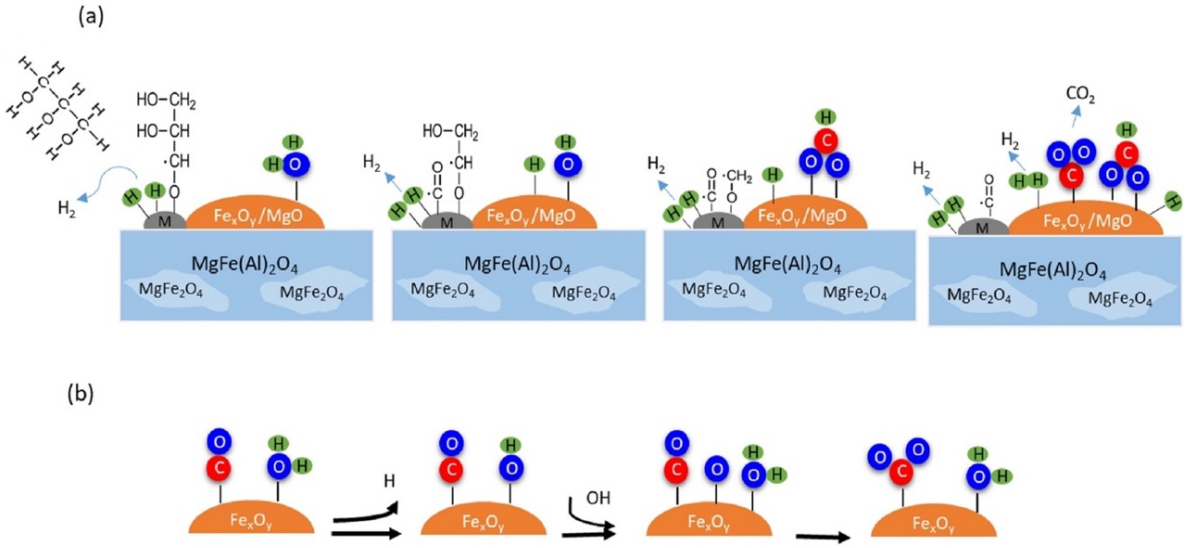


**Fig. 45** Proposed GSR mechanism over M-UGSO catalysts involving **(a)** associative and/or **(b)** regenerative (redox) processes in the WGS component. [Reproduced with permission from ref. 499]

One preparative approach to optimise the metal-promoter/ support interactions necessary to impart stability in GSR is by atomic inter-dispersion of the elements in a mixed-oxide(s) precursor form, e.g., via solid solution as indicated above for NiO-MgO, or via perovskites like $LaNiO_3$ or $CeNiO_3$ [500]. This facilitates a *controlled* (rate and degree of) reduction of the transition metal ions with the aim of restricting the size of the resulting metal nanoparticles and stabilising these by any strong metal-support interaction (SMSI). However, the reducibility of such mixed-oxide precursors is not necessarily guaranteed at practical temperatures. For example, Ni can be "lost" in the activation (calcination) stage of $Ni/Al_2O_3$ preparation due to its transformation into a highly-stable $NiAl_2O_4$ spinel, not reducible below 800°C. $Ni\text{-}La_2O_3$ ($d_{Ni} \approx$ 20 nm) was obtained from reduction of $LaNiO_3$ in $H_2$ at 500°C [501]. $Ni\text{-}La_2O_3/ZrO_2$ ($d_{Ni} \approx 8$ nm) was obtained from $La_{0.3}Zr_{0.7}NiO_3$ prepared by flame pyrolysis and pre-reduced in $H_2$ at 700°C [502]. Both showed high glycerol conversion, $X_{gly}$ = 68% and 100%, respectively,

and excellent stability over 20 h at 650°C, while supported Ni-$La_2O_3$ catalysts obtained by usual methods have given less impressive results [503,504].

Interest is also growing in carbon as a GSR catalyst support, primarily due to evidence that it confers good activity to supported metals already at low temperatures, i.e., 350-450°C. This is possibly inspired by the early work of the Dumesic group in glycerol aqueous-phase reforming [505], Carbon as support was found to confer the best catalyst stability, attributed to its superior resistance to hydrothermal degradation. Liu et al. [506] have prepared and tested carbon nanotube (CNT)-supported Ni over a range of loadings, 3-15%. While numerical data for glycerol conversion and stability during TOS were not provided, low-temperature activities were impressive. Conversion to gas ($X_{gas}$) at 375°C increased steadily with Ni loading, ranging from 55.9 to 86.4% for 3Ni and 15Ni. Selectivity to $H_2$ ($S_{H2}$) showed a similar trend, ranging from 38.2 to 72.9 %, respectively. However, $CO_2$ selectivity only exceeded that of CO, a measure of WGS activity, at $\geq$ 10Ni ($S_{CO2}/S_{CO} \approx 1.2$). On this basis, along with the acceptably low $CH_4$ level ($S_{CH4} < 4\%$), 10Ni was selected for further study. The effect of temperature on activity was evaluated between 350 and 450°C, $X_{gas}$ ranging from 63.3 to 80.7%, respectively. Accordingly, $S_{H2}$ ranged from 47.0 to 83.6% with a dramatic improvement in WGS evident by 400°C ($S_{CO2}/S_{CO} \approx 4.9$) and no detectable $CH_4$. Such impressive behaviour implicates the CNT support in regulating one or more features specific to the active phase as revealed by extensive characterization. For 5Ni and 10Ni, the particle size was found to be very small, $d_{Ni} \approx 4.76$ and 5.33 nm by TEM or 12.1 and 14.2 nm by $H_2$ chemisorption. The sintering resistance was also good, $d_{Ni}$ increasing by only 5-10% relative after testing. CNTs have the ability to confer WGS activity to Ni, linked to stabilisation of electron deficient ($Ni^{\delta+} \leftrightarrow Ni^{2+}$) species, even in the absence of $CeO_2$, a known promoter [507]. Suspecting that the high metal dispersion [$D_{Ni}$ = 19.2% (5Ni) and 10.6% (10Ni)] might be due to low absolute amounts of metal available, the reduction degree by TPR was found to be low only for 3Ni (17.6%), but otherwise quite high,

viz., 52.8% (5Ni) and 75.1% (10Ni), respectively. Alternatively, attributes unique to CNTs may be playing a significant role, e.g., internal confinement and its effect(s) on electronic and catalytic properties of guest metal nano-clusters [508].

In follow-up work, Wang et al. [509] used the same 10Ni/CNT sample as control in a study of 5% Ni-based (1:1) bimetallic (Co, Cu, Fe)/CNT catalysts in GSR at 375°C. Metal (mean) particle sizes by TEM were similar at 6.9 nm (NiCo), 5.8 nm (NiCu), 6.5 nm (NiFe), and 5.3 nm (Ni). The nanoparticles were also thermally stable, diameters ($d_{spent}$) remaining below 10 nm after testing in all cases. Glycerol conversion ($X_{gly}$) was 80% for the 10Ni control but higher for all the bimetallics, $X_{gly}$ = 85% (NiFe), 90% (NiCu) and 91% (NiCo), respectively. Conversion to gas ($X_g$) for the 10Ni control, $X_g$ = 51%, was slightly lower than previously (65.8%) [506] due to a doubling of the liquid reactant (10% aqueous glycerol) delivery rate to 6 ml.h$^{-1}$. This was surpassed by all the bimetallics, giving $X_g$ = 58%, 74%, and 80% for NiCo, NiCu, and NiFe, respectively.

In summary, NiCo performed best overall in terms of giving the highest $X_{gly}$ (91%), $S_{H2}$ (57%), $S_{CO2}/S_{CO}$ ratio (3.7), and the lowest $S_{CH4}$ (2%). The NiCo system was subjected to more intensive studies based on a preparative method allowing control of the locality of deposition, i.e., selectively in the interior "caverns" [Ni(i),Co(i)] and/or on the outside surface [Ni(o),Co(o)] of the CNTs [510]. Ni(i)Co(i) gave the best performance in GSR at 400°C in terms of activity/ selectivity ($X_{gly}$ = 95.7%, $X_g$ = 94.6%, $S_{H2}$ = 86.5%), followed by Ni(o)Co(i) ($X_{gly}$ = 92.2%, $X_g$ = 92.6%, $S_{H2}$ = 80.6%). Ni(i)Co(i) also gave the best stability during TOS, as shown in Fig. 46, probably due to its greater resistance to sintering ($d_{red}$ = 2.97 nm, $d_{spent}$ = 4.19 nm, a 40% increase). This was in turn attributed to a confinement effect inside the CNTs. The Ni(o)Co(o) variant gave the least stable catalytic performance and the lowest resistance to sintering ($d_{red}$ = 3.84 nm, $d_{spent}$ = 13.0 nm, a 240% increase).

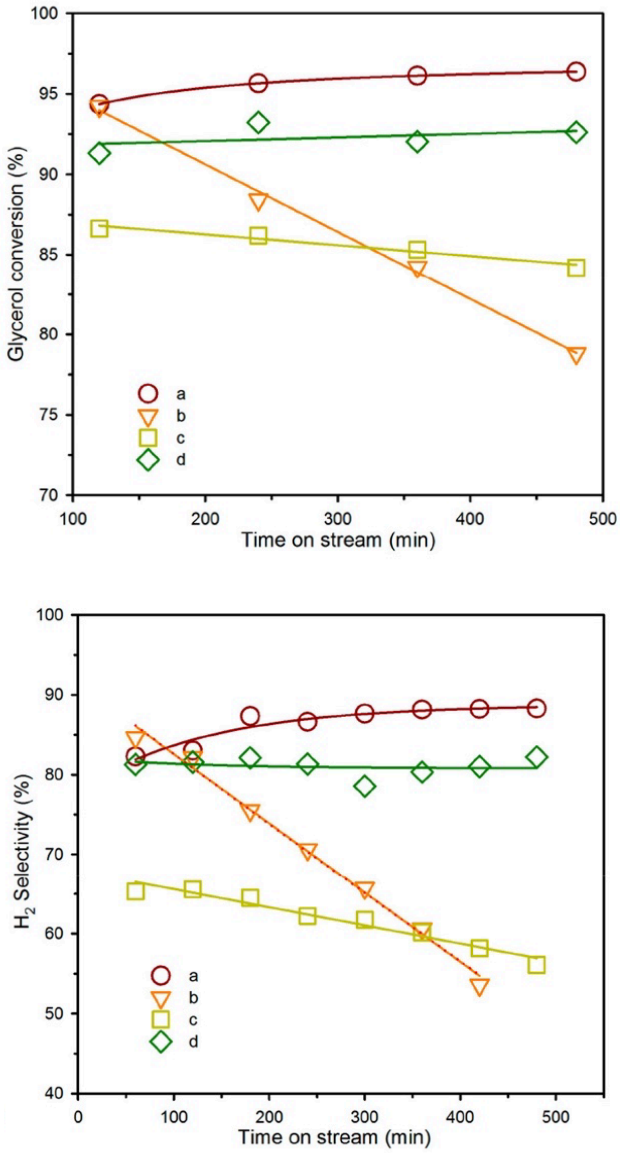


**Fig. 46** Stability of NiCo/CNTs during TOS in GSR at 400°C. **a.** Ni(i)Co(i) – purple circles. **b.** Ni(o)Co(o) – orange triangles. **c.** Ni(i)Co(o) – yellow squares. **d.** Ni(o)Co(i) – green diamonds. [Reproduced with permission from ref. 510]

Pastor-Pérez and Sepúlveda-Escribano [511] chose activated carbon as support for tests in GSR at low temperature (350°C) on the basis of its low acidity, minimising the risk of coking via dehydration reactions. Ni-based catalysts were doubly-promoted by $CeO_2$ and Sn to impart WGS activity and sintering resistance, respectively. As shown in Fig. 47A, addition of $CeO_2$

2506 (30 wt%) extended the initial period of high conversion to gas ($X_g$>90%) for up to 5 h. However,
2507 all $NiCeO_2$/C samples deactivated strongly over 30 h although not as rapidly or completely as
2508 the Ni/C control, which gave a low final $X_g$=15%.
2509

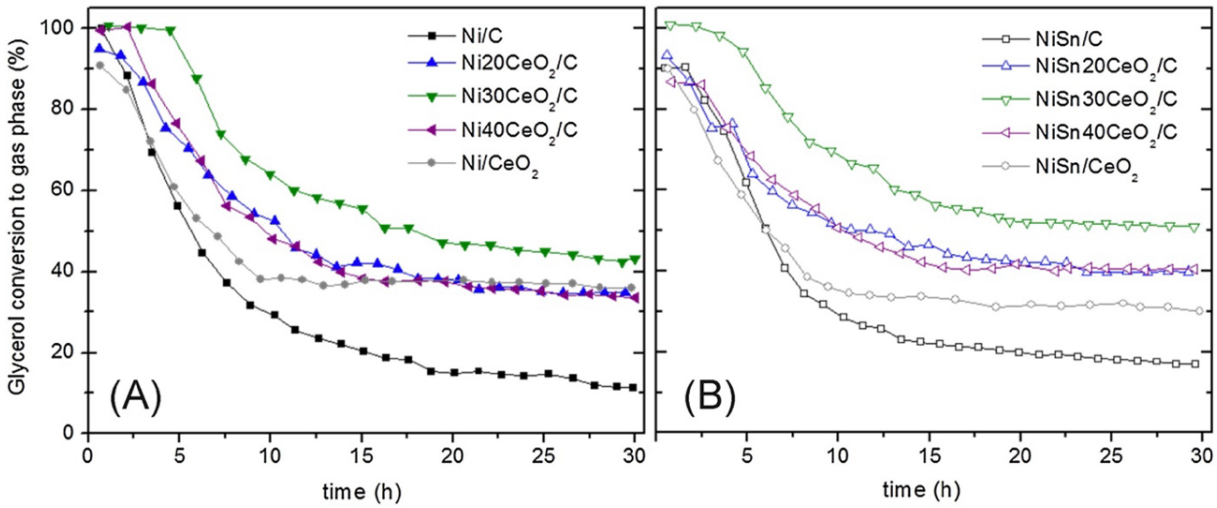


2510

2511 **Fig. 47** Conversion of glycerol to gas products (Xg) over **(A)** $NiCeO_2$/C, and **(B)** $NiSnCeO_2$/C
2512 at 350°C during 30 h TOS. [Reproduced with permission rom ref. 510].
2513

2514 $Ni30CeO_2$/C gave the best result in terms of stability, maintaining $X_g$ = 45% and $Y_{H2}$ =
2515 32% after 30 h TOS. It was also the most highly selective catalyst for $CO_2$ ($S_{CO2}/S_{CO}$ = 18.5),
2516 verifying the importance of $CeO_2$ in WGS. As shown in Fig. 47B, inclusion of Sn had an
2517 additional stabilising effect and resulted in the highest steady-state conversion to gas ($X_g$=52%)
2518 and $H_2$ yield ($Y_{H2}$=48%) over $NiSn30CeO_2$ /C, albeit at the expense of lower $CO_2$ selectivity
2519 ($S_{CO2}/S_{CO}$ = 2.1). All catalysts produced very low levels of $CH_4$ ($S_{CH4}/S_{H2} \leq 0.016$).
2520 From the foregoing examples, it is clear that the pervasive instability in GSR catalysis not
2521 only results in rapid loss in initial activity, but seriously impedes the measurement of kinetic
2522 parameters necessary to define the working (Arrhenius) rate equation:
2523

$$- r_{GSR} = k p_g^{\alpha} p_w^{\beta} \quad (44)$$

where k is the rate constant (= $Ae^{-Ea/RT}$), $p_g$ and $p_w$ are glycerol and water pressure/concentrations, α and β are their respective order coefficients, A is the pre-exponential factor, and $E_a$ is the apparent activation energy. Accurate kinetic parameters, preferably supported by a plausible reaction mechanism [313,512], can only be obtained for a catalyst that has reached steady-state activity. In their absence, no serious progress can be made towards reactor design, modelling and/or process optimization. In this regard, the dearth of information (or related discussion) in the GSR literature is perhaps not surprising [313,356,357]. It also emphasises the need for a theoretical (calculational) approach to evaluate and distinguish between elementary mechanistic steps and provide quantitative estimates as benchmarks for the least-reliable empirical values. Some progress is being made in first principles (DFT) modelling of glycerol reactivity [489], but it is challenged by the high (cost of) computer time needed to deal with the molecular complexity of the $C_3$ polyol [513]. This point will be taken up in more detail shortly.

Studies in supercritical water reforming (SCWR) of glycerol have been more encouraging from an empirical viewpoint. In a series of related studies, Gutiérrez Ortiz et al. [514-516] characterised and compared the performances of commercial samples of 66.4 % $Ni/SiO_2/Al_2O_3$ and 3% $Ru/Al_2O_3$ over a wide range of temperature (500-800°C), feed concentrations (5-20 % aqueous glycerol), and weight-hourly space velocities (2.5-12.5 $g_{gly}g_{cat}^{-1}h^{-1}$) under a pressure of 240 bar. These conditions resulted in full conversion of glycerol at or above 550°C but the selectivities to gaseous products were quite different. While both catalysts achieved high carbon-to-gas conversion efficiencies (~95% at 600°C) at the lowest (5%) feed concentration, only the Ni-based sample was selective for $H_2$, its yield ($Y_{H2} \approx 47\%$) approaching the equilibrium limit of 55.5% (3.9 mol/mol glycerol), as shown in Fig. 48*top*.

2549

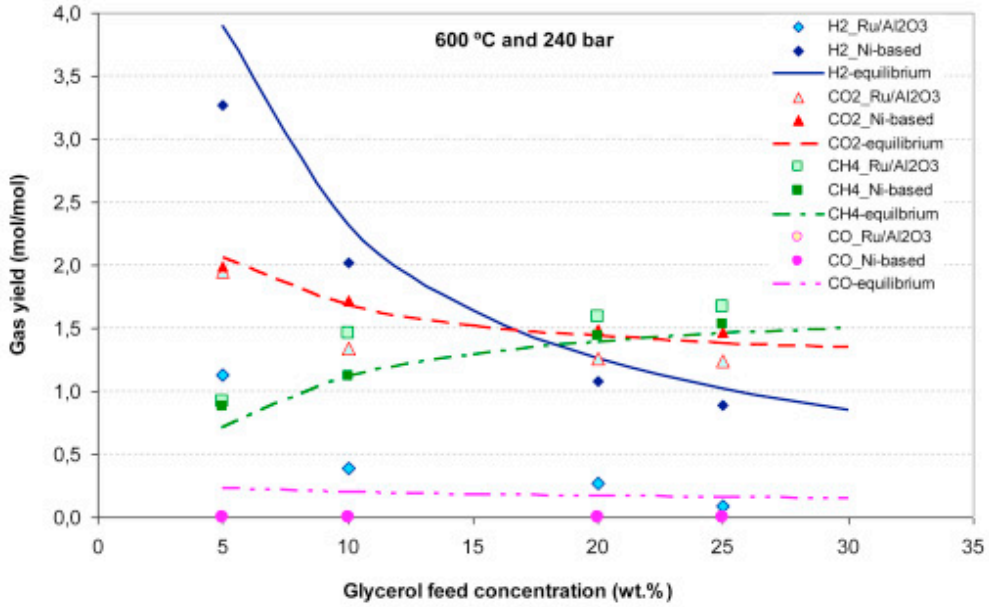


2550

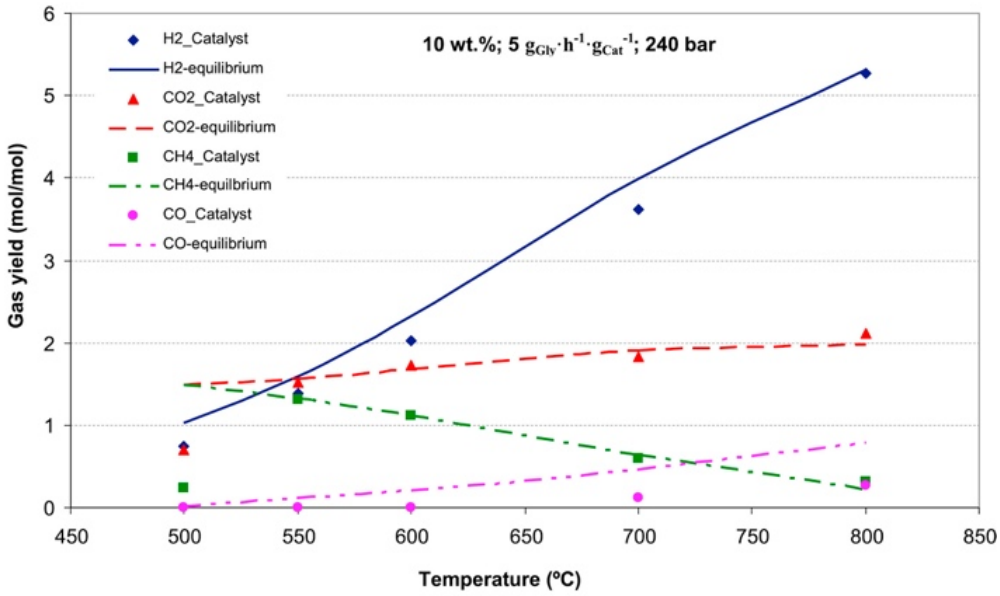


2551

2552 **Fig. 48 (top)** Effect of glycerol feed concentration on gas yields at 600°C (240 bar) over

2553 $Ni/SiO_2/Al_2O_3$ and $Ru/Al_2O_3$. [Reproduced with permission from ref. 515] ; **(bottom)** Effect

2554 of temperature on gas yields at a glycerol feed concentration of 10 % (240 bar) over

2555 $Ni/SiO_2/Al_2O_3$. [Reproduced with permission from ref. 514]

2556

The effect of temperature, favouring $H_2/CO_2$ production at the expense of $CH_4$, and the general approach to equilibrium at a slightly higher (10% glycerol) feed rate over $Ni/SiO_2/Al_2O_3$ is shown in Fig. 48*bottom*. The vanishingly small levels of CO, well-below the equilibrium limit, suggests a high degree of kinetic control in the WGS stage, possibly linked to the high fugacity of the water reactant in the supercritical condition. More importantly, the catalytic behaviour was time-invariant, i.e., stable enough to allow a realistic determination of turnover frequencies (TOF) [516], the level of coking being restricted to < 0.5 %. above 500°C. TOFs over Ni ranged from 0.08 to 0.637 molecules per metal site per second depending on temperature (550-800°C), weight-hourly space velocity (2.5-10 $g_{gly}g_{cat}^{-1}h^{-1}$), and pre-conditioning in SCWG. Due to the high loading, the mean particle size of Ni was quite large at ~50 nm or a dispersion ($D_{Ni}$) of just 2.05%. Despite this limitation, the high TOFs obtained suggest the mechanistic importance of a large ensemble size for effective catalysis. Apparent activation energies ($E_a$) ranged from 30-40 $kJ.mol^{-1}$, increasing slightly with WHSV, and can be taken as quite accurate. These are consistent with the bulk of the literature, although the latter values are widely spread (30-135 $kJmol^{-1}$) [313,356,357,505], probably due to systematic errors caused by catalytic instability.

Similar results for Ni at lower loadings of 5-10 % on a variety of oxidic supports were reported by Pairojpiriyakul et al. [517], although only $Ni/La_2O_3$ was stable during TOS. Ni on $\alpha$-$Al_2O_3$, $\gamma$-$Al_2O_3$, or $ZrO_2$ suffered operational failure due to excessive carbon deposition in the range 475-550°C. In contrast, Li et al. [518] studied long-term stability trends in SCWG of glycerol over Ni at 15-25% loadings on CNTs, $\alpha$-$Al_2O_3$, and Mg-promoted $\gamma$-$Al_2O_3$, but found little or no deactivation linked to carbon deposition. However, metal leaching (as $Ni^{2+}$, $Al^{3+}$, $Mg^{2+}$) was found to be one factor, along with slight sintering, contributing to very slow activity loss during 48 h TOS. This was especially notable for Ni leaching from the larger metal particles ($d_{Ni} \approx 28$ nm) in Ni/$\alpha$-$Al_2O_3$, although $Al^{3+}$ loss from the same source was relatively more

2582 serious, estimated to reach completion within 700 h. Gasification efficiencies for all catalysts
2583 exceeded 80% in low-temperature tests at 425°C and 250 bar, but $H_2$ yields were limited to
2584 1.46, 0.98, and 0.78 mol/mol for Ni/$MgAl_2O_4$, Ni/α-$Al_2O_3$, and Ni/CNT, respectively. In
2585 follow-up work [519], the same group sought to control catalyst degradation via metal leaching,
2586 eschewing Al-based supports in favour of $TiO_2$, $ZrO_2$, and $Ta_2O_5$. In the latter two cases,
2587 gasification efficiency grew from 30-90% in the first 5 h on-stream, and was subsequently
2588 maintained for up to 80 h. Evidence was found that these supports confer superior leaching
2589 resistance to Ni via formation of mixed-oxide forms, e.g., $NiTa_2O_6$. It was proposed that such
2590 "operando" pre-conditioning should be properly investigated and optimized to promote the
2591 continuous processing of glycerol. Taking the data set of Gutiérrez Ortiz et al. [514],
2592 computational fluid dynamics (CFD) modelling of glycerol SCWG over Ni/$SiO_2$/$Al_2O_3$ was
2593 reported by Dumbrava et al. [520]. This involved the use of a lumped kinetic expression based
2594 on formation and decomposition of an intermediate (Int) of nominal empirical formula $C_2H_4O$
2595 produced via pyrolysis/WGS (Reaction 45):
2596
2597 $C_3H_8O_3 \rightarrow Int + CO_2 + 2H_2 \qquad (\Delta H = +131\ kJ.mol^{-1})$ (45)
2598
2599 Agreement between CFD-calculated and experimental values was good, giving a nearly
2600 rectilinear plot of $H_2$ yield for feed concentrations of 5-20 wt.% with a variance ($R^2$) of 0.969,
2601 as shown in Fig. 49*top*. The best fit has an apparent activation energy ($E_a$) of 52 $kJ.mol^{-1}$ for
2602 Reaction 43, i.e., slightly higher than the measured values at ~40 $kJ.mol^{-1}$ [516]. Fig. 49*bottom*
2603 reveals details on the reaction sequence and approach to equilibrium conversion along the
2604 reactor bed length at 600°C and 10% feed concentration. The intermediacy of CO (peaking in
2605 the 1st 10 cm) and the progressive loss of $H_2$ (via methanation) after ~15 cm is evident. The
2606 near-superposition of estimates for instantaneous internal (pellet) and external (fluid)

concentrations verified the high catalytic effectiveness factor and the absence of intra-pellet diffusional limitations. The best compromise between glycerol conversion and $H_2$ product selectivity (lower $CH_4$) was found at a residence time of 2.4 s, as utilised experimentally.

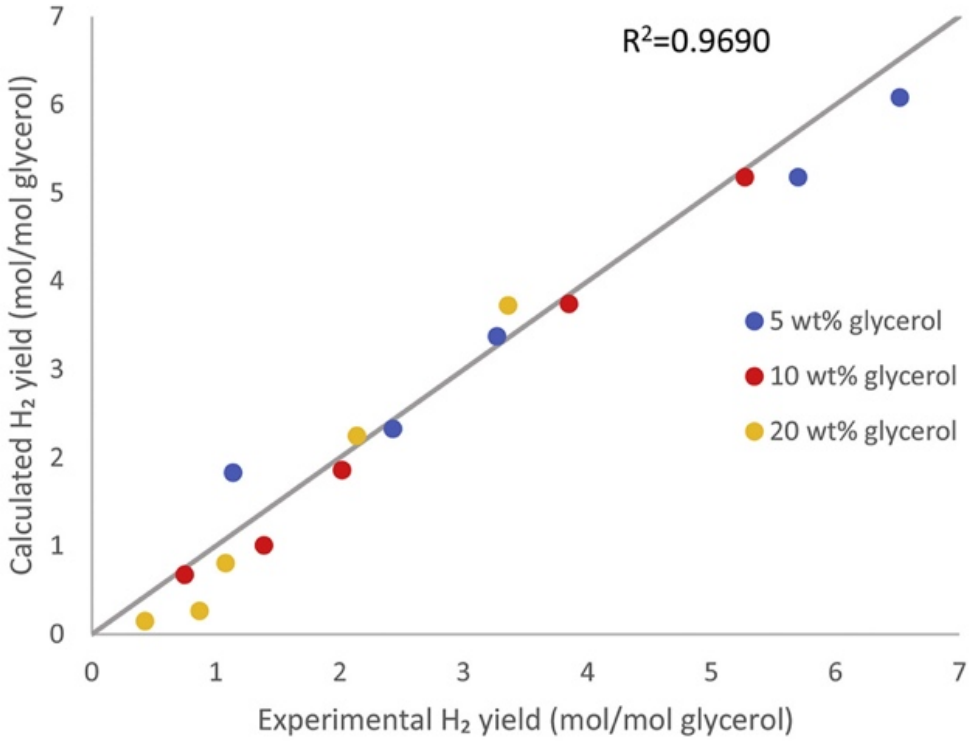


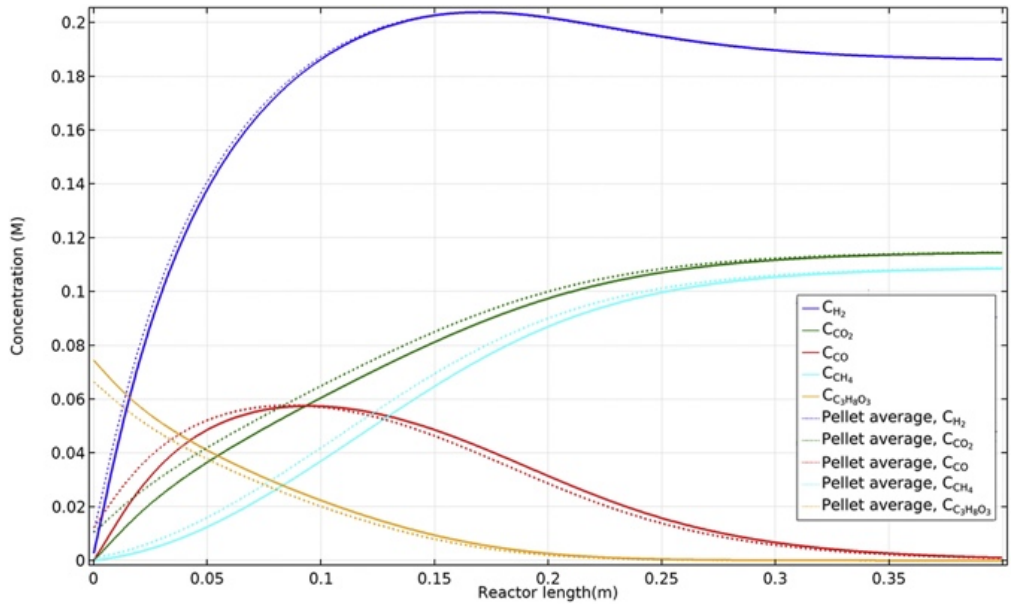

**Fig. 49 (Top)** Parity plot of CFD-predicted vs. measured values (taken from Ref. 514) of $H_2$ yield in glycerol SCWR ; **(bottom)** Glycerol conversion sequence along reactor with intermediate CO and loss of $H_2$ to methanation. [Reproduced with permission from ref. 520]

Glycerol aqueous-phase reforming (APR) has been the focus of several recent reviews [449,477,491]. It offers the advantages of SCWR, i.e., reactants are supplied in the liquid state, but at far lower temperature. This lightens the burden on process energy demand and minimises the risk of thermal degradation. However, as shown schematically in Fig. 50*top*, the main issue in glycerol APR is that the milder conditions necessary to maintain reactants in the liquid state under workable pressures (T = 150-265°C, P = 15-70 bar) typically result in lower conversions and generate both gaseous and liquid products, i.e., the process is not exclusively for renewable $H_2$ [523]. Ultimately techno-economics and market forces will determine the balance in production between pressurised gas ($H_2$, $CO_2$, CO, $CH_4$, etc.) and value-added liquid products like propylene and ethylene glycols (diols), $C_1$-$C_3$ alcohols, acetone, acetic acid, acetol, and lactic acid. As this review article focuses on oxygenates as hydrogen (energy) carriers, the emphasis here is placed on processes, reactors, and catalyst optimization for $H_2$ release. Already supplied in pressurised form, the $H_2$ component is a valuable resource for on-site (biorefinery) processing and energy production in fuel cells. However, it must first be separated, e.g., by pressure-swing absorption (PSA), perm-selective membranes, etc., from contaminant gases.

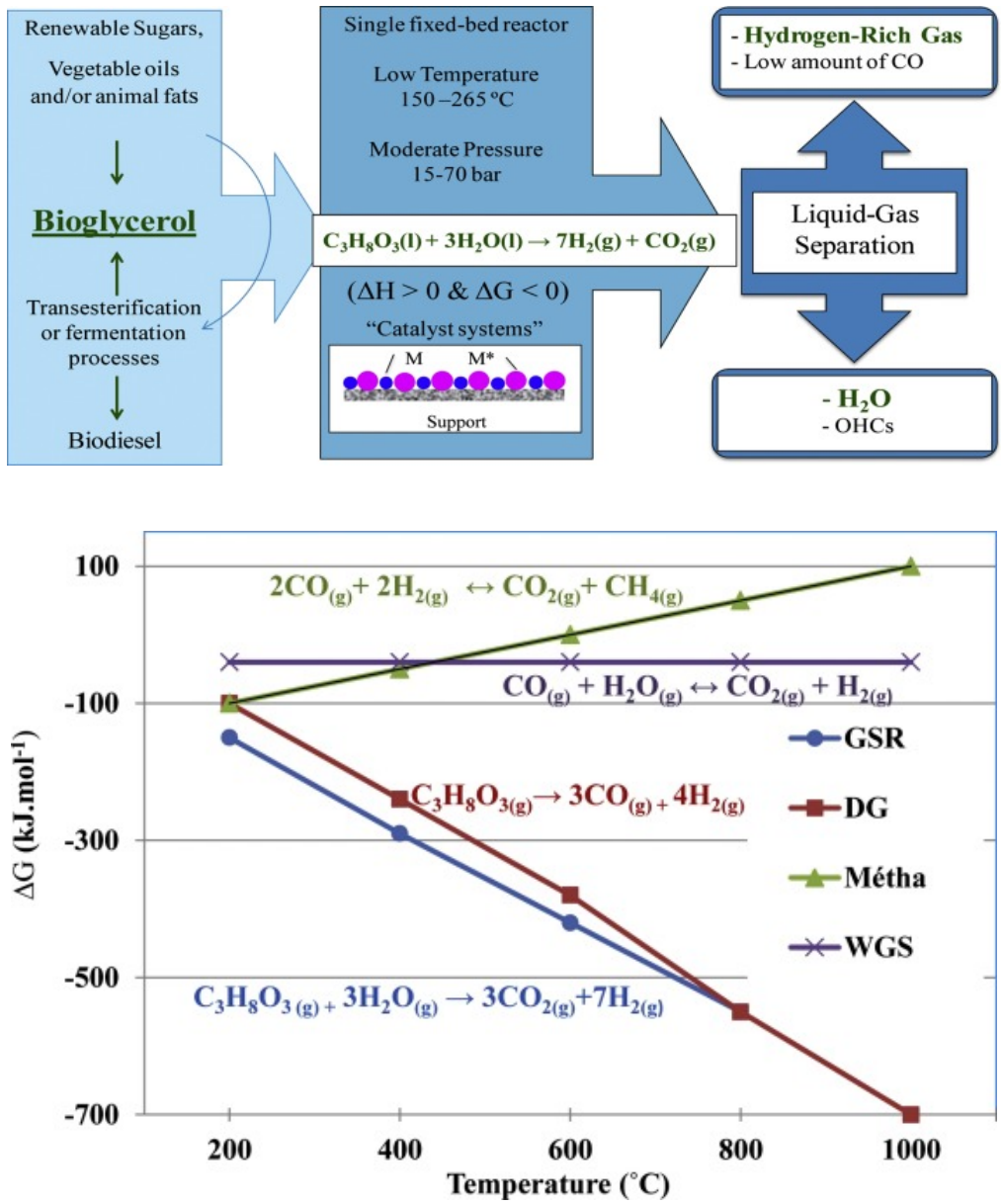


**Fig. 50 (Top)** Bioglycerol valorization scheme via APR ; **(bottom)** Thermodynamics of glycerol reforming [Reproduced with permission from ref. 523]

As shown in the generalised reaction network depicted in Fig. 51, supported metals are needed to promote consecutive dehydrogenation pathways (via glyceraldehyde and/or dihydroxyacetone), followed by CO elimination, ultimately yielding the desired renewable syngas ($H_2/CO_2$) after conversion of CO via the WGS process.

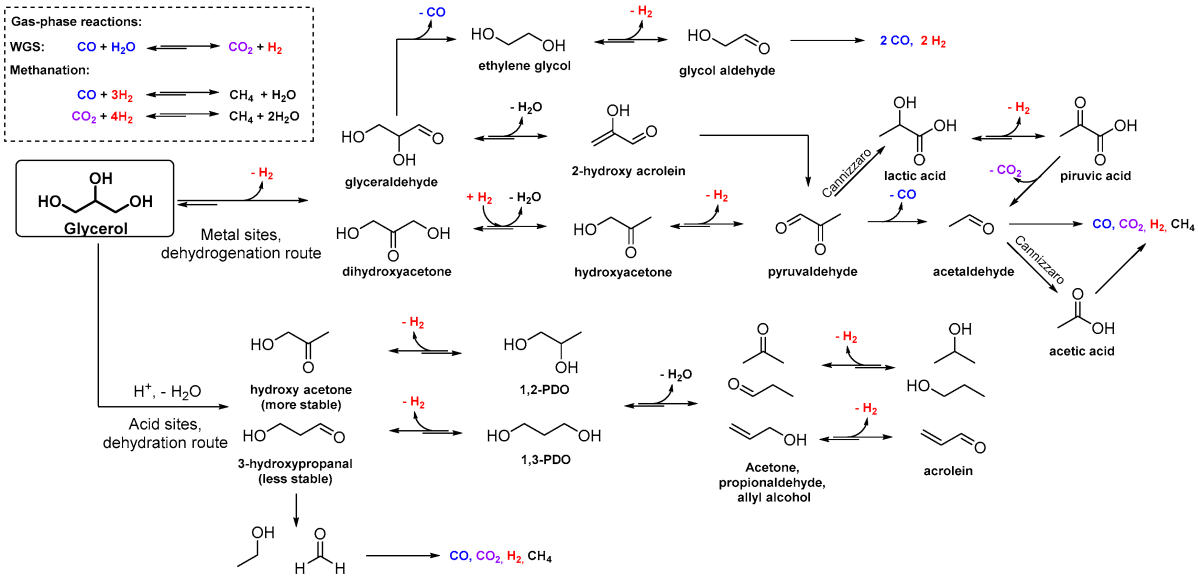


**Fig. 51** Reaction network in glycerol APR: supported metals favour dehydrogenation and CO elimination prior to WGS, leading to $H_2$ and $CO_2$. Alternative routes in glycerol valorization are favoured by tuning the support acidity, resulting in combined dehydration/dehydrogenation to valuable liquid products, e.g., propanediols, acetone, acrolein, etc. [Reproduced with permission from ref. 530]

Glycerol APR has been under sustained investigation over the last decade, notably by the Arias group in Bilbao. They have focussed on a γ-$Al_2O_3$-supported Pt/Ni catalyst originally identified, along with Pt-Co and Pt-Fe, in high-throughput screening of Pt-based bimetallics by Huber et al. in ethylene glycol APR [477]. The Pt/Ni system is one of the most studied alloys in surface science investigations [521], stemming from its value as a fuel cell anode material. The presence of Ni atoms shifts the d-band centre of Pt, moderating the well-known "CO poisoning" effect by lowering its heat of adsorption (binding strength). A similar catalytic synergy may be operative in oxygenates APR, but with effects on both CO and H atom adsorption energetics [477,522]. Fig. 50*bottom* reaffirms the spontaneous (favourable)

2661 thermodynamics of glycerol reforming (Reactions 41 & 42 – see also Fig. 43), with high and
2662 negative free energy changes already at 150°C.

2663 In the original study by Huber et al. [477], the best phase(s) composition in terms of metal
2664 mass-specific activity, was found to be Pt:Ni = 1:1. However, most follow-up studies have been
2665 made on "Pt-modified Ni", more realistic from a materials cost and sustainability perspective,
2666 with typical loadings of < 2.5% Pt and 8-10 % Ni. In their early work, the Arias group found
2667 that Ni/γ-$Al_2O_3$ catalysts were of impracticably low activity, in part due to their high resistance
2668 in pre-reduction to the metallic state, most remaining as $Ni^{2+}$ in a stable aluminate framework
2669 ($NiAl_2O_4$) [524]. It was clear that the presence of Pt improved glycerol conversion (> 30%) by
2670 promoting more complete reduction of $Ni^{2+}$ via the "$H_2$ spill-over" mechanism [525]. The key
2671 issues of catalyst activity and durability, linked mainly to Ni reducibility, Pt/Ni interdispersion,
2672 alloy formation, inclusion of basic promoters $M_xO_y$ (M = Zr, Ce, La or Mg) for enhanced WGS
2673 properties, and resistance to deactivation (via metal/support sintering, carbon laydown, etc.)
2674 were dealt with in their preparative methodology. This included sequential and simultaneous
2675 impregnation by incipient wetness (IWI), sol-gel methods in acid (SGA) or base (SGB), and
2676 combinative sol-gel/impregnation (SGI). The superiority activity and stability of Pt/Ni/Al was
2677 demonstrated in studies on Pt-Ni, Pt-Co and Pt-Fe -based materials prepared by the sol-gel acid
2678 (SGA) route. Glycerol conversion at 250°C was initially high at $X_{gly}$ = 97% as compared to Ni-
2679 only (68%) or Pt-only (25%). The selectivity to gaseous products was also high ($Y_{gas}$ ≈ 58%),
2680 or 3x and 7x the Ni-only (22%) and Pt-only (8%) values, respectively. Stability tests after 32h
2681 gave favourable results, $X_{gly}$ and $Y_{gas}$ dropping slightly to 74% and 35%, respectively [527].
2682 These good results were linked to Pt-Ni interactions, evidenced by the smaller mean Ni particle
2683 size obtained in the bimetallic state (7 nm) as compared to the Ni-only control (12 nm).

2684 Similar behaviour was seen in Pt/Ni/Al prepared via the sol-gel base (SGB) route, with
2685 good selectivity toward $H_2$ ($H_2$/alkane ≈ 2.5, $H_2/CO_2$ ≈ 1.5) [526]. The main cause of

deactivation was found to be instability in the γ-$Al_2O_3$ support, tending to hydrolyse to boehmite (AlOOH). Associated losses in porosity and surface area resulted in limited access to the metal active sites [528]. An additional deactivation mechanism was slight but reversible re-oxidation of $Ni^0$. A "state-of-the-art" formulation more-resistant to hydrolysis consisted of 9% Ni and 2% Pt prepared by basic sol-gel methods (SGB), either directly or by simultaneous impregnation (SGI) onto a pre-formed (SGB) γ-$Al_2O_3$. The performances of both types, NiPt/ASGB7 and NiPt/ASGI7 (7- denoting pre-calcination up to 750°C prior to reduction) were impressive and quite similar, although a difference was seen in stability [529]. The initially most active catalyst was the directly-prepared Ni/Pt/Al sol-gel material ASGB7, showing ideal (2h) levels of glycerol conversion $X_{gly}$ = 100%, and efficiency of conversion to gas $Y_{gas}$ = 98% (see Fig. 52*top*). However, this was a less-stable form and by 8 h the activity had dropped to below the values for the impregnated material ASGI7 at $X_{gly}$ = 92% and $Y_{gas}$ = 71%, which were more time-invariant as shown in Fig. 52*bottom*. The same trend was maintained during long-term testing, finally leading to steady-state behaviour. The residual activity/selectivity for ASGI7 was still impressive ($X_{gly}$ = 79%, $Y_{gas}$ = 57%) but that for ASGB7 less so ($X_{gly}$ = 60% and $Y_{gas}$ = 40%). A key step in the optimization of catalyst stability was high-temperature pre-treatment. A sample pre-calcined at 550°C (ASGB5) gave $X_{gly}$ = 80.3% and $Y_{gas}$ = 46.6% after just 8 h. The last was 30% lower than after optimum pre-treatment at 750°C ($Y_{gas}$ = 67.1%). Detailed TEM characterization of fresh and spent catalysts shows the development of needle-like morphology (typical of AlOOH) in used ASGB7 that was absent in ASGI7. This suggests that high-temperature calcination of the pure support imparts greater resistance to hydrothermal deterioration and thereby also better catalytic stability. In TPR studies, Pt was found to facilitate a higher degree of reduction in the Ni component, exceeding 90% in ASGI7 as compared to below 50% in the corresponding Ni-only control. The high initial conversion in ASGB7 was probably due to the higher Ni dispersion ($d_{Ni} \approx 4$ nm) as compared to ASGI7 ($d_{Ni} \approx 9$ nm).

However, the former sintered faster such that after 8h, there was little or no difference in particle size ($d_{Ni}$ ≈15 nm).

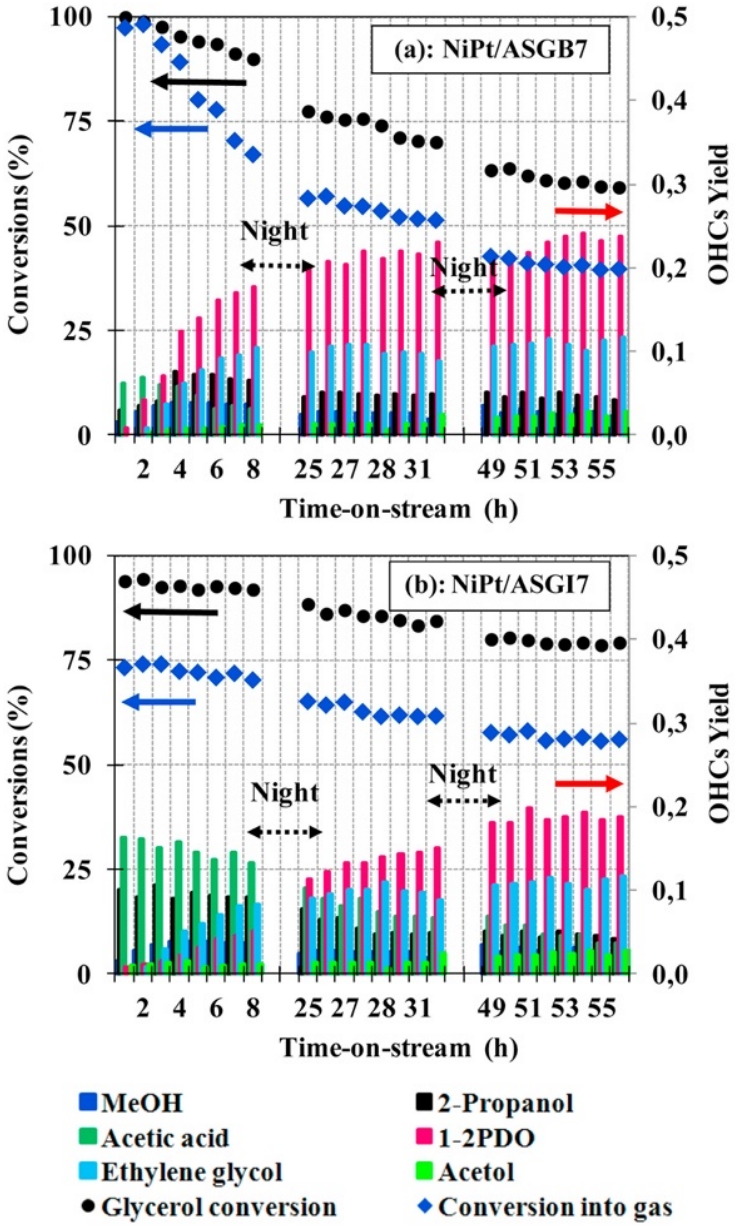


**Fig. 52** Activity, selectivity and durability of 9%Ni/2%Pt/©-$Al_2O_3$ in 10% glycerol APR (230°C, 30 bar, WHSV = 2.6 h-1). Catalysts were prepared by **(top)** base sol-gel (SGB) methods or **(bottom)** combined with impregnation (SGI) on pre-formed ©-$Al_2O_3$. [Reproduced with permission from ref. 529]

A study on 3% $CeO_2$-promoted Ni/Pt/$Al_2O_3$ with higher base metal contents (3-18% Ni, 1% Pt) was reported by *Rahman et al*. [531]. Under APR conditions (1% glycerol, WHSV = 12 $h^{-1}$, 240°C, 40 bar), the best results were obtained at the composition 6%Ni-1%Pt. The glycerol conversion ($X_{gly}$ = 96%) and hydrogen yield ($Y_{H2}$ = 86%) were matched by Pt mono-metallic samples from earlier work [532], but only at triple the loading (3% Pt), implying that the bimetallic Ni/Pt system offers a significant economisation in materials. These values well-exceeded those for the Pt-free 6Ni3CeAl control ($X_{gly}$ = 26%, $Y_{H2}$ = 13%), which incidentally suffered complete deactivation after 15h. In addition, the lesser performance of a physical mixture of separately-prepared (Ni and Pt) mono-metallic components at the same loadings ($X_{gly}$ = 90%, $Y_{H2}$ = 70%) was indicative of a Ni-Pt bimetallic synergy operative on the atomic scale. Although the XRD peak widths for metallic Ni were too broad to be measured, possible alloying was indicated in the greater dispersion of Pt in the best (6% Ni-1% Pt) sample, with $D_{Pt}$ = 25% or $d_{Pt}$ = 4.6 nm.

In the search for alternative supports to optimise and/or direct the Ni/Pt synergy to suitable ends, valuable studies have been done by the Chen team in Newark, DE. From DFT calculations and in-situ (batch) FTIR studies of model reactions, ethanol reforming and 1,3-butadiene hydrogenation, over 1%Ni-1%Pt on γ-$Al_2O_3$ (vs. amorphous $TiO_2$), they found that the support has a strong effect *indirectly* by its degree of interaction with nickel, the more-reactive metal. The γ-$Al_2O_3$ stabilises a Ni-rich interfacial layer terminated by Pt. This "Ni-promoted" Pt surface has higher hydrogenation activity than pure (bulk or nanocrystalline) Pt but shows little or no synergy in ethanol reforming due to its known susceptibility to CO poisoning. This suggests that γ-$Al_2O_3$ should be the preferred support in the production of liquid products which involves mainly hydrogenation and hydrogenolysis. In contrast, on amorphous $TiO_2$ the metal nanoclusters are still Pt-terminated but CO adsorption is suppressed via the

SMSI effect (decoration by $TiO_x$) which leads to greater reforming/WGS activity [533]. There is a general consensus that the ideal surface for reforming should be Ni-terminated but it's still debatable if the chemical environment under APR conditions is sufficiently oxidising to "draw out" the sub-surface Ni. On this issue, the same team has used *in-situ* XANES/EXAFS to show that there is a similar synergy in ethylene glycol reforming over a carbon-supported Ni/Pt bimetallic linked with surface enrichment of Ni, which exists in partially oxidised state under APR conditions [534].

$TiO_2$ and carbons as supports have been less-explored in glycerol APR although their early application in ethylene glycol APR gave promising results [535]. Recent fixed-bed flow reactor studies with a focus on long-term stability testing were made on two Ni-rich bi-metallic systems, Ni/Pt and Ni/Cu, supported on carbon multi-wall nanotubes (MWNT) [536]. The most active and selective catalyst compositions were found to be 1wt% Pt - 3wt% Ni and 1wt% Cu - 12wt% Ni. These gave glycerol conversions ($X_{gly}$) of > 99% and 84%, and gas yields ($Y_{gas}$) of 99 and 76%, respectively. The bimetallics clearly out-performed the monometallic controls [1% Pt: $X_{gly}$ = 54%, $Y_{gas}$ = 46%); 12% Ni: ($X_{gly}$ = 44%, $Y_{gas}$ = 39%)]. The results of rigorous long-term (stability) testing of these bimetallics are shown in Fig. 53A. An excellent $H_2$ yield ($Y_{H2}$) of > 90% was maintained during 100h on-stream over 1Pt-3Ni, followed by a respectable steady yield ($Y_{H2}$ = 65%) for 1Cu-12Ni. As seen in Fig. 53B, only repetitive testing (x5 – 100 h each) revealed signs of catalyst deterioration, $H_2$ yields over 1Pt-3Ni and 1Cu-12Ni falling by 10 and 15%, respectively. Additional tests in WGS, a key step in overall reforming, illustrated further their effectiveness, giving CO conversions > 85% and $H_2/CH_4$ ratios in the range 8-30. As shown in Fig. 53A, the pure Ni control suffered strong deactivation, becoming totally inactive after ~70 h.

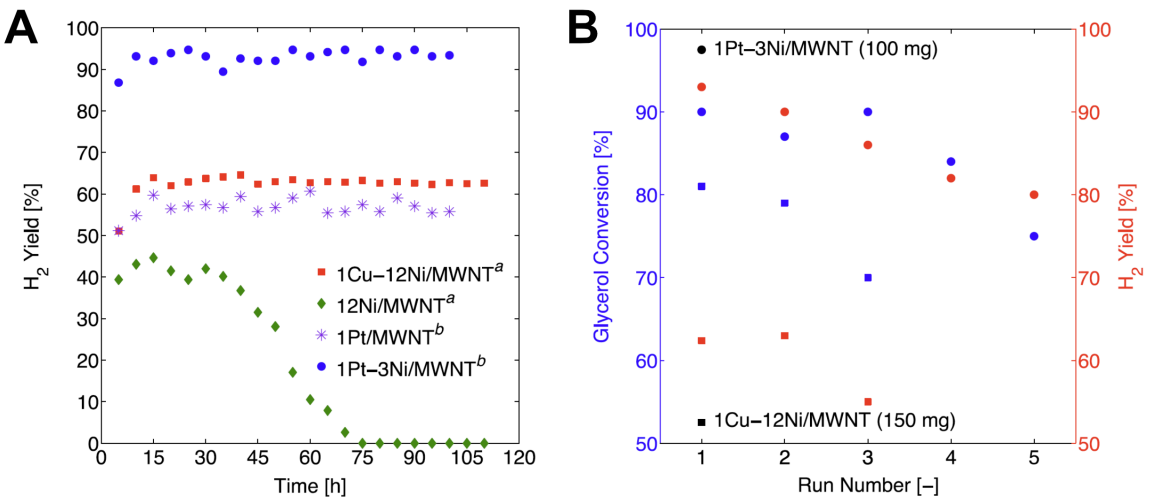


**Fig. 53.** Stability of the most active carbon MWNT-supported catalysts in glycerol APR. **(A)** Single tests over 100 h [**a** 1Cu-12Ni mcat = 150 mg **b** 1Pt-3Ni mcat = 100 mg]. **(B)** Repeated (x5) testing (each run = 100 h with intermediate Ar purge). Reaction conditions: 240°C, 40 bar, 1% glycerol, feed rate = 0.05 ml/min (WHSV = 20-30 $h^{-1}$). [Reproduced with permission from ref. 536].

This recurring pattern, seen in both SR and APR, i.e., under wide-ranging testing environments, almost certainly originates via different mechanisms specific to each. Ni in SR suffers primarily from sintering, i.e., migration of atoms and nanoclusters as metallic species at the high temperatures involved [537]. In contrast, *van Haasterecht et al.* [538] have convincingly shown that a similar mechanism, i.e., sintering via *Ostwald ripening* (growth in larger particles at the expense of small ones), is operative in EGAPR, a surprising result in view of the mild conditions associated with the process. In this case, Ni migrates between particles in soluble oxidised form as $Ni^{2+}$, its formation promoted by the prevailing acidic aqueous liquid environment (aqueous oxygenates under conversion *in-situ* have a pH ≈ 3.5).

Their Ni-on-carbon nanofiber (12.5%Ni/CNF) catalyst deactivated under typical APR conditions (10% EG, 230 °C, 29 bar/Ar purge) over 50 h, losing 93% of its peak activity (~11

mmol $H_2$ $g_{cat}^{-1}h^{-1}$ after 2 h). This was correlated with a proportionate drop in active metal area (91% by $H_2$ chemisorption) in the spent form due to sintering, viz., particle growth from 8 to 58 nm as estimated by TEM and XRD line broadening. This dissolution/re-deposition mechanism under typical APR conditions could be fully suppressed by operating at pH ≈ 8 by KOH addition, after which a steady evolution rate of 26 mmol $H_2$ $g_{cat}^{-1}h^{-1}$ at 99% selectivity was maintained for 10h. It is unclear why this effective remedy via low alkali addition was not proposed by the authors as a practical solution to deactivation of Ni APR catalysts. A similar deactivation profile for $Ni/Al_2O_3$ (derived from a spinel) in glycerol APR, accompanied by high particle growth (10 → 45 nm), was reported more recently but with no suggestions for improving sintering resistance [539]. The Ni/MWT-based bimetallic catalysts reported by *Rahman* [536] as discussed above, showed good resistance to particle growth (10 → 13 nm) probably via alloying effects, Cu and Pt stabilising the Ni against attack by acid, chemical oxidation and dissolution.

Separate studies on Ni-Cu and Pt-Cu bimetallic catalysts prepared from hydrotalcite Mg/Al (LDH) precursors have shown that inclusion of Cu results in various beneficial effects. For example, glycerol conversion on 5Ni1Cu and 10Ni1Cu reached 100% at 270°C [540], with $H_2$ production rates of ~25 mmol $g_{cat}^{-1}h^{-1}$, $S_{H2}$ ≈ 40%, and $S_{CH4}$ ≈ 2.5%. These high rates may have been due to the high initial dispersion induced by Cu ($d_{NiCu}$ = 6.5-7.7 nm, $d_{Ni}$ = 12 nm). Activities remained stable for 6h despite a modest degree of sintering in the spent form ($d_{NiCu}$ ≈ 20 nm). Partial alloy formation in a 0.9%Pt0.4%Cu/Mg(Al)O sample, as verified by EXAFS spectroscopy [541], may have been responsible for its raised selectivity to hydrogen ($S_{H2}$ = 55.3%) and lowered selectivity to methane ($S_{CH4}$ = 1.9%) in glycerol APR at 220°C.

While the foregoing section deals with pure glycerol in laboratory testing, any technical process for $H_2$ production must be based on crude glycerol feedstock, i.e., the by-product from the biodiesel (FAME) process, typically contaminated by alkali, methanol, mineral and fatty

2812 acid salts. This avoids the expensive purification steps otherwise necessary for value-added
2813 chemicals production. Unfortunately, studies dealing with direct conversion of crude glycerol
2814 are quite rare and the prospects do not look entirely positive. In a worst-case scenario, Boga et
2815 al. [542] found that certain impurities caused a dramatic fall in $H_2$ yield from 65 to 1% in 3 h
2816 batch tests of crude glycerol APR at 225°C (29 bar) over 1% $Pt/Al_2O_3$. Specifically, as revealed
2817 by TGA and ATR-IR, this was linked to more- or less-irreversible lay-down of sodium salts of
2818 oleic and/or stearic fatty acids over the catalytic sites. These "soaps", adjusted to < 2% in actual
2819 tests, were obtained by dilution from 16% as supplied by SK Innovations. Catalysts with higher
2820 Pt loadings or deposited on novel supports, e.g., 5% Pt/C and 1%Pt/Mg(Al)O [LDH-type] at
2821 similar dispersion (~3-4 nm), were more stable, reaching over 40 % crude glycerol conversion
2822 and nearly 20% $H_2$ yield, i.e., about one half the level obtained from pure glycerol. The
2823 absorption capacities (high internal surface areas and intercalation properties) of these supports
2824 were found to impede the access of long chain contaminants to the metal sites. Recognition of
2825 the importance of research into feedstock clean-up strategies involving the use of cheap high-
2826 capacity adsorbents, e.g., bio-chars, is a positive indicator [491]. Interestingly, the selectivity
2827 to liquid products, especially lactic acid (possibly via pyruvaldehyde) and propylene glycol
2828 (1,2-propanediol), reached high (> 10%) levels in the early stages of exposure to crude and pure
2829 glycerol, respectively.

2830 A similar one-pot (batch) reactor study reported by Seretis and Tsiakaras [543] involved
2831 reforming and hydrogenolysis (by $H_2$ generated *in-situ*) in crude glycerol over 65% $Ni\text{-}SiO_2\text{-}$
2832 $Al_2O_3$ catalyst from 200-240°C and with varying glycerol concentration (10-40%) but at fixed
2833 catalyst mass/glycerol ratio (1:4). Higher temperatures and lower glycerol concentrations
2834 favoured slightly gas production (35-45%, mainly $CO_2$), but conversion to liquid products
2835 (propylene glycol, ethanol, acetol, etc.) was predominant. $H_2$ levels were always low (<10%)
2836 and generally below those of $CH_4$. Little difference was seen between the conversion of both

pure and crude forms after 4 h (>90% at 240°C) from 20% glycerol solution, suggesting no clear disadvantage was incurred by utilisation of the latter. However, unlike in the study of Boga et al. [542], the more pernicious "soaps" encountered were seemingly absent in the study based here on a Cargill-Dow product [543]. Thus, variation in the quality of crude glycerol deriving from current practices in biodiesel production will clearly be a major factor in proper benchmarking into the effects (and selective mitigation) of the most deleterious impurities.

It is regrettable but true that remarkably little research on glycerol reforming has been done at a fundamental level to investigate kinetics and mechanism. Without a rate equation, no serious engineering of a scaled-up process is possible. The few apparent activation energies ($E_a$) documented pertain almost entirely to steam-reforming [313] and, to the knowledge of these authors, the only value relevant to glycerol APR is a statement in early work by the Dumesic group "*The rate increases with increasing temperature from 573 to 623K (with an activation energy of about 70 kJmol$^{-1}$)"* [505]. This is a lamentable situation in view of the fact that empirically-determined kinetic parameters are urgently needed to act as benchmarks for those estimated with increasing accuracy and reliability by first principles (DFT) calculation.

Indeed, the high value placed on glycerol as a renewable feedstock, whose molecular complexity lies on the edge of what is feasible (cost-efficient) with modern computing power incentivises its modelling and has led to significant advances in the last decade. Studies by surface science have convincingly shown that the similarity in reforming activity of glycerol with those of simpler analogues, ethylene glycol and ethanol, over Ni-Pt bimetallic alloys is indicative of parallel mechanistic steps and generic intermediates [522]. As shown in Fig. 55A-a, $H_2$ is desorbed from the Ni-terminated cluster in two main stages and in similar amounts. The first stage involves $H_2$ alone and is shared by all oxygenates near 370 K (~100°C), whereas the 2$^{nd}$ evolution peak near 425 K (150°C) is closely followed by CO at 429K (~155°C) as seen in Fig. 54A-b. This suggests that reforming proper is preceded by an initial stage of pure

dehydrogenation. The measured reforming yield is in the order Ni-Pt-Pt > Pt > Pt-Ni-Pt and correlates with the shift in the d-band centre to higher energy due to alloying (see Fig. 54B).

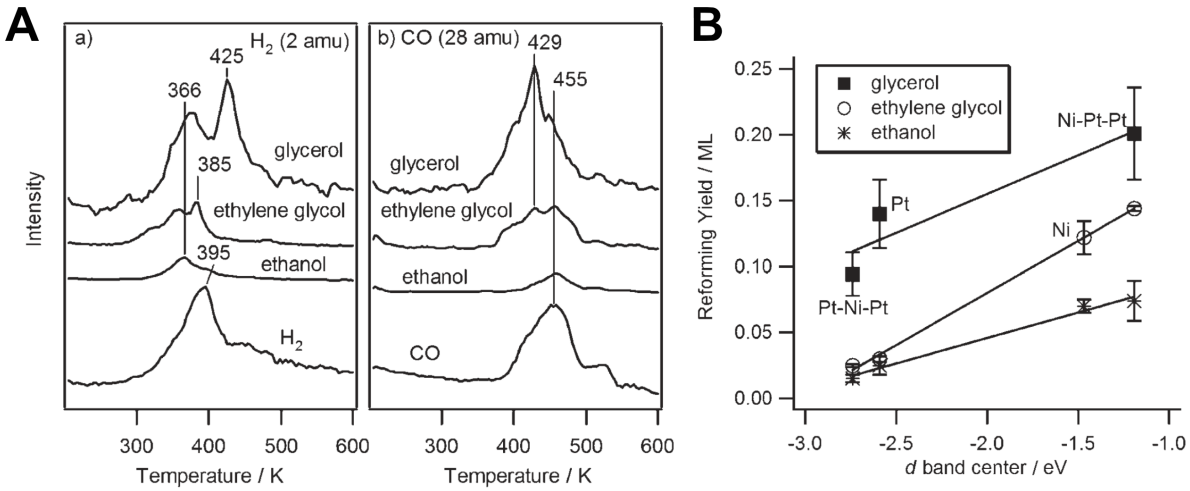


**Fig. 54 (A)** TPD spectra of **a.** $H_2$ and **b.** CO after exposure of Ni-Pt-Pt to glycerol, ethylene glycol, ethanol, and $H_2$/CO. **(B)** Effect of d-band centre shifts in Ni-Pt due to alloying on the reforming yield. [Reproduced with permission from ref. 522].

Consistent with this pattern, DFT modelling of the pure metals shows that the lowest-energy intermediates on Pt (as shown by the black squares in Fig. 55) derive from successive steps in dehydrogenation, the cleavage of C-H bonds being favoured over O-H bonds [544]. Fig. 56 also shows the transition state energies for these dehydrogenation steps (blue diamonds). Up until the empirical formula $C_3H_4O_3$ (CHOH-COH-COH), the energetics distinctly favour the order of bond cleavage C-H > O-H > C-C > C-O. Beyond this point C-C bond cleavage (with implicit CO evolution) is favoured. A similar pattern exists for Ni(111) except that the C-H/O-H dehydrogenation selectivity is mixed, driven by its greater O-affinity, and transition state energies for C-C bond cleavage straddle those for C-O. In the latter case, the resulting C adatoms would be expected to lead to hydrocarbons consistent with the known catalytic behaviour of Ni. It should be noted that the data for Ni and other metals (Pd, Rh, Cu) in this work by Liu & Greeley [544] were obtained by applying scaling relations in the binding energy

calculations and combining these with Brønsted-Evans-Polanyi (BEP) correlation involving transition-state ($E_{TS}$) and final state ($E_{FS}$) energies. This is now standard practice in DFT work (to ease the calculational burden) and generally leads to values that lie within an acceptable error range, viz., a standard or absolute error of ± 0.10 eV.

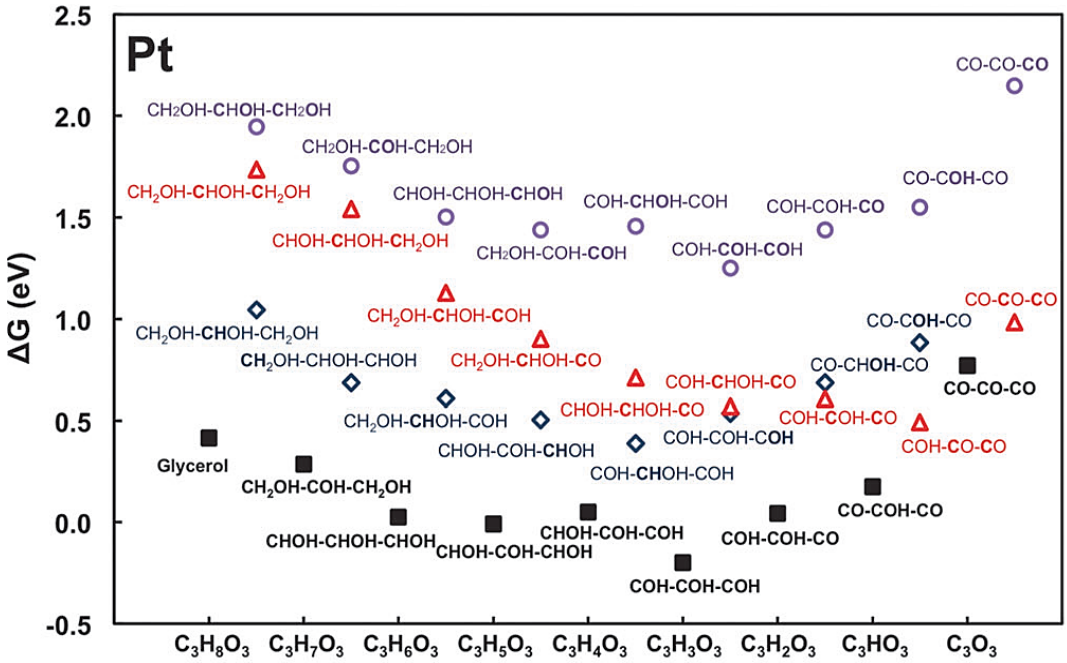


**Fig. 55** DFT-calculated free energies of adsorption at 210°C on Pt(111) for the most stable intermediates (black squares) from successive dehydrogenation of glycerol ($C_3H_8O_3$). Estimates of the C-H/O-H related transition state energies are also shown (blue diamonds) and compared with those for C-C (red triangles) and C-O bond cleavage (purple circles). [Reproduced with permission from ref. 544].

According to Sautet group [513], a similar accuracy results from using a databank based on 6 mono-alcohols (encompassing 29 elementary C-H and O-H dissociation steps) as linear BEP predictors of activation energies for early stage glycerol dehydrogenation, according to:

$$E_a = \alpha \Delta E + \beta \quad (46)$$

where the slope α is a measure of the "earliness" or "lateness" of the transition state, and ΔE is the reaction energy, i.e., the difference between the initial state and final state energies ($E_{IS}$ - $E_{FS}$). In follow up work [545], they were able to show that there is an inevitable trade-off between accuracy and universality in linear energy relations for alcohol dehydrogenation over a range of transition metals, including Co, Ni, Ru, Rh, Pd, Ir and Pt. Only the global BEP formulism accommodates effectively the full range of metal types and their relative oxophilicity.

Unfortunately, systematic errors are associated with the other popular approach, the so-called "transition state" scaling (TSS) model, which correlates $E_a$ directly with $E_{TS}$ and/ or $E_{IS}$. Here, the data for the individual metals must be incorporated to bring the error span within acceptable bounds. The strategy of trying to predict polyalcohol reactivity based on data input from a sub-set of simpler model compounds is a meritorious advance. However, this approach is made more challenging by the problem associated with intramolecular H-bond interactions in the complex molecule and any influence on adsorption geometries (steric confinement), and thence the energy of any related transition state. This has been simulated by introducing so-called mono-molecular "water-assisted" transitions and found to be sufficiently corrective in glycerol dehydrogenation, resulting in lowering or raising, respectively, of $E_a$ depending on which elementary step is involved (O-H or C-H bond scission) [546]. The former is facilitated by H-bonding interaction whereas the latter (transition state energy) is raised due to greater molecular rigidity in the adsorbed intermediate. Sufficient energetic distinction ($\Delta E_a^1 - \Delta E_a^2 >$ 0.12 eV) permitted a reasonably confident assignment that glycerol proceeds to glyceraldehyde over Pt via the intermediate enol, i.e., C-H scission (and rearrangement) is followed by O-H scission.

Recent work from the Getman group [547] has sought data more representative of APR conditions over Pt(111). By assessing the effect of liquid water, both as a solvent and reactant,

their work has corroborated much of the foregoing detail. As shown in Fig. 56, an aqueous environment has almost no effect on the activation energies in the early stages of dehydrogenation (via C-H bond scission) but disfavours significantly the onset of C-C cleavage (decarbonylation). When water is a co-reactant, activation energies ($E_a$) in dehydrogenation via C-H scission are drastically raised, most exceeding 1 eV [549]. In contrast, $E_a$ values for dehydrogenation via O-H scission are close to zero. Negligible barriers are associated with proton transfer reactions in liquid water [550]. Furthermore, according to microkinetic modelling water-mediated dehydrogenation via C-H scission in COH-COH-CHOH* is kinetically competitive with its non-water-mediated analogue. Subsequent O-H scission leads to almost barrier-less decarbonylation of CO-COH-COH*.

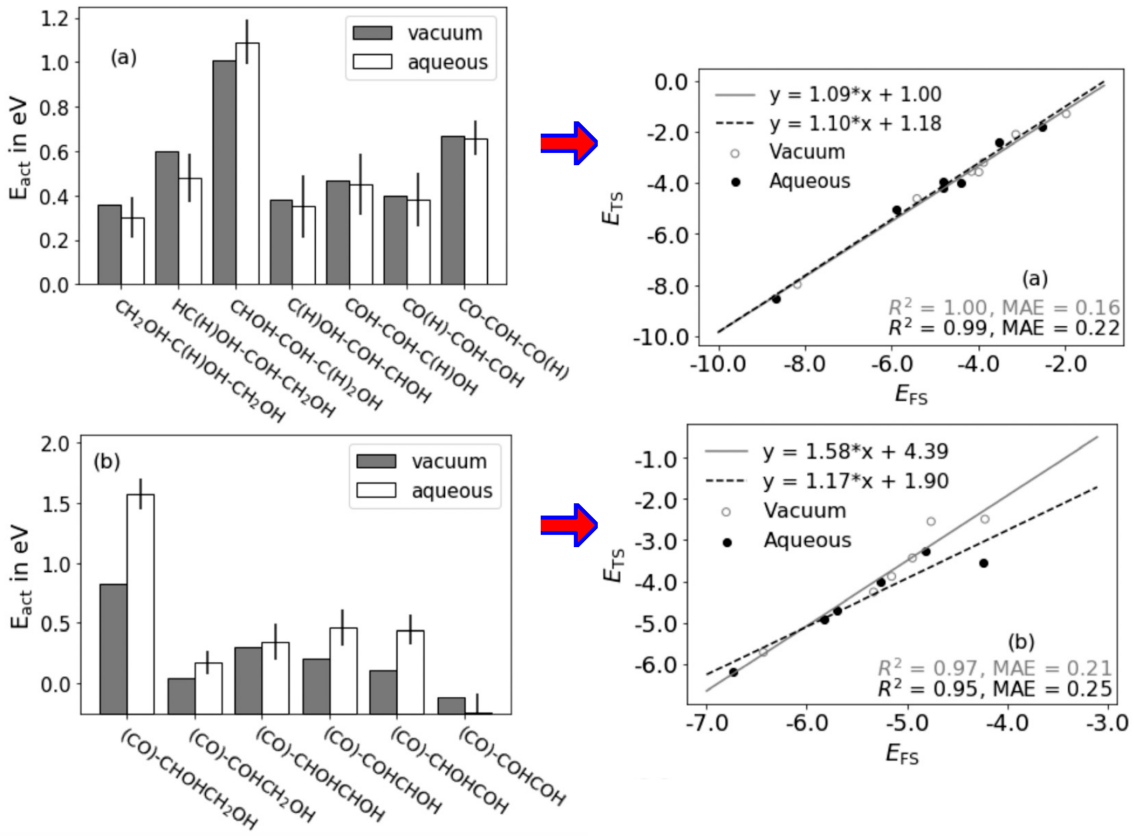

**Fig. 56. (Left)** Activation energies in vacuum vs. aqueous medium **(a)** in initial dehydrogenation (C-H scission) in glycerol, **(b)** later decarbonylation (C-C scission). Their corresponding transition-state-scaling (TSS) relationships are also shown **(Right)**. [Reproduced with permission from ref. 547].

Shan & Liu [548] have used density functional theory (DFT) to evaluate the solvent stabilisation energies of glycerol ($C_3H_8O_3$) adsorption on Pt(111), including its mono- and di-dehydrogenated intermediates $C_3H_7O_3$* and $C_3H_6O_3$* , due to the progressive build-up of water molecules and their evolving H-bonding network. As shown in Fig. 58, the first water molecule (n = 1) associates intimately with the adsorbate, resulting in a dramatic increase in binding energy (from -0.46 eV to -1.07 eV) as compared to the solvent-free (n = 0) case, most notably in glycerol itself (indicated by black stars) but clearly visible also in some of the mono-dehydrogenated intermediates (shown in red and blue triangles). After successive addition of more $H_2O$ (2 to 5), the stabilising effect is progressively weakened by the redistribution of H-bonding interactions away from glycerol and towards nearest neighbour water molecules. Under full solvation ($n_{H2O} \geq 5$), the binding energies of most intermediates converge towards -0.6 ± 0.2 eV. This thermodynamic "levelling effect" in the final state energies, and presumably also transition energy barriers, would seem to run counter to achieving desirable selectivity to a unique product under *kinetic* control, i.e., by suitable manipulation of catalyst properties and/or reaction conditions. This may also be a causal factor in the wide product distribution typically obtained under APR conditions.

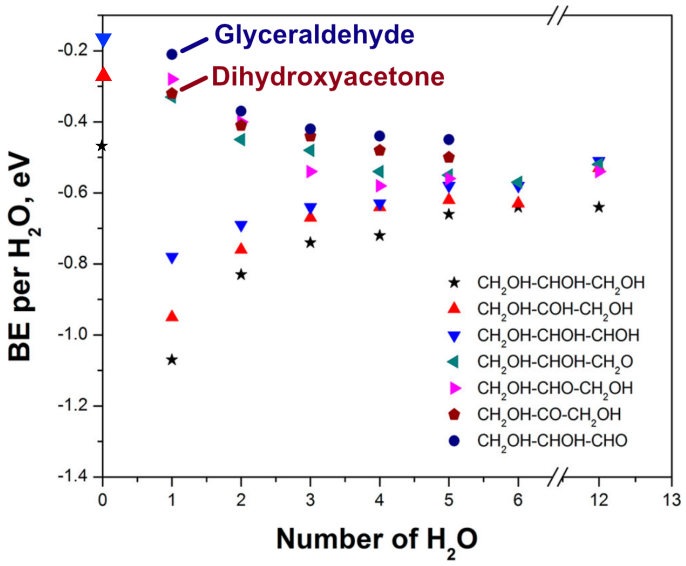


**Fig. 57** Trends in DFT-calculated binding energies for glycerol and selected $C_3H_7O_3$ and $C_3H_6O_3$ intermediates [$BE_{C3H8O3*(aq)}$] per added $H_2O$ molecule on Pt(111). [Adapted and reproduced with permission from ref. 643. Data points at $n_{H2O} = 0$ are taken from Table 3 in ref. 548]

As regards alternative *non-thermal* activation modes for glycerol, Valter et al. [551] have reported on the likely pathways for the 1st- and 2nd-step deprotonations for glycerol electro-oxidation (assuming proton-coupled electron transfer) over the close-packed surfaces of Pt, Ag, Pd, Ru, Ir, Rh, Cu, Ni, Co and Au. Using energy descriptors E($CH_3O$*) and E(*$CH_2OH$) as affinities for $O_{ads}$ and $C_{ads}$ respectively, the carbon-preferring binding order was determined as Cu < Co < Ag < Ni < Ru < Rh < Ir < Au < Pd < Pt. As shown in Fig. 58 (left in red), the first 5 metals Ru, Ni, Co, Cu and Ag prefer a transition via intermediate G1c (1st deprotonation at the central OH leading to an M-O bond), whereas Rh, Ir, Au, Pd and Pt prefer a route through intermediate G1a obtained by deprotonation at the central carbon to form a M-C bond. At the 2nd deprotonation stage, a greater range of intermediates becomes available. Alternation of C-H (G1a) and C-O scission (G2a1) leads to an isolable product dihydroxyacetone (DHA), favoured especially over Au and Ag, while the route for Ru, Rh and Ir still leads to DHA but

proceeds via the doubly (C- and O-) bonded intermediate G2a2. Pt and Pd are selective towards glyceraldehyde (GLYD, formally G2c1) via the double C-M bound intermediate G2b2 (propene, 1,2,3-triol), which has not been isolated but transforms into GLYD or DHA depending on solution pH. Co, Ni and Cu all prefer two successive (and adjacent) O-H bond scissions leading to a surface-bound O-M-M-O ring structure G2j, a tentative precursor to hydroxypyruvic acid (HPA, $C_3H_4O_4$) under alkaline conditions, although HPA is also an electro-oxidation product of DHA [552]. In nearly all cases, the theoretical potential (vs. the computational hydrogen electrode) is close to 0 V, as expected for this almost thermoneutral process [336]. However, in view of its proximity (within 0.3 V) to the onset potential of base metal oxidation/dissolution in acid, confirmatory experiments on Ni, Co, and Cu would need to be conducted at low overpotentials.

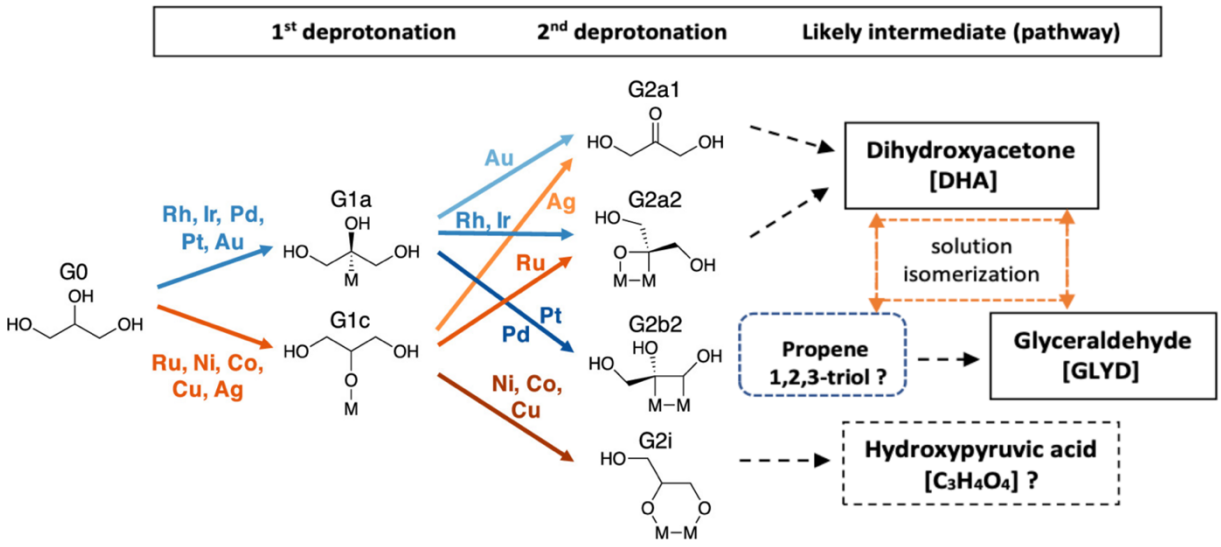


**Fig. 58** Thermodynamically favoured routes for the 1st and 2nd deprotonation steps (and likely intermediate pathways) over various close-packed transition metal surfaces. Blue colours

denote routes starting from deprotonation at carbon, and red-brown colour denotes deprotonation at oxygen. [Adapted and reproduced with permission from ref. 551].

Non-thermal (photo-, electro-) catalytic activation methods for glycerol reforming to $H_2$ and/or value-added liquid products have recently been reviewed [553-555], but there is insufficient scope to elaborate on the latter. While electro-oxidation of glycerol to $CO_2$ can yield up to $7H_2$ in principle (via full reforming - Reaction 41), the high overpotentials (> 1V vs. NHE) necessary to drive this complex (14 $e^-$ transfer) process renders any energy saving (vs. water electrolysis) marginal, and is restricted to the use of expensive rare metals [556,557]. Nonetheless, a case can still be made for coupling anodic partial reforming to value-added products with cathodic proton discharge. For example, hydroxypyruvic acid ($C_3H_4O_4$) or mesoxalic acid ($C_3H_2O_5$) could potentially yield 3 or 5 $H_2$ per glycerol molecule, respectively [557,558]. Base metals are good candidates to explore in crude glycerol electro-reforming due to adventitious alkali contamination (pH > 8) [538,559]. Alternatively, deliberate alkalization facilitates $CO_2$-free high-pressure $H_2$ recovery via the CAPER process [560].

In technique-oriented photocatalytic studies over $TiO_2$-supported noble metals, the Niemantsverdriet group at Synfuels China Tech. (Beijing) extended their earlier work on ethylene glycol (EG) to glycerol using *in-situ* FTIR-MS [561]. However, unlike for the $C_2$ diol [292], no evidence for coverage-dependent multiple degradation pathways was reported. Nevertheless, the greater complexity of the $C_3$ polyol resulted in low levels of $C_2$-$C_3$ liquid intermediates, including dihydroxyacetone, glycolaldehyde and formic acid (according to NMR), in addition to $H_2$ as main product. This affirmed earlier kinetic and mechanistic work by Panagiotopoulou et al. [562] showing that UV irradiation over $Pt/TiO_2$ converts glycerol to gas-phase products $H_2/CO_2$ in a 7/3 ratio (consistent with full reforming - see Reaction 41) via liquid-phase intermediates. Decomposition pathways were proposed initiated by

dehydrogenation (to glyceraldehyde) and/or dehydration (to acetol), the former route leading to glycolaldehyde via EG. Photo-scission of a C-C bond in glycerol by direct electron transfer is known to yield glycolaldehyde ($C_2H_4O_2$), formaldehyde ($CH_2O$) and $H_2$ as co-products, but only at high coverage on $TiO_2$ [563]. Furthermore, glycolaldehyde is known to photolyze to methanol and CO [564], while the reverse coupling reaction methanol-to-EG can be driven by visible light over $MoS_2$ nanofoam-modified CdS [565]. These are strong indications that a viable photo-route may exist in glycerol-to-methanol (GtM) conversion [41,288,566]. 1% Pd/$TiO_2$ ($d_{Pd} \approx 8$ nm) was substantially more active than Au/$TiO_2$ ($d_{Au} \approx 3$ nm), possibly linked to the more energetic d-band centre in Pd.

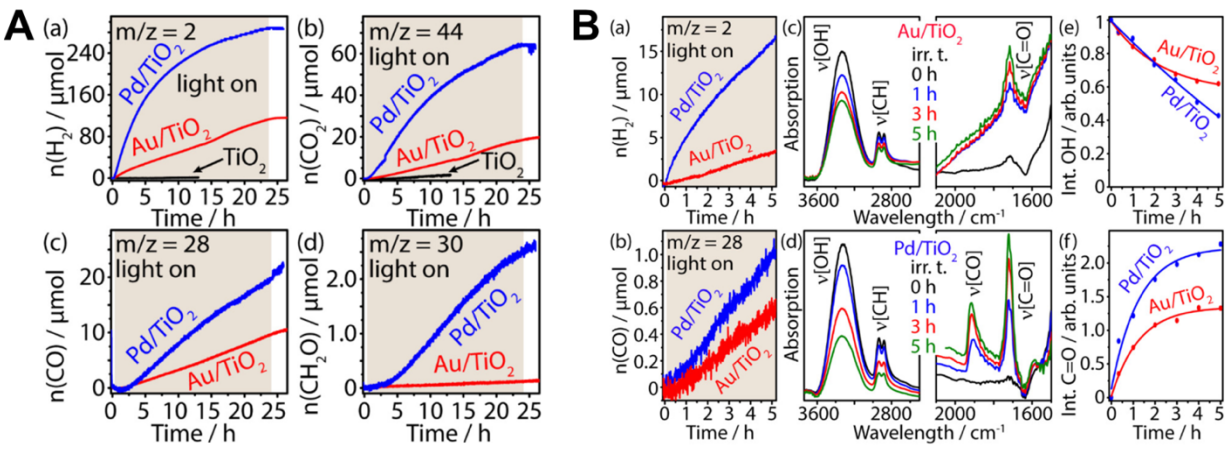


**Fig. 59 (A)** Gas products $H_2$, $CO_2$, CO, and HCHO (from glycerol) by QMS over Pd/$TiO_2$ and Au/$TiO_2$ under UV/24h ; **(B)** In-situ FTIR-MS of IR band development in the early stages (1-5h) of UV irradiation in the presence of glycerol. [Reproduced with permission from ref. 561]

Other clear but puzzling differences with EG were the evolution of significant levels of $CO_2$ and CO ($H_2$:$CO_2$:CO = 12:3:1), as shown in Fig. 59A. The main ($H_2$, $CO_2$) products reached plateau levels during 24h UV irradiation (LED @ 365 nm, 50 mW.cm$^{-2}$) indicative of 1$^{st}$ order kinetics. Apparent quantum efficiencies (AQE) for $H_2$ production were estimated at

1.4% and 0.6% for $Pd/TiO_2$ and $Au/TiO_2$, respectively. In this relatively inert testing environment, there are few mechanisms that could conceivably yield $CO_2$. Glycerol dehydration can lead to formic acid (produced by CO hydration) that could then back-equilibrate to $CO_2$ (and $H_2$) via the forward WGS reaction. CO disproportionation seems less likely since it implies the build-up of surface carbide leading to methanation, for which there is no evidence. In short (1-5 h) tests by *in-situ* FTIR-MS, a linear (zero-order) rate of consumption of glycerol might be concluded from Fig. 59B, as indicated by weakening of the $\nu_{OH}$ band at 3322 $cm^{-1}$. However, supporting studies by XPS clearly show that the main change in the O 1s contribution upon dosing glycerol in the dark is the growth of a surface hydroxyl ($O_H$) signal at 532.9 eV, especially over $Pd/TiO_2$. This is significantly stronger than the $O_C$ signal linked to intact glycerol at 531.5 eV and weakens under UV irradiation. In other words, glycerol dissociation occurs by routes involving O-H scission even in the dark, possibly promoted by adventitious water.

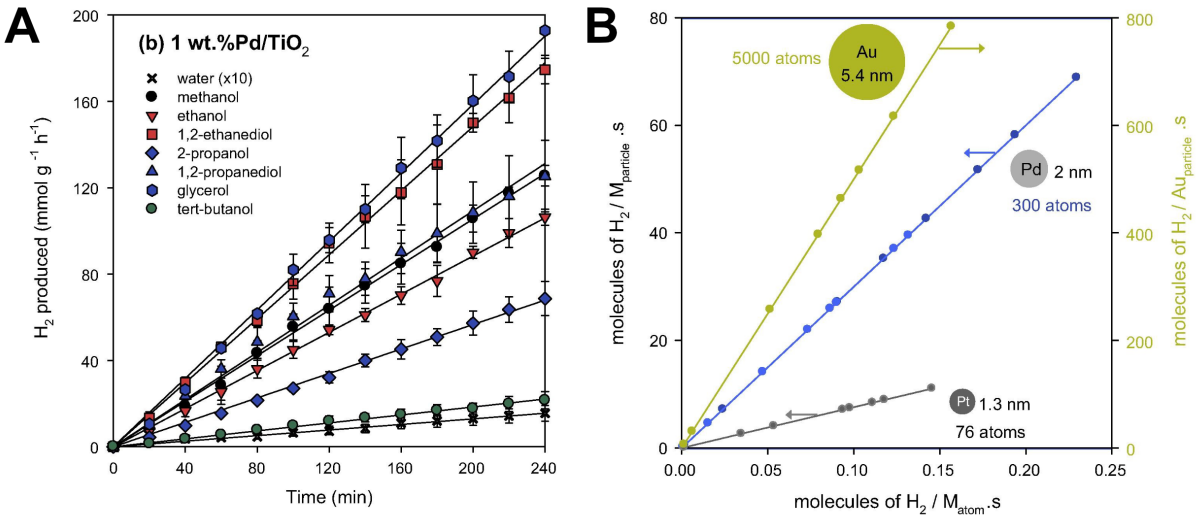


**Fig. 60 (A)** $H_2$ production from a range of alcohols (10%) over 1%$Pd/TiO_2$ under UV irradiation (5 mW.cm-2) ; **(B)** UV-driven $H_2$ production rate per metal particle vs. rate per

metal atom. Points are rate data for different alcohols. [Reproduced with permission from ref. 336]

Studies of photo-reforming proper i.e., in stoichiometric levels of water (see Reaction 41), by the Waterhouse group (Al-Azri et al. [336]) have shown that glycerol, among a wide range of simple alcohols and polyols, is the most reactive hole scavenger. This is consistent with previous spectroscopic and photocatalytic studies, showing that the efficiency of hole trapping in deaerated aqueous $TiO_2$ suspensions increases with the number of -CH(OH)- CH(OH) groups towards $C_5$-$C_6$ polyols and sugars [567,568]. For a metal loading of 1wt%, the order of activity in $H_2$ production was Pd > Pt > Au, with plots for Pd shown in Fig. 60A. To the knowledge of these authors, the measured rate for glycerol (47.5 mmol $H_2$ $g_{cat}^{-1}h^{-1}$ over 1% Pd) remains the highest yet recorded under a defined near-solar UV intensity of ~5 $mW.cm^{-2}$. As a perspective, the analogous sample of $Au/TiO_2$ gave a lower rate of 32.7 mmol $H_2$ $g_{cat}^{-1}h^{-1}$ but this still corresponded to a high quantum efficiency $\varphi \approx 0.43$ [409]. When the rates in Ref. 336 are re-plotted normalised per metal particle, the activity order changes to Au >> Pd > Pt, as seen in Fig. 60B. This re-emphasises the importance of the spatial distribution and size relation between noble metal nanoparticles. As in the case of Au, large particles ($d_{Au} \approx 5.4$ nm) widely spaced are just as effective per metal atom (or per unit mass) basis as small particles ($d_{Pt} \approx 1.3$ nm) with a low mean separation where overlapping zones of charge polarisation may become detrimental to photo-activity (see EPAO model in Fig. 26). Higher rates over noble metals have been claimed but in the absence of any stated value of optical exciting power, so that AQEs could not be estimated.

For example, Ribao et al. [569] have compared $H_2$ evolution rates from pure and crude glycerol over $TiO_2$ (P25) co-loaded with Pt and 3% reduced graphene oxide (rGO) to act as an electron shuttle. Rates of 70.8 ± 0.4 and 12.7 ± 0.2 mmol $H_2$ $g_{cat}^{-1}h^{-1}$ were obtained for pure and crude glycerol, respectively, the latter containing 3% salts and ashes. While these rates are

impressive, it is also fair to point out that an excessive (unrealistic) Pt loading of 3.8% was used. As regards earth-abundant resources, a range of base transition metals Cu, Co, Cr, Ag, and Ni were explored as co-catalysts deposited at 2 wt % on $TiO_2$ hollow spheres (THS) [570]. The order of activity (mmol.$g_{cat}^{-1}h^{-1}$) in $H_2$ evolution from 5% aqueous glycerol was found to be Cu (17) > Ag (6.4) > Co (1.9) > Ni (1.5) > Cr (0.6). This is not entirely consistent with other work showing that $TiO_2$-supported Cu and Ni are both active and promising earth-abundant co-catalysts, giving AQEs of $\varphi_{Cu} \approx 0.25$ and $\varphi_{Ni} \approx 0.37$ under near-solar UV irradiation [408,409].

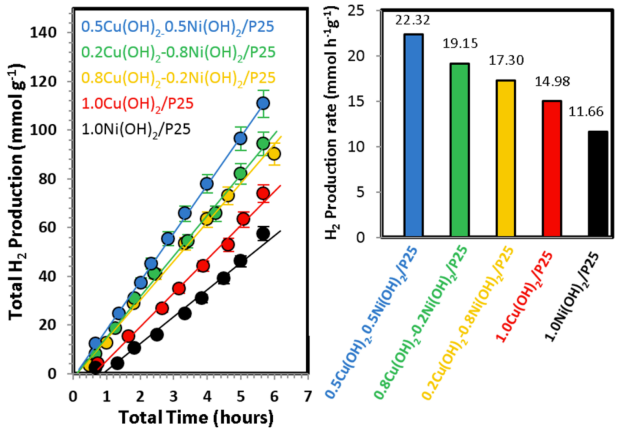


**Fig. 61** UV-driven $H_2$ evolution rates from glycerol (5%) over bimetallic 1%Cu/Ni/$TiO_2$ (P25) in various metal ratios [reproduced with permission from ref. 571]

A synergy was also reported between Cu and Ni in $H_2$ evolution from 5% aqueous glycerol [571]. As seen in Fig. 61, the rate was highest (22.3 mmol.$g_{cat}^{-1}h^{-1}$) for a mixed sample of uncalcined 0.5%$Cu(OH)_2$-0.5%$Ni(OH)_2$ /$TiO_2$ (P25). Reduction of $Cu(OH)_2$ to $Cu^0$ is assumed to proceed under UV excitation *in-situ* as the redox potential ($E^0$ = -0.22 V) is less negative than the conduction band potential of anatase ($E^0$ = -0.26 V). An induction period was also observed and attributed to a slower indirect reduction of $Ni(OH)_2$, via dissolution as $Ni^{2+}$ followed by photo-deposition as $Ni^0$, possibly leading to Cu/Ni alloy formation.

Similar beneficial alloying effects in ethanol photo-reforming have already been described [465,468,469]. However, although the metallic state of Cu and Ni is deemed essential to provide Schottky-type barriers (for electron trapping, proton discharge, $H_2$ evolution) and visible-light sensitization (plasmonic $Cu^0$), the oxide forms of these elements and can also act as photo-active species through other mechanisms. For example, CuO and $Cu_2O$ have narrow (visible-responsive) bandgaps [101,406], and along with NiO they are all p-type semiconductors and valuable co-catalysts for hindering charge recombination via the resulting p-n (type II) junction created on n-$TiO_2$ [463, 572].

Unfortunately, the limited energetic range for copper redox couples often leads to co-existence of oxidation states, e.g., via $Cu^+$ ($Cu_2O$) disproportionation [571,573]. These are difficult to distinguish and quantify without careful instrumental analysis [463,484]. In addition, induction periods (prior to $H_2$ evolution) and fluctuating photo-reforming rates are symptomatic of the *in-situ* dynamics of chemical response in $CuO_x/TiO_2$ [406]. *Petala et al.* [574] found $CO_2$ evolution, i.e., full photo-reforming of glycerol, to proceed immediately over nano-dispersed CuO on $TiO_2$ whereas the associated photoelectrons were not available for proton discharge, being sufficiently energetic to initially convert CuO to $Cu_2O$ preferentially. As shown in Fig. 62A, the delay in $H_2$ evolution extended for up to 2h with increasing Cu loading suggesting its origin in sample pre-conditioning. However, at a certain point, the loss of CuO (and its related photo-oxidation function) resulted in a drop in $CO_2$ evolution (see Fig. 62B) while the intrinsic instability of $Cu_2O$, reactive with electrons (to $Cu^0$) and/or holes (back to CuO) led to recovery of $CO_2$ evolution and stabilisation of $H_2$ evolution at a rate dependent on the instantaneous levels of $Cu_2O$ and Cu.

Among the highest $H_2$ evolution rates obtained to date over $CuO_x/TiO_2$, several exploit graphene (rGO) as an electron shuttle and to hinder charge recombination. After optimisation of co-catalyst loadings at 0.5% Cu and 4% rGO on $TiO_2$ hollow spheres, Seadira et al. [575]

reported a $H_2$ evolution rate of 37 mmol.$g_{cat}^{-1}h^{-1}$. More impressive still, Babu et al. [576] found a rate of 111 mmol.$g_{cat}^{-1}h^{-1}$ over a $Cu_2O$-rGO/$TiO_2$ nanocomposite, stable over 4 successive 2h test cycles. While this exceeded the performance of the best noble-metal based photocatalysts [336,409], the level of (absorbable) optical power and/or estimates for AQEs were unfortunately not stated. The influence of co-catalyst loadings on performance is shown in Figs. 63, eventually optimised at 1% Cu, 3% rGO.

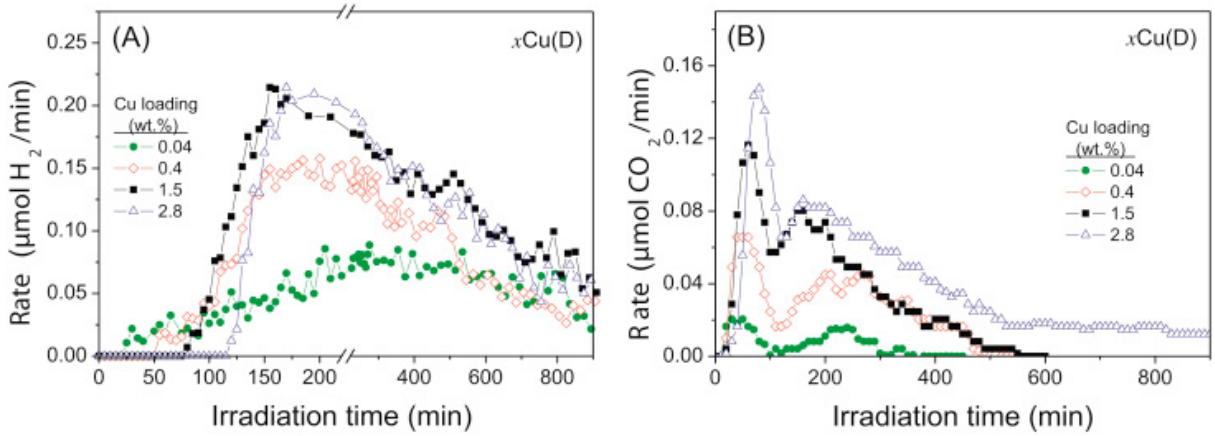


**Fig. 62** Induction in $H_2$ evolution **(A)**, oscillating $CO_2$ evolution rate in glycerol photo-reforming **(B)**, and effect of Cu loading in $CuO_x/TiO_2$. [reproduced with permission from ref. 574]

Elsewhere, Trang et al. [577] made a composite of 1.5% $Cu_2O$ on $TiO_2$ nanotubes that reached a $H_2$ evolution rate of 48 mmol.$g_{cat}^{-1}h^{-1}$ under natural sunlight, suggesting that unusual structural forms of $TiO_2$ are important. As regards the p-n heterojunction between NiO and $TiO_2$, upward band-bending facilitates vectorial charge separation. Photoexcited electrons in NiO migrate into the lower energy conduction band of $TiO_2$ while highly-energetic (oxidising) holes from $TiO_2$ transfer to the less positive valence band in NiO. However, unlike $Cu_2O$, which has a narrow bandgap ($E_g$ = 2.0 eV) capable of visible sensitization ( $\lambda_{max} \approx 500$ nm), the wide

bandgap in NiO ($E_g$ = 3.4 eV) only allows UV-driven photoexcitation. Nevertheless, a weak visible-driven electron transfer from the NiO valence band to the $TiO_2$ conduction band occurs depending on the contact area and spacing of the nanoparticle interface [572,578].

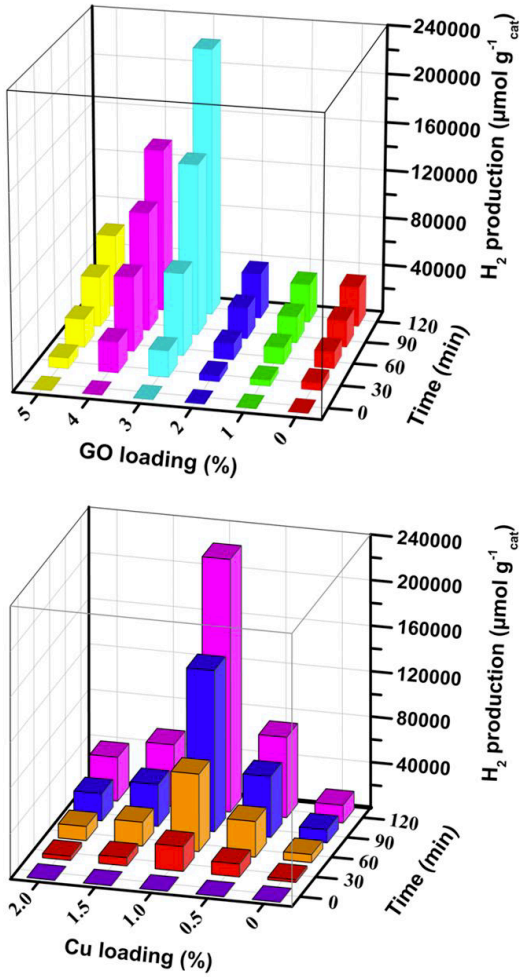


**Fig. 63. (top)** Effect of graphene loading on 1% $Pt/TiO_2$ ; **(down)** Effect of Cu loading on 3% $rGO/TiO_2$ [reproduced with permission from ref. 576]

Reddy et al. [579] prepared $TiO_2$ nanotubes loaded with 2% NiO quantum dots of 8.4 nm size and found $H_2$ evolution rates of 45.6 and 4.7 $mmol.g_{cat}^{-1}h^{-1}$ from pure and crude glycerol, respectively. The first corresponded to an AQE of 15%. Gao et al. [580] reported interesting

work based on a photo-thermal synergy in $H_2$ production from 20% glycerol and contemporaneous (localised) steam evaporation from seawater over $SiO_2$/Ag@$TiO_2$ core-shell nanocomposites under natural sunlight focussed into the base of a top-insulated quartz tube. The field test temperature attained 100 °C due to broadband visible absorption by the $SiO_2$-dispersed Ag deposit, and evolved $H_2$ at 13.3 mmol. $g_{cat}^{-1}h^{-1}$ at the Ag/$TiO_2$ interface. Figs. 64 show the broadened and intensified visible-NIR absorption spectrum of the $SiO_2$/Ag combination, relative to isolated Ag nanoparticles, and the superior photo-thermal response of glycerol over methanol, ethylene glycol and glucose.

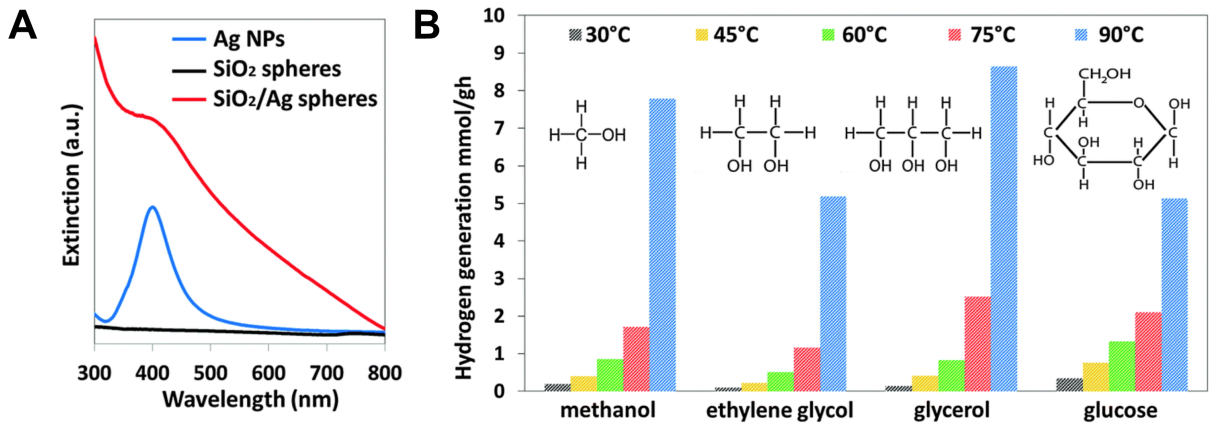


**Fig. 64 (A)** Absorption spectrum of Ag dispersed in $SiO_2$ ; **(B)** Photo-thermal response in $H_2$ evolution from glycerol, methanol, ethylene glycol and glucose solution. [reproduced with permission from ref. 580]

### *7.3.3 Acetic acid and bio-oil*

As reported earlier [308,309,581], bio-oil is a complex water-based mixture obtained from catalytic flash pyrolysis of raw biomass in the range 400-600°C. While its composition is highly variable depending on the feedstock and processing conditions, it largely consists of generic fractions of up to 30% organic acids, and 5-10% each of ketones, phenols, furans,

aldehydes, and alcohols [582]. Since the acidity (pH = 3.2) renders bio-oil impracticable for direct use as a renewable fuel, the pre-reforming of this corrosive low-heating-value mixture (HHV = 13.86 MJ/kg) takes on special significance. Acetic acid (AA) is a valuable model oxygenate, and is the simplest molecule containing the 5 main types of organic (CHO) chemical bond, viz., C-O, C-C, C-H, O-H and C=O. Furthermore, its chemistry occupies a key position in reaction networks for the reforming of a multitude of mono-ols and polyols (see Reactions 33-37, Fig. 32) [420,453,470]. While the H-content of AA is just 6.7 wt%, this is compensated by a high thermal recuperation factor in the vapour state, exceeding 30% due to its high endothermicity in steam reforming [583,584]:

$$CH_3COOH + 2\,H_2O \rightarrow 2\,CO_2 + 4\,H_2 \qquad (\Delta H^0 = +135\ kJ\ mol^{-1}) \qquad (46)$$

and reactions more favoured by thermodynamics intervene. These include dehydration to ketene [583] :

$$CH_3COOH \rightarrow CH_2C{=}O + H_2O \qquad (\Delta H^0 = +132\ kJ\ mol^{-1}) \qquad (47)$$

or, more readily, bimolecular ketonization to produce acetone [585] :

$$2CH_3COOH \rightarrow CH_3COCH_3 + CO_2 + H_2O \qquad (\Delta H^0 = +36\ kJ\ mol^{-1}) \qquad (48)$$

In a comparison between acetic acid, acetone and ethylene glycol as model oxygenates [583], decomposition leads in all cases to deposited carbon, reaching 33% in the case of acetone as shown in Fig. 65. Carbon-free operation is only assured above 600 K for high steam-to-fuel ratios of 3/1 and 6/1 for acetic acid and acetone, respectively. This suggests that simple C-C and O-H cleavage, (with C-H formation), i.e., decarboxylation to $CH_4$ [586] :

$H_3COOH \rightarrow CH_4 + CO_2$ ($\Delta H^0 = -8.6$ kJ mol$^{-1}$; $\Delta G^0 = -17$ kJ mol$^{-1}$) (49)

does not proceed exclusively even at low temperature. The basic mechanistic picture is that adsorbed acetate is converted to an acetyl species over noble metals (Pt, Pd, Rh) as depicted in Fig. 66. The left-hand route, proceeding via ketene and acetone also leads unsurprisingly to oligomers and coke, whereas the right-hand route involves decarbonylation and oxidative dehydrogenation of $*CH_3$ to $CO_2$ and $H_2$ (WGS) [587]. Even then, if water is not well-activated, undesirable results may follow. For example, $*CH_3$ may be released as $CH_4$ and/or progressively dehydrogenated to carbon over Pd (100) or Pd/Au(100) [588]. Avoidance or minimization of coke is not a trivial objective as oxides are well-known to be beneficial in water activation and WGS, e.g., $ZrO_2$ and $CeO_2$, also promote the ketene/ acetone route via fast abstraction of the acidic α-H, i.e., dissociative adsorption as acetate $*CH_3COO$. Only the close-packed (low-energy) surface planes of supported metals favour de-oxygenation, de-carbonylation and WGS, so a rigorous preparative approach is needed that promotes ease of reducibility of the metal to crystallites of intermediate size. These are mainly Ni or Ni-containing alloys with other base metals (Cr, Fe, Co, Cu) for economic reasons [587,589,590].

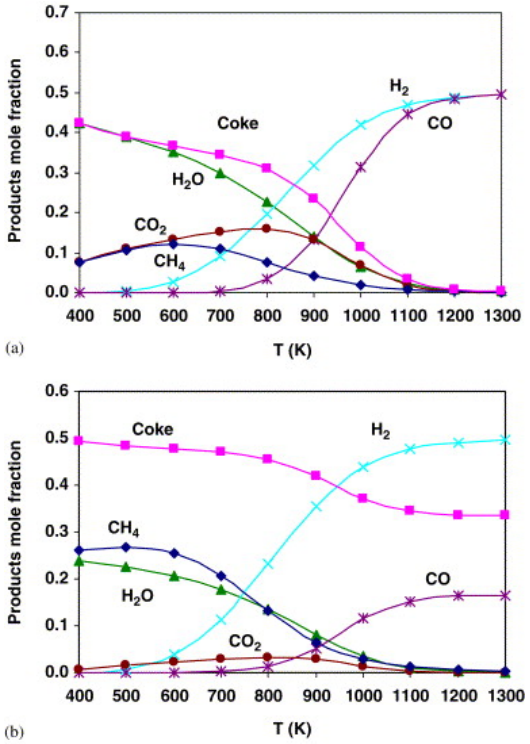


**Fig. 65** Thermodynamics of **(top)** acetic acid decomposition, and **(down)** acetone decomposition. [reproduced with permission from ref. 583]

Aiming for greater restriction of catalyst deactivation by metal sintering and coking, Luo et al. [591] explored an unusual support combination of two basic reducible oxides $CeO_2$ and ZnO. However, from catalyst testing in AASR (800°C, S/C = 3, WHSV = 5 $h^{-1}$), the only improvement over the Ce-free Ni/ZnO control was at a Ce:Zn mass ratio (CZMR) of 1:3. With an optimum Ni loading of 15%, yields of $H_2$ and CO were stable over 6h and raised from $Y_{H2}$ = 20.6 % to 73.5% and $Y_{CO}$ = 15% to 40%. The methane yield was also lowered significantly from $Y_{CH4}$ = 16.5% to 7% (or 3% of total gas composition).

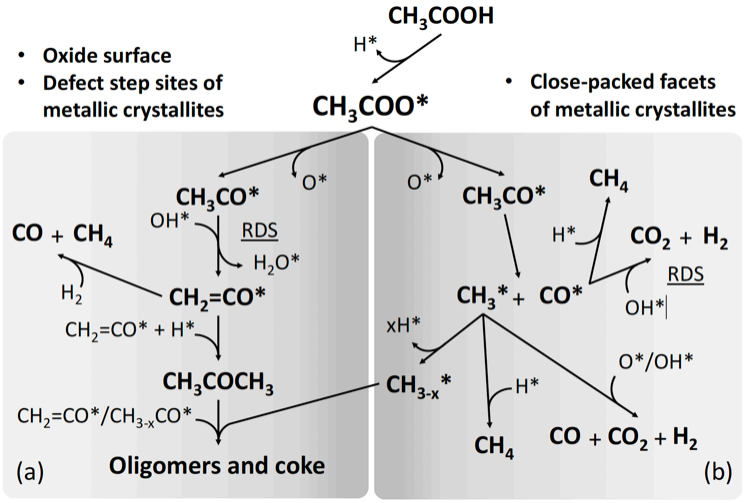


3232

3233

3234 **Fig. 66** Reaction mechanism in acetic acid reforming over noble metals. After adsorption of
3235 acetate, **(a)** dehydration leads to ketene, acetone, oligomers and coke; or **(b)** decarbonylation
3236 leads to $CH_3^*$ followed by H-abstraction and desorption as $CH_4$ or oxidative dehydrogenation
3237 of $CH_3^*$ (and CO) to $CO_2$ and $H_2$ (WGS). [Reproduced with permission from ref. 587]

3238

3239 However, the modest $CO_2$/CO ratio (1.3) suggested only limited WGS activity was
3240 achieved over the Ni/$CeO_2$ component. Hu et al. [592] have explored the multi-metallic Co-Cu-
3241 Zn(O) system where Co behaves like Ni, cleaving C-C and C-H bonds and serving as the main
3242 driver in AASR, while Cu/ZnO is the classic binary combination for methanol reforming and
3243 WGS. The importance of Co is shown in Fig. 67A, the ternary system reaching full conversion
3244 already by 350°C, with high selectivities to $H_2$ ($S_{H2}$ > 90%) and $CO_2$ ($S_{CO2}$ > 95%) and low
3245 selectivity to methane ($S_{CH4}$ < 5%). The high $CO_2$/CO ratio (>50) confirmed the effectiveness
3246 of Cu in WGS. As shown in Fig. 67B, the long-term stability of Co-Cu-Zn(O) 1:1:1 was
3247 excellent, conversion being maintained near 100% with only a slight decay in $S_{H2}$ and $S_{CO2}$ (90
3248 → 80%) during 100 h TOS. Wang et al. [593] have explored AASR over 15%Ni/$Ca_x Fe_y O$ (x/y
3249 = 2:1, 1:1, 1:2) in which iron oxide acts as a WGS catalyst while basic and reducible Ca/Fe

3250 mixed oxides ($Ca_2Fe_2O_5$, $CaFe_2O_4$) supply lattice O for carbon gasification. After pre-reduction

3251 at 800°C, the active metals identified by XRD were $Fe_{0.64}Ni_{0.36}$ and $FeNi_3$, both around 20 nm

3252 in size, and probably derived from a reducible $NiFe_2O_4$ intermediate.

3253

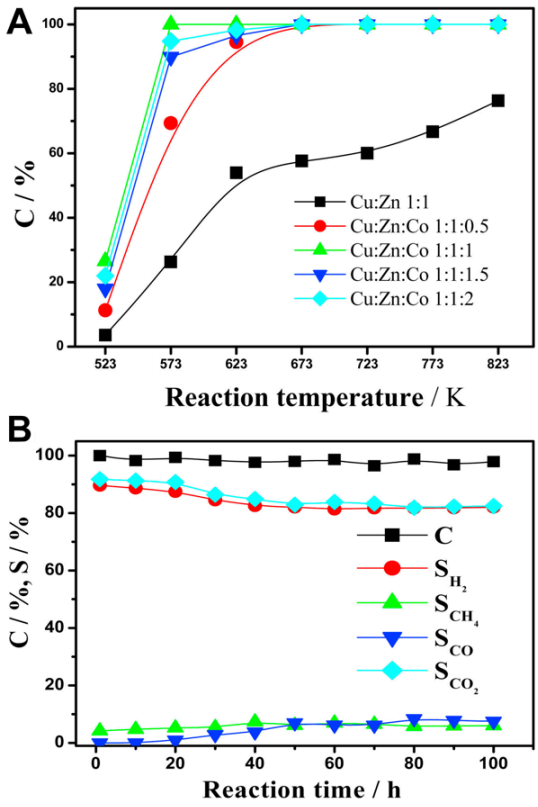


3254

3255 **Fig. 67 (A)** Activity of ternary Co-Cu-Zn(O) catalyst in acetic acid reforming (S/C = 7.5, LHSV

3256 = 5.1 $h^{-1}$) ; **(B)** Stability of Co-Cu-Zn(O) = 1:1:1 during 100 h TOS at 500°C (S/C = 7.5, LHSV

3257 = 5.1 $h^{-1}$) [reproduced with permission from ref. 592]

3258

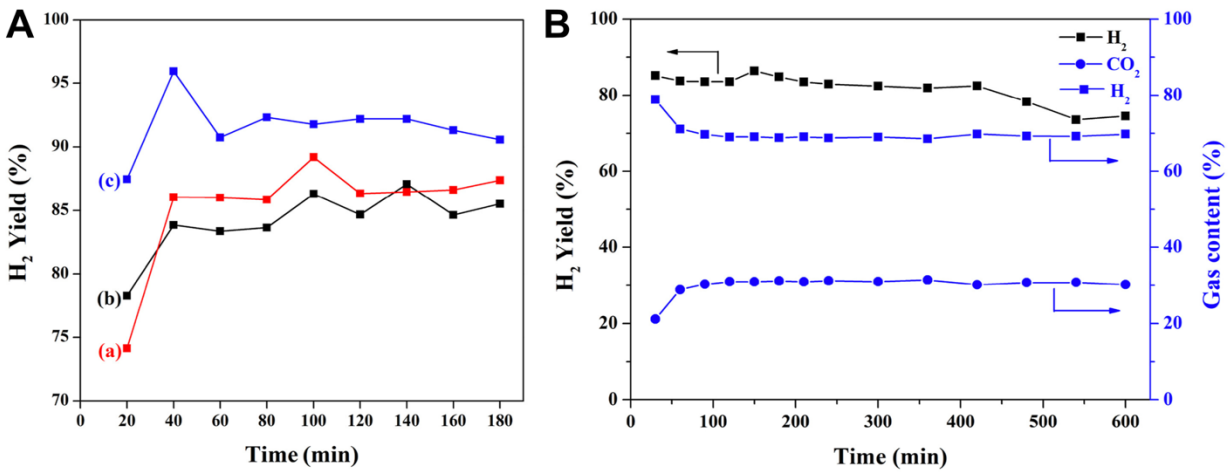


**Fig. 68 (A)** $H_2$ yield in AASR on (a) $Ni/Ca_2Fe_2O_5$-CaO, b) $Ni/Ca_2Fe_2O_5$, (c) $Ni/CaFe_2O_4$ ; **(B)** Stability test in AASR over $Ni/CaFe_2O_4$ during 10 h TOS (T = 600°C, S/C = 5, LHSV = 3.4 $h^{-1}$) [reproduced with permission from ref. 593]

As shown in Fig. 68A, $Ni/CaFe_2O_4$ was found to be the most active catalyst giving an initial $H_2$ yield of ~90% at 600°C. This was likely due to its better coking resistance, limited to just 0.1% carbon deposition (vs. 3.1% and 9.1% for $Ni/Ca_2Fe_2O_5$ and $Ni/Ca_2Fe_2O_5$-CaO, respectively, by TPO). In an extended stability test during 10 h TOS, $Y_{H2}$ fell only slightly to 76%, as shown in Fig. 68B. The gas composition was almost exclusively $H_2$ and $CO_2$ at 70% and 30%, respectively, with CO and $CH_4$ barely detectable.

In view of the aforementioned mixed benefits from the use of typical basic promoters like $La_2O_3$, $CeO_2$, $ZrO_2$, etc., nominally acidic oxides like niobia ($Nb_2O_5$) are now being more seriously explored, e.g., in methane SR [594]. Its value as a structural promoter in enhancing selectivity to higher hydrocarbons over Co-based Fischer-Tropsch catalysts is well-known [595]. Despite its Brönsted acidity, $Nb_2O_5$ actually moderates the Lewis acidity of any underlying $Al_2O_3$ layer and, being partially reducible, behaves like $TiO_2$ via the "decoration effect", leading to modification of adsorption properties and/or oxidation state of the underlying

metal. As reported above [493], niobia addition to Ni/ $Al_2O_3$ imparted extended stability in glycerol SR by its effects on Ni reducibility, improved sintering resistance, and restricted deposition of more pernicious coking forms. Menezes et al. [596] have explored a similar NiNbAl combination in n-butanol SR. This alcohol is considered to be a model compound, being the highest mono-ol component in bio-oil. While the level of coking was higher over NiNbAl than NiAl (82.6 % vs. 63.5%), the former was more active and stable, as shown in Fig. 69A, achieving full conversion (X =100%) at 500°C and maintaining higher gas conversion ($X_g$ = 80%) and $H_2$ yield ($Y_{H2}$ = 60%) during 30 h TOS. The presence of 10% $Nb_2O_5$ enabled full Ni reduction (99% vs. 90%), a higher dispersion ($d_{Ni}$ = 7.6 nm vs. 8.4 nm), and resulted in markedly lower acidity (185 vs. 460 µmol $NH_3$ $g_{cat}^{-1}$). As shown in Fig. 69B, the $CO_2$/CO ratio was high at ~15:1, indicative of good WGS activity. However, the increase in $CO_2$ yield over NiNbAl (60 → 80%), seemingly decoupled from any associated rise in $H_2$ yield, implied a growing supply of $CO_2$ from other sources. One possibility is coke burning linked to O supply from reducible $Nb_2O_5$.

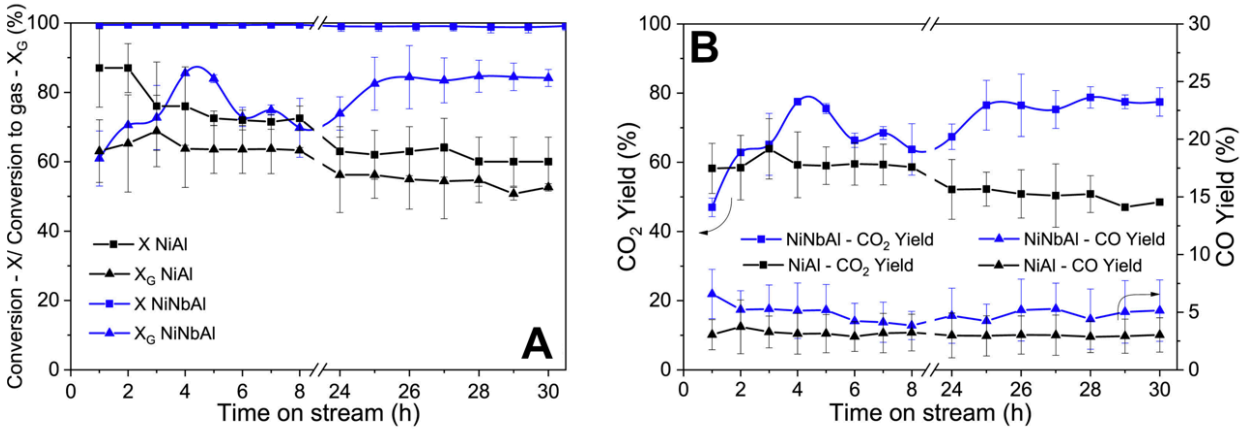

**Fig. 69 (A)** Stability in conversion (X) and gas production ($X_g$) in n-butanol SR over NiNbAl and NiAl at 500°C ; **(B)** $CO_2$ and CO yields over NiNbAl and NiAl during 30 h TOS at 500°C [reproduced with permission from ref. 596]

In terms of 1st-principles DFT modelling, mechanistic and microkinetics of bio-oil decomposition and steam-reforming, *acetic acid* has invariably been used as model compound. Nevertheless, it is important to distinguish data calculated for flat metal planes, e.g., Ni(111) [597], from stepped Co [598], and stepped Ni [599] surfaces. The latter are known to be more reactive and may open up alternative kinetic pathways due to their accommodation of a wider structural range of adsorbed intermediates and transition states. Acetic acid dissociation is uniquely favoured over Ni(111): $CH_3COOH^* \rightarrow CH_3COO^* + H^*$ ($E_a = 0.45$ eV - with the usual formalism "*" for the adsorbed species) while all other elementary processes have energy barriers exceeding 1.25 eV [597]. However, acetate is strongly-adsorbed and highly-stable versus dehydrogenation: $CH_3COO^* \rightarrow CH_2COO^* + H^*$ ($E_a = 4.48$ eV), suggesting entry to a kinetic *cul-de-sac* with quasi-equilibration. The next most favoured transition is deoxylation to an acyl species: $CH_3COO^* \rightarrow CH_3CO^* + O^*$ ($E_a = 1.29$ eV). Although thermodynamics favour decarboxylation of acetate (see Reaction 49), this has a high associated activation energy barrier ($E_a = 3.22$ eV) [597]. Thus, the acetyl species is a key intermediate in AA decomposition. Furthermore, over stepped metals it can be readily produced directly by dehydroxylation (C-O bond cleavage): $CH_3COOH^* \rightarrow CH_3CO^* + OH^*$ [$E_a = 0.45$ eV & 0.68 eV over Co [598], and Ni [599], respectively].

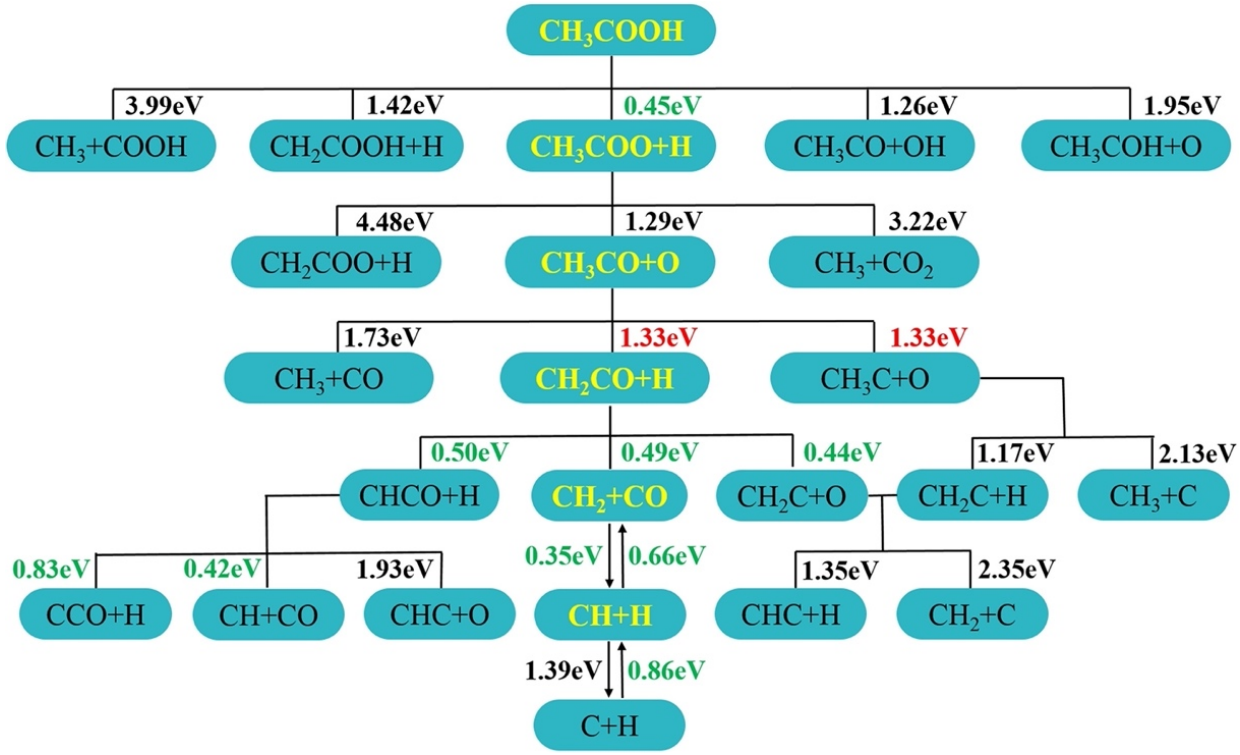


**Fig. 70.** Most likely decomposition scheme and intermediates (highlighted in yellow) for acetic acid over Ni(111) by DFT calculations. The numbers correspond to the activation energies. The activation energies below 1 eV are in green numbers. (RDS for acyl to ketene or ethylidene has same Ea - highlighted in red). (For interpretation of the references to colour in this figure legend, the reader is referred to the web version of this article.) [reproduced with permission from ref. 597]

As shown in Fig. 70 [highlighted in red as probable rate-determining steps (RDS)], the acetyl species on Ni(111) can either be dehydrogenated to ketene: $CH_3CO^* \rightarrow CH_2CO^* + H^*$ ($E_a$ = 1.33 eV) or deoxylated to ethylidyne: $CH_3CO^* \rightarrow CH_3C^* + O^*$ with low but even probability ($E_a$ = 1.33 eV). However, while ketene can be decarbonylated to hydrocarbonaceous ($CH_x$) residues: $CH_2CO^* \rightarrow CH_2^* + CO^* \rightarrow CH^* + H^*$ ($E_a$ = 0.49 eV), dehydrogenation or C-C

cleavage of the strongly adsorbed ethylidene is kinetically disfavoured ($E_a$ = 2.12 eV). It must be noted that both routes lead to carbyne species ($CH_x$* and $CH_3C$*) implicated in coking and deactivation in the absence of water.

Consistent with this basic mechanistic picture, surface science investigations by TPD/MS/HREELS did not detect any $CO_2$ during thermolysis of deuterated acetic acid ($CH_3COOD$) over Pt(111), resulting in complete decomposition by 220°C [600]. Desorption peaks at ~100°C (mass 2,3,4), 215°C (mass 28), and 220°C (mass 2) were attributed to loss of $H_2$/HD/$D_2$ from the acid carboxylate, decarbonylation, and loss of $H_2$ from the methyl group, respectively.

Water in the form of $OH^*$ has a promoter effect in the RDS of acetyl dehydrogenation by converting the abstracted $H^*$ to water according to: $CH_3CO^* + OH^* \rightarrow CH_2CO^* + H_2O^*$, thereby lowering $E_a$ from 1.33 to 1.18 eV [601]. An indirect benefit of such scavenging is the effective diversion of acetyl species, the most abundant reaction intermediate, from a pathway otherwise leading to acetone, an intermediate linked to coking: $CH_3CO^* + CH_3^* \rightarrow CH_3COCH_3^*$. Potential energy surfaces for the elimination of CH* by O* and OH* derived from water are shown in Fig. 71. The favoured route energetically is P4 (marked in red): $CH^* + OH^* \rightarrow CHOH^* \rightarrow CHO^* + H^* \rightarrow CO^* + H^*$ in which the initiatory step is the RDS with $E_a$ = 1.15 eV. CO* then enters the WGS conversion pathway, where $E_a$ for direct or indirect oxidation (to $CO_2$* or cis-COOH*, respectively) is quite high ($\geq$ 1.75 eV) and rate-determining for the overall process of acetic acid SR.

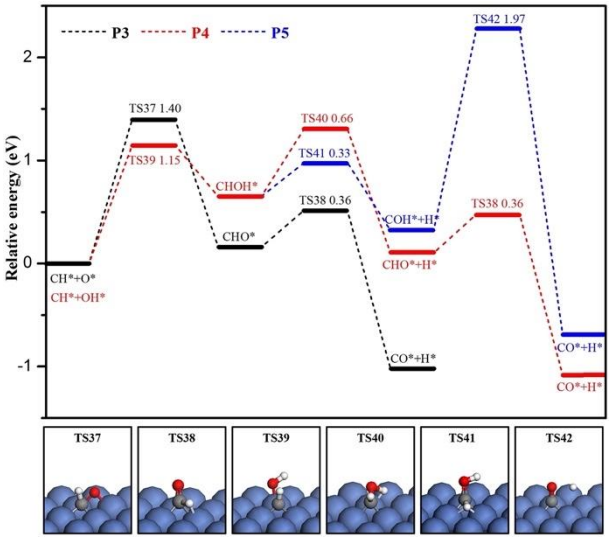


**Fig. 71** Potential energy surfaces and transition state (TS) configurations for CH* elimination by O* and OH* on Ni(111) [reproduced with permission from ref. 597]

Activation energies for elementary steps posing substantial kinetic barriers over flat surfaces can be dramatically lowered over stepped surfaces. Thus, dehydrogenation of acyl to ketene, otherwise the RDS over Ni(111), proceeds rapidly over stepped Co ($E_a$ = 0.52 eV) [598], or stepped Ni ($E_a$ = 0.34 eV) [599]. In addition, processes ordinarily subject to high energy penalties, e.g., those involving C-C and C-O bond cleavage, can become kinetically important at earlier stages in the mechanism. Thus, decarboxylation/decarbonylation over stepped Co can be initiatory: $CH_3COOH^* \rightarrow CH_3^* + COOH^*$ ($E_a$ = 0.85 eV), stage II: $CH_2COOH^* \rightarrow CH_2^* + COOH^*$ ($E_a$ = 0.82 eV), stage IIIa: $CH_2COO^* \rightarrow CH_2^* + CO_2^*$ ($E_a$ = 0.92 eV), or stage IIIb: $CH_3CO^* \rightarrow CH_3^* + CO^*$ ($E_a$ = 0.56 eV). The stage I process is of special interest in terms of the effect of metal dispersion on the process $CO_2 + CH_4 \rightarrow CH_3COOH$, i.e., the reverse of Reaction 49, serving to recycle $C_1$ intermediates via oxygenates in a process with 100% atom economy [602]. The view that ketonization:

$$2\ CH_3COOH \rightarrow CH_3COCH_3 + CO_2 + H_2O \quad (50)$$

leads to rapid coking is mechanistically complex insofar as acetone is itself a stable and volatile intermediate whose 1st dehydrogenation product $CH_3COCH_2$* is highly-resistant to subsequent breakdown even over stepped Co ($E_a$ > 1 eV for a range of C-C and C-H bond scissions).

In brief, there are four viable pathways for AA decomposition over stepped Co, with potential energy surfaces as shown in Fig. 72. The kinetically favoured pathway has the lowest activation energy as RDS. Thus, the formal sequence is P2 > P1 > P3 > P4. Nevertheless, with all $E_a$ values lying below 1 eV, this renders most pathways kinetically competitive. The potential energy surfaces in AA decomposition over stepped Ni [599] are similar to those over stepped Co [598]. However, while the two fastest RDSs over stepped Co involve C-H bond cleavage, 3 out of 4 kinetically favoured pathways over stepped Ni hinge on dehydroxylation. These RDS (not shown) occur at stage I (acetyl formation by direct dehydroxylation of the acid) slightly more readily for P1 and P2 ($E_a^1 = E_a^2 = 0.68$ eV) than for P4 at stage III $CH_2COO^* \rightarrow CHCOO^*$ ($E_a$ = 0.71 eV) or P3 at stage II $CH_2COOH^* \rightarrow CH_2CO^*$ ($E_a$ = 0.89 eV). The predominance of dehydroxylation is consistent with the known ability of stepped Ni to promote C-O bond scission [544].

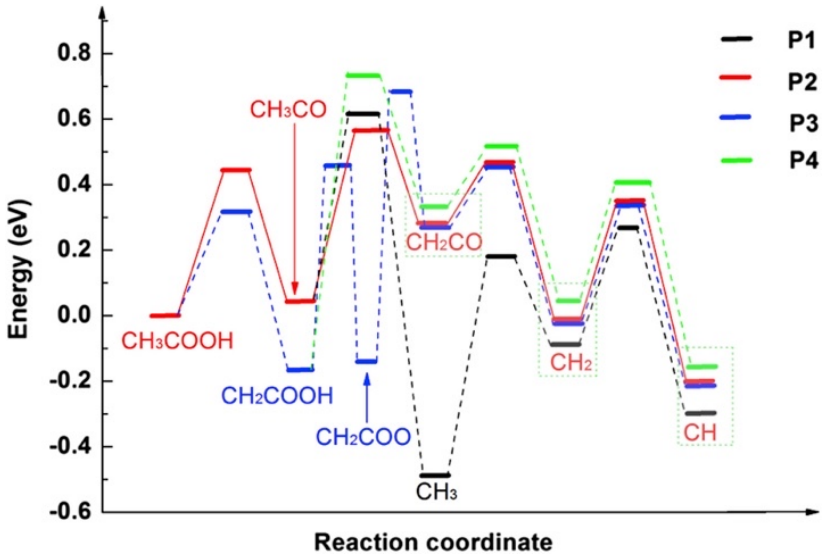


3385

3386

3387 P1: $CH_3COOH \xrightarrow{E_a=0.67\ eV\ (rds)} CH_3CO \rightarrow CH_3 \rightarrow CH_2 \rightarrow CH$

3388 P2: $CH_3COOH \rightarrow CH_3CO \xrightarrow{E_a=0.52\ eV\ (rds)} CH_2CO \rightarrow CH_2 \rightarrow CH$

3389 P3: $CH_3COOH \rightarrow CH_2COOH \xrightarrow{E_a=0.69\ eV\ (rds)} CH_2COO \rightarrow CH_2CO$

3390 P4: $CH_3COOH \rightarrow CH_2COOH \xrightarrow{E_a=0.90eV\ (rds)} CH_2CO \rightarrow CH_2 \rightarrow CH$

3391

3392 **Fig. 72.** Potential energy surfaces for acetic acid decomposition over stepped Co and the four
3393 kinetically relevant pathways. [reproduced with permission from ref. 598]

3394

3395 Despite the unclarities that remain in the aforementioned studies with acetic acid as a
3396 model compound, the added complexity of working with genuine bio-oils and/or proprietary
3397 mixtures relates primarily to catalyst coking and deactivation [603]. One of the most extensive
3398 studies made to date in identifying the key factors in deactivation of a Ni-$La_2O_3$/α-$Al_2O_3$
3399 catalyst and its relation with the properties and composition of deposited coke at different
3400 temperatures and S/C ratios for a typical bio-oil is that of Ochoa et al. [604] They used a two-
3401 stage process in which phenolics, likely sources of deactivating coke, were pre-deposited on-

3402 stream as pyrolytic lignin at 500°C, albeit perhaps incompletely [605,606], before SR proper in
3403 a fluidized bed reactor operating between 550 and 700°C. Unfortunately, the familiar pattern
3404 of rapid deactivation ensued at 550°C, conversion dropping to below X = 0.2 after just 4h, and
3405 hydrogen yield ($Y_{H2}$) reaching almost zero in the same time at S/C = 1.5. In contrast, at 700°C,
3406 conversion was maintained near X = 0.8 and $Y_{H2}$ near 40% under the same conditions.
3407 Furthermore, a significant contributor to deactivation at the higher temperature may have been
3408 Ni metal sintering, mean diameters roughly doubling from 7 to 15 nm. As shown in Fig. 73A,
3409 the level, location, and reactivity of deposited coke as determined by TPO was highly dependent
3410 on reactant composition, temperature, and S/C ratio. At 550°C, this was mainly of the
3411 encapsulating type (4:1) according to TEM and more readily combustible ($T_{max}$ = 400°C),
3412 whereas the coke deposited at 700°C, although similar in amount (9.9 wt%), was principally of
3413 the filamentous and graphitic type (19:1), only oxidising at much higher temperature ($T_{max}$ =
3414 600°C).
3415

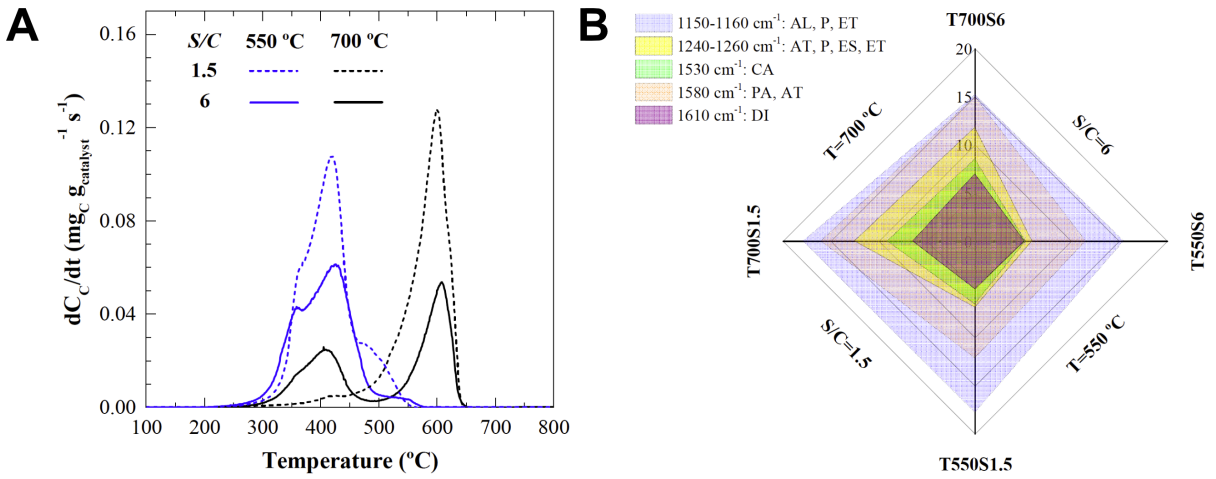

3416

3417 **Fig. 73 (A)** TPO of deposited coke from bio-oil SR over Ni-$La_2O_3$/α-$Al_2O_3$ ; **(B)** Effect of
3418 reaction conditions on principal IR functional group intensities present in deposited coke.
3419 [reproduced with permission from ref. 604]

As depicted in Fig. 73B, an IR functional group analysis of oxygenate structures within the coke deposited under a range of conditions was found to correlate with the balance of oxygenate products recovered in the reaction medium. Significant changes in respective components induced by heating were taken as provisional indicators of their severity in deactivation. For example, the coke band corresponding to aliphatics (AL), phenolics (P) and ethers (ET) at 1160-1150 $cm^{-1}$ (blue shading) was predominant at 550°C, making them likely sources of coke. In contrast, heating induced a growth in dienes (DI) at 1610 $cm^{-1}$ (purple) and polycondensed aromatic (PA) or "coke" bands (1580 $cm^{-1}$ – pink) suggestive of a more ordered and less reactive (filamentous) graphitic structure.

In a sensitivity analysis depicted in Fig. 74, the slopes show that relatively small changes in phenols and alkoxy levels caused strong assimilation of related structures into the (encapsulating) coke, whereas large changes in levels of carboxylic acids, ketones and aldehydes had lesser impact. A scheme summarising the effect of experimental conditions on key parameters in deactivation, viz., coke location, morphology and composition, is shown in Fig. 75.

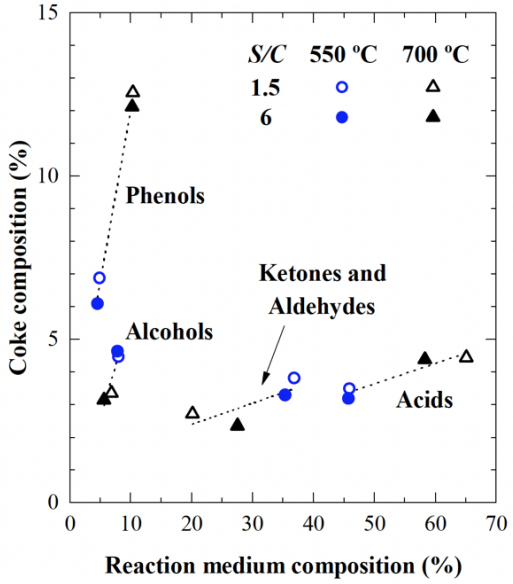

**Fig. 74** Sensitivity of oxygenated moieties in coke to changes in composition in the reaction medium during bio-oil SR. [reproduced with permission from ref. 604]

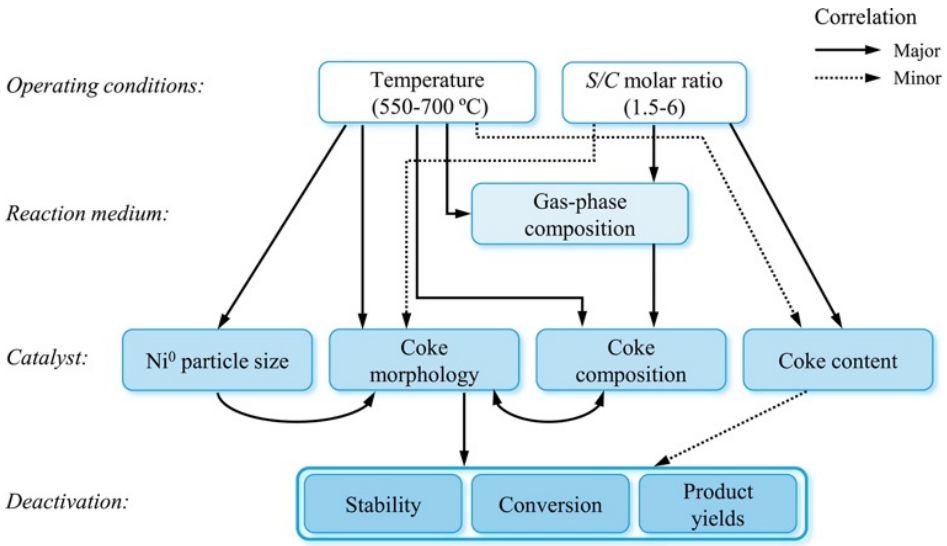


**Fig. 75** Deactivation scheme. Effect of temperature and S/C on coke morphology and composition [reproduced with permission from ref. 603]

An effective way to bypass issues of on-line stability and minimise coking is to work under mild conditions as facilitated by APR, photocatalytic and/or photo-thermal (dual) modes of excitation.

Early studies by the Dumesic group identified acetic acid (AA) as a common but essentially unreactive intermediate in ethanol, acetaldehyde, and ethylene glycol [470,476]. AA is also implicated in catalyst deactivation of $Al_2O_3$-supported Pt and Pt-Ni via $Al(OH)_x$ deposition [607]. This somewhat bleak outlook has been corroborated in more recent studies of bio-oil model compound conversion over Ni-based catalysts [608,609]. After 3h TOS, conversion ($X_{AA}$), $H_2$ evolution rate ($r_{H2}$), and $H_2$ yield ($Y_{H2}$) from a 10% aqueous AA solution over

Ni/La(Ce)/Al tri-component catalysts at 230°C were 3.5%, 1 mmol/$g_{cat}$/h, and 0.7%, respectively. These were much lower than the corresponding values for ethanol ($X_{AA}$ = 15%, $r_{H2}$ = 18 mmol/$g_{cat}$/h, $Y_{H2}$ = 12%). The corrosive (AA) environment also resulted in substantial (> 50%) leaching of Ni metal [608]. Acidification in most (neutral) oxygenate liquid reactants during APR (to pH ≈ 3.5) is virtually inevitable and attributed to build-up of carbonic acid (via $CO_2$ product dissolution and carboxylic acid by-products in situ. It is probably the root cause of frequent catalyst deactivation, e.g., by base metal oxidation and/or hydrothermal degradation of the oxide support. For example, it has been linked to drastic sintering of Ni (via a dissolution/re-deposition mechanism) during ethylene glycol conversion [538]. Related APR studies of bio-oil [609], tested as individual model compounds - 5% AA, 5% acetol, 5% n-butanol, over 10Ni-Co/20Al-5Mg found that AA was over an order of magnitude less active and the probable cause of deactivation in the synthetic mixture. AA conversions exceeding 90% in concentrated (25%) form have been achieved under supercritical conditions (400°C, 250 bar) over 10%Ru/CNT, but the selectivity to $H_2$ was below 20% [610]. Of the two main products, the selectivity to $CO_2$ (~60%) slightly exceeded that of $CH_4$ (35%), but these became closely similar under sub-critical conditions (T < 300°C). The predominance of AA decarboxylation was attributed to the activity of Ru in C-C bond cleavage.

Conversion of acetic acid (AA) via selective decarboxylation (C-C bond scission) yielding $CO_2$ and $CH_4$ in comparable amounts (see Reaction 49) is one example of a so-called "photo-Kolbe" process over Pt/$TiO_2$ originally reported by Kraeutler and Bard in 1978 [611]. Recent studies by Hamid et al. [612] have shown that the product distribution can be steered towards $H_2$ as co-product over Pt as co-catalyst by judicious adjustment of reactant concentration and pH. The photo-Kolbe mechanism is of the radical type [613] and involves the following sequence of elementary steps:

$$TiO_2 + h\nu \rightarrow TiO_2\,(h^+ + e^-) \quad (51)$$

$$TiO_2(h^+) + CH_3COOH \rightarrow TiO_2 + CH_3COO^\circ + H^+ \quad (52)$$

$$TiO_2(e^-) + H^+ \rightarrow TiO_2 + H^\circ \quad (53)$$

$$H^\circ + H^\circ \rightarrow H_2 \quad (54)$$

$$CH_3COO^\circ \rightarrow {}^\circ CH_3 + CO_2 \quad (55)$$

$$^\circ CH_3 + H^\circ \rightarrow CH_4 \quad (56)$$

$$^\circ CH_3 + {}^\circ CH_3 \rightarrow C_2H_6 \quad (57)$$

in which the product selectivity is governed by radical recombination, e.g., dimerization (to $H_2$, Reaction 54) and/or $C_2H_6$ (Reaction 57), or cross-recombination of $^\circ CH_3$ and $H^\circ$ to $CH_4$ (Reaction 56). In the last case, the overall balance corresponds to Reaction 49, a weakly exothermic process favoured by thermodynamics. Assuming that the carboxyl proton in AA acts as the sole source of H radicals leading exclusively to $CH_4$, the stoichiometric relation $CH_4/CO_2$ would be unity whereas it typically lies in the range 0.3-0.5 in acidic environment (pH = 2). On the other hand, complete H radical dimerization (Reaction 54) would lead to a $H_2/CO_2$ ratio = 0.5, which is closely approached or even exceeded (0.40-0.84). This mass imbalance in H can only be explained by assuming that the solvent water provides a significant number of protons for discharge via Reaction 53, a conclusion recently confirmed by studies of the product distribution obtained from deuterated reactants [613]. The sum of products formed

from H radical reactions approaches $\Sigma_{H^\circ} = \{2[H_2] + [CH_4]\}/CO_2 \approx 2$ at low AA concentration, and implies partial reforming involving 25% of the stoichiometric amount of water according to Reaction 46. The generation of protons implies oxidation of adsorbed water by photo-holes according to:

$$TiO_2(h^+) + H_2O \rightarrow H^+ + {}^\circ OH \quad (58)$$

The photogeneration of hydroxyl radicals in dilute aqueous acetic acid has been verified by Kraeutler et al. [614] and provides a rationale for the detection of minor levels of Hofer-Moest products [615] viz., methanol, ethanol and derivatives, again by a radical mechanism:

$$^\circ CH_3 + {}^\circ OH \rightarrow CH_3OH \quad (59)$$

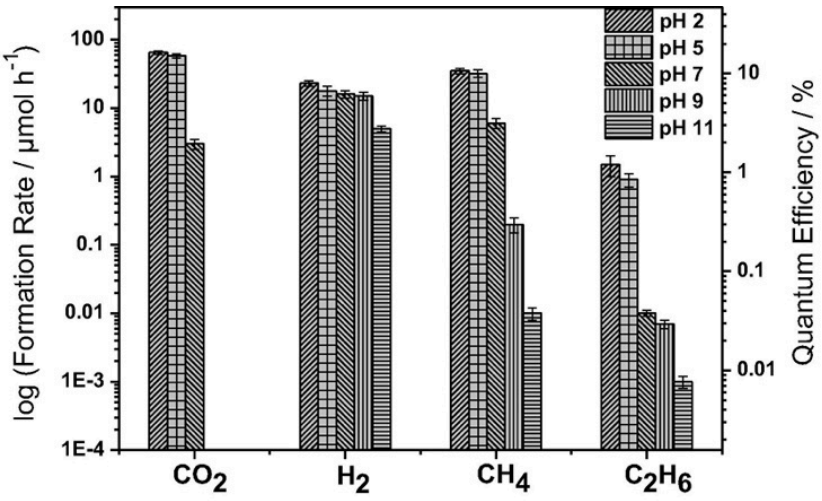


**Fig. 76** Photo-Kolbe product selectivity, effect of pH, and quantum efficiency in conversion of aqueous acetic acid (0.5 M) over 1% $Pt/TiO_2$ (P25). Irrad. time = 15 h at 30 mW $cm^{-2}$ UV. [reproduced with permission from ref. 615]

Since methanol is more readily decomposed (to $H_2$ and $CO_2$) than acetic acid [383,411], such a route offers prospects of raising the efficiency of photo-reforming of AA to $H_2$ (Reaction 46). While renewable methane is potentially valuable as a source of combustion process heat, hydrogen is a more valuable product. Hamid et al. [615] have shown (see Fig. 76) that the selectivity in AA photo-reforming can be effectively steered towards $H_2$ by easy adjustment of pH. While the quantum efficiency of $H_2$ production remains fairly constant (QE = 8 → 3%) over the pH range 2-9, the $CH_4$ yield falls dramatically from being the main product (QE = 10%) at pH = 2 by two orders of magnitude (QE = 0.3%) at pH = 9. In view of the high kinetic barriers ($E_a$ = 1-4 eV) [588,597,616] estimated for dehydrogenation of the acetoxy radical to carboxylmethylidene over transition metal terraces:

$$CH_3COO^\circ \rightarrow CH_2COO^\circ + H^\circ \qquad (60)$$

the fate of the methyl radical needs to be steered towards dehydrogenation rather than hydrogenation. Indeed, this is kinetically favoured over Pd(100) [588]. As shown in Fig. 77 the energy barriers estimated for successive dehydrogenation (in red, kcal.mol$^{-1}$): $^\circ CH_3 \rightarrow {}^\circ CH_2 + H^\circ \rightarrow {}^\circ CH + H^\circ$ ,viz., 31.8 and 11.3 kcal.mol$^{-1}$, respectively, are both lower than $^\circ CH_3 + H^\circ \rightarrow CH_4$ at 51.6 kcal.mol$^{-1}$. In summary, despite the adverse suppression of C-C bond scission in an aqueous environment [547], sufficiently energetic $TiO_2$ band-gap photons (~3eV) are effective in promoting decarboxylation, while thermal (dark) excitation is known to favour dehydrogenation [544]. Thus, acetic acid reforming (Reaction 46) is an interesting candidate to explore by dual-mode photo-thermal excitation [249].

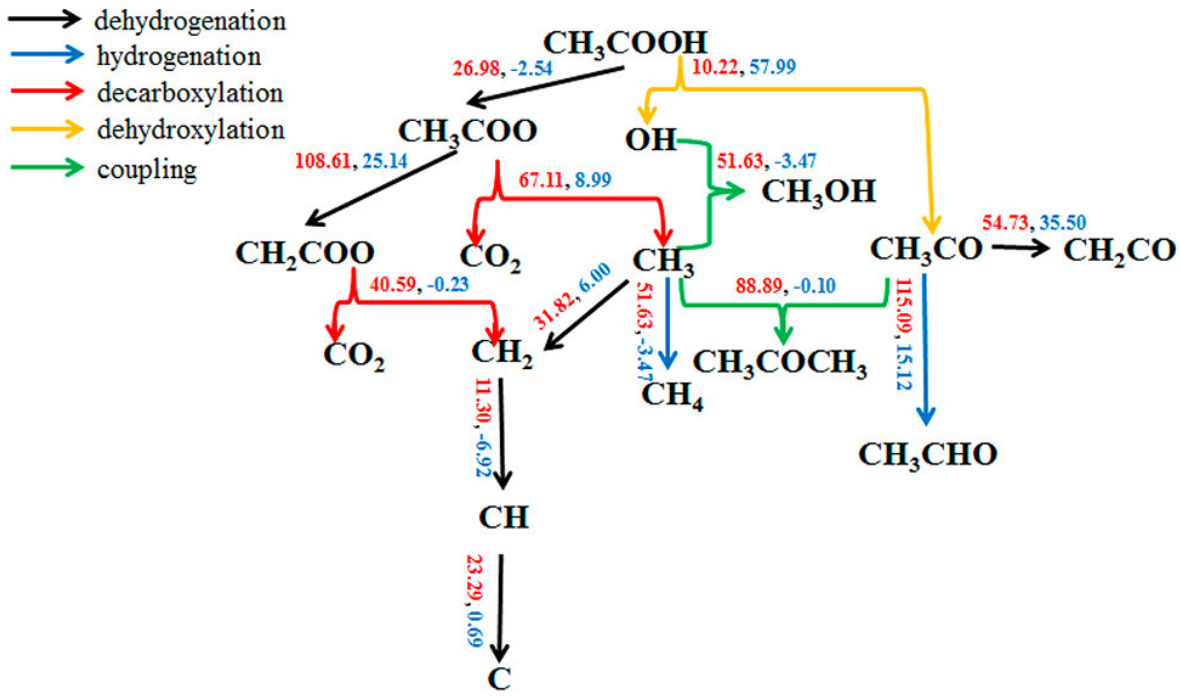


**Fig. 77.** DFT-estimated energetics (in kcal/mol) of acetic acid decomposition over Pd(100) [reproduced with permission from ref. 588]

The prospects for substituting Pt with Cu in acetic acid photo-reforming over $M/TiO_2$ has been assessed briefly by Imizcos and Puga [617]. A key condition in promoting $H_2$ generation instead of $CH_4$ was to photo-deposit Cu *in-situ*, thereby ensuring the presence of metallic copper. This raised the activity and eliminated the characteristic induction time of several hours linked to photo-reduction of copper oxides in conventionally-prepared (impregnated) catalysts. However, the selectivity towards hydrogen remained low at $H_2/CH_4$ = 0.1.

# 8. Oxygenates as liquid storage forms of renewable hydrogen – closing the carbon cycle

In view of the advanced state of technical maturity in the applied thermal catalytic synthesis of methanol from industrial (non-renewable) syngas [618,619]:

$$CO + 2\,H_2 \rightarrow CH_3OH_{(g)} \qquad (\Delta H^0 = -91\ kJ.mol^{-1}) \qquad (61)$$

its adaptation to conversion of *renewable syngas*, with recycled $CO_2$ as dominant or sole carbon source:

$$CO_2 + 3\,H_2 \rightarrow CH_3OH_{(g)} + H_2O_{(g)} \qquad (\Delta H^0 = -50\ kJ.mol^{-1}) \qquad (62)$$

is kinetically and thermodynamically feasible over Cu-ZnO-$Al_2O_3$ (CZA) [17,21,26-28,365-367]. This simple $C_1$ fuel, a high-density liquid storage form for hydrogen generated from renewable primary sources, e.g., solar PV coupled to PEM electrolysis of water [See *Introduction* (Fig. 1) and Section 4], serves as a vital component in any integrated biorefinery, especially one with a fuel-based platform centred on its $C_2$ homologue ethanol obtained by fermentation of sugars (cellulose) and/or biosyngas. As already considered in section 6 (*Solar refineries and hydrogen storage),* an independent industrial source of methanol as a carbon-neutral fuel and chemical feedstock increases operational efficiency and versatility, and is a valuable strategic safeguard against certain limitations inherent in biomass resources *viz.,* the shortfall in $H_2$ that typically accrues in syngas obtainable by gasification [73]. Comparing this $C_1$ alcohol with the analogous hydrocarbon methane, the high thermal efficiency of producing

3583 $CH_3OH$ from 3 $H_2$ (84.6%) in Reaction 62 exceeds that of $CH_4$ from 4 $H_2$ (77.8%) in the
3584 Sabatier reaction:
3585
3586 $CO_2 + 4H_2 \rightarrow CH_4 + 2\,H_2O \qquad (\Delta H^0 = -165\ kJ.mol^{-1})$ (63)
3587
3588 Furthermore, the original enthalpy is readily recovered via SR (reverse of Reaction (48))
3589 at 300°C [365]. In contrast, $CH_4$ reforming suffers from high kinetic and thermodynamic
3590 barriers, becoming viable only above 700°C. In any event Reaction 63 is a dissatisfactory
3591 method of $CO_2$ sequestration since it converts one greenhouse gas into a more pernicious
3592 variant.
3593

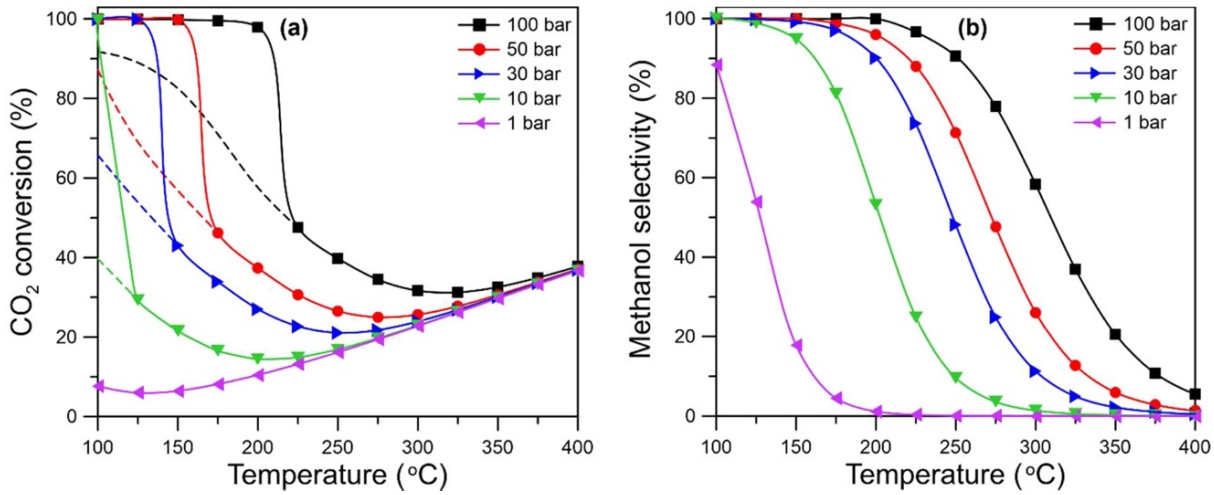


3594
3595 **Fig. 78.** Thermodynamics of $CH_3OH$ synthesis from $CO_2$:$H_2$ = 1:3. **(a)** $CO_2$ conversion, **(b)**
3596 $CH_3OH$ selectivity [reproduced by permission from ref. 623]
3597
3598 *Sensu stricto*, syngas is originally a mixture of CO and $H_2$ that is currently obtained from
3599 coal, oil or natural gas. However, depending on the feedstock and the process involved, the
3600 composition of syngas can vary significantly, and up to 5-15% of $CO_2$ can be typically present

in real syngas flows to be processed downstream. Additionally, with the objective of a future in which circular carbon is used as feedstock, renewable syngas often refers also directly to a mixture of $H_2$ and recycled $CO_2$ as dominant or sole carbon source, so that hereby renewable syngas can refer to both $CO/H_2$ and $CO_2/ H_2$ configurations.

What follows in this Section is primarily an overview of methanol synthesis from renewable syngas ($CO_2/H_2$) and a strategy for exceeding thermodynamic (gas-phase) equilibrium limitations by co-production of higher oxygenates, e.g., dimethyl ether (DME) and ethanol. By raising the dew point and promoting higher yields per pass via the "condensing product" principle, this may circumvent the costly recycling stage, one major limitation of the conventional process. As valuable diversification of biorefinery plant operations, the prospects for other low-energy routes to methanol and its interconversion with higher oxygenates will be important. These include valorization of glycerol and renewable methane. The last can be co-converted with $CO_2$ by so-called "dry reforming" of biogas [251], an endothermic process that stores enthalpy via formation of renewable syngas:

$$CH_4 + CO_2 \rightarrow 2\,CO + 2\,H_2 \qquad (\Delta H^0 = +247\ \text{kJ.mol}^{-1}) \qquad (64)$$

for subsequent conversion into liquid oxygenates. Alternative processes for the direct valorisation of $CH_4$, e.g., by partial oxidation to methanol, and especially those operating under mild conditions are now attracting serious interest [247,620,621]. Regrettably, this review lacks the scope to consider these or to include formic acid as a H-carrier. Despite some process advantages, e.g., low-temperature H-cycling [36,622], CO-free $H_2$ supply for fuel cells [39], etc., formic acid as H-carrier depends largely on the application of noble metal-based homogeneous catalysts with their high cost and traditionally challenging separation, recovery

and recycling issues. It also has an intrinsically low capacity in H-storage (4.4 wt%) and handling issues due to its corrosive properties.

### 8.1. Methanol from renewable syngas ($CO_2/H_2$)

Reaction 62 is an excellent example of a mildly exothermic process that proceeds under *kinetic* control. Despite the thermodynamics in $CO_2$ hydrogenation favouring methane and higher hydrocarbon products, very high selectivities (>95%) to $CH_3OH$ are typical over $Cu/ZnO/Al_2O_3$ (CZA) catalysts operating under 50-100 bar pressure ($CO_2$:$H_2$ = 1:3) at 240-250°C, as shown in Fig. 78b [623]. A selectivity trend away from $CH_3OH$ towards CO occurs beyond 250°C due to increasing influence of the endothermic reverse water-gas shift reaction (RWGS):

$$CO_2 + H_2 \leftrightarrow CO + H_2O \qquad (\Delta H^0 = +41.2\ kJ.mol^{-1}) \qquad (65)$$

In contrast, the beneficial effect of operating near the dew point at 100 bar (197-206°C) can be appreciated in the marked discontinuity, i.e., the sudden rise in $CO_2$ conversion (from 50 to 99%) evident in Fig. 78a due to the onset of product condensation. In practice, the CZA catalyst is not sufficiently active below 240°C and an upper limit on conversion (< 40%) per pass is imposed characteristic of gas-phase equilibrium limitations. This can only be exceeded, and the process made techno-economically viable, with the aid of a costly recycle sub-unit. Strategies to improve the CZA catalyst performance and/or seek alternatives that are sufficiently active at low temperature, i.e., nominally below 200°C [624], has been a key topic in several recent reviews [43,365-367,625-627].

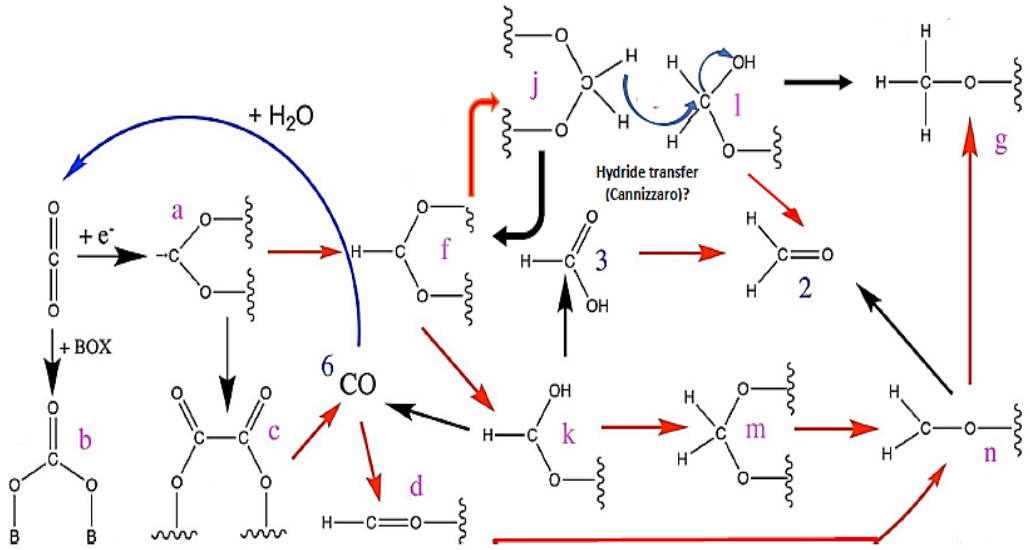


**Fig. 79** Mechanistic pathways in $CO_2$ hydrogenation and methanol synthesis according to Schlögl. The original has been adapted to include hydride transfer (Cannizzaro disproportionation into formate and methoxy) from dioxymethylene $H_2CO_2$ [intermediate (j) and/or (m)] and hydroxymethoxy $H_2CO(OH)$ [intermediate (l)]. Both can be considered as deprotonated forms of methanediol [$H_2C(OH)_2$] such as obtained by hydration of formaldehyde in a basic environment. Red arrows denote reduction reactions, black arrows denote redox reactions. [Reproduced with permission from ref. 625].

A good illustration of the mechanistic complexity in methanol synthesis from $CO_2/H_2$ over CZA is given in Fig. 79 (detail adapted from the original by Schlögl. [625]). It is generally agreed that the linear $CO_2$ molecule must first be activated by partial electron transfer, transforming it into the bent configuration of a metal/ion-adsorbed bidentate carboxylate [intermediate (a)]. Under typical reaction conditions this is rapidly hydrogenated to the formate species [intermediate (f)], whose vibrational signature dominates the spectrum of adsorbed species obtained, e.g., by in-situ (FTIR) spectroscopy [628,629]. This is frequently accompanied by weaker bands of methoxy species [intermediate (g)], especially in carbon-rich

(H-lean) syngas mixtures. The general consensus is that formate is a pivotal (kinetically-relevant) intermediate that undergoes subsequent hydrogenolysis via a dioxymethylene (DOM) intermediate [21,243,630]. An outstanding controversy about whether formate is an active intermediate or merely a spectator species stems primarily from studies on unsupported or supported Cu in the absence of Zn [631]. However, recent mechanistic and DFT modelling studies appear to reconcile this issue, showing that the activity in formate hydrogenation to methanol is highly complex, being locality- and coverage-dependent, a strong function of the *in-situ* state of the catalyst and of syngas composition (carbon source). The role of ZnO as a reducible oxide capable of decorating stepped Cu in an SMSI type interaction, and thereby creating a highly active interfacial formate species with ready access to $H_{ad}$ spilt over from the metal, appears crucial to performance [628,629,632,633].

Considering the mechanism in Fig. 79 in more detail, dioxymethylene (DOM) can be formed directly in adsorbed bidentate form via attack by $H_{ad}$ at the carbon atom [intermediate (j)], or indirectly via protonation to a hydrocarboxy species, viz., adsorbed monodentate formic acid [intermediate (k)], before C-H bond formation [intermediate (m)]. The scarcity of direct spectroscopic evidence for DOM on supported Cu catalysts under synthesis conditions suggests it is much more reactive than formate. The main evidence for its existence has come from studies in methanol decomposition [634], or by direct dosing of formaldehyde [see Fig. 79 compound 2] on basic and amphoteric oxides at low temperature [293]. Its conversion to methanol (or methoxy) and formate in a Cannizzaro-type (hydride transfer) dismutation has been shown to be facile in surface science investigations [635]. Assuming direct hydrogenation [(f) → (j)] as depicted at the top of Fig. 80 (slightly modified from the original by Schlögl) [625], it implies recycling of formate as below:

$$HCOO^* + H^* \rightarrow H_2COO^* \quad (66)$$

(f) (j)

$$H_2COO + H_2CO(OH) \rightarrow HCOO^* + H_3CO^* + HO^* \quad (67)$$

(j) (l) (f) (g)

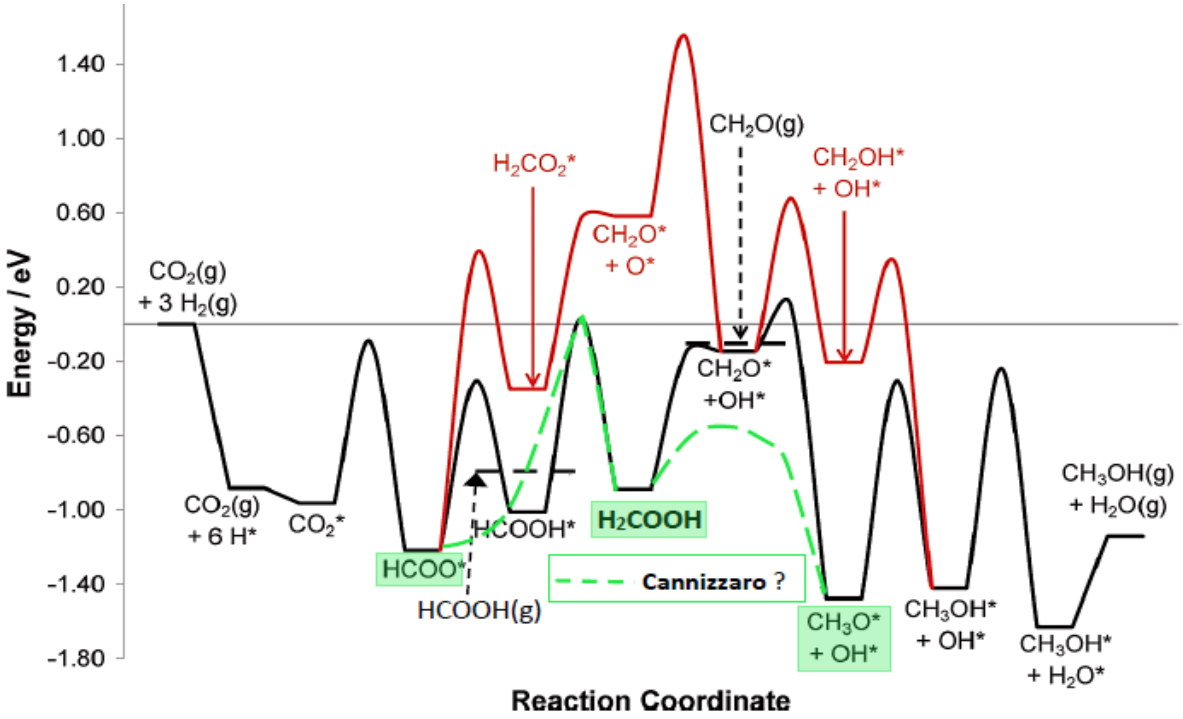


**Fig. 80.** Potential energy surfaces in methanol synthesis via $CO_2$ hydrogenation according to Grabow and Mavrikakis [636]. A stable formate (HCOO*) initiates two distinct mechanistic pathways – a favoured low-energy route (exothermic, black) via formic acid and hydroxymethoxy ($H_2COOH$*), or a disfavoured high-energy route (endothermic, red) via dioxymethylene ($H_2CO_2$*). The trace in green (adapted from the original) represents a Cannizzarro dismutation between two adjacent hydroxymethoxy species involving hydride transfer (back to formate and onward to methoxy), driven by the simultaneous lowering of product enthalpies. It also circumvents the high-energy activation step via formaldehyde

3705 ($CH_2O$) intermediate. The related activation energy curves are only schematic based on the
3706 assumption of microscopic reversibility. [reproduced with permission from ref. 636]

3707

3708 It should be noted that dismutation (Reaction 67) as shown involves DOM (j) and its
3709 related hydroxymethoxy form (l). The DFT estimates of the energetics by Grabow and
3710 Mavrikakis [636], as shown in Fig. 80, reveal that the formation of both intermediates [(l) and
3711 (j)] is exothermic but $H_2CO(OH)^*$ is considerably more stable than $H_2CO_2^*$ ,with potential
3712 energy surfaces of -0.84 eV and -0.3 eV, respectively. This can be taken as the energy penalty
3713 associated with full deprotonation of methanediol [$H_2C(OH)_2$], the parent compound formed
3714 by rapid hydration of formaldehyde. The lowest-energy route to methoxy (and methanol) is
3715 indicated in black and follows the sequence formate → formic $acid_{ads}$ → $hydroxymethoxy_{ads}$ →
3716 $formaldehyde_{ads}$.. Intervention of the Cannizzaro dismutation reaction (indicated in green)
3717 between two adjacent $hydroxy\text{-}methoxy_{ads}$ groups forming the stable co-product adsorbed
3718 water, further reinforces this route (Reaction 68) and avoids the high energy barrier (via
3719 $formaldehyde_{ads}$), in yielding $methoxy_{ads}$ directly:

3720

3721 $2\ H_2CO(OH)^* \rightarrow HCOO^* + H_3CO^* + H_2O^*$ (68)

3722 2 (l) (f) (g)

3723

3724 Detailed kinetic, mechanistic, and DFT modelling studies of methanol synthesis over
3725 CZA (as compared to a Cu/MgO control of similar metal size and shape) under differential
3726 conditions by Studt et al. [637] have now reconciled some long-standing controversies as to the
3727 origin of the Cu-Zn synergy and provided a rationale for the complex interplay between CO
3728 and $CO_2$ as competing carbon sources, depending on the absence or presence of ZnO, and the
3729 ambiguity in formate reactivity. In view of its structure-sensitive character, methanol synthesis
3730 was modelled for Cu/MgO as a stepped Cu(211) surface, but in the case of CZA the same (211)

stepped surface decorated by a full $ZnO_x$ overlayer, resulting from "strong metal-support interaction" (SMSI).

As shown in Fig. 81*top*, Cu/MgO attains high activity in pure CO as carbon source but this is dramatically suppressed by the addition of $CO_2$. This causes the build-up of a formate species preferentially bonding through the carbon atom that acts as a poison by occupying Cu sites otherwise needed for CO adsorption, the initial step in a mechanism that proceeds via formyl (HCO*) and oxymethylene ($H_2CO$*) species [intermediates (d) and (n) in Fig. 79]. Addition of $ZnO_x$ promotes $CO_2$ hydrogenation by stabilising a highly active formate intermediate bonding through its O atom(s) at the Zn-O-Cu interface. The suppression of CO hydrogenation in the presence of $CO_2$ over Cu/MgO is so dramatic that over 90% of the methanol is produced from $CO_2$ even at the resulting low overall activity (TOF ~ 0.001 $s^{-1}$) as revealed by isotopic ($^{13}C$) labelling. In the presence of ZnO, the activity is markedly enhanced (by up to x19) as compared to Cu alone in various forms. Fig. 81*bottom* provides a qualitative descriptive summary of the kinetics in terms of relative rates, apparent activation energies, and surface coverage by more or less active formate intermediates.

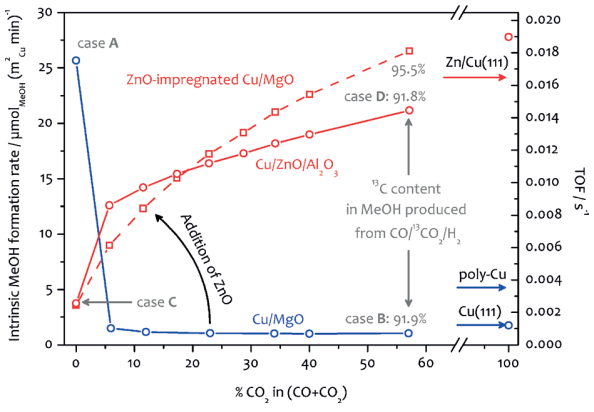

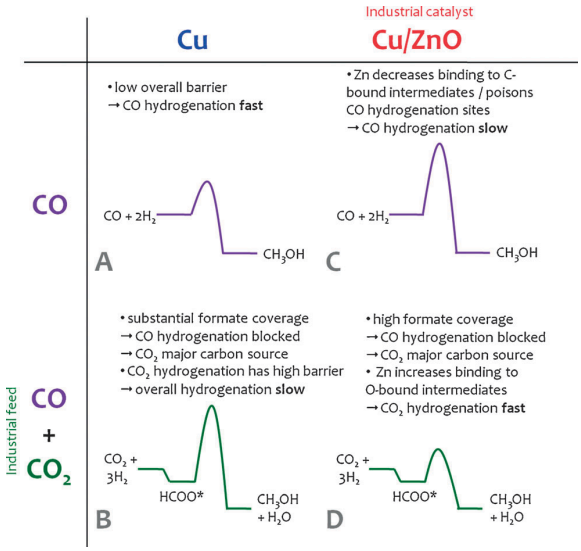


**Fig. 81 (top)** Suppression of methanol synthesis from CO over Cu/MgO by $CO_2$ as carbon source and growth in CO activity from $CO_2$ by addition of ZnO ; **(bottom)** Kinetic factors in Cu/MgO and CZA responsible for the paradoxical (mutually exclusive) activities in CO and $CO_2$ hydrogenation in the absence or presence of ZnO. [Reproduced with permission from ref. 637]

### 7.2. Ethanol from methanol, dimethyl ether (DME), and/or renewable syngas ($CO_2/H_2$)

Unlike methanol synthesis, the main issue in higher ($C_{2+}$) oxygenates and hydrocarbons synthesis is one of selectivity control. Traditionally, the *Higher Alcohol Synthesis (HAS)* aims specifically for a product cut in which ethanol is a single component among several, typically ranging from $C_2$-$C_6$. HAS works best starting from conventional non-renewable (CO-rich) syngas over modified Fischer-Tropsch (FT) catalysts that promote limited chain growth via "CO insertion", a key mechanistic step [638,639]. The viability of the approach consisting in synthesising selectively ethanol from renewable ($CO_2$-rich) syngas remains as of today under debate. It appears that gas compositional tuning towards an optimal balance within the carbon sources, *e.g.*, by *in-situ* generation of CO from $CO_2$ *via* the RWGS reaction, may be a relevant option. Certainly the thermodynamics are favourable, even towards liquid products [640]:

$$2\ CO_2\ +\ 6\ H_2\ \rightarrow\ C_2H_5OH_{(l)}\ +\ 3\ H_2O_{(l)}$$

$$(\Delta H_{298K} = -87\ kJ.mol^{-1};\ \Delta G_{298K} = -32\ kJ.mol^{-1}) \qquad (69)$$

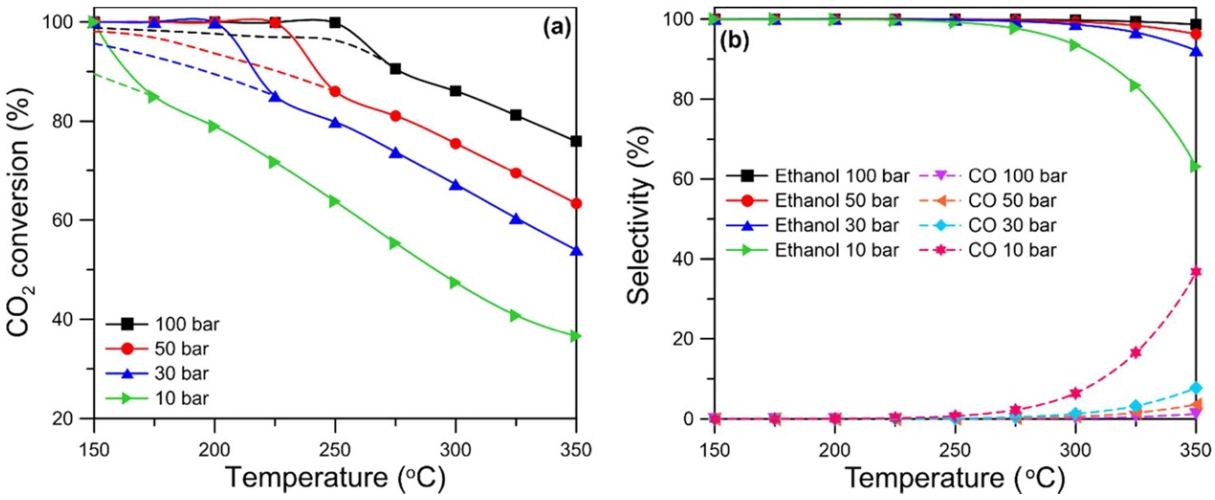


**Fig. 82. (a)** $CO_2$ conversion and **(b)** ethanol and CO selectivity in $CO_2$ hydrogenation at 10-100 bar. [reproduced with permission from ref. 627].

This may be important because the aforementioned "condensing product" principle offers even greater prospects for overcoming (gas-phase) equilibrium limitations, as shown in Fig. 82a. The dew point at 100 bar pressure ($H_2/CO_2$ = 3/1) rises to 270°C, as compared to 200°C for methanol synthesis (see Fig. 78), and the $CO_2$ conversion (to ethanol) exceeds 95% at 250°C, i.e., the operating temperature range for the commercial CZA catalyst, potentially facilitating single-pass operation. Recognizing that catalyst ineffectiveness below 200°C is due to inhibition (steric effects) from adsorbed water rather than any intrinsic lack of activity [628], there are clear implications for ethanol synthesis, albeit operating at higher temperature. In view of the higher (3x) water levels expected according to the stoichiometry of Reaction 69, a judicious regime of water elimination *in-situ* is clearly indicated, e.g., via thermally-resistant perm-selective polymer membrane reactors [627].

Probably the best prospects of attaining adequate *kinetic control* in selectivity towards ethanol from $CO_2$ may derive from the use of Cu-based ($C_1$) catalysts suitably modified by judicious inclusion of chain growth (FT-type) promoters such as Co. Such bimetallic combinations show promising results at least in the case of CO conversion. A probable mechanism is via an aldol-type addition of methanol-derived formyl species leading to an acetyl intermediate in a process akin to homologation [638,639,641,642]. It is known that $C_1$ chemistry is a viable platform to relevant and multitudinous $C_2$-$C_3$ intermediates and products, offering the advantage that each stage is of intrinsically high selectivity. A typical sequence is $CO_2$ → dimethyether (DME) → methyl acetate (MA) → ethanol, where some stages may be coupled, e.g., DME → ethanol, due to the versatile properties of Cu-promoted solid acids (H-ZSM 5, H-mordenites, etc.). Thus, DME is readily produced from $CO_2$ by adding a *dehydration* function, viz., Brønsted acidity, to a conventional methanol synthesis catalyst [43,623,643,644]:

$$2\ CO_2 + 6\ H_2 \rightarrow CH_3OCH_3 + 3\ H_2O \qquad (\Delta H_{298K} = -122\ kJ.mol^{-1}) \qquad (70)$$

DME can then, in principle, be isomerized to ethanol over a superbasic catalyst that promotes H abstraction to yield a carbanion intermediate favouring 1,2-rearrangement to an ethoxy species:

$$CH_3OCH_3 \rightarrow C_2H_5OH \qquad (\Delta H_{298K} = -53\ kJ.mol^{-1}) \qquad (71)$$

However, an increasingly popular route is via DME carbonylation to methyl acetate (MA) [645,646]:

$$CH_3OCH_3 + CO \rightarrow CH_3COOCH_3 \qquad (\Delta H_{298K} = -70\ kJ.mol^{-1}) \qquad (72)$$

after which MA hydrogenolysis [647,648]:

$$CH_3COOCH_3 + 2\ H_2 \rightarrow C_2H_5OH + CH_3OH \quad (73)$$

results in an equimolar mixture of simple alcohols from which the methanol component is recycled to a dehydration unit for DME regeneration:

$$2\ CH_3OH \rightarrow CH_3OCH_3 + H_2O \qquad (\Delta H_{298K} = -23.4\ kJ.mol^{-1}) \quad (74)$$

Coupling of Reactions 72 & 73, converting DME directly to ethanol, is also feasible [649]. The alternate (ENSOL) [650] route proceeds by methanol carbonylation to acetic acid (AA):

$$CH_3OH + CO \rightarrow CH_3COOH_{(g)} \qquad (\Delta H_{298K} = -123\ kJ.mol^{-1}) \quad (75)$$

followed by AA hydrogenation to ethanol:

$$CH_3COOH_{(g)} + 2\ H_2 \rightarrow C_2H_5OH_{(g)} + H_2O_{(g)} \qquad (\Delta H_{298K} = -41.7\ kJ.mol^{-1}) \quad (76)$$

Reactions 74 & 75 can also be combined, corresponding to a one-pot methanol homologation process in conventional syngas. With the exception of Reaction 75, requiring the precious metal Rh, all the above-listed indirect reactions to ethanol proceed over earth-abundant (Cu-based) catalysts at 250°C or below.

The thermocatalytic $CO_2$-based route as described above (Reactions 70-74) is estimated to yield ethanol at a fairly competitive cost of USD 1.23/L via DME, or USD 1.48/L via RWGS and CO hydrogenation. However, as shown in Fig. 83, this is still nearly double the price obtainable via sugar fermentation or biomass gasification/syngas fermentation [28,765148].

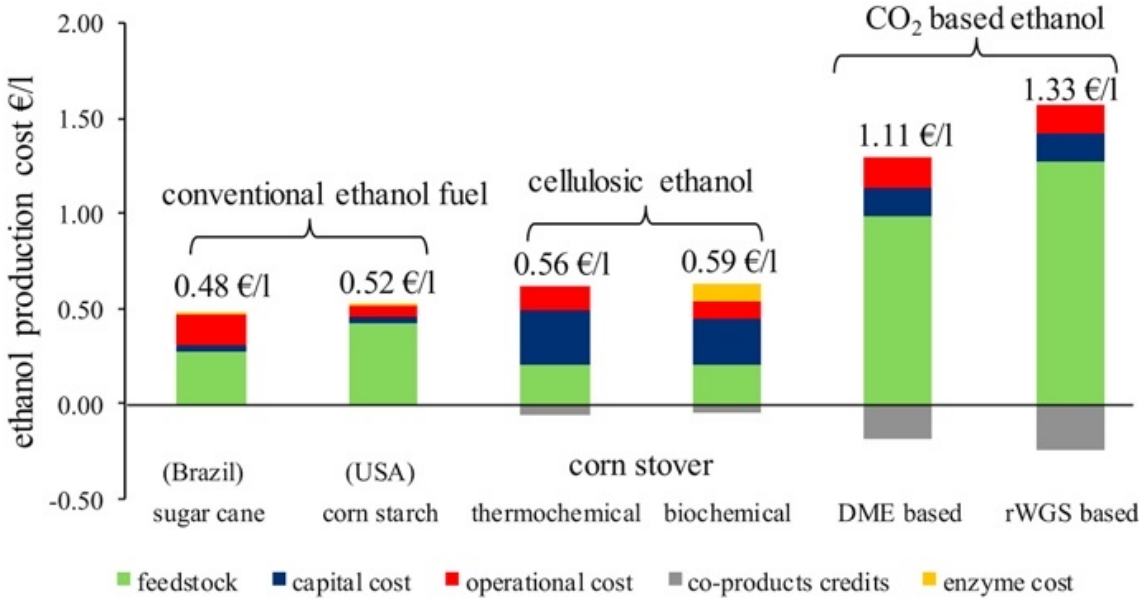


**Fig. 83** Ethanol production cost analysis for thermocatalytic ($CO_2$-based) routes vs. conventional (sugar cane fermentation) and cellulose (corn stover) gasification/syngas fermentation. [Reproduced with permission from ref. 28]

Reviews on catalysts for direct routes to ethanol from renewable syngas ($CO_2/H_2$ – see Reaction 55) have appeared recently [652,653]. A clear parallel exists with HAS synthesis from conventional syngas, for which Co (111), Cu and binary alloys [642,654] are effective as predicted by DFT calculation [655]. Wang et al. [656] have reported on non-noble $CoAlO_x$ (prepared from Co-Al layered double hydroxides, LDH) and the effect of activation procedure at 300-650°C on selectivity in $CO_2$ conversion to ethanol in aqueous suspension and 40 bar pressure ($H_2/CO_2$ = 3/1). As shown in Figs. 84a (T =140°C) and 84b (T = 200°C), the most active and selective catalyst was obtained after pre-reduction at 600°C, yielding 0.444 $mmol.g_{cat}^{-1}.h^{-1}$ of normal ($c_1$-$c_4$) alcohols (92% ethanol) at 140°C, rising to 1.003 $mmol.g_{cat}^{-1}.h^{-1}$ (89% ethanol) at 200°C. A commercial $Co_3O_4$ sample reduced likewise gave a poor yield (15%) and low selectivity (25% ethanol). XANES revealed the co-existence of metallic cobalt ($Co^0$, d ~ 4.6 nm) and oxidic cobalt (CoO) while *operando* FTIR spectroscopy gave evidence

for a mechanism involving acetate intermediate (via *$CH_x$ insertion into formate) followed by hydro-deoxygenation to ethoxy, etc.

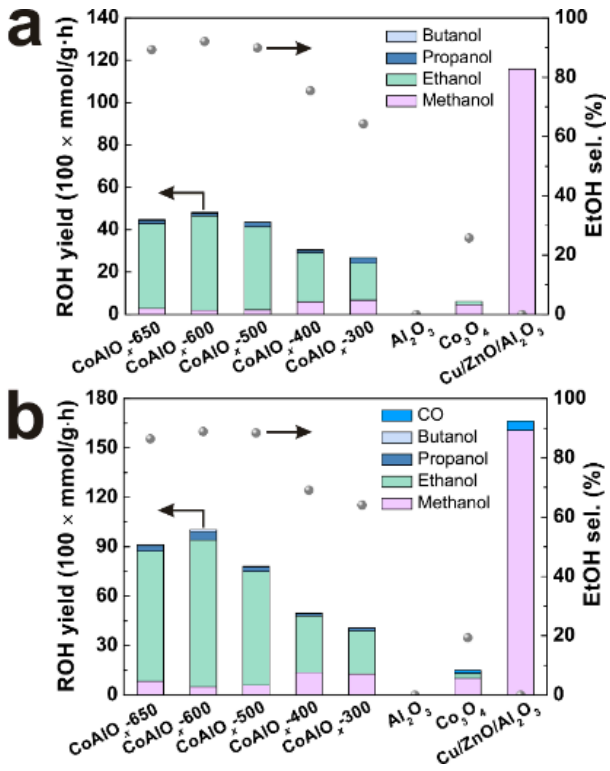


**Fig. 84 (a).** $CO_2$ hydrogenation at 140°C, and **(b)** $CO_2$ hydrogenation at 200°C after 15h TOS. Reactor conditions – 20 mg catalyst, 2 mL water, P = 40 bar ($H_2/CO_2$ = 3/1). [Reproduced with permission from ref. 656]

Follow-up work by the same group [657] explored alloying Co with Ni in the same LDH preparative methodology and found increased productivity of 1.32 $mmol.g_{cat}^{-1}.h^{-1}$ for an optimum composition $Co_{0.52}Ni_{0.48}AlO_x$, albeit at a price of slightly lower ethanol selectivity (85.7%) due to raised levels of $C_1$ products (methanol, CO and $CH_4$) characteristic of $NiAlO_x$. In contrast, Zhang et al. [658], found that unless Na-promoted Co metal is converted to cobalt carbide [$Co_2C$ (111)] during pre-reduction in CO at 300°C, and/or restabilised *in-situ* ($H_2/CO_2$

3873 = 3/1) via RWGS at 250°C (see Fig. 85), $CO_2$ is preferentially converted to $CH_4$ ( >70%) over
3874 $Al_2O_3$-, ZnO-, activated carbon- and $TiO_2$-supported forms. Only $SiO_2$ and $Si_3N_4$ promote long-
3875 term (up to 300h) stability of Na-$Co_2C$, the key formulation for enhanced productivity towards
3876 $C_1$-$C_5$ alcohols (> 9%), and ethanol in particular (6%). However, this was at the price of lower
3877 $CO_2$ conversion (< 20%) and raised CO levels (30-40%).
3878

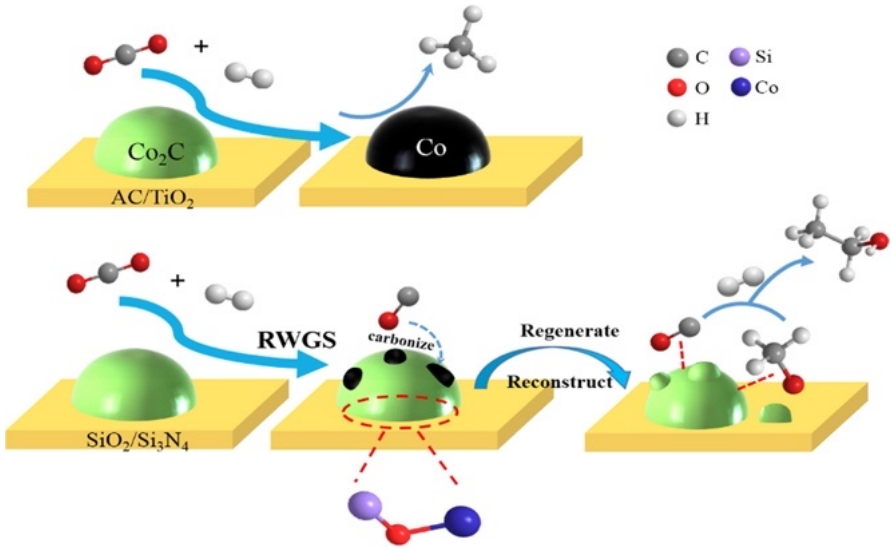


3879
3880
3881 **Fig. 85** Preferential stabilisation of Na-promoted $Co_2C$ (111) over Si-containing supports in
3882 $CO_2$ hydrogenation to ethanol {Reproduced with permission from ref. 658]
3883
3884 Ding et al. [659] have reported that Cu (8 wt%), encapsulated (initially as CuO) into Na-
3885 Beta zeolite in a two-stage dry gel conversion and crystallisation method shows remarkably
3886 high selectivity to ethanol (~100%) and CO (0-40%) from $CO_2/H_2$ (= 1/3) under a wide range
3887 of operating conditions (100-350°C, 6-21 bar, GHSV = 2-18 $L.g_{cat}^{-1}.h^{-1}$). However, conversion
3888 was quite restricted (< 20%) under all conditions as shown in Figs. 86A-C. The catalyst
3889 maintained its performance in extended stability testing at 300 °C and 13 bar, as shown in Fig.
3890 86D. Collection of liquid products during 24h TOS yielded 0.71 g aqueous ethanol (in the 3/1

stoichiometry of Reaction 55), corresponding to a yield of 5% and a respectable space-time productivity of 3.0 $mmol.g_{cat}^{-1}.h^{-1}$. Curiously the selectivity to hydrocarbons and simple alcohols obtained from conventional CO-based syngas (see Fig. 86E) appears quite unlike

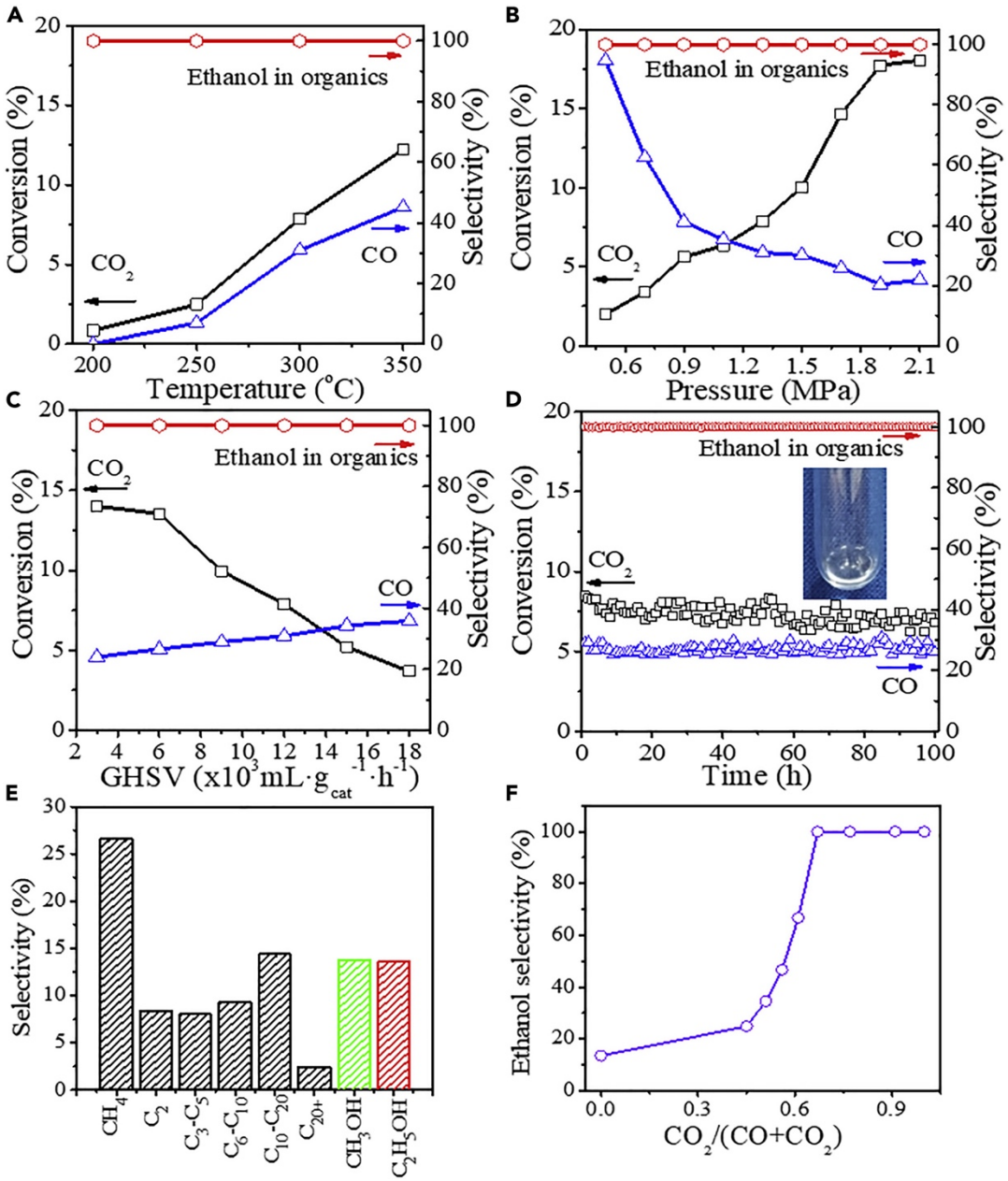


Cu(111) [752], resembling instead the behaviour of Co. This can best be rationalised by the high dispersion of the Cu nanoparticles (d ~ 3nm), raising the probability of exposure of Cu steps, together with the well-known effect of modification by alkali-doping.

**Fig. 86** Sensitivity in conversion and ultra-high selectivity to ethanol from $CO_2/H_2$ (= 1/3) over 8% Cu@Na-Beta (Zeolite) across temperature **(A)**, pressure **(B)**, space velocity **(C)**, and long-term stability **(D)** at 300°C and 13 bar; **(E)** Product selectivity from $CO/H_2$ (= 1:3); **(F)** Sensitivity of ethanol selectivity to syngas carbon source [$CO_2/(CO + CO_2)$]. [Reproduced with permission from ref. 659]

DFT calculations have shown that K-doped Cu(211) has a high selectivity towards higher alcohols provided that the surface is well-covered by methoxy species. The mechanism is linked to the higher probability of sourcing hydrocarbonaceous species like $*CH_3$ (by methoxy C-O bond scission) for coupling with CO to form acetyl, $*CH_3CO$ [660]. Other possibilities are $CH_x$ insertion into formate [661], (or $CO_2$), leading to acetate $*CH_3COO$, or dimerisation of *CHO to glyoxal (*OHCCHO), hydrogenation to glycolaldehyde ($*OHCCH_2OH$), and subsequent C-O scission to $*OHCCH_2$, etc. [662] The first of these is suggested by the authors' own *in-situ* FTIR observations and is more consistent with the trend in ethanol selectivity (see Fig. 86F), which rises dramatically towards 100% for syngas compositions trending to $CO_2$-rich [$(CO_2/(CO + CO_2) > 0.6$]. The absence of more polar products like $CH_3OH$, HCOOH, and $CH_3COOH$ was attributed to their strong interaction and breakdown (as $CO_x$) over the Beta zeolite framework, as shown by direct dosing and TPD. In view of the less impressive results obtained over other zeolite supports, electronic effects of the highly-polarising alumino-silicate environment on Cu may also play a significant role.

The most effective way of modifying single metals to obtain novel catalytic properties is by the addition of a second metal offering a cooperative functionality, preferably leading to bimetallic alloy formation although this is not always essential. While Cu effectively hydrogenates the C-O bond (as in methanol synthesis), Co is better at C-O bond dissociation. If the propensity for methanation typical of monometallic Co is suitably tempered by alloying,

this can lead to a raised probability of insertion of $*CH_x$ into a di-oxygenated methanol synthesis intermediate (located on Cu) leading to $C_2$ precursors susceptible to hydro-deoxygenation to ethanol. Furthermore, novel properties may accrue from the fact that any alloy formed from this inexpensive and earth-abundant combination will be *metastable*, the components being immiscible in bulk form. This underpins the well-known surface restructuring (segregation) behaviour in supported Cu/Co, e.g., under CO [426,663]. Whether such a spontaneous constraint conflicts with optimization of the balance of carbon sources, a necessary empirical objective from kinetic and mechanistic considerations, is as yet unclear. After showing by DFT and microkinetic modelling that Cu/Co alloys favour ethanol whereas Cu and Co as individual metals yield mainly methanol and methane, Prieto et al. [663] took great care to ensure intimate mixing of Cu and Co in molybdate ($Cu_xCo_{1-x}MoO_4$) precursors prior to reduction.

3935

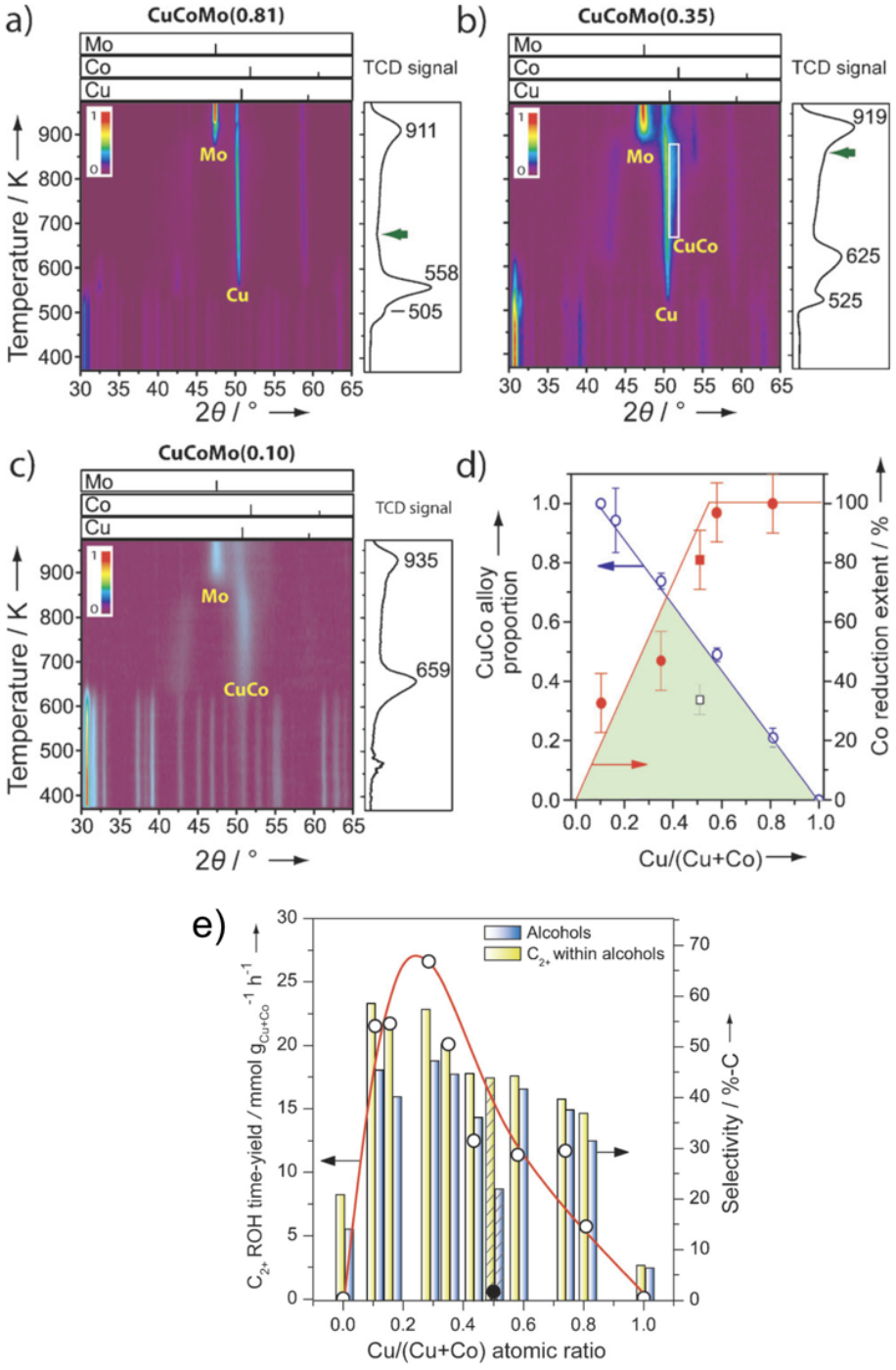


3936

3937 **Fig. 87** In-situ XRD and TPR ($H_2$) of CuCoMo catalysts at **(a)** Cu/Cu+Co = 0.81, **(b)** 0.35, **(c)**

3938 0.10. **(d)** Evolution of $Co^{2+}$ reduction at 400°C and CuCo alloy growth with composition ; **(e)**

3939 Activity of K-CuCoMo (o), K-CuCoCr (●), and selectivity to alcohols (blue/yellow bars) in

3940 $CO/H_2$ (1/1) at 270°C and 40 bar (Xco < 2%). [Reproduced with permission from ref. 663]

As shown by *in-situ* XRD and TPR in Figs 87a-d, this was done in $H_2$ at 400°C, a temperature ensuring substantial reduction of the Co component promoted by the more easily-reduced Cu effecting $H_2$ dissociation. The highest proportion of alloy derived from slightly Co-rich compositions [(Cu/(Cu+Co) ~0.35]. This also assured zero exsolution of free Cu, a typical problem in such preparations. As shown in Fig. 87e, the catalytic performance of K-doped formulations at 270°C and 40 bar ($CO/H_2$ = 1) under differential conditions (Xco < 2%) peaked at close to the same (alloy) composition. The activity (open circles) exceeded that of K-CuCoCr, a typical performance benchmark (filled circle) by up to two orders of magnitude, reaching an impressive 27 $mmol.g_{cu+Co}^{-1}.h^{-1}$. Selectivites to total and higher ($C_{2+}$) alcohols (yellow bars and blue bars, respectively) were both high at around 50%.

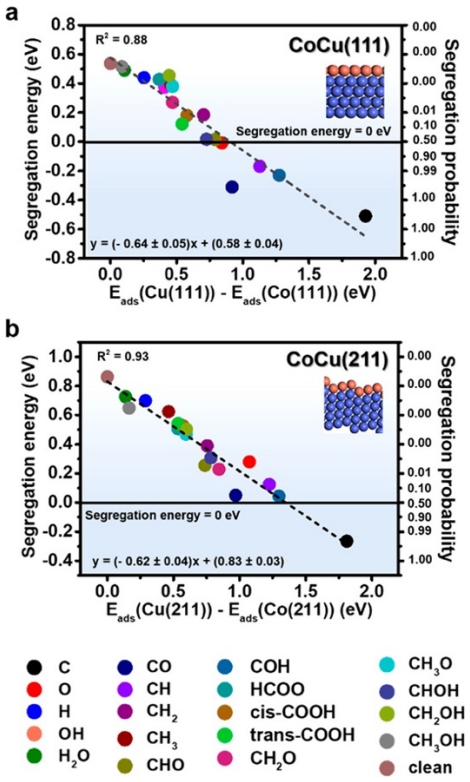

**Fig. 88** Linear scaling of segregation energy vs. adsorption preference on bimetallic alloy surfaces. **(a)** CuCo(111) terrace and **(b)** CuCo (211) step. Adsorbates tending to extract Co from the equilibrium vacuum condition (Cu overlayer) include many unsaturated carbonaceous species. [Reproduced with permission from ref. 664]

Despite substantial progress in the theory and practice of Cu/Co alloy catalysis in CO-based atmospheres, advances in the surface description and optimisation of bimetallic active sites in renewable ($CO_2$-rich) syngas conversion have been reported only recently. For example, Liu et al. [664] have introduced a low-cost computational approach to model metastable alloys, offering rapid and incisive predictions based on the scaling relation between *segregation energy* and *adsorption preference.* As shown in Fig. 88, good linear fits were obtained across a wide range of adsorbates relevant to $CO_2$ hydrogenation over model CuCo alloy surfaces (111 terrace, 211 step) at a reference temperature of 250°C. Strongly-binding adsorbates, e.g., unsaturated carbonaceous species C, CH, and $CH_2$, result in negative segregation energies and are expected to extract Co from the sub-surface layer of the equilibrium (*in vacuo*) state of the alloy onto the surface. The top layer consists primarily of pure Cu, being the metal component of lowest surface energy.

These predictions were verified experimentally for a $CuCo_2$ model catalyst prepared from mixed oxalate precursors, pre-reduced in $H_2$ or CO at 350°C, followed by cyclical testing at 250, 350, and back to 250°C to address irreversible changes due specifically to exposure to reactants [$CO_2/H_2$ = 1:3] at 350°C. For diagnostic purposes, selectivities trending away from CO and/or $CH_3OH$ (C-O bond remaining intact) towards rapid $CH_4$ production (via C-O bond scission), were taken as *prima facie* evidence of an initially intact Cu surface layer subject to progressive segregation (Co enrichment), as monitored by XPS. As shown in Fig. 89a and 89b, almost linear increases in $CO_2$ conversion and selectivity to $CH_4$ were evident vs. fractional Co

enrichment ($X_{Co}$–$X_{Cu}$). Fig. 89c shows the effect of pre-reductant gas on product selectivity. The sample pre-reduced in $H_2$ (H250-1) initially yields mainly oxygenates (80% vs. 20% $CH_4$) indicative of an intact Cu surface. Intermediate testing at 350°C (H350) resulted in a sharp inversion in selectivity suggesting Co enrichment. An irreversible change in the surface state of the alloy under $CO_2/H_2$ at 350°C was confirmed in a control test back at 250°C, showing now a mixed selectivity of 60% oxygenates and 40% $CH_4$. As expected, pre-reduction in strongly-adsorbing CO resulted in an initial selectivity more reflective of a Co-rich surface (CO250-1, 80% $CH_4$). This was more pronounced at 350°C (> 90% $CH_4$). Curiously, the control test back at 250°C (CO250-2) showed a mixed selectivity suggestive of partial surface re-enrichment by Cu (30% oxygenates). In summary, this work has introduced and validated the fundamental concepts underpinning the development of an empirical approach towards "tuning" of catalytic properties in metastable alloys, e.g., by judicious choice of pre-reduction conditions and/or *operando* chemical and structural "tailoring" during reaction (self-regulation).

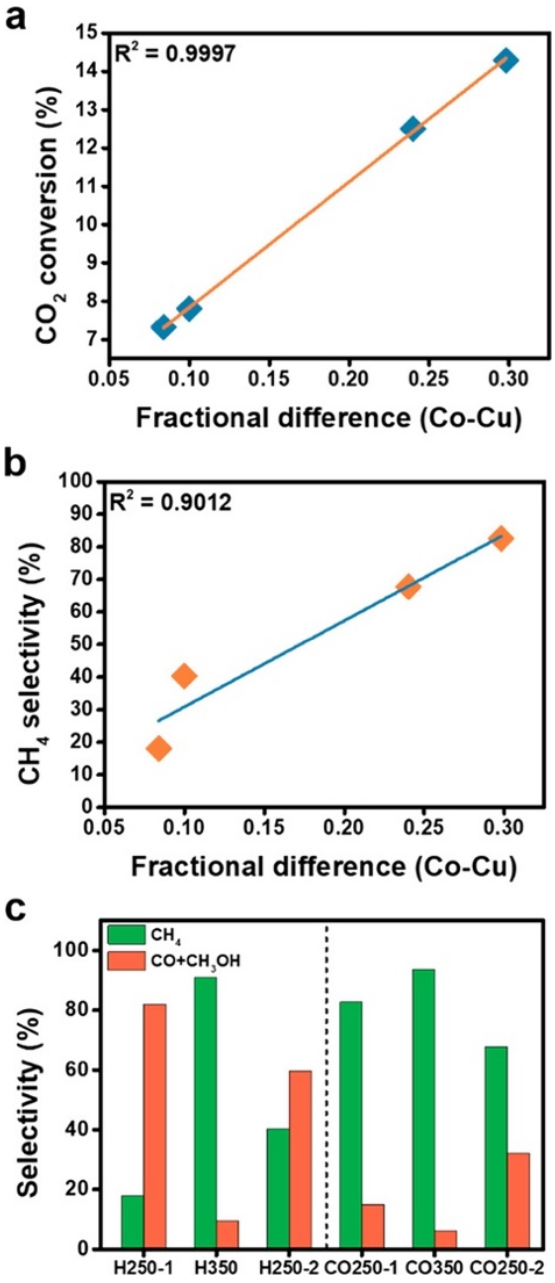


**Fig. 89.** Trends in $CO_2$ conversion **(a)** and $CH_4$ selectivity **(b)** in $CO_2$ hydrogenation at 250°C vs. fractional enrichment in surface Co level ($X_{Co} - X_{Cu}$) estimated by XPS. **(c)** Trends in selectivity (CO + $CH_3OH$) vs. $CH_4$ at 250, 350, and back to 250°C , after pre-reduction in $H_2$ (left group) or CO (right group) at 350°C. [Reproduced with permission from ref. 664]

The same (Zhao/Gong) group have now extended their computational/empirical strategy to the optimisation of selectivity to ethanol from $CO_2/H_2$ over Cu/Co [665]. Alloy samples with

varying degrees of Co segregation were obtained via a two-stage pre-reduction sequence culminating in exposure to varying partial pressures of CO (in $N_2$) at 450°C. As depicted in Fig. 90, samples with a moderate level of Co surface enrichment (Cu:Co = 1:1) were obtained under just 1% CO. Energy barriers were modelled and estimated for CO hydrogenation to $CH_4$, $CH_3OH$ and $C_2H_5OH$ based on the assumption of $CO_2$ reduction via RWGS. Three model surfaces [nCO-(3x3)-CuCo(111)] were considered, viz., (1/9Co, 2/9CO), (4/9Co, 4/9CO) and (5/9Co, 5/9CO). Due to strong Co-Co bonding, as compared to Cu-Cu and Cu-Co, Co surface atoms group into islands, as depicted in the moderately segregated case in Fig. 90A.

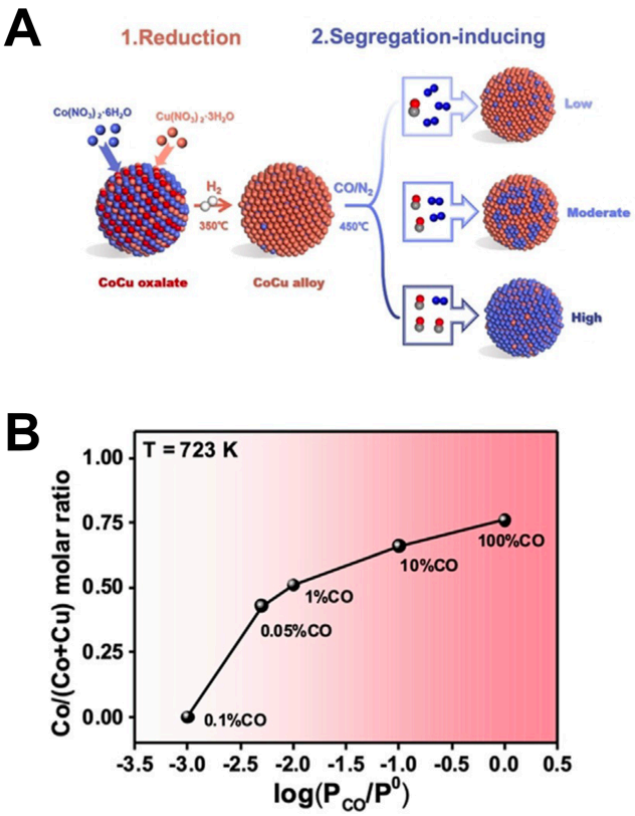


**Fig. 90 (A).** Pre-reduction scheme for Cu/Co alloys subjected to controlled (Co) surface segregation. **(B)** An equi-atomic surface composition (Cu:Co = 1:1) was obtained by reduction at 450°C under 1% $CO/N_2$ [Reproduced with permission from ref. 665]

In mechanistic terms, CO is preferentially adsorbed on Co, leaving the Cu surface available to fulfil its complementary functions of $H_2$ dissociation and non-dissociative adsorption of weakly-bound CO at the Cu/Co interfaces, potentially facilitating CO insertion. H-assisted C-O bond scission over Co is not energetically favoured until the dihydrogenated species $*CH_2O$ forms. At this stage, a key trifurcation in the reaction network occurs, as shown in Fig. 91. The moderately-segregated (5/9 Co) surface offers the lowest barrier to C-O scission ($*CH_2O + 2H* \rightarrow *CH_2 + *OH$, $E_a = 0.96$ eV), i.e., towards $CH_4$ and/or ethanol. This route is also energetically favoured over further hydrogenation to $*CH_3O$ (1.16 eV) or $*CH_2OH$ (1.28 eV), i.e., towards methanol, on the same surface. After $*CH_2O$ is split into $*CH_2$, CO insertion to form $*CH_2CO$, a key ethanol precursor, is energetically favoured over hydrogenation to $*CH_3$ (0.51 vs. 0.67 eV). CO insertion at a later stage, $*CH_3 + *CO \rightarrow *CH_3CO$, is disfavoured over methanation (0.93 vs. 0.60 eV).

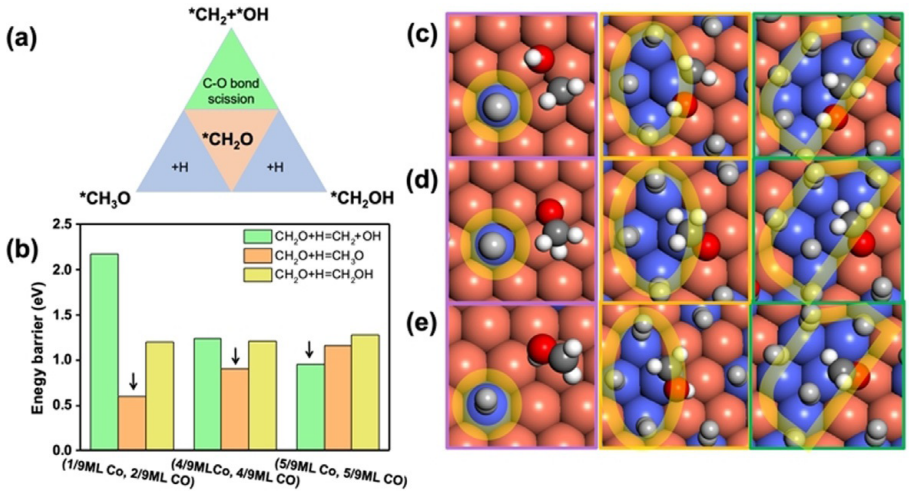


**Fig. 91** Competitive reaction network **(a)** and energy profiles **(b)** of C-O scission vs. hydrogenation of $*CH_2O$ over the 3 model Cu/Co surfaces. Transition states in C-O bond scission **(c)**, further hydrogenation to $*CH_3O$ **(d)**, or further hydrogenation to $*CH_2OH$ **(e)**.

Interfacial Cu sites effective in moderating CO adsorption and facilitating insertion into *$CH_2$ on Co are marked in transparent yellow. [Reproduced with permission from ref. 665]

In catalytic testing ($CO_2$:$H_2$ = 1:3, P = 40 bar, T = 200°C), the selectivity to ethanol reached 60% after pre-reduction in 1% CO/$N_2$ (see Fig. 92A). The main catalytic trends are shown in Fig. 92B. Activities in ethanol and methanol synthesis after pre-reduction in 1% CO both peaked at 10 and 6.5 mmol.$g_{Cu+Co}^{-1}$.$h^{-1}$ , respectively. In the absence of CO pre-treatment, methanol was the main product (80% selectivity), as expected for a Cu-rich surface, but some ethanol (20%) was also formed. In contrast, more aggressive segregation pre-treatments (10-100% CO) gave only modest yields of alcohols but resulted also in methanation (10-20% selectivity), behaviour more typical of Co. Elsewhere, Xiao et al. [666] reported a good productivity of 0.528 mmol.$g_{cat}^{-1}$.$h^{-1}$ over $CoMoC_x$, stable in multiple (x7) recycling tests, and with remarkably high selectivity to ethanol (~97%) in a static (autoclave) reactor [T = 180 °C, P = 40 bar, $H_2/CO_2$ =3/1] with added DMF. Inclusion of the solvent (for $CO_2$ enrichment) had a strong influence on catalytic performance, productivity in water falling to 0.210 mmol.$g_{cat}^{-1}$.$h^{-1}$ and 98.4% selectivity, and even lower in aniline or DMA (0.064 and 0.097 mmol.$g_{cat}^{-1}$.$h^{-1}$, respectively).

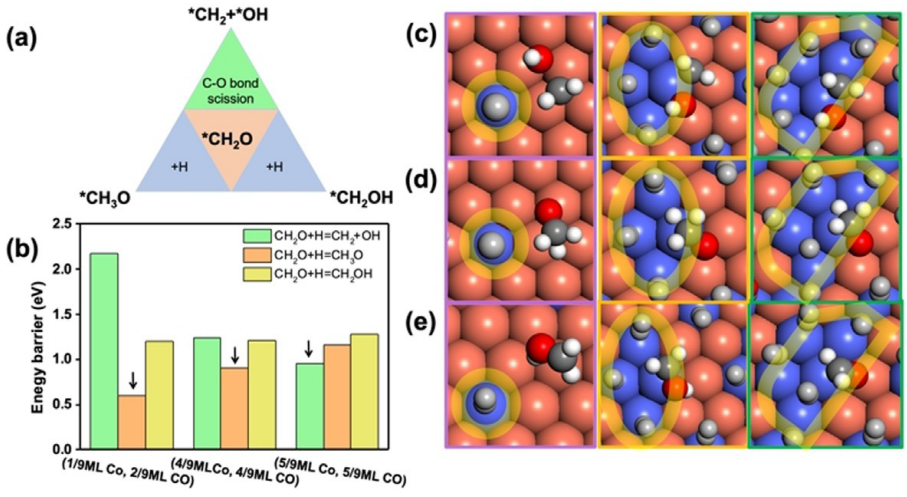

**Fig. 92 (A)** Relation between selectivity to ethanol over $CuCo/SiO_2$ and $P_{co}$ during pre-reduction. **(B)** Overall activity/selectivity trends in $CO_2$ hydrogenation. [Reproduced with permission from ref. 763]

## 9. Critical summary and outlook

Hereby we aim at taking a wider view of prospects for such a fuels-based solar-biorefinery as a pre-commercial model. An disclaimer has to be made, that it does not constitute a "negative emissions" technology except under special circumstances, as described in the text. It goes on to critically summarize the authors' view of the most appealing advances in renewable (solar) $H_2$ production, $CO_2$ recycling, and aqueous-reforming of the oxygenates concerned.

This monograph presents a holistic vision of the physico-chemical sciences, primarily applied heterogeneous catalysis and reaction engineering, underpinning the workings of a future carbon-neutral and sustainable solar biorefinery in which $H_2$ needed for a wide range of on-site hydro-processing operations is made available from low-temperature reforming of aqueous mixtures of simple ($C_1$-$C_3$) mono- and polyols, readily obtained from biomass, and solar ($e^-$) methanol by catalytic synthesis from renewable syngas.

- **Carbon-neutral H carrier based energy cycles envisaged as part of a long-term perspective.** Based as it is on a fuels platform, the energy cycle under consideration as a pre-commercial model rests implicitly on its long-term outlook as a source of marketable high-volume fuels for net-zero emission vehicular applications. Combustion of transportation fuels releases ~10 Gt $CO_2$ into the atmosphere annually (or 25% of total emissions) and is the most challenging energy sector to decarbonize. Biofuels today

comprise just 3% of transportation fuel consumption, with the ethanol component largely constrained by regulation as a low-level blending agent in gasoline.

**Growth of biorefineries.** In view of its high expansion potential, a high (6x) growth in the biofuels industry was mandated to reach 650 billion litres per annum before 2050 according to the low-carbon pathway of the International Renewable Energy Agency (IRENA). This target was originally considered to be realistic based on rapid growth in 1st generation (1G, sugar-based) biorefineries, accounting for ~100 billion litres of ethanol in 2016. However, it has signally failed to anticipate technical and regulatory constraints associated with the pioneering of sustainable 2G plants based on cellulosic feedstocks, with their notoriously high *recalcitrance*, i.e., resistance to solubilisation. 2G bioethanol as currently produced becomes competitive when the oil price exceeds USD 100 per barrel, which has already occurred periodically in the last decade. It is still the cheapest fermentation-derived liquid fuel and is likely to remain so indefinitely. However, its contribution to net-zero-emissions will only become significant when its blending level is drastically raised, e.g., as in E85 (50-85 vol% ethanol), along with a massive increase in production of compatible flex-fuel vehicles. Ethanol is also a potential precursor for higher-molecular-weight drop-in fuels urgently needed for aviation, ocean shipping, and long-haul trucking. Furthermore, when on-board fuel pre-reforming is commercialized, thermochemical recuperation of ethanol offers the prospect of a 25% increase in combustion efficiency.

- **Renewable hydrogen from splitting of water.** With the US DOE efficiency target for solar-to-hydrogen conversion (≥ 10%) now being regularly surpassed in Lab-based multi-junction PV-electrolyser devices, and steadily approached in photoelectrochemical (PEC) and suspended particulate photo-catalytic (PC) systems, renewable $H_2$ for e-methanol

synthesis could soon be competitively-priced (USD 2.50/kg). Advances have been reported in solution-processed perovskite halides as substitutes for PV-Si, computational design and screening of new multinary oxide photoelectrodes, and visible-light sensitization of photocatalysts. For PV-E, PEC, PC strategies, scale-up, adaptation for field testing and process intensification (*via* solar concentrating optics), should be urgent priorities.

- **Pivotal emerging technologies based on carbon capture utilisation and sequestration.** Advances have been made at lab and technical scale, and the *chilled ammonia* process moderates the high energetics of regeneration (< 4 GJ/$t_{CO2}$) and obviates the degradative losses typical in classical amine-based $CO_2$ scrubbing. Nanoporous adsorbents come in a burgeoning variety of classes and computational predictive power in materials discovery is advancing. The most promising candidates need to be carried forward into practical testing and engineering (micro-encapsulation, etc.) at scale. Most adsorbents for $CO_2$ suffer from competitive adsorption by water, but materials are now being developed that exploit co-adsorptive synergies in a so-called *humidity-swing* principle. Emerging processes based on *electrification* of $CO_2$ recovery offer a technology-disruptive advance. Electro-swing adsorption (ESA) will likely soon displace the more cumbersome usual pressure-and temperature-swing methodologies. There is growing interest in exploiting recycled $CO_2$ as a sustainable carbon source for green fuels and chemicals, notably where technical synergies that avoid or reduce the principal energy demands of permanent $CO_2$ storage/disposal can be exploited. Methyl formate synthesis from renewable syngas is a case in point, where methanol doubles as solvent for $CO_2$ and as co-reactant.

Critical reviews of the main methodologies for $H_2$ release *via* catalytic aqueous reforming (AR) from selected $C_1$-$C_3$ mono- and polyols – that is almost ideal in terms of thermal efficiency

– and key advances and prospects for $C_1$-$C_2$ alcohols synthesis from methanol and/or renewable syngas are further itemised below.

- **Aqueous reforming of methanol in steam** is already well-advanced in terms of technological readiness, offering stable and full conversion selectively to CO-free $H_2$ at 250°C over the benchmark $Cu/ZnO/Al_2O_3$ catalyst. Recent advances in Cu/Zn-based systems are now enabling the same performance to be achieved below 200°C, making them compatible with high-temperature PEM fuel cells working in the range 160-180°C. The close similarity in catalyst compositions with the methanol synthesis implies *microscopic reversibility*, and could lead to a stationary cyclic H-storage processor (closed $CO_2$ loop) based on a single catalyst and reactor, with substantial savings on capital expenditure.

- **Steam-reforming (SR) of higher ($C_{2+}$) oxygenates and bio-oil** to $H_2$-rich gaseous products is more problematic. Despite the thermodynamics being favourable already at T $\geq$ 250°C, temperatures to maintain significant conversion are much higher (T = 400-600°C) due to limitations in the catalysts. Most practical (economic) compositions, e.g., $Al_2O_3$-supported 1$^{st}$-row transition metals (Ni, Co, Fe), produce excessive $CH_4$ levels and are prone to deactivate *via* coking, derived mainly from polymerization of $C_2$ precursors and phenolics. Advances in catalyst stability have been made by proper incorporation of basic and rare-earth promoters that activate steam and carbon gasification, *eg.* $CeO_2$, but stable operation at temperatures close to that of methanol SR remain out-of-reach and would impose a substantial burden on net-zero emissions systems for waste heat recycling, *eg.* from biomass gasification and/or biogas ($CH_4$) combustion. Cu-based systems, *eg.*, as stable (Cu/Ni) or metastable (Cu/Co, Cu/Fe) multinary alloys, appear to offer the best prospects in future research.

- **Aqueous-phase reforming (APR)** is a promising alternative route, notably for converting higher oxygenates, *eg.*, sugars, polysaccharides, etc., that are hard or impossible to vaporise whilst avoiding thermal degradation. Unfortunately the mild conditions that prevail in APR, with reforming temperatures (175-250°C) close to the thermodynamic limits for many oxygenates, are compounded by kinetic limitations (high activation energies), often resulting in low conversions. Depending on substrate complexity, partially deoxygenated liquid intermediates can be generated beside the desired gaseous end-products. The most practical way forward is to reach an optimal balance in the product distribution, satisfying the need for $H_2$ (for on-site bio-processing), set against direct production of liquid mixtures whose value-add as individual components largely depends on their economic separation. APR is not free of issues with catalyst instability, *eg.* metal sintering (by oxidation/dissolution/re-deposition), hydrothermal degradation of the oxide support (leading to metal encapsulation), etc. Nonetheless, operation under less acidic conditions, *eg.* by simple pH adjustment, may offer a simple and practical solution.

- **Photo-reforming (PR) at near-ambient conditions** offers promise as a sustainable low-energy alternative to drive $H_2$ release from oxygenates whilst avoiding the high activation energies and on-stream deactivation (coking mechanisms) to which thermal catalytic activation is susceptible. However, the impressively-high apparent quantum efficiencies in UV-driven photo-dehydrogenation over traditional $TiO_2$-supported noble (Pt, Pd, Au), and non-noble (Ni and Cu), metal nano-deposits need to be seen in perspective. Even a catalyst with ideal UV-responsive photoefficiency ($\varphi_{UV} = 1$) offers a solar-to-hydrogen conversion efficiency ($\eta_{STH}$) restricted to just 4%., *ie.* still below the US DOE threshold value (10%) for technical viability. Furthermore, conversion rates under photonic activation, typically in the range 10-100 mmol/$g_{cat}$/h for the best photocatalysts, will only

become workable in the field under process intensification, *ie.* excitation by multiple suns power equivalent (0.5-1 $W.cm^{-2}$). This aspect has not yet been well-explored even in the laboratory with lamp-based optics. It is also fair to point out that insufficient mechanistic work has been done to establish the atom economy of "photo-reforming", *ie.* that the oxygenate of interest and water co-reactant are indeed converted selectively to renewable syngas ($H_2$ and $CO_2$ in the correct stoichiometry), with no other $C_1$ products or organic intermediates. While this has been shown for methanol, ethylene glycol, and glycerol, there remains some ambiguity for ethanol, depending on the supported metal and oxygenate concentration. Over $CuO_x/TiO_2$, vapour-phase photo-reaction yields just 1 $H_2$ per ethanol molecule. This has been justified on the basis of its high (> 90%) selectivity to acetaldehyde, a co-product providing a substantial value-add over "full" photo-reforming.

- **Synergistic dual-mode (photo-thermo) excitation may provide advantages**, viz. in methanol SR over supported Cu/Zn, and ethanol dehydrogenation to acetaldehyde over $Cu(Ni)/SiO_2$, all under mild heating ($T \approx 200°C$). The last case is an instructive example of their complementarity. Photon activation offers a new route in ethanol dehydrogenation proceeding *via* a lower-energy transition state, as reflected in the substantial lowering of the apparent activation energy, while simultaneous heating overcomes the associated thermal barrier, acting as the new rate-determining step. Cooperative light/heat effects in oxygenates reforming even extend to the mechanistic level. Photonic excitation tends to promote both C-C and C-H bond scission at comparable rates, e.g., as in decarbonylation of glycerol to formaldehyde (and $H_2$) *via* ethylene glycol intermediate, and glycolaldehyde to methanol. A mechanistic sequence of known (photo-driven) dehydrogenation and decarbonylation steps can be delineated, implying that there may be a low-energy photo-route for glycerol-to-methanol (GtM).

In the given examples on methanol SR, addition of broadband illumination, preferably at multiple sun power, raised $H_2$ production rates typically by a factor of 3x-4x over the dark (thermal) rates, with important contributions from visible absorption by the Cu component, either as a plasmonic metal or oxide ($Cu_2O$) semiconductor. The striking success of the Cu/Zn/Zr oxide nanocomposite, leading to a remarkably-high solar-to $H_2$ conversion efficiency ($\eta_{STH} \approx 45\%$), is attributed to its broad (vis-NIR) optical response, absorbing photons and generating localised heat *via* photothermal relaxation. Research into pan-spectral absorption materials is intensifying, e.g., composites based on narrow-bandgap semiconductors, and nanosized plasmonic metal co-catalysts. The last group, pertaining originally to the coinage metals, Cu, Ag, Au, Pd, etc., has rapidly been extended to include earth-abundant metals such as Al, Mg, Ti, Fe, Co, Ni and their alloys, oxides of molybdenum and tungsten, and titanium nitride. These absorb in the visible/NIR and perform catalytic action, either directly on metal adsorbates, e.g., $H_2$ dissociation on Au, or by injecting "hot" (vibrationally-excited) electrons into the underlying substrate for subsequent surface redox processes. Description of the fundamental photophysical mechanisms underpinning the so-called "localised surface plasmon resonance (LSPR) effect" is beyond the scope of this article. The ultimate objective is photo-thermo catalyst materials that integrate localised energy deposition from the entire solar spectrum.

- **Renewable methanol (RM) and ethanol synthesis from solar $H_2$ and recycled $CO_2$.** It must be said that advances have been made in the fundamentals of RM synthesis over the benchmark $Cu/ZnO/Al_2O_3$ catalyst. However, driving down the currently high cost of RM (USD 400 per ton), will depend on a breakthrough in kinetics. If catalysts can be found that are sufficiently active near the dew-point of methanol (~200°C at 100 bar), gas-phase equilibrium limitations can be overcome by the "condensing product" principle. This would lead to >99% conversion in a single pass and obviate the need for

the costly recycle sub-unit. The analogous case for ethanol synthesis from renewable syngas ($CO_2/3H_2$) is even stronger, with the dew-point (270°C) located close to the working temperature of existing catalysts. However, the selectivity remains problematic and more practical indirect ($C_1$) routes exist from methanol (*via* dimethylether and methyl acetate) over supported Cu at 250°C, yielding ethanol at roughly twice the cost of biomass fermentation. While most photo-(thermo)-activated processes in syngas conversion are confined to (exothermic) $CO_2$ methanation and reverse water-gas shift, photo-promoted methanol synthesis looks more promising.

- **The ubiquitous role of theoretical (DFT) modelling**. Even the casual reader will have recognized the growing contribution from theoretical DFT modelling in fundamental and applied catalysis, due primarily to advances in reliability, accuracy, (of prediction), and computational speed. Its value as an increasingly-more incisive tool to model the complexities of surfaces or evaluation of any influence of the aqueous environment, is well-illustrated. Better estimates of the energetics (of bound intermediates) and kinetics, *eg.* bond-type reactivity sequencing, activation energies, etc., lead to informed choices in advancing catalyst and reactor design even when accurate measurements are precluded, *eg.* by catalyst instability, a frequent problem in oxygenates steam-reforming. Empirical verification (and/or re-assessment) of DFT predictions, preferably by experiments on well-defined (model) surfaces, is ultimately indispensable to progress in the field.

- In the final analysis, catalysts for aqueous reforming of $C_{2+}$ oxygenates are needed with higher stability (resistance to coking) and better selectivity, *ie.* suppression of the mechanistic steps forming the stable $CH_4$ molecule, the main (undesirable) by-product with formal loss of two $H_2$ molecules. Priority must be given to advances in emerging catalytic

processes for converting $CH_4$, *eg.* dry reforming, pyrolysis to C (and 2 $H_2$), a potentially carbon-negative process, non-thermal plasma reforming, or partial oxidation to methanol.

## Conflicts of interest

There are no conflicts to declare.


## Acknowledgements

We would like to express our deep gratitude to James G. Highfield for his exceptional involvement in the genesis and realization of this monograph. This work could not have been completed without his unwavering commitment, perseverance, and the energy and meticulousness he devoted to this project. His dedication and expertise have been invaluable assets, and we are sincerely grateful to him.


## References


1. C.C. Ummenhofer and G.A. Meehl. Extreme weather and climate events with ecological relevance: a review. *Phil. Trans. R. Soc. B,* 2017, **372**, 20160135.
2. S. Ornes. How does climate change influence extreme weather? Impact attribution research seeks answers. *PNAS*, 2018, **115**, 8232-8235.
3. Q. Schiermeier. Droughts, heatwaves and floods: How to tell when climate change is to blame. *Nature*, 2018, 30 July, vol. 560, 20-22.
4. S.J. Davis, N.S. Lewis, M. Shaner, S. Aggarwal, D. Arent, I.L. Azevedo et al. Net-zero emissions energy systems. *Science*, 2018, **360**, eaas9793.
5. J.J. Brecha. Ten reasons to take peak oil seriously. *Sustainability*, 2013, **5**, 664-694.
6. U. Bardi. Peak oil, 20 years later: Failed prediction or useful insight? *Energy Research & Social Science*, 2019, **48**, 257-261.

7. N. P. Brandon. and Z. Kurban. Clean energy and the hydrogen economy. *Phil. Trans. R. Soc. A,* 2017, **375**: 20160400.

8. A. Sartbaeva, V.L. Kuznetsov, S.A. Wells and P.P. Edwards. Hydrogen nexus in a sustainable energy future. *Energy Environ. Sci.*, 2008, *1*, 79-85.

9. A. Valera-Medina, H. Xiao, M. Owen-Jones, W.I.F. David and P.J. Bowen. Ammonia for power. *Prog. Energy & Combustion Sci.*, 2018, **69**, 63-102.

10. A. Schneemann, J.L. White, S.Y. Kang, S. Jeong, L.F. Wan, E.S. Cho, et al. Nanostructured metal hydrides for hydrogen storage. *Chem. Rev.*, 2018, **118(22)**, 10775-10839.

11. T. He, P. Pachfule, H. Wu, Q. Xu and P. Chen. Hydrogen carriers. *Nature Reviews: Materials*, 2016, article number 16059.

12. K.E. Lamb, M.D. Dolan and D.F. Kennedy. Ammonia for hydrogen storage; A review of catalytic ammonia decomposition and hydrogen separation and purification. *Int. J. Hydrogen Energy*, 2019, **44**, 3580-3593.

13. M. Niermann, S. Drünert, M. Kaltschmitt and K. Bonhoff. Liquid organic hydrogen carriers (LOHCs) – techno-economic analysis of LOHCs in a defined process chain. *Energy Environ. Sci.*, 2019, **12**, 290-307.

14. P. T. Aakko-Saksa, C. Cook, J. Kiviaho and T. Repo. Liquid organic hydrogen carriers for transportation and storing of renewable energy - Review and discussion. *J. Power Sources*, 2018, **396**, 803-823.

15. A. Goeppert, M. Czaun, G.K.S. Prakash, G.A. Olah. Air as the renewable carbon source of the future: An overview of $CO_2$ capture from the atmosphere. *Energy Environ. Sci.*, 2012, 5, 7833.

16. T.J. Jacobsson, V. Fjällstrom, M. Edoff and T. Edvinsson, Sustainable solar hydrogen production: From photoelectrochemical cells to PV-electrolyzers and back again. *Energy Environ. Sci.*, 2014, **7**, 2056-2070

17. M. Bowker, Methanol synthesis from $CO_2$ hydrogenation. *ChemCatChem.*, 2019, **11**, 4238.

18. D.R. Palo, R.A. Dagle and J.D. Holladay, Methanol steam reforming for hydrogen production. *Chem. Rev.*, 2007, **107**, 3992-4021.

19. H.Y. Lee, I.C. Jung, G.T. Roh, Y.S. Na and H.K. Kang. Comparative Analysis of On-Board Methane and Methanol Reforming Systems Combined with HT-PEM Fuel Cell and $CO_2$ Capture/Liquefaction System for Hydrogen Fueled Ship Application. *Energies*, 2020, **13**, 224.

20. J.R. Rostrup-Nielsen. Steam reforming and chemical recuperation. *Catal. Today*, 2009, **145**, 72.

21. J.G. Highfield. The central role of catalysis in a future energy cycle based on renewable hydrogen and carbon dioxide as reactive liquefier. *Trends in Physical Chemistry*, Research Trends, Trivandrum, India, 1995, **5**, 91-156.

22. L. Tartakovsky and M. Sheintuch. Fuel reforming in internal combustion engines. *Prog. Energy Combust. Sci.*, 2018, **67**, 88- 114.

23. G. Liu, D. Willcox, M. Garland and H.H. Kung. The role of CO2 in methanol synthesis on Cu/Zn oxide: An isotope labelling study. *J. Catal.*, 1985, **96**, 251-260.

24. E.Y. García and M.A. Laborde. Hydrogen production by the steam reforming of ethanol: Thermodynamic analysis. *Int. J. Hydrogen Energy*, 1996, **16**, 307-312.

25. C.J. Jiang, D.L. Trimm, M.S. Wainwright and N.W. Cant. Kinetic mechanism for the reaction between methanol and water over a Cu-ZnO-$Al_2O_3$ catalyst. *Appl. Catal. A: Gen.*, 1993, **97**, 145.

26. G.A. Olah, A. Goeppert and G.K.S. Prakash. Beyond oil and gas: The methanol economy, 2006, 1st ed.; Wiley-VCH: Weinheim, Germany.

27. A. Goeppert, M. Czaun, J.P. Jones,G.K.S. Prakash and G.A. Olah Recycling of carbon dioxide to methanol and derived products – Closing the loop. *Chem. Soc. Rev.*, 2014, **43**, 7995–8048.

28. K. Atsonios, K.D. Panopoulos and E. Kakaras. Thermocatalytic CO2 hydrogenation for methanol and ethanol production: Process improvements. *Int. J. Hydrogen Energy*, 2016, **41**, 792- 806.

29. L.V. Mattos, G. Jacobs, B.H. Davis and F.B. Noronha. Production of hydrogen from ethanol: Review of reaction mechanism and catalyst deactivation. *Chem. Rev.*, 2012, **112**, 4094–4123.

30. R.D. Cortright, R.R. Davda and J.A. Dumesic. Hydrogen from catalytic reforming of biomass-derived hydrocarbons in liquid water. *Nature*, 2002, **418**, 964-967.

31. D. Li., X. Li and J. Gong. Catalytic reforming of oxygenates: State of the art and future prospects. *Chem. Rev.*, 2016, **116**, 11529- 11653.

32. M. Bowker. Sustainable hydrogen production by the application of ambient temperature photocatalysis. *Green Chem.*, 2011, **13**, 2235-2246.

33. A.V. Puga. Photocatalytic production of hydrogen from biomass-derived feedstocks. *Coord. Chem. Rev.,* 2016, **315**, 1- 66.

34. B. Han and Y.H. Hu. Highly efficient temperature induced visible light photocatalytic hydrogen production from water. *J. Phys. Chem. C*, 2015, **119**, 18927-18934.

35. L. Palmisano, E.I. García-López and G. Marci. Inorganic materials acting as heterogeneous photocatalysts and catalysts in the same reactions. *Dalton Trans.*, 2016, **45**, 11596-11605.

36. D. Mellman, P. Sponholz, H. Junge and M. Beller. Formic acid as a hydrogen storage material - development of homogeneous catalysts for selective hydrogen release. *Chem. Soc. Rev.*, 2016, **45**, 3954-3988.

37. J.S. Yoo, F. Abild-Pedersen, J.K. Nørskov and F. Studt. Theoretical analysis of transition-metal catalysts for formic acid decomposition. *ACS Catal.*, 2014, **4**, 1226-1233.

38. M. Navlani-García, K. Mori, Y. Kuwahara, H. Yamashita. Recent strategies targeting efficient hydrogen production from chemical hydrogen storage materials over carbon-supported catalysts. *NPG Asia Materials,* 2018, **10**, 277-292.

39. I. Yuranov, N. Autissier, K. Sordakis, A.F. Dalebrook, M. Grasemann, V. Orava et al. Heterogeneous catalytic reactor for hydrogen production from formic acid and its use in polymer electrolyte fuel cells. *ACS Sustainable Chem. Eng.*, 2018, **6***,* 6635-6643.

40. F. Valentini*,* V. Kozell, C. Petrucci, A. Marrocchi, Y. Gu, D. Gelman, L. Vaccaro. Formic acid, a biomass-derived source of energy and hydrogen for biomass upgrading. *Energy Environ. Sci.*, 2019, **12**, 2646-2664.

41. M.H. Haider, N.F. Dummer, D.W. Knight, R.L. Jenkins, M. Howard, J. Moulijn et al. Efficient green methanol synthesis from glycerol. *Nature Chem.*, 2015*,* **7**, 1028-1032.

42. F. Yang, M.A. Hanna and R. Sun. Value-added uses for crude glycerol–a byproduct of biodiesel production. *Biotechnol. Biofuels*, 2012, **5**:13.

43. A. Alvarez, A. Bansode, A. Urakawa, A.V. Bavykina, T.A. Wezendonk, M. Makkee et al. Challenges in the greener production of formates/formic acid, methanol, and DME by heterogeneously catalyzed CO2 hydrogenation processes. *Chem. Rev.*, 2017, **117**, 9804-9838.

44. S. Abate, G. Centi, P. Lanzafame, S. Perathoner. The energy- chemistry nexus: A vision of the future from sustainability perspective. *J. Energy Chem.*, 2015, **24**, 535-547.

45. R.A. Sheldon. Green and sustainable manufacture of chemicals from biomass: state of the art. *Green Chem.*, 2014, **16**, 950-963.

46. A. Tursi. A review on biomass: importance, chemistry, classification, and conversion. *Biofuel Research Journal*, 2019, **22**, 962-979.

47. G.C. Cawley. On the atmospheric residence time of anthropogenically sourced carbon dioxide. *Energy & Fuels*, 2011, **25**, 5503–5513

48. P. Ciais, C. Sabine, G. Bala, L. Bopp, V. Brovkin, J. Canadell, et al. (2013). *Carbon and other biogeochemical cycles*. In: Climate Change 2013: The Physical Science Basis. Contribution of Working Group I to the Fifth Assessment Report of the Intergovernmental Panel on Climate Change [eds., T.F. Stocker et al.] Cambridge University Press, Cambridge, UK and New York, USA

49. H. Kobayashi and A. Fukuoka. Synthesis and utilization of sugar compounds derived from lignocellulosic biomass. *Green Chem.*, 2013, **15**, 1740-1763.

50. S.V. Vassilev, D. Baxter, L.K. Andersen and C.G. Vassileva. An overview of the chemical composition of biomass. *Fuel*, 2010, **89**, 913-933.

51. D.M. Alonso, J.Q. Bon and J.A. Dumesic. Catalytic conversion of biomass to biofuels. *Green Chem.*, 2010, **12**, 1493–1513.

52. P.S. Shuttleworth, M. de Bruyn, H.L. Parker, A.J. Hunt, V.L. Budarin, A.S. Matharu and J.H. Clark. Applications of nanoparticles in biomass conversion to chemicals and fuels., *Green. Chem.*, 2014, **16**, 573-584.

53. A.M. Ruppert, K. Weinberg and R. Palkovits. Hydrogenolysis goes bio: from carbohydrates and sugar alcohols to platform chemicals. *Angew. Chem. Int. Ed.*, 2012, **51**, 2564–2601.

54. P.N.R. Vennestrøm, C.M. Osmundsen, C.H. Christensen and E. Taarning. Beyond petrochemicals: the renewable chemicals industry. *Angew. Chem. Int. Ed.*, 2011, **50**, 10502.

55. W. Matsumura and Z. Adam. Fossil fuel consumption subsidies bounced back strongly in 2018. International Energy Agency (IEA) – Commentary 13 June 2019. [www.iea.org/commentaries/fossil-fuel-consumption-subsidies-bounced-back-strongly-in-2018]

56. R. Meyer. The World Spends $400 Billion Propping Up Oil Companies. Is That Bad? The Atlantic, Feb. 08 2018. [https://www.theatlantic.com/science/archive/2018/02/maybe-cutting-fossil-fuel-subsidies-I-do-much-good/552668/]

57. D. Coady, I. Parry, N.P. Le and B. Shang. Global fossil fuel subsidies remain large: An update based on country-level estimates. International Monetary Fund (IMF) working paper no. 19/89. [https://www.imf.org/en/Publications/WP/Issues/2019/05/02/Global-Fossil-Fuel-Subsidies-Remain-Large-An-Update-Based-on-Country-Level-Estimates-46509]

58. C.O. Tuck, E. Perez, I.T. Horváth, R.A. Sheldon and M. Poliakoff, Valorization of biomass: Deriving more value from waste. *Science*, 2012, **337**, 695-699.

59. B. Kamm and M. Kamm. Principles of biorefineries. *Appl. Microbiol. Biotechnol.*, 2004, **64**, 137–145.

60. M. Aresta, A. Dibenedetto and F. Dumeignil. *Biorefineries: An Introduction.* 2015, Walter de Gruyter GmbH & Co KG, Germany.

61. E. de Jong and G. Jungmeier. Biorefinery concepts in comparison to petrochemical refineries. Chap. 1 in *Industrial Biorefineries and White Biotechnology:* 1st Edition (eds., Pandey, A. et al.), Elsevier, 2015.

62. J.B. Guinée, R. Heijungs, G. Huppes, A. Zamagni, P. Masoni, R. Buonamici et al., Life cycle assessment: Past, present, and future. *Environ. Sci. Technol.*, 2011, **45**, 90-96.

63. M.Q. Wang, J.W. Han, Z. Haq, W.E. Tyner, M. Wu and A. Elgowainy. Energy and greenhouse gas emission effects of corn and cellulosic ethanol with technology improvements and land use changes. *Biomass & Bioenergy,* 2011, **35**, 1885-1896.

64. Walter, A., Galdos, M. V., Scarpare, F. V., Leal, M. R. L. V., Seabra, J. E. A., da Cunha, M. P. et al. (2014). Brazilian sugarcane ethanol: developments so far and challenges for the future. *WIREs Energy Environ.*, 2014, **3**, 70-92. [https://onlinelibrary.wiley.com/doi/abs/10.1002/wene.87]

65. C. Valdes. Brazil's Ethanol Industry: Looking Forward. USDA Economic Research Service – Bioenergy No. (BIO-02), June 2011, 46 pp. **[**https://www.ers.usda.gov/publications/pub-details/?pubid=35829]

66. G.M. Souza, R.M. Filho, L. Cassinelli, C.H. de Brito Cruz and R.D. Godinho. *Biofuels production and consumption in Brazil: Status, advances and challenges* in IEA Bioenergy Task 39 – Commercializing conventional and advanced transport biofuels from biomass and other renewable feedstocks. Newsletter 51, April 2019. [http://task39.sites.olt.ubc.ca/files/2019/05/IEA-Bioenergy-Task-39-Newsletter-Issue-51-Final-Draft-Brazil-1.pdf.]

67. F. Cherubini and G. Jungmeier. LCA of a biorefinery concept producing bioethanol, bioenergy, and chemicals from switchgrass. *Int. J. Life Cycle Assess.*, 2010, **15**, 53-66.

68. G.A. Dantas, L.F.L. Legey and A. Mazzone. Energy from sugarcane bagasse in Brazil: An assessment of the productivity and cost of different technological routes. *Renew. Sustain. Energy Rev.*, 2013, **21**, 356-364.

69. L. Canilha, A.K. Chandel, T.S.S. Milessi, F.A.F. Antunes, W.L.C. Freitas, M.G.A. Felipe and S.S. da Silva. Bioconversion of sugarcane biomass into ethanol: An overview about

composition, pretreatment methods, detoxification of hydrolysates, enzymatic saccharification, and ethanol fermentation. *J. Biomed. Biotechnol.*, 2012, article ID 989572.

70. Dias, M. O. S., Junqueira, T. L., Cavalett, O., Cunha, M. P., Jesus, C. D. F., Rossell, C. E. et al. (2012). Integrated versus stand- alone 2nd generation ethanol production from sugarcane bagasse and trash. Bioresource Technol., *103*, 152-161.

71. Brethauer, S., Studer, M. H. (2015). Biochemical conversion processes of lignocellulosic biomass to fuels and chemicals – A review. Chimia, *69*, 572-581.

72. Angelici, C., Weckhuysen, B.M., Bruijnincx, P.C.A. (2013). Chemocatalytic conversion of ethanol into butadiene and other bulk chemicals. ChemSusChem., *6*, 1595-1614.

73. Hu, J., Yu, F., Lu, Y. (2012) Application of Fischer-Tropsch synthesis in biomass to liquid conversion. Catalysts, *2*, 303-326.

74. Rezende, C. A., de Lima, M.A., Maziero, P., de Azevedo, E.R., Garcia, W., Polikarpov, I. (2011). Chemical and morphological characterization of sugarcane bagasse submitted to a delignification process for enhanced enzymatic digestibility. Biotechnol. Biofuels, *4*, 54 (19 pages).

75. Pinaud, B. A., Benck, J. D., Seitz, L. C., Forman, A. J., Chen, Z.; Deutsch, T. G. et al. (2013) Technical and economic feasibility of centralized facilities for solar hydrogen production via photocatalysis and photoelectrochemistry. Energy Environ. Sci*., 6*, 1983-2002.

76. Shaner, M. R., Atwater, H. A., Lewis, N. S., McFarland, E. W. (2016). A comparative technoeconomic analysis of renewable hydrogen production using solar energy. Energy Environ. Sci., *9*, 2354-2371

77. Glenk, G., Reichelstein, S. (2019). Economics of converting renewable power to hydrogen. Nature Energy, *4,* 216-222.

78. Liu, G., Sheng, Y., Ager, J. W., Kraft, M., Xu, R. (2019). Research advances towards large-scale solar hydrogen production from water. EnergyChem., *1*, 100014 (51 pages).

79. Jia, J. Y., Seitz, L. C., Benck, J. D., Huo, Y., Chen, Y., Ng, J. W. et al. (2016). Solar water splitting by photovoltaic-electrolysis with a solar-to-hydrogen efficiency over 30%. Nat. Commun., *7*, 13237.

80. Nakamura, A., Ota, Y, Koike, K., Hidaka, Y., Nishioka, K., Sugiyama, M., Fujii, K. (2015). A 24.4% solar to hydrogen energy conversion efficiency by combining concentrator photovoltaic modules and electrochemical cells. Appl. Phys. Express**,** *8*, 107101 (4 pages).

81. Turan, B., Becker, J.-P., Urbain, F., Finger, F., Rau, U., Haas, S. (2016). Upscaling of integrated photoelectrochemical water splitting devices to large areas. Nat. Commun., *7*, 12681.

82. Finger, F., Welter, K., Urbain, F., Smirnov, V., Kaiser, B., Jaegermann, W. (2019). Photoelectrochemical water splitting using adapted silicon based multi-junction solar cell structures: Development of solar cells and catalysts, upscaling of combined photovoltaic-electrochemical devices and performance stability. Z. Phys. Chem., 2019, AOP (https://doi.org/10.1515/zpch-2019-1453).

83. Holmes-Gentle, I., Agarwal, H., Alhersh, F., Hellgardt, K. (2018). Assessing the scalability of low conductivity substrates for photoelectrodes via modelling of resistive losses. Phys.Chem.- Chem.Phys., *20*, 12422-12429.

84. Rowell, M. W., McGehee, M. D. (2011). Transparent electrode requirements for thin film solar cell modules. Energy Environ. Sci., *4*, 131-134.

85. Dixon, S. C., Scanlon, D. O., Carmalta, C. J., Parkin, I. P. (2016). n- Type doped transparent conducting binary oxides: an overview. J. Mater. Chem. C, *4*, 6946-6961.

86. J.P. Correa-Baena, A. Abate, M. Saliba, W. Tress, T.J. Jacobsson, M. Grätzel and A. Hagfeldt. The rapid evolution of highly efficient perovskite solar cells. *Energy Environ. Sci.*, 2017, **10**, 710-727.

87. NREL (2020). Best research cell efficiency chart [www.nrel.gov/pv/cell-efficiency.html]

88. Li, X., Bi, D., Yi, C., Décoppet, J.-D., Luo, J., Zakeeruddin, S. M., Hagfeldt, A., Grätzel, M. (2016). A vacuum flash–assisted solution process for high-efficiency large-area perovskite solar cells. Science, vol. 353, issue #6294, pp. 58-62.

89. Yun, S., Qin, Y., Uhl, A. R., Vlachopoulos, N., Yin, M., Li, D., Han X., Hagfeldt, A. (2018). New-generation integrated devices based on dye-sensitized and perovskite solar cells. Energy Environ. Sci., *11*, 476-526.

90. Khan, M. A., Zhao, H., Zou, W., Chen, Z., Cao, W., Fang, J. et al. (2018). Recent progresses in electrocatalysts for water electrolysis. Electrochem. Energy Rev., *1*, 483-530.

91. Wijten, J. H. J., Riemersma, R. L., Gauthier, J., Mandemaker, L. D. B. Verhoeven, M. W. G. M., Hofmann, J. P. et al. (2019). Electrolyte effects on the stability of Ni-Mo cathodes for the hydrogen evolution reaction. ChemSusChem., *12*, 3491-3500.

92. Vidales, A. G., Omanovic, S. (2018). Evaluation of nickel-molybdenum-oxides as cathodes for hydrogen evolution by water electrolysis in acidic, alkaline, and neutral media. Electrochim. Acta, *262*, 115-123.

93. Hunter, B. M., Gray, H. B., Müller, A. M. (2016). Earth-abundant heterogeneous water oxidation catalysts. Chem. Rev., *116*, 14120-14136.

94. Mavrokefalos, C. K., Patzke, G. R. (2019). Water oxidation catalysts: The quest for new oxide-based materials. Inorganics, *7*, 29 (37 pages). [https://doi.org/10.3390/inorganics7030029]

95. Montoya, J. H., Seitz, L. C., Chakthranont, P., Vojvodic, A., Jaramillo, T. F., Nørskov, J. K. (2016). Materials for solar fuels and chemicals. Nat. Mater., *16*, 70-81.

96. Takanabe, K. (2017). Photocatalytic water splitting: Quantitative approaches toward photocatalyst by design. ACS Catal., *7*, 8006-8022.

97. Weh, I.Z., Kibsgaard, J., Dickens, C.F., Chorkendorff, I., Nørskov, J. K., Jaramillo, T.F. (2017). Combining theory and experiment in electrocatalysis: Insights into materials design. Science, Vol. 355*,* issue 6321, [eaad4998].

98. Stein, H. S., Gregoire, J. M. (2019). Progress and prospects for accelerating materials science with automated and autonomous workflows. Chem. Sci., *10*, 9640-9649.

99. Yan, Q., Yu, J., Suram, S. K., Zhou, L., Shinde, A., Newhouse, P. F. et al. Solar fuels photoanode materials discovery by integrating high-throughput theory and experiment. *PNAS*, 2017, **114 (12)**, 3040-3043.

100. Castelli, I. E., Hüser, F., Pandey, M., Li, H., Thygesen , K. S., Seger, B. et al. (2015). New light-harvesting materials using accurate and efficient bandgap calculations. Adv. Energy Mater., 5, 1400915.

101. Pan, L., Kim, J. H., Mayer, M. T., Son, M.-K., Ummadisingu, A., Lee, J. S. et al. (2018). Boosting the performance of Cu2O photocathodes for unassisted solar water splitting devices. Nat. Catal., *1*, 412-420.

102. Pan, L., Liu, Y., Yao, L., Ren, D., Sivula, K., Grätzel, M., Hagfeldt, A. (2020). Cu2O photocathodes with band-tail states assisted hole transport for standalone solar water splitting. Nat. Commun., *11*, article no. 318.

103. Tamirat, A. G., Rick, J., Dubale, A. A., Sub, W.-N., Hwang, B.-J. (2016). Using hematite for photoelectrochemical water splitting: a review of current progress and challenges. Nanoscale Horiz., *1,* 243-267.

104. Segev, G., Dotan, H., Malviya, K. D., Kay, A., Mayer, M. T., Grätzel, M., Rothschild, A. (2015). High solar flux concentration water splitting with hematite (α-Fe2O3) photoanodes. Adv. Energy Mater., 1500817 (7 pages).

105. Liardet, L., Katz, J. E., Luo, J., Grätzel, M., Hu, X. (2019). An ultrathin cobalt-iron oxide catalyst for water oxidation on nanostructured hematite photoanodes. J. Mater. Chem. A, *7*, 6012-6020.

106. Tilley, S. D. (2019). Recent advances and emerging trends in photoelectrochemical solar energy conversion. Adv. Energy Mater., 9, 1802877.

107. Jian, J., Jiang, G., van de Krol, R., Weia, B., Wang, H. (2018). Recent advances in rational engineering of multinary semiconductors for photoelectrochemical hydrogen generation. Nano Energy, *51*, 457-480.

108. Pihosh, Y., Turkevych, I., Mawatari, K., Uemura, J., Kazoe, Y., Kosar, S. et al. (2015). Photocatalytic generation of hydrogen by core-shell WO3/BiVO4 nanorods with ultimate water splitting efficiency. Sci. Rep., *5*, 1114 (10 pages).

109. Kim, T. W., Choi, K. S. (2016). Improving Stability and photoelectrochemical performance of BiVO4 photoanodes in basic media by adding a ZnFe2O4 layer. J Phys Chem Lett., *7***,** 447-451.

110. Zachäus, C., Abdi, F. F., Peter, L. M., van de Krol, R. (2017). Photocurrent of BiVO4 is limited by surface recombination, not surface catalysis. Chem. Sci., *8*, 3712-3719.

111. Sullivan, I., Zoellner, B., Maggard, P. A. (2016). Copper(I)-based *p*-type oxides for photoelectrochemical and photovoltaic solar energy conversion. Chem. Mater., *28*, 5999-6016.

112. Septina, W., Tilley, S. D. (2017). Emerging earth-abundant materials for scalable solar water splitting. Curr. Op. Electrochem., 2, 120-127.

113. Prévot M. S., Li, Y., Guijarro, N., Sivula, K. (2016). Improving charge collection with delafossite photocathodes: A host-guest CuAlO2/CuFeO2 approach**.** J. Mater. Chem. A*,* *4,* 3018-3026.

114. Patil, R., Kelkar, S., Naphadeab, R., Ogale, S. (2014). Low-temperature grown CuBi2O4 flower morphology and its composite with CuO nanosheets for photoelectrochemical water splitting. J. Mater. Chem. A, *2*, 3661-3668.

115. Sharma, G., Zhao, Z., Sarker, P., Nail, B. A., Wang, J., Huda, M. N., Osterloh, F. E. (2016). Electronic structure, photovoltage, and photocatalytic hydrogen evolution with p-CuBi2O4 nanocrystals. J. Mater. Chem. A, *4*, 2936-2942.

116. Ida**,** S.**,** Yamada, K., Matsunaga, T., Hagiwara, H., Matsumoto, Y., Ishihara, T. (2010). Preparation of p-type CaFe2O4 photocathodes for producing hydrogen from water. J. Am. Chem. Soc., *132*, 17343-17345.

117. Gottesman, R., Song, A., Levine, I., Krause, M., Nazmul-Islam, A. T. M., Abou-Ras, D. et al. (2020). Pure CuBi2O4 photoelectrodes with increased stability by rapid thermal processing of Bi2O3/CuO grown by psed laser deposition. Adv. Funct. Mater., 1ul910832.

118. Ida, S., Kearney, K., Futagami, T., Hagiwara, H., Sakai, T., Watanabe, M. et al. (2017). Photoelectrochemical H2 evolution using TiO2-coated CaFe2O4 without an external applied bias under visible light irradiation at 470 nm based on device modeling. Sustain. Energy Fuels, *1*, 280-287.

119. Bloesser, A., Timm, J., Kurz, H., Milius, W., Hayama, S., Breu, J. et al. (2020). A novel synthesis yielding macroporous CaFe2O4 sponges for solar energy conversion. Sol. RRL, *4*, 1900570.

120. Huang, H., Pradhan, B., Hofkens, J., Roeffaers, M. B. J., Steele, J.A. (2020). Solar-driven metal halide perovskite photocatalysis: Design, stability, and performance. ACS Energy Lett., *5*, 1107- 1123.

121. Liu, Y., Yang, Z., Cui, D., Ren, X., Sun, J., Liu, X., Zhang, J. et al. (2015). Two-inch-sized perovskite CH3NH3PbX3 (X = Cl, Br, I) crystals: Growth and characterization. Adv. Mater., *27*, 5176- 5183.

122. Luo, J. S., Im, J.-H., Mayer, M. T., Schreier, M., Nazeeruddin, M. K., Park, N.-G., Tilley, S. D. et al. (2014). Water photolysis at 12.3% efficiency via perovskite photovoltaics and earth- abundant catalysts. Science, Vol. 345, Issue 6204, pp. 1593- 1596.

123. Poli, I., Hintermair, U., Regue, M., Kumar, S., Sackville, E. V., Baker, J. et al. (2019). Graphite-protected CsPbBr3 perovskite photoanodes with water oxidation catalyst for oxygen evolution in water. Nat. Commun., *10*, 2097 (10 pages).

124. Li, Z.-J., Hofman, E., Li, J., Davis, A. H., Tung, C.-H., Wu, L.-Z., Zheng, W. (2018). Photoelectrochemically active and environmentally stable CsPbBr3/TiO2 core/shell nanocrystals. Adv. Funct. Mater., *28*, 1704288 (7 pages).

125. Han, N., Liu, P., Jiang, J., Ai, L., Shao, Z., Liu, S. (2018). Recent advances in nanostructured metal nitrides for water splitting. J. Mater. Chem. A, *6*, 19912-19933

126. Garcia-Muñoz, P., Fresno, F., de la Peña O'Shea, V. A., Keller, N. (2020). Ferrite materials for photo-assisted environmental and solar fuels applications. Top. Curr. Chem., *378*, article number: 6.

127. Lee, T. H., Kim, S. Y., Jang, H. W. (2016). Black phosphorus: Critical review and potential for water splitting photocatalyst. Nanomaterials, *6*, 194 (16 pages).

128. Liu, J., Ma, N., Wu, W., He, Q. (2020). Recent progress on photocatalytic heterostructures with full solar spectral responses. Chem. Eng. J., *393*, 124719 (21 pages).

129. Wang, Q., Domen, K. (2020). Particulate photocatalysts for light-driven water splitting: Mechanisms, challenges, and design strategies. Chem. Rev., *120*, 919-985.

130. Liu, J., Liu, Y., Liu, N., Han, Y., Zhang, X., Huang, H. et al. (2015). Metal-free efficient photocatalyst for stable visible water splitting via a two-electron pathway. Science, vol. 347, issue 6225, pp. 970-974.

131. Guo, H.-L., Du, H., Jiang, Y.-F., Jiang, N., Shen, C., Zhou, X. et al. (2017). Artificial photosynthetic Z-scheme photocatalyst for hydrogen evolution with high quantum efficiency. J. Phys. Chem. C, *121*, 107-114.

132. Hafeez, H. Y., Lakhera, S. K., Narayanan, N., Harish, S., Hayakawa, Y., Lee, B.-K., Neppolian, B. (2019). Environmentally sustainable synthesis of a CoFe2O4−TiO2/rGO ternary photocatalyst: A highly efficient and stable photocatalyst for high production of hydrogen (solar fuel). ACS Omega, *4*, 880-891.

133. Li, W., Elzatahry, A., Aldhayan, D., Zhao, D. (2018). Core–shell structured titanium dioxide nano-materials for solar energy utilization. Chem. Soc. Rev., *47*, 8203-8237.

134. Liao, L., Zhang, Q., Su, Z., Zhao, Z., Wang, Y., Li, Y. et al. (2014). Efficient solar water-splitting using a nanocrystalline CoO photocatalyst. Nat. Nanotechnol., *9*, 69-73.

135. Tian, B., Tian, B., Smith, B., Scott, M. C, Hua, R., Lei, Q., Tian, Y. (2018). Supported black phosphorus nanosheets as hydrogen- evolving photocatalyst achieving 5.4% conversion efficiency at 353K. Nat. Commun., *9*, 1397 (11 pages).

136. Shi, Y., Zhang, B. (2016). Recent advances in transition metal phosphide nanomaterials: synthesis and applications in hydrogen evolution reaction. Chem. Soc. Rev., *45*, 1529-1541.

137. Goto, Y., Hisatomi, T., Wang, Q., Higashi,T., Ishikiriyama, K., Maeda, T. et al. (2018). A particulate photocatalyst water- splitting panel for large-scale solar hydrogen generation. Joule, *2*, 509-520.

138. Wang, Z., Li, C., Domen, K. (2019). Recent developments in heterogeneous photocatalysts for solar-driven overall water splitting. Chem. Soc. Rev., *48*, 2109-2125.

139. Wang, Y., Suzuki, H., Xie, J., Tomita, O., Martin, D. J., Higashi, M. et al. (2018). Mimicking natural photosynthesis: Solar to renewable H2 fuel synthesis by Z-scheme water splitting systems. Chem. Rev., *118*, 5201-5241.

140. Chandran, R. B., Breen, S., Shao, Y., Ardo, S., Weber, A. Z. (2018). Evaluating particle-suspension reactor designs for Z-scheme solar water splitting *via* transport and kinetic modeling. Energy Environ. Sci., *11*, 115-135.

141. Rogelj, J., D. Shindell, K. Jiang, S. Fifita, P. Forster, V. Ginzburg, C. et al. (2018). Mitigation pathways compatible with 1.5°C in the context of sustainable development. In: *Global Warming of 1.5°C. An IPCC Special Report on the impacts of global warming of 1.5°C above pre-industrial levels and related global greenhouse gas emission pathways, in the context of strengthening the global response to the threat of climate change, sustainable development, and efforts to eradicate poverty.* Mason-Delmotte, V. et al., eds. IPCC, Switzerland. [https://www.ipcc.ch/sr15/.]

142. 170 Gambhira, A., Rogelj, J., Luderer, G., Fewa, S., Nappa, T. (2019). Energy system changes in 1.5°C, well below 2°C and 2°C scenarios. Energy Strat. Rev., *23*, 69-80.

143. 171 Bui, M., Adjiman, C. S., Bardow, A., Anthony, E. J., Boston, A., Brown, S. et al. (2018). Carbon capture and storage (CCS): the way forward. Energy Environ. Sci., *11*, 1062-1176.

144. Renforth, P., Wilcox, J. (2019). Specialty grand challenge: Negative emission technologies. Front. Clim. 1:1 [https://doi.org/10.3389/fclim.2019.00001]

145. Anderson, K., Peters, G. (2016). The trouble with negative emissions. Science, *354*, 182-183.

146. McLaren, D. P., Tyfield, D. P., Willis, R., Szerszynski, B., Markusson, N. O. (2019). Beyond “net-zero”: A case for separate targets for emissions reduction and negative emissions. Front. Clim. 1:4.

147. Chakravartya, S., Chikkaturb, A., de Coninck, H., Pacala, S., Socolow, R., Tavonia, M. (2009). Sharing global CO2 emission reductions among one billion high emitters. PNAS, *106*, 11884– 11888.

148. Shue, H. (2018). Mitigation gambles: uncertainty, urgency and the last gamble possible. Phil. Trans. R. Soc. A *376*, 20170105 (11 pages).

149. Klinsky, S., Winkler, H. (2018). Building equity in: Strategies for integrating equity into modelling for a 1.5°C world. Phil. Trans. R. Soc*., 376*, 20160461.

150. Larkin, A., Kuriakose, J., Sharmina, M., Anderson, K. (2018). What if negative emission technologies fail at scale? Implications of the Paris Agreement for big emitting nations. Climate Policy, *18*, 690-714. [https://doi.org/10.1080/14693062.2017.1346498]

151. Net social benefits of carbon dioxide removal: Carbon cycle feedbacks and strategic advantages (CDRECON). Environment and Natural Resources Unit [Project: 12/2019-12/2022], IFW Kiel Institute for the World Economy.

152. Fasihi, M., Efimova, O., Breyer, C. (2019). Techno-economic assessment of CO2 direct air capture plants. J. Cleaner Prod., *224,* 957-980.

153. Keith, D. W., Holmes, G., St. Angelo, D., Heidel, K. (2018). A process for capturing CO2 from the atmosphere. Joule, *2*, 1573- 1594.

154. Shi, X., Xiao, H., Azarabadi, H., Song, J., Wu, X., Chen, X., Lackner, K. S. (2020). Sorbents for the direct capture of CO2 from ambient air. Angew. Chem. Int. Ed., *59*, 2-25.

155. Mortezaei, K., Amirlatifi, A., Ghazanfari, E., Vahedifard, F. (2018). Potential CO2 leakage from geological storage sites: Advances and challenges. Environ. Geotechnics, paper 1800041. [https://doi.org/10.1680/jenge.18.00041]

156. Kelermen, P., Benson, S. M., Pilorgé, H., Psarras, P., Wilcox, J. (2019). An overview of the status and challenges of CO2 storage in minerals and geological formations. Front. Clim. 1:9 [https://doi.org/10.3389/fclim.2019.00009]

157. Construction work progresses at large-scale carbon capture demonstration facility. Mar. 2019. [https://www.toshiba- energy.com/en/thermal/topics/ccs-1.htm]

158. Voegele, E. (2019). Drax aims to become carbon negative by 2030. Dec. 2019. [biomassmagazine.com/articles/16664/drax- aims-to-become-carbon-negative-by-2030]

159. Strapasson, A., Woods, J., Chum, H., Kalas, N., Shah, N., Rosillo- Calle, F. (2017). On the global limits of bioenergy and land use for climate change mitigation. GCB Bioenergy, *9*, 1721-1735.

160. Garnett, T., Roos, E., Little, D. (2015). Lean, green, mean, obscene.? What is efficiency? And is it sustainable? Animal production and consumption reconsidered. Food Climate Research Network.

161. Fasihi, M., Efimova, O., Breyer, C. (2019). Techno-economic assessment of CO2 direct air capture plants. J. Clean Prod., *224*, 957-980.

162. Lackner, K.S., Brennan, S., Matter, J.M., Alissa Park, A.-H, Wright, A., v.d. Zwaana, B. (2012). The urgency of the development of CO2 capture from ambient air. PNAS, *109*, 13156-13162.

163. IEA. *Tracking Transport 2019* [www.iea.org/reports/tracking- transport-2019/transport-biofuels]

164. Lehtveer, M., Brynolf, S., Grahn, M. (2019). What future for electrofuels in transport? Analysis of cost competitiveness in global climate mitigation. Environ. Sci. Technol., *53*, 1690-1697.

165. Abanades, J. C., Rubin, E. S., Mazzotti, M., Herzog, H. J. (2017). On the climate change mitigation potential of CO2 conversion to fuels. Energy Environ. Sci., *10*, 2491-2499.

166. MacDowell, N., Fennell, P. S., Shah, N., Maitland, G. C. (2017). The role of CO2 capture and utilization in mitigating climate change. Nat. Clim. Change, *7*, 243-249.

167. Friedlingstein, P., Jones, M. W., O'Sullivan, M., Andrew, R. M., Hauck, J., Peters, G. P. et al. (2019). Global carbon budget 2019. Earth Syst. Sci. Data, *11*, 1783-1838.

168. Walsh, B., Ciais, P., Janssens, I. A., Peñuelas, J., Riahi, K., Rydzak, F. et al. (2017). Pathways for balancing CO2 emissions and sinks. Nat. Comm., *8*, 14856 (12 pages).

169. Gielena, D., Boshella, F., Saygin, D., Bazilian, M. D., Wagner, N., Gorini, R. (2019). The role of renewable energy in the global energy transformation. Energy Strat. Rev., *24*, 38-50.

170. Figueres, C. et al. (2017). Three years to safeguard our climate. Nature, *546*, 593-595.

171. Al-Mamoori, A., Krishnamurthy, A., Rownaghi, A. A., Rezaei, F. (2017). Carbon capture and utilization update. Energy Technol., *5*, 834-849.

172. Nwaoha, C., Saiwan, C., Tontiwachwuthikul, P., Supap, T., Rongwong, W., Idem, R. et al. (2016). Carbon dioxide (CO2) capture: Absorption-desorption capabilities of 2-amino-2-methyl-1-propanol (AMP), piperazine (PZ) and monoethanolamine (MEA) tri-solvent blends. J. Nat. Gas Sci. Eng., *33*, 742-750.

173. Augustsson, O., Baburao, B., Dube, S., Bedell, S., Strunz, P., Balfe, M., Stallmann, O. (2017). Chilled ammonia process scale-up and lessons learned. GHGT-13. Energy Procedia *114*, 5593- 5615.

174. Jiang,K., Li, K., Yu, H., Feron, P. H. M. (2018). Piperazine- promoted aqueous-ammonia-based CO2 capture: Process optimization and modification. Chem. Eng. J., *347*, 334-342.

175. Nematollahi, M. H., Carvalho, P. J. (2019). Green solvents for CO2 capture. Curr. Op. Green & Sust. Chem., *18*, 25-30.

176. Mahurin, S. M., Hillesheim, P. C., Yeary, J. S., Jiang, D., Dai, S. (2012). High CO2 solubility, permeability and selectivity in ionic liquids with the tetracyanoborate anion. RSC Advances, *2*, 11813-11819.

177. Ma, C., Laaksonen, A., Liu, C., Lu, X., Ji, X. (2018). The peculiar effect of water on ionic liquids and deep eutectic solvents. Chem. Soc. Rev., *47*, 8685-8720.

178. Kaviania, S., Kolahchyan, S., Hickenbottom, K. L., Lopez, A. M., Nejati, S. (2018). Enhanced solubility of carbon dioxide for encapsulated ionic liquids in polymeric materials. Chem. Eng. J., *354*, 753-757.

179. Zeeshan, M., Nozari, V., Yagci, M. B., Isık, T., Unal, U., Ortalan, V. et al. (2018). Core-shell type ionic liquid/metal organic framework composite: An exceptionally high CO2/CH4 selectivity. J. Am. Chem. Soc., *140*, 10113-10116.

180. Oschatz, M., Antonietti, M. (2018). A search for selectivity to enable CO2 capture with porous adsorbents. Energy Environ. Sci., *11*, 57-70.

181. Modak, A., Jana, S. (2019). Advancement in porous adsorbents for post-combustion CO2 capture. Micropor. Mesopor. Mater., *276*, 107-132.

182. Ünveren, E. E., Monkul, B. O., Sarıoglan, S., Karademir, N., Alper, E. (2017). Solid amine sorbents for CO2 capture by chemical adsorption: A review. Petroleum, *3*, 37-50.

183. Ding, M., Flaig, R. W., Jiang, H.-L., Jaghi, O. M. (2019). Carbon capture and conversion using metal–organic frameworks and MOF-based materials. Chem. Soc. Rev., *48*, 2783-2828.

184. Xu, C., Yu, G., Yuan, J., Strømme, M., Hedin, N. (2020). Microporous organic polymers as CO2 adsorbents: advances and challenges. Mater. Today Adv., *6*, 100052 (9 pages).

185. Zhang, Z., Cano, Z. P., Luo, D., Dou, H., Yu, A., Chen, Z. (2019). Rational design of tailored porous carbon-based materials for CO2 capture. J. Mater. Chem. A, *7*, 20985-21003.

186. Dissanayake, P. D., You, S., Igalavithana, A. D., Xia, Y., Bhatnagar, A., Gupta, S. et al. (2020). Biochar-based adsorbents for carbon dioxide capture: A critical review. Renew. Sustain. Energy Rev., *119*, 109582 (14 pages).

187. Jin, S., Ho, K., Lee, C.-H. (2018). Facile synthesis of hierarchically porous MgO sorbent doped with CaCO3 for fast CO2 capture in rapid intermediate temperature swing sorption. Chem. Eng. J. *334*, 1605-1613.

188. Varghese, A. M., Karanikolos, G. N. (2020). CO2 capture adsorbents functionalized by amine-bearing polymers: A review. Int. J. Green. Gas Contr., *96,* 103005 (33 pages).

189. Avci, G., Velioglu, S., Keskin, S. (2018). High-throughput screening of MOF adsorbents and membranes for H2 purification and CO2 capture. ACS Appl. Mater. Interfaces, *10*, 33693-33706.

190. Borboudakis, G., Stergiannakos, T., Frysali, M., Klontzas, E., Tsamardinos, I., Froudakis, G. E. (2017). Chemically intuited, large-scale screening of MOFs by machine learning techniques. NPJ Comput. Mater., *3*, 40 (7 pages).

191. Lee, Y., Barthel, S. D., Dłotko, B., Moosavi, S. M., Hess, K., Smit, B. (2018). High-throughput screening approach for nanoporous materials genome using topological data analysis: Application to zeolites. J. Chem. Theory Comput., *14*, 4427-4437.

192. Ongari,D., Yakutovich, A.V., Talirz, L., Smit, B. (2019). Building a consistent and reproducible database for adsorption evaluation in covalent–organic frameworks. ACS Cent. Sci., *5*, 1663-1675.

193. Furukawa, H., Cordova, K. E., O'Keeffe, M., Yaghi, O. M. (2013). The chemistry and applications of metal-organic frameworks. Science, *341*, 1230444 (12 pages).

194. Moosavi, S. M., Xu, H., Chen, L., Cooper, A. I., Smit, B. (2020). Geometric landscapes for material discovery within energy– structure–function maps. Chem. Sci., *11*, 5423-5433.

195. Cooper, A. I. (2017). Porous Molecular Solids and Liquids. ACS Cent. Sci., *3*, 544-553.

196. Yaghi, O. M. (2019). Reticular chemistry in all dimensions. ACS Cent. Sci., 5, 1295-1300.

197. Hou, J., Sapnik, A. F., Bennett, T. D. (2020). Metal-organic framework gels and monoliths. Chem. Sci., *11*, 310-323.

198. Siegelman, R.L., Milner, P.J., Forse, A.C., Lee, J.-H., Colwell, K.A., Neaton, J.B. et al. (2019). Water enables efficient CO2 capture from natural gas flue emissions in an oxidation-resistant diamine-appended metal–organic framework. J. Am. Chem. Soc., *141*, 13171-13186.

199. Boyd, P. G., Chidambaram, A., García-Díez, E., Ireland, C., Daff, T., Bounds, R. et al. (2019). Data-driven design of metal-organic frameworks for wet flue gas CO2 capture. Nature, *576*, 253-256.

200. Potter, M. E., Cho, K.M., Lee, J. J., Jones, C. W. (2017). Role of alumina basicity in CO2 uptake in 3-aminopropylsilyl-grafted alumina adsorbents. ChemSusChem., *10*, 2192-2201.

201. Shi, X., Li, Q., Wang, T., Lackner, K. S. (2017). Kinetic analysis of an anion exchange absorbent for CO2 capture from ambient air. PLoS ONE, 12, e0179828 (12 pages).

202. Xiao, H., Shi, X., Zhang, Y., Liao, X., Hao, F., Lackner, K. S., Chen, X. (2017). The catalytic effect of H2O on the hydrolysis of CO32− in hydrated clusters and its

implication in the humidity driven CO2 air capture. Phys. Chem. Chem. Phys., *19*, 27435-27441.

203. Song, J., Zhu, L., Shi, X., Liu, Y., Xiao, H., Chen, X. (2019). Moisture swing ion-exchange resin-PO4 sorbent for reversible CO2 capture from ambient air. Energy Fuels, *33*, 6562-6567.

204. Wang, T., Gea, K., Chen, K., Hou, C., Fang, M. (2016). Theoretical studies on CO2 capture behaviour of the quaternary ammonium- based polymeric ionic liquids. Phys. Chem. Chem. Phys., *18*, 13084-13091.

205. Robeson, L. M. (2008). The upper bound revisited. J. Membr. Sci., *320*, 390-400.

206. Zhao, S., Feron, P. H. M., Deng, L., Favre, E. Chen, V. (2016). Status and progress of membrane contactors in post-combustion carbon capture: A state-of the-art review of new developments. J. Membr. Sci., *511*, 180-206.

207. Xie, K., Fu, Q., Qiao, G. G., Webley, P.A. (2019). Recent progress on fabrication methods of polymeric thin film gas separation membranes for CO2 capture. J. Membr. Sci., *572*, 38-60.

208. Wang, S., Li, X., Wu, H., Tian, Z., Xin, Q., He, G. et al. (2016). Advances in high permeability polymer-based membrane materials for CO2 separations. Energy Environ. Sci., *9*, 1863- 1890.

209. Liu, J., Hou, X., Park, H. B., Lin, H. (2016). High-performance polymers for membrane CO2/N2 separation. Chem. Eur. J., *22*, 15980-15990.

210. Li, Y., Xin, Q., Wu, H., Guo, R., Tian, Z., Liu,Y. et al. (2014). Efficient CO2 capture by humid-ified polymer electrolyte membranes with tunable water state. Energy Environ. Sci., *7*, 1489-1499.

211. Dai, Z., Ansaloni, L., Ryan, J. J., Spontak, R. J., Deng, L. (2018). Nafion/IL hybrid membranes with tuned nanostructure for enhanced CO2 separation: Effects of ionic liquid and water vapor. Green Chem., *20*, 1391-1404.

212. Ma, C., Urban, J. J. (2018). Polymers of intrinsic microporosity (PIMs) gas separation membranes: A mini review. Proc. Nat. Res. Soc*., 2,* 02002 (19 pages).

213. Kim, J., Abouelnasr, M., Lin, L.-C., Smit, B. (2013). Large-scale screening of zeolite structures for CO2 membrane separations. J. Am. Chem. Soc., *135*, 7545-7552.

214. Zhao, R., Liu, A., Zhao, L., Deng, S., Li, S., Zhang, Y. (2019). A comprehensive performance evaluation of temperature swing adsorption for post-combustion carbon dioxide capture. Renew. Sust. Energy Rev., *114*, 109285 (13 pages).

215. Ribeiro, R. P. P. L., Grande, C. A., Rodrigues, A. E. (2014). Electric swing adsorption for gas separation and purification: A review. Sep. Sci. Technol., *49*, 1985-2002.

216. Regufe, M. J., Ferreira, A. F. P., Loureiro, J. M., Rodrigues, A., Ribeiro**,** A. F. (2020). Development of hybrid materials with activated carbon and zeolite 13X for CO2 capture from flue gases by electric swing adsorption. Ind. Eng. Chem. Res., *59*, 12197-12211.

217. Wilcox. J. (2020). An electro-swing approach. Nature Energy, *5*, 121-122.

218. Voskian, S., Hatton, T. A. (2019). Faradaic electro-swing reactive adsorption for CO2 capture. Energy Environ. Sci., *12*, 3530- 3547.

219. Daggash, H. A., Patzschke, C. F., Heuberger, C. F., Zhu, L., Hellgardt, K., Fennell, P. S. et al. (2018). Closing the carbon cycle to maximise climate change mitigation: Power-to-methanol vs. power-to-direct air capture. Sustainable Energy Fuels, *2*, 1153- 1169.

220. Legrand, L., Schaetzle, O., de Kler, R. C. F., Hamelers, H. V. M. (2018). Solvent free CO2 capture using membrane capacitive deionization (MCDI). Environ. Sci. Technol., *52*, 9478-9485.

221. Rahimi, M., Catalini, G., Hariharan, S., Wang, M., Puccini, M., Hatton, T. A. (2020). Carbon dioxide capture using an electrochemically driven proton concentration process. Cell Rep. Phys. Sci., *1*, 100033 (19 pages).

222. Zhu, X., Imtiaz, Q., Donat, F., Müller, C. R., Li, F. (2020). Chemical looping beyond combustion – a perspective. Energy Environ. Sci., *13*, 772-804.

223. Valverde, J. M. (2013). Ca-based synthetic materials with enhanced CO2 capture efficiency. J. Mater. Chem. A, *1*, 447-468.

224. Chen, Z. X., Song, H. S., Portillo, M., C. Lim, J., Grace, J. R., Anthony, E. J. (2009). Long-term calcination/carbonation cycling and thermal pretreatment for CO2 Capture by limestone and dolomite. Energy & Fuels, *23,* 1437-1444.

225. Sun, H., Wu, C., Shen, B., Zhang, X., Zhang, Y., Huang, J. (2018). Progress in the development and application of CaO-based adsorbents for CO2 capture - a review. Mater. Today Sustain., *1- 2* 1-27

226. Liu, W., Low, N. W. L., Feng, B., Wang, G., da Costa, J. C. D. (2010). Calcium precursors for the production of CaO sorbents for multicycle CO2 capture. Environ. Sci. Technol., *44*, 841-847.

227. Kurlov, A., Armutlulu, A., Donat, F., Studart, A. R., Müller**,** C. R. (2020). CaO-based CO2 sorbents with a hierarchical porous structure made via microfluidic droplet templating. Ind. Eng. Chem. Res., *59*, 7182-7188.

228. Zeng, l., Cheng, Z., Fan, J. A., Fan, L.-S., Gong, J. (2018). Metal oxide redox chemistry for chemical looping processes. Nat. Rev. Chem., *2*, 349-364.

229. Lyngfelt, A., Linderholm, C. (2017) Chemical looping combustion of solid fuels – status and recent progress (GHG-13, Lausanne). Energy Procedia, *114*, 371-386.

230. Zhao, X., Zhou, H., Sikarwar, V. S., Zhao, M., Park, A.-H. A., Fennell, P. S. et al. (2017). Biomass-based chemical looping technologies: The good, the bad and the future. Energy Environ. Sci., *10*, 1885-1910.

231. Hu, J., Galvita, V. V., Poelman, H., Marin, G. B. (2018). Advanced chemical looping materials for CO2 utilization: A review. Materials, *11*, 1187 (32 pages).

232. Artz, J., Müller, T. E., Thenert, K., Kleinekorte, J., Meys, R., Sternberg, A., Bardow, A., Leitner, W. (2018). Sustainable conversion of carbon dioxide: An integrated review of catalysis and life cycle assessment. Chem. Rev., *118*, 434-504.

233. Joos, L., Huck, J. M., van Speybroeck, V., Smit, B. (2016). Cutting the cost of carbon capture: A case for carbon capture and utilization. Faraday Discuss., *192*, 391-414.

234. Ho, H.-J., Iizuka, A., Shibata, E. (2019). Carbon capture and utilization technology without carbon dioxide purification and pressurization: A review on its necessity and available technologies. Ind. Eng. Chem. Res., *58*, 8941-8954.

235. Kar, S., Goeppert, A., Surya Prakash, G. K. (2019). Integrated CO2 capture and conversion to formate and methanol: Connecting two threads. Acc. Chem. Res., *52*, 2892-2903.

236. Rumayor, M., Dominguez-Ramos, A., Irabien, A. (2018). Formic acid manufacture: Carbon dioxide utilization alternatives. Appl. Sci., *8*, 914 (12 pages).

237. Hietala, J., Vouri, A., Pekka, J., Ilkka, P., Reutemann, W., Heinz, K. (2000). Formic Acid. In Ullmann's Encyclopedia of Industrial Chemistry; Wiley-VCH:Weinheim, Germany, pp. 1-22.

238. Jens, C.M., Müller, L., Leonhard, K., Bardow, A. (2019). To integrate or not to integrate - techno-economic and life cycle assessment of CO2 capture and conversion to methyl formate using methanol. ACS Sustainable Chem. Eng. 7, 12270–12280.

239. Gatti, M., Martelli, E., Marechal, F., Consonni, F. (2014). Review, modeling, heat integration, and improved schemes of Rectisol®-based processes for CO2 capture. Appl. Thermal Eng., *70*, 1123-1140.

240. Scott, M., Molinos, B. B., Westhues, C., Francio, G., Leitner, W. (2017). Aqueous biphasic systems for the synthesis of formates by catalytic CO2 hydrogenation: integrated reaction and catalyst separation for CO2-scrubbing solutions. ChemSusChem., *10*, 1085-1093.

241. Scott, M., Westhues, C. G., Kaiser, T., Baums, J. C., Jupke, A., Franciò, G., Leitner, W. (2019). Methylformate from CO2: an integrated process combining catalytic hydrogenation and reactive distillation. Green Chem., *21*, 6307-6317

242. Herron, J. A., Kim, J., Upadhye, A. A., Huber, G. W., Maravelias, C. T. (2015). A general framework for the assessment of solar fuel technologies. Energy Environ. Sci., *8*, 126-157.

243. Singha, M. R., Clark, E. L., Bell, A. T. (2015). Thermodynamic and achievable efficiencies for solar-driven electrochemical reduction of carbon dioxide to transportation fuels. PNAS E6111–E6118

244. Spitler, M. T., Modestino, M. A., Deutsch, T. G., Xiang, C. X., Durrant, J. R., Esposito, D. V. et al. (2019). Practical challenges in the development of photoelectrochemical solar fuels production. Sustainable Energy & Fuels, *4*, 985-995.

245. Vu, N. N., Kaliaguine, S., Do, T.O. (2019). Critical aspects and recent advances in structural engineering of photocatalysts for sunlight-driven photocatalytic reduction of CO2 into fuels. Adv. Funct. Mater., *29*, 1901825 (44 pages).

246. Chang, X. X., Wang, T., Gong, J. L. (2016). CO2 photo-reduction: Insights into CO2 activation and reaction on surfaces of photocatalysts. Energy Environ. Sci., ***9***, 2177-2196.

247. Chen, G. B., Waterhouse, G. I. N., Shi, R., Zhao, J. Q., Li, Z. H., Wu, L. Z. et al. (2019). Solar-to-fuels: Recent advances in light-driven C1 chemistry. Angew. Chem. Int. Ed., *58*, 17528-17551.

248. Xie, B. Q., Wong, R. J., Tan, T. H., Higham, M., Gibson, E. K., Decarolis, D. et al. (2020). Synergistic ultraviolet and visible light photoactivation enables intensified low-temperature methanol synthesis over copper/zinc oxide/alumina. Nature Commun., *11*, 1615 (11 pages). [https://doi.org/10.1038/s41467-020- 15445-z]

249. Keller, N., Ivanez, J., Highfield, J., Ruppert, A. M. (2021). Photo-/thermal synergies in heterogeneous catalysis: towards low- temperature (solar-driven) processing for sustainable energy and chemicals. Appl. Catal. B: Environ., 2021, **296**, 120320.

250. Xu, Y., Isom, L., Hanna, M.A. (2010). Adding value to carbon dioxide from ethanol fermentations. Bioresource Technol., *101*, 3311-3319.

251. Yentekakis, I.V., Goula, G. (2017). Biogas management: Advanced utilization for production of renewable energy and added-value chemicals. Front. Environ. Sci., 16 February 2017.

252. He, X. Z. (2018). A review of material development in the field of carbon capture and the application of membrane-based processes in power plants and energy-intensive industries. Energy, Sustainability and Society, *8*, 34 (14 pages). [energsustainsoc.biomedcentral.com/articles/10.1186/s13705-018-0177-9]

253. Abate, S., Lanzafame, P., Perathoner, S., Centi, G. (2015). New sustainable model of biorefineries: Biofactories and challenges of integrating bio- and solar refineries. ChemSusChem., *8*, 2854-2866.

254. Schlögl, R. (2012). The Solar Refinery. *Chemical Energy Storage*. Chap. 1, 1-34. Walter de Gruyter GmbH & Co KG, Germany.

255. Smith, P.J., Smith, L., Dummer, N.F., Douthwaite, M., Willock, D. J., Howard, M. et al. (2019). Investigating the influence of reaction conditions and the properties of ceria for the valorisation of glycerol. Energies, *12*, 1359.

256. Bozell, J. J., Petersen, G. R. (2010). Technology development for the production of biobased products from biorefinery carbohydrates - the US Department of Energy's "Top 10" revisited. Green Chem., *12*, 539-554.

257. Nda-Umar, U. I., Ramli, I., Taufiq-Yap, Y. H., Muhamad, E. N. (2019). An overview of recent research in the conversion of glycerol into biofuels, fuel additives and other bio-based chemicals. Catalysts, *9*, 15 (47 pages).

258. Kostyniuk, A., Bajec, D., Likozar, B. (2020). One step synthesis of ethanol from glycerol in a gas phase packed bed reactor over hierarchical alkali-treated zeolite catalyst materials. Green Chem., *22*, 753-765.

259. Simpson, S. (2017). *Syngas fermentation to ethanol*. Lanza Tech presentation at BETO Project Peer Review Meeting & Workshop, March 6th-9th 2017, Colorado State University. [www.energy.gov/sites/prod/files/2017/07/f35/BETO_2017W TE-Workshop_SeanSimpsonLanzaTech.pdf]

260. Ao, M., Pham, G. H., Sunarso, J., Tade, M. O., Liu, S. (2018). Active centers of catalysts for higher alcohol synthesis from syngas: A review. ACS Catal., *8*, 7025-7050.

261. Schievano, A., Pant, D., Puig, S. (2019). Editorial: Microbial synthesis, gas-fermentation and bioelectroconversion of CO2 and other gaseous streams. Front. Energy Res., *7*, 110.

262. Alvarez, A., Bansode, A., Urakawa, A., Bavykina, A. V., Wezendonk, T. A., Makkee, M. et al. (2017). Challenges in the greener production of formates/formic acid, methanol, and DME by heterogeneously catalyzed CO2 hydrogenation processes. Chem. Rev., *117*, 9804-9838.

263. Eagen, N. M., Kumbhalkar, M. D., Buchanan, J. S., Dumesic, J. A., Huber, G. W. (2019). Chemistries and processes for the conversion of ethanol into middle-distillate fuels. Nature Reviews Chem., *3*, 223-249.

264. Blanc, P., Espinar, B., Geuder, N., Gueymard, C., Meyer, R., Pitz- Paal, R. et al. (2014). Direct normal irradiance related definitions and applications: The circumsolar issue. Solar Energy, *110,* 561-577.

265. Muhich, C. L., Ehrhart, B. D., Al-Shankiti, I., Ward, B. J., Musgrave, C. B. (2016). A review and perspective of efficient hydrogen generation via thermal water splitting. WIREs Energy Environ., *5*, 261-287.

266. Rao, C. N. R., Deya, S. (2017). Solar thermochemical splitting of water to generate hydrogen. PNAS, *114*, 13385-13393.

267. Luoa, M., Yia, Y., Wang, S., Wang, Z., Dua, M., Pan, J., Wang, Q. (2018). Review of hydrogen production using chemical-looping technology. Renew. Sustain. Energy Rev., *81*, 3186-3214.

268. Kruesi, M., Jovanovic, Z. R., Steinfeld, A. (2014). A two-zone solar-driven gasifier concept: Reactor design and experimental evaluation with bagasse particles. Fuel, *117*, 680-687.

269. Madala, S., Boehm, R. F. (2017). A review of non-imaging solar concentrators for stationary and passive tracking applications. Renew. Sustain. Energy Rev., *71,* 309-322

270. Berrizbeitia, S. E., Gago, E. J., Muneer, T. (2020). Empirical models for the estimation of solar sky-diffuse radiation. A review and experimental analysis. Energies, *13*, 701.

271. Jiang, C., Yu, L., Yang, S., Li, K., Wang, J., Lund, P. D., Zhang, Y. (2020). A review of the compound parabolic concentrator (CPC) with a tubular absorber. Energies, *13*, 695.

272. Cao, F., Wei, Q., Liu, H., Lu, N., Zhao, L., Guo, L. (2018). Development of the direct solar photocatalytic water splitting system for hydrogen production in Northwest China: Design and evaluation of photoreactor. Renew. Energy, *121*, 153-163.

273. Bonke, S.A., Wiechen, M., MacFarlane, D.R., Spiccia, L. (2015). Renewable fuels from concentrated solar power: Towards practical artificial photosynthesis. Energy Environ. Sci., *8*, 2791- 2796.

274. Chen, Y. K., Xiang, C. X., Hu, S., Lewis, N. S. (2014). Modeling the performance of an integrated photoelectrolysis system with 10x solar concentrators. J. Electrochem. Soc., *161* (10), F1101- F1110.

275. Khamooshi, M., Salati, H., Egelioglu, F., Faghiri, A. H., Tarabishi, J., Babadi, S. (2014). A review of solar photovoltaic concentrators. Int. J. Photoenergy, article ID 958521 (17 pages).

276. Angulo, A., v. d. Linde, P., Gardeniers, H., Modestino, M., Fernández Rivas, D. (2020). Influence of bubbles on the energy conversion efficiency of electrochemical reactors. Joule, *4*, 555- 579.

277. Modestino, M. A., Mohammad, S., Hashemi, H., Haussener, S. (2016). Mass transport aspects of electrochemical solar- hydrogen generation. Energy Environ. Sci., *9,* 1533-1551.

278. Cambié, D., Zhao, F., Hessel, V., Debije, M. G., Noël, T. (2017). A leaf-inspired luminescent solar concentrator for energy efficient continuous-flow photochemistry. Angew. Chem. Int. Ed., *56*, 1050-1054.

279. Modestino, M. A., Fernandez-Rivas, D., Hashemi, S. M. H., Gardeniers, J. G. E., Psaltis, D. (2016). The potential for microfluidics in electrochemical energy systems. Energy Environ. Sci., *9*, 3381-3391.

280. Suman, S., Khan, M. K., Pathak, M. (2015). Performance enhancement of solar collectors - A review. Renew. Sustain. Energy Rev., *49*, 192-210.

281. Jiang, L., Widyolara, B., Winston, R. (2015). Characterization of novel mid-temperature CPC solar thermal collectors. Energy Procedia, *70*, 65-70.

282. Kulkarni, G. N., Kedare, S. B., Bandyopadhyay, S. (2008). Design of solar thermal systems utilizing pressurized hot water storage for industrial applications. Solar Energy, *82*, 686-699.

283. Chamsa-ard, W., Brundavanam, S., Fung, C. C., Fawcett, D., Poinern, G. (2017). Nanofluid types, their synthesis, properties and incorporation in direct solar thermal collectors: A review. Nanomaterials, *7*, 131.

284. Su, L., Hu, Y., Ma, Z., Miao, L., Zhou, J., Ning, Y. et al. (2020). Synthesis of hollow copper sulfide nanocubes with low emissivity for highly efficient solar steam generation. Sol. Energy Mater. Sol. Cells, *210*, 110484.

285. Cantero, D., Jara, R., Navarrete, A., Pelaz, L., Queiroz, J., Rodríguez-Rojo, S., Cocero, M. J. (2019). Pretreatment processes of biomass for biorefineries: Current status and prospects. Annu. Rev. Chem. Biomol. Eng., *10*, 289-310.

286. Neumann, O., Neumann, A. D., Tian, S., Thibodeaux, C., Shubhankar, S., Mueller, J. et al. (2017). Combining solar steam processing and solar distillation for fully off-grid production of cellulosic bioethanol. ACS Energy Lett., *2*, 8-13.

287. M. Wang, M. Liu, J. Liu and F. Wang, Photo splitting of bio- polyols and sugars to methanol and syngas. *Nat. Commun.,* 2020, **11**, 1083.

288. M. A. Sainna, S. Nanavati, C. Black, L. Smith, K. Mugford, H. Jenkins et al. A combined periodic DFT and QM/MM approach to understand the radical mechanism of the catalytic production of methanol from glycerol. *Faraday Discuss.*, 2021, **229**, 108-130.

289. H. R.Yue, H. R., Zhao, Y. J., Ma, X. B. and J. L. Gong. Ethylene glycol: properties, synthesis, and applications. *Chem. Soc. Rev*., 2012, **41**, 4218-4244.

290. A. Y. Yin, X. Y. Guo, W. L. Dai and K. N. Fan. The synthesis of propylene glycol and ethylene glycol from glycerol using Raney Ni as a versatile catalyst**.** *Green Chem.,* 2009, **11**, 1514-1516

291. C. T. Wu, K. M. K. Yu, F. L. Liao, N. Young, P. Nellist, A. Dent et al. A non-syngas catalytic route to methanol production. *Nat. Comm*., 2012, **3**, 1050 (8 pages).

292. X. Jin, C. Li, C. Xu, D. Guan, A. Cheruvathur, Y. Wang et al. (2017). Photocatalytic C-C bond cleavage in ethylene glycol on $TiO_2$: A molecular level picture and the effect of metal nanoparticles. *J. Catal*., 2017, **354**, 37-45.

293. G. Busca, J. Lamotte, J.-C. Lavalley and V. Lorenzelli. FTIR study of the adsorption and transformation of formaldehyde on oxide surfaces. *J. Am. Chem. Soc*., 1987, **109**, 5197-5202.

294. Y. Y. Birdja and M. T. M. Koper. The importance of Cannizzaro- type reactions during electrocatalytic reduction of carbon dioxide. *J. Am. Chem. Soc*., 2017, **139**, 2030-2034.

295. M. Bursová, T. Hložek and R. Čabala, R. Simultaneous determination of methanol, ethanol and formic acid in serum and urine by headspace GC-FID. *J. Anal. Toxicol*., 2015, **39**, 741- 745.

296. T. Lepage, M. Kammoun, Q. Schmetz and A. Richel. Biomass-to-hydrogen: A review of main routes production, processes evaluation and techno-economical assessment. *Biomass and Bioenergy,* 2021, **144**, 105920.

297. V. S. Sikarwar, M. Zhao, P. Clough, J. Yao, X. Zhong, M. Z. Memon et al. An overview of advances in biomass gasification. *Energy Environ. Sci*., 2016, **9**, 2939-2977.

298. A. Arregi, M. Amutio, G. Lopez, J. Bilbao and M. Olazar. Evaluation of thermochemical routes for hydrogen production from biomass: A review. *Energy Conv. Manage*. 2018, **165**, 696- 719.

299. W. Nabgan, T. A. T. Abdullaha, R. Mat, B. Nabgan, Y. Gambo, M. Ibrahim et al. Renewable hydrogen production from bio-oil derivative via catalytic steam reforming: An overview. *Renew. Sustain. Energy Rev*., 2017, **79**, 347-357.

300. C. Guizani, M. Jeguirim S. Valin, L. Limousy and S. Salvador. Biomass chars: The effects of pyrolysis conditions on their morphology, structure, chemical properties and reactivity. *Energies*, 2017, **10**, 796 (18 pages).

301. A. Giuliano, C. Freda and E. Catizzone. Techno-economic assessment of bio-syngas production for methanol synthesis: A focus on the water–gas shift and carbon capture sections. *Bioengineering,* 2020**, 7,** 70 (19 pages).

302. V. Dieterich, A. Buttler, A. Hanel, H. Spliethoff and S. Fendt. Power-to-liquid via synthesis of methanol, DME or Fischer– Tropsch fuels: a review, *Energy Environ. Sci.*, 2020, **13**, 3207– 3252.

303. M. Zhu and I. E. Wachs. Iron-based catalysts for the high- temperature water–gas shift (HT-WGS) reaction: A review. *ACS Catal*., 2016, **6**, 722-732.

304. A Iulianelli, S Liguori, J Wilcox and A Basile. Advances on methane steam reforming to produce hydrogen through membrane reactors technology: A review. *Catal. Rev.- Sci. Eng*., 2016, 58, 1-35.

305. H. Ishak and I. Dincer. Comparative assessment of renewable energy-based hydrogen production methods. *Renew. Sustain. Energy Rev*., 2021, **135**, 110192 (13 pages).

306. J. Grams and A. M. Ruppert. Development of heterogeneous catalysts for thermo-chemical conversion of lignocellulosic biomass. *Energies*, 201**7**, **10**, 545 (25 pages).

307. J. Ren, J.-P. Cao, X. Y. Zhao, F. L. Yang and X. Y. Wei. Recent advances in syngas production from biomass catalytic gasification: A critical review on reactors, catalysts, catalytic mechanisms and mathematical models. *Renew. Sustain. Energy Rev.,* 2019, **116**, 109426 (25 pages)

308. A. Oasmaa, J. Lehto, Y. Solantausta and S. Kallio. Historical review on VTT fast pyrolysis bio-oil production and upgrading. *Energy Fuels,* 2021, **35**, 5683−5695.

309. B. Luna-Morillo, M. Pala, A. L. Paioni, M. Baldus, F. Ronsse, W. Prins, P. M. A. Bruijnincx and B. M. Weckhuysen. Catalytic fast pyrolysis of biomass: Catalyst characterization reveals the feed-dependent deactivation of a technical ZSM-5-based catalyst. *ACS Sustainable Chem. Eng*., 2021, **9**, 291-304.

310. J. Grams and A. M. Ruppert. Catalyst stability-Bottleneck of efficient catalytic pyrolysis. *Catalysts*, 2021, **11**, 265 (24 pages).

311. A. M. Ranjekar and G. D. Yadav. Steam reforming of methanol for hydrogen production: A critical analysis of catalysis, processes, and scope. *Ind. Eng. Chem. Res*., 2021, **60**, 89−113.

312. E. C. Vagia and A. A. Lemonidou. Thermodynamic analysis of hydrogen production via steam reforming of selected components of aqueous bio-oil fraction. *Int. J. Hydrogen Energy*, 2007, **32**, 212-223.

313. J. M. Silva, M. A. Soria and L. M. Madeira. Challenges and strategies for optimization of glycerol steam reforming process. *Renew. Sustain. Energy Rev.,* 2015, **42**, 1187-1213.

314. Y. Lwin, W. R. W. Daud, A. B. Mohamad and Z. Yaakob. Hydrogen production from steam-methanol reforming: Thermodynamic analysis. *Int. J. Hydrogen Energy*, 2000, **25**, 47-53.

315. D. Pashchenko. Thermochemical recuperation by ethanol steam reforming: Thermodynamic analysis and heat balance *Int. J. Hydrogen Energy*, 2019, **44**, 30865-30875.

316. P. Biswas and D. Kunzru. Steam reforming of ethanol for production of hydrogen over Ni/ $CeO_2$–$ZrO_2$ catalyst: Effect of support and metal loading. *Int. J. Hydrogen Energy*, 2007, **32**, 969-980.

317. X. Li, Z. Zhang, L. Zhang, H. Fan, X. Li, Q. Liu, S. Wang and X. Hu. Investigation of coking behaviors of model compounds in bio-oil during steam reforming. *Fuel*, 2020, **265**, 116961.

318. G. Chen, J. Tao, C. Liu, B. Yan, W. Li and X. Li. Hydrogen production via acetic acid steam reforming: A critical review on catalysts. *Renew. Sustain. Energy Rev*., 2017, **79**, 1091–1098.

319. C. R. Correa and A. Kruse. Supercritical water gasification of biomass for hydrogen production – Review. *J Supercrit. Fluids*, 2018, **133**, 573-590.

320. D. Castello, T. H. Pedersen and L. A. Rosendahl. Continuous hydrothermal liquefaction of biomass: A critical review. *Energies*, 2018, **11**, 3165 (35 pages).

321. O. Yakaboylu, J. Harinck, K. G. Smit and W. de Jong Supercritical water gasification of biomass: A literature and technology overview. *Energies,* 2015, **8**, 859-894.

322. F. A. P. Voll, C. R. S. Rossi, C. Silva, R. Guirardello, R. O. M. A. Souza, V. F. Cabral and L. Cardozo-Filho. Thermodynamic analysis of supercritical water gasification of methanol, ethanol, glycerol, glucose and cellulose. *Int. J. Hydrogen Energy,* 2009, **34**, 9737-9744.

323. G. W. Huber, J. W Shabaker and J. A. Dumesic. Raney Ni-Sn catalyst for $H_2$ production from biomass-derived hydrocarbons. *Science*, 2003, **300**, 2075-2077.

324. A. Fasolini, R. Cucciniello, E. Paone, F. Mauriello and T. Tabanelli. A short overview on the hydrogen production via aqueous phase reforming (APR) of cellulose, $C_6$-$C_5$ sugars and polyols. *Catalysts***,** 2019, **9**, 917 (16 pages).

325. D. M. Alonso, S. G. Wettstein and J. A. Dumesic. Bimetallic catalysts for upgrading of biomass to fuels and chemicals. *Chem. Soc. Rev.*, 2012, **41**, 8075-8098.

326. J. S. Luterbacher, D. M. Alonso and J. A. Dumesic. Targeted chemical upgrading of lignocellulosic biomass to platform molecules. *Green Chem*., 2014, **16**, 4816–4838.

327. M. Alvear, A. Aho, I. L. Simakova, H. Grénman, T. Salmi and D. Y. Murzin. Aqueous phase reforming of xylitol and xylose in the presence of formic acid. *Catal. Sci. Technol.,* 2020, **10**, 5245–5255

328. J. Zhang, W. Yan, Z. An, H. Song and J. He. Interface-promoted dehydrogenation and water-gas shift toward high-efficient $H_2$ production from aqueous phase reforming of cellulose. *ACS Sustainable Chem. Eng*., 2018, **6**, 7313−7324.

329. J. Zhang, Y. Zhu, Z. An, X. Shu, X. Ma, H. Song et al. Mg-vacancy-induced Ni-vacancy clusters: Highly efficient hydrogen production from cellulose. *J. Mater. Chem. A*, 2020, **8**, 14697- 14705.

330. M. El Doukkali, A. Iriondo, J. F. Cambra, I. Gandarias, L. Jalowiecki-Duhamel, F. Dumeignil and P. L. Arias. Deactivation study of the Pt and/or Ni-based □-$Al_2O_3$ catalysts used in the aqueous phase reforming of glycerol for $H_2$ production. *Appl. Catal. A: Gen.,* 2014, **472**, 80-91.

331. A. Bogaerts, X. Tu, J. C. Whitehead, G. Centi L. Lefferts, O. Guaitella, F. Azzolina-Jury, H.-H. Kim et al. The 2020 plasma catalysis roadmap. *J. Phys. D: Appl. Phys.* 2020, **53**, 443001.

332. L. Wang, Y. Yi, C. Wu, H. Guo and X. Tu. One-step reforming of $CO_2$ and $CH_4$ into high-value liquid chemicals and fuels at room temperature by plasma-driven catalysis. *Angew. Chem. Int. Ed.,* 2017, **56**, 13679-13683.

333. R. Zhou, R. Zhou, Y. Xian, Z. Fang, X. Lu, K. Bazaka, A. Bogaerts and K. Ostrikov. Plasma-enabled catalyst-free conversion of ethanol to hydrogen gas and carbon dots near room temperature. *Chem. Eng. J*., 2020, **382**, 122745.

334. C. M. Du, J. M. Mo and H. X. Li. Renewable hydrogen production by alcohols reforming using plasma and plasma-catalytic technologies: Challenges and opportunities. *Chem. Rev.* 2015, **115**, 1503-1542.

335. X. Zhao, L. Du, B. You and Y. Sun. Integrated design for electrocatalytic carbon dioxide reduction. *Catal. Sci. Technol.,* 2020, **10**, 2711-2720.

336. Z. H. N. Al-Azri, W.-T. Chen, A. Chan, V. Jovic, T. Ina, H. Idriss and G. I. N. Waterhouse. The roles of metal co-catalysts and reaction media in photocatalytic hydrogen production: Performance evaluation of $M/TiO_2$ photocatalysts (M = Pd, Pt, Au) in different alcohol-water mixtures. *J. Catal*., 2015, **329**, 355-367.

337. M. F. Kuehnel and E. Reisner. Solar hydrogen generation from lignocellulose. *Angew. Chem. Int. Ed.*, 2018, **57**, 3290-3296.

338. T. Uekert, C. M. Pichler, T. Schubert and E. Reisner. Solar-driven reforming of solid waste for a sustainable future. *Nature Sustain.,* 2021, **4**, 383-391.

339. D. S. Achilleos, W. Yang, H. Kasap, A. Savateev, Y. Markushyna, J. R. Durrant and E. Reisner. Solar reforming of biomass with homogeneous carbon dots. *Angew. Chem. Int. Ed*., 2020, **59**, 18184-18188.

340. D. W. Wakerley, M. F. Kuehnel, K. L. Orchard, K. H. Ly, T. E. Rosser and E. Reisner. Solar -driven reforming of lignocellulose to $H_2$ with a $CdS/CdO_x$ photocatalyst. *Nature Energy,* 2017**, 2**, 17021.

341. A. Caravaca, W. Jones, C. Hardacre and M. Bowker. $H_2$ production by the photocatalytic reforming of cellulose and raw biomass using Ni, Pd, Pt and Au on titania. *Proc. R. Soc. A,* 2016*,* **472**, 20160054 (21 pages).

342. J. R. Bolton. Solar Photoproduction of Hydrogen: A Review. *Solar Energy*,1996, **57**, 37-50.

343. N. Serpone and A. V. Emeline. Semiconductor Photocatalysis—Past, Present, and Future Outlook. *J. Phys. Chem. Lett.,* 2012, **3**, 673–677.

344. S. L. Kollmannsberger, C. A. Walenta, C. Courtois, M. Tschurl and U. Heiz. Thermal control of selectivity in photocatalytic, water-free alcohol photo-reforming. *ACS Catal.*, 2018, **8**, 11076-11084.

345. S. I. Nikitenko, T. Chave, C. Cau, H.-P. Brau and V. Flaud. Photothermal hydrogen production using noble metal-free Ti@$TiO_2$ core-shell nanoparticles under visible-NIR light irradiation. *ACS Catal.*, 2015, **5**, 4790–4795.

346. L. Lin, W. Zhou, R. Gao, S. Yao, X. Zhang, W. Xu, S. Zheng, Z. Jiang et al. Low-temperature hydrogen production from water and methanol using Pt/α-MoC catalysts. *Nature*, 2017, **544**, 80-96.

347. B. Frank, F.C. Jentoft, H. Soerijanto, J. Kröhnert, R. Schlögl and R. Schomäcker. Steam reforming of methanol over copper-containing catalysts: influence of support material on microkinetics. J. Catal., 2007, 246, 177-192.

348. M. A. Nadeem and H. Idriss. Photo-thermal reactions of ethanol over Ag/$TiO_2$ catalysts. The role of silver plasmon resonance in the reaction kinetics, *Chem. Commun.*, 2018, **54**, 5197–5200.

349. T. Hou, S. Zhang, Y. Chen, D. Wang and W. Cai. Hydrogen production from ethanol reforming: Catalysts and reaction mechanism. *Renew. Sust. Energy Rev.,* 2015, **44**, 132–148.

350. S. Luo, H. Songa, D. Philo, M. Oshikiri, T. Kako and J. Ye. Solar-driven production of hydrogen and acetaldehyde from ethanol on Ni-Cu bimetallic catalysts with solar-to-fuels conversion efficiency up to 3.8 %. *Appl. Catal. B: Environ.,* 2020, **272**, 118965 (9 pages).

351. R. Wang, H. Liu and Z. Zheng. Low temperature light-assisted hydrogen production from aqueous reforming ethylene glycol over $Pt/Al_2O_3$ and $Pd/Al_2O_3$ catalysts. *J. Fuel Chem. Technol.,* 2019, **47**, 1486-1494.

352. M. Faheem, M. Saleheen, J. Lu and A. Heyden. Ethylene glycol reforming on Pt (111): First-principles microkinetic modeling in vapor and aqueous phases. *Catal. Sci. Technol.*, 2016, **6**, 8242-8256.

353. S. L. Kollmannsberger, C. A. Walenta, C. Courtois, M. Tschurl, and U. Heiz. Thermal control of selectivity in photocatalytic, water-free alcohol photo-reforming. *ACS Catal.* 2018, **8**, 11076-11084.

354. F. J. Gutiérrez Ortiz and F. J. Campanario. Hydrogen production from supercritical water reforming of acetic acid, acetol, 1-butanol and glucose over Ni-based catalyst. *J. Supercrit. Fluids*, 2018, **138**, 259–270.

355. X. Li, S. Wang, Y. Zhu, G. Yang and P. Zheng. DFT study of bio-oil decomposition mechanism on a Co stepped surface: Acetic acid as a model compound. *Int. J. Hydrogen Energy*, 2015, **40**, 330-339.

356. B. V. Ayodele, T. A. Abdullah, M. A. Alsaffar, S. I. Mustapa and S. F. Salleh. Recent advances in renewable hydrogen production by thermo-catalytic conversion of biomass-derived glycerol: Overview of prospects and challenges. *Int. J. Hydrogen Energy*, 2020, 45, 18160-18185.

357. G. Bagnato, A. Iulianelli, A. Sanna and A. Basile. Glycerol production and transformation: A critical review with particular emphasis on glycerol reforming reaction

for producing hydrogen in conventional and membrane reactors. *Membranes,* 2017, **7**, 17 (31 pages).

358. A. G. Gayubo, B. Valle, B. Aramburu, C. Montero and J. Bilbao. Kinetic model considering catalyst deactivation for the steam reforming of bio-oil over $Ni/La_2O_3$-$\alpha Al_2O_3$. *Chem. Eng. J.*, 2018, **332**, 192–204.

359. M. Bakhtiari, M. A. Zahid, H. Ibrahim, A. Khan, P. Sengupta and R. Idem. Oxygenated hydrocarbons steam reforming over $Ni/CeZrGdO_2$ catalyst: Kinetics and reactor modeling. *Chem. Eng. Sci.,* 2015, **138**, 363-374.

360. A.S. Oliveira, A. Aho, J.A. Baeza, L. Calvo, I.L. Simakova, M.A. Gilarranz and D. Y. Murzin. Enhanced $H_2$ production in the aqueous-phase reforming of maltose by feedstock pre-hydrogenation. *Appl. Catal. B: Environ*., 2021 **281**, 119469.

361. K.C. Christoforidis and P. Fornasiero. Photocatalytic hydrogen production: A rift into the future energy supply. *ChemCatChem*., 2017, **9**, 1523-1544.

362. M. Melchionna and Paolo Fornasiero. Updates on the roadmap for photocatalysis. *ACS Catal*. 2020, **10**, 5493-5501.

363. M. Ghoussoub, M. Xia, P.N. Duchesne, D. Segal, G. Ozin, Principles of photothermal gas-phase heterogeneous $CO_2$ catalysis, *Energy Environ. Sci.*, 2019,**12**, 1122-1142.

364. Z. Wang, H. Song, H. Liu and J. Ye, Coupling of solar energy and thermal energy for carbon dioxide reduction: status and prospects, *Angew. Chem. Int. Ed*., 2020, **59**, 8016-8035.

365. M. S. Frei, C. Mondelli, M. I. M. Short and J. Pérez-Ramírez. Methanol as a hydrogen carrier: Kinetic and thermodynamic drivers for its $CO_2$-based synthesis and reforming over catalysts. *ChemSusChem,* 2020, **13(23)**, 6330-6337.

366. S. Sarp, S. G. Hernandez, C. Chen and S. W. Sheehan. Alcohol production from carbon dioxide: Methanol as a fuel and chemical feedstock. *Joule*, 2020, **5**, 59-76.

367. A. A. Tountas, X. Peng, A. V. Tavasoli, P. N. Duchesne, T. L. Dingle, Y. Dong, L. Hurtado, A. Mohan, W. Sun, U. Ulmer, L. Wang, T.E. Wood, C.T. Maravelias, M.M. Sain, G.A. Ozin. Towards solar methanol: Past, present, and future. *Adv. Sci.,* 2019, **6**, 1801903 (52 pages).

368. V. Palma, C. Ruocco, M. Cortese and M. Martino. Bioalcohol reforming: An overview of the recent advances for the enhancement of catalyst stability. *Catalysts*, 2020, **10**, 665.

369. J. Zhao, R. Shi, Z. Li, C. Zhou and T. Zhang. How to make use of methanol in green catalytic hydrogen production? *Nano Select.,* 2020, **1**, 12-29.

370. X. Sun, S.C. Simonsen, T. Norby and A. Chatzitakis. Composite membranes for high temperature PEM fuel cells and electrolysers: A critical review. *Membranes*, 2019, **9**, 83.

371. J. Papavasiliou, A. Paxinou, G. Słowik, S. Neophytides and G. Avgouropoulos. Steam reforming of methanol over nanostructured $Pt/TiO_2$ and $Pt/CeO_2$ catalysts for fuel cell applications. *Catalysts*, 2018, **8**, 544 (20 pages).

372. S. Yao, X. Zhang, W. Zhou, R. Gao, W. Xu, Y. Ye, L. Lin, X. Wen et al. Atomic-layered Au clusters on □□-MoC as catalysts for the low-temperature water-gas shift reaction. *Science*, 2017, **357**, 389-393.

373. Z. Li, L. Yu, C. Milligan, T. Ma, L. Zhou, Y. Cui, Z. Qi, N. Libretto, B. Xu, J. Luo, E. Shi, Z. Wu, H. Xin, W. Nicholas Delgass, J. T. Miller and Y. Wu. Two-dimensional transition metal carbides as supports for tuning the chemistry of catalytic nanoparticles. *Nature Commun.,* 2018*,* **9**, 5258 (8 pages).

374. Z. Li, S. Ji, Y. Liu, X. Cao, S. Tian, Y. Chen, Z. Niu and Y. Li**.** Well-defined materials for heterogeneous catalysis: From nanoparticles to isolated single-atom sites. *Chem. Rev.,* 2020, **120**, 623-682.

375. F. Caia, J. J. Ibrahim, Y. Fu, W. Kong, J. Zhang and Y. Sun. Low-temperature hydrogen production from methanol steam reforming on Zn-modified Pt/MoC catalysts. *Appl. Catal. B: Environ.,* 2020, **264**, 118500 (13 pages).

376. J. Yu, X. Li, Q. Wu, H. Wang, Y. Liu, H. Huang, Y. Liu, M. Shao, J. Fan, H. Li and Z. Kang. Effective low-temperature methanol aqueous phase reforming with metal-free carbon dots/ $C_3N_4$ composites. *ACS Appl. Mater. Interfaces*, 2021, **13**, 24702-24709.

377. P. Ribeirinha**,** C. Mateos-Pedrero, M. Boaventura, J. Sousa and A. Mendes. $CuO/ZnO/Ga_2O_3$ catalyst for low temperature MSR reaction: Synthesis, characterization and kinetic model. *Appl. Catal. B: Environ*., 2018, **221**, 371-379.

378. H.-S. Wang, C.-P. Chang, Y.-J. Huang, Y.-C. Su and F.-G. Tseng. A high-yield and ultra-low-temperature methanol reformer integratable with phosphoric acid fuel cell (PAFC). *Energy*, 2017, **133**, 1142-1152.

379. J. Papavasiliou, A. Paxinou, G. Słowik, S. Neophytides and G. Avgouropoulos. Steam reforming of methanol over nanostructured $Pt/TiO_2$ and $Pt/CeO_2$ catalysts for fuel cell applications. *Catalysts,* 2018, **8,** 544 (20 pages).

380. K. A. Davis, S.Yoo, E. W. Shuler, B. D. Sherman, S. Lee and G. Leem. Photocatalytic hydrogen evolution from biomass conversion. *Nano Convergence,* 2021, **8**, 6 (19 pages).

381. Z. Chai. Light-driven alcohol splitting by heterogeneous photocatalysis: Recent advances, mechanism and prospects. *Chem Asian J.,* 2021, **16**, 460-473.

382. Q. Guo, Z. Ma, C. Zhou, Z. Ren and X. Yang. Single molecule photocatalysis on $TiO_2$ surfaces. *Chem. Rev*., 2019, **119**, 11020-11041.

383. A. Mills, M. Bingham, C. O'Rourke and M. Bowker. Modelled kinetics of the rate of hydrogen evolution as a function of metal catalyst loading in the photocatalyzed reforming of methanol by Pt (or Pd)/$TiO_2$. *J. Photochem. Photobiol. A: Chem*., 2019, **373**, 122-130.

384. M. Bowker, D. James, P. Stone, R. Bennett, N. Perkins, L. Millard, J. Greaves, A. Dickinson, Catalysis at the metal-support interface: exemplified by the photocatalytic reforming of methanol on Pd/$TiO_2$, *J. Catal.,* 2003, **217**, 427-433.

385. A. Mills, M. Bingham and C. O'Rourke. Ring photocatalysis: Bands of activation surrounding macro-sized (≥1 mm radius) Pt islands deposited on $TiO_2$ films. *J. Phys. Chem. C.,* 2020, **124**, 13550-13559.

386. C. A. Walenta, C. Courtois, S. L. Kollmannsberger, M. Eder, M. Tschurl and U. Heiz. Surface species in photocatalytic methanol reforming on Pt/$TiO_2$(110): Learning from surface science experiments for catalytically relevant conditions. *ACS Catal*., 2020, **10**, 4080-4091.

387. C. A Walenta , M. Tschurl and U. Heiz. Introducing catalysis in photocatalysis: What can be understood from surface science studies of alcohol photoreforming on $TiO_2$. *J. Phys.: Condens. Matter.* 2019, **31**, 473002 (19 pages).

388. Y. Lu, W.-J. Yin, K.-L. Peng, K. Wang, Q. Hu, A. Selloni, F.-R. Chen, L.-M. Liu and M.-L. Sui. Self-hydrogenated shell promoting photocatalytic $H_2$ evolution on anatase $TiO_2$. *Nat. Comm*., 2018, **9**, 2752 (9 pages).

389. L. Jin and Y. Wang. Surface chemistry of methanol on different ZnO surfaces studied by vibrational spectroscopy. *Phys. Chem. Chem. Phys.*, 2017, **19**, 12992-13001.

390. Y. Wang and C. Wöll. IR spectroscopic investigations of chemical and photochemical reactions on metal oxides: Bridging the materials gap. *Chem. Soc. Rev.*, 2017, **46**, 1875-1932.

391. X. Li and G. Rupprechter. Sum frequency generation spectroscopy in heterogeneous model catalysis: A mini-review of CO-related processes. *Catal. Sci. Technol*., 2021, **11**, 12-26.

392. G. M. Haselmann and D. Eder. Early-stage deactivation of platinum-loaded $TiO_2$ using in situ photodeposition during photocatalytic hydrogen evolution. *ACS Catal*., 2017, **7**, 4668-4675.

393. C. Courtois, M. Eder, S. L. Kollmannsberger, M. Tschurl, C. A. Walenta and U. Heiz. Origin of poisoning in methanol photo-reforming on $TiO_2$ (110): The importance of thermal back-reaction steps in photocatalysis. *ACS Catal.,* 2020, **10**, 7747-7752.

394. M. Setvin, X. Shi, J. Hulva, T. Simschitz, G. S. Parkinson, M. Schmid, C. Di Valentin, A. Selloni and U. Diebold. Methanol on anatase $TiO_2$ (101): Mechanistic insights into photocatalysis. *ACS Catal.,* 2017, **7**, 7081-7091.

395. M. Eder, C. Courtois, T. Kratky, S. Günther, M. Tschurl and U. Heiz. Nickel clusters on $TiO_2$ (110). Thermal chemistry and photocatalytic hydrogen evolution of methanol. *Catal. Sci. Technol.*, 2020, **10**, 7630-7639.

396. U. Heiz, F. Vanolli, A. Sanchez and W.-D. Schneider. Size-dependent molecular dissociation on mass-selected, supported metal clusters. *J. Am. Chem. Soc*., 1998, **120**, 9668-9671.

397. C. Dong, Y. Li, D. Cheng, M. Zhang, J. Liu, Y.-G. Wang, D. Xiao, and D. Ma. Supported metal clusters: Fabrication and application in heterogeneous catalysis. *ACS Catal*., 2020, **10**, 11011-11045.

398. Y.-H. Chung, K. Han, C.-Y Lin, D. O'Neill, G. Mul, B. Mei and C.-M. Yang. Photocatalytic hydrogen production by photo-reforming of methanol with one-pot synthesized Pt-containing $TiO_2$ photocatalysts. *Catal. Today*, 2020, **356**, 95-100.

399. W. Zhao, Z. Chen, X. Yang, X. Qian, C. Liu, D. Zhou, T. Sun, M. Zhang, G. Wei, P. D. Dissanayake and Y. S. Ok. Recent advances in photocatalytic hydrogen evolution with high-performance catalysts without precious metals. *Renew. Sust. Energy Rev*., 2020, **132**, 110040 (15 pages).

400. R. Shen, J. Xie, Q. Xiang, X. Chen, J. Jiang and X. Li. Ni-based photocatalytic $H_2$-production cocatalysts. *Chin. J. Catal*., 2019, **40**, 240-288.

401. S. Rej, M. Bisetto, A. Naldoni and P. Fornasiero. Well-defined $Cu_2O$ photocatalysts for solar fuels and chemicals. *J. Mater. Chem. A,* 2021, **9**, 5915-5951.

402. H. Bahruji, M. Bowker, P. R. Davies, J. Kennedy and D. J. Morgan. The importance of metal reducibility for the photo-reforming of methanol on transition metal-$TiO_2$ photocatalysts and the use of non-precious metals. *Int. J. Hydrogen Energy*, 2015, **40**, 1465-1471.

403. T. K. Townsend, N. D. Browning and F. E. Osterloh. Overall photocatalytic water splitting with $NiO_x$-$SrTiO_3$ – A revised mechanism. *Energy Environ. Sci*., 2012, **5**, 9543-9550.

404. J. S. Schubert, J. Popovic, G. M. Haselmann, S. P. Nandan, J. Wang, A. Giesriegl, A. S. Cherevan and D. Eder. Immobilization of Co, Mn, Ni and Fe oxide co-catalysts on $TiO_2$ for photocatalytic water splitting reactions. *J. Mater. Chem. A*, 2019, **7**, 18568-18579.

405. M. Okazaki, Y. Wang, T. Yokoi and K. Maeda. Visible-light-driven water oxidation using anatase titania modified with first-row transition-metal-oxide nanoclusters. *J. Phys. Chem. C,* 2019, **123**, 10429-10434.

406. L. Díaz, V. D. Rodríguez, M. González-Rodríguez, E. Rodríguez-Castellón, M. Algarra, P. Núñez and E. Moretti. M/$TiO_2$ (M = Fe, Co, Ni, Cu, Zn) catalysts for photocatalytic hydrogen production under UV and visible light irradiation. *Inorg. Chem. Front.,*2021, **8**, 3491-3500

407. C. G. Morales-Guio, S. D. Tilley, H. Vrubel, M. Graetzel and X. Hu. Hydrogen evolution from a copper(I) oxide photocathode coated with an amorphous molybdenum sulphide catalyst. *Nat. Commun.,* 2014, **5**, 3059 (7 pages).

408. W.-T. Chen, Y. Dong, P. Yadava, R. D. Aughterson, D. Sun-Waterhouse and G. I. N. Waterhouse. Effect of alcohol sacrificial agent on the performance of $Cu/TiO_2$ photocatalysts for UV-driven hydrogen production. *Appl. Catal. A: Gen*., 2020, **602**, 117703 (17 pages).

409. W.-T. Chen, A. Chan, D. Sun-Waterhouse, J. Llorca, H. Idriss and G. I. N. Waterhouse. Performance comparison of $Ni/TiO_2$ and $Au/TiO_2$ photocatalysts for $H_2$ production in different alcohol-water mixtures. *J. Catal*., 2018, **367**, 27-42.

410. Z. Sun, S. Fang, Y. Lin and, Y. H. Hua. Photo-assisted methanol steam reforming on solid solution of Cu-Zn-Ti oxide. *Chem. Eng. J.,* 2019, **375**, 121909 (9 pages).

411. X. Yu, L. Yang, Y. Xuan, X. Lei Liu and K. Zhang. Solar-driven low-temperature reforming of methanol into hydrogen via synergetic photo- and thermocatalysis. *Nano Energy*, 2021, **84**, 105953 (10 pages).

412. D.-J. Yuan, A. M. Hengne, Y. Saih, and K.-W. Huang. Nonoxidative dehydrogenation of methanol to methyl formate through highly stable and reusable CuMgO-based catalysts. *ACS Omega,* 2019, **4**, 1854-1860.

413. S. Fang, Z. Sun and Y. H. Hu. Insights into the thermo-photo catalytic production of hydrogen from water on a low-cost $NiO_x$-loaded $TiO_2$ catalyst. *ACS Catal.,* 2019, **9**, 5047-5056.

414. V. N. Kuznetsov and N. Serpone. On the origin of the spectral bands in the visible absorption spectra of visible-light-active $TiO_2$ specimens analysis and assignments. *J. Phys. Chem. C* 2009, **113**, 15110-15123.

415. X. Liu, C. Bao, Z. Zhu, H. Zheng, C. Song and Q. Xu. Thermo-photo synergic effect on methanol steam reforming over mesoporous $Cu/TiO_2$-$CeO_2$ catalysts. *Int. J. Hydrogen Energy,* 2021, **46(53)**, 26741-26756.

416. T. Maihom, M. Probst, J. Limtrakul, Density functional theory study of the dehydrogenation of ethanol to acetaldehyde over the Au-exchanged ZSM-5 zeolite: Effect of surface oxygen, *J. Phys. Chem. C.,* 2014, **118**, 18564-18572.

417. G. Giannakakis, A. Trimpalis, J. Shan, Z. Qi, S. Cao, J. Liu, J. Ye, J. Biener and M. Flytzani-Stephanopoulos. NiAu single atom alloys for the non-oxidative dehydrogenation of ethanol to acetaldehyde and hydrogen. *Top. Catal.,* 2018*,* **61**, 475-486

418. Q. Li, R. García-Muelas and N. López. Microkinetics of alcohol reforming for $H_2$ production from a FAIR density functional theory database. *Nat. Commun*., 2018, **9**, 526.

419. Q.-N. Wang, L. Shi, W. Li, W.-C. Li, R. Si, F. Schüth and A.-H. Lu Cu supported on thin carbon layer-coated porous $SiO_2$ for efficient ethanol dehydrogenation. *Catal. Sci. Technol*., 2018, **8**, 472-479.

420. H. Xiong, A. DeLaRiva, Y. Wang and A. K. Datye. Low-temperature aqueous-phase reforming of ethanol on bimetallic PdZn catalysts. *Catal. Sci. Technol*., 2015, **5**, 254-263.

421. S. Ogo and Y. Sekine. Recent progress in ethanol steam reforming using non-noble transition metal catalysts: A review. *Fuel Process. Technol.,* 2020, **199**, 106238.

422. D. Zanchet, J. Batista O. Santos, S. Damyanova, Jean M. R. Gallo and J. M. C. Bueno. Toward understanding metal-catalyzed ethanol reforming. *ACS Catal*., 2015, **5**, 3841-3863.

423. M. Bowker, L. Cookson, J. Bhantoo, A. Carley, E. Hayden, L. Gilbert, C. Morgan, J. Counsell and P.Yaseneva. The decarbonylation of acetaldehyde on Pd crystals and on supported catalysts. *Appl. Catal. A: Gen*., 2011, **391**, 394-399.

424. Y. Han, Y. Wang, T. Ma, W. Li, J. Zhang and M. Zhang. Mechanistic understanding of Cu-based bimetallic catalysts. *Front. Chem. Sci. Eng*., 2020, **14**, 689-748.

425. D. Spanu, S. Recchia, S. Mohajernia, O. Tomanec, S. Kment, R. Zboril, P. Schmuki and M. Altomare. Templated dewetting–alloying of NiCu bilayers on $TiO_2$ nanotubes enables efficient noble-metal-free photocatalytic $H_2$ evolution. *ACS Catal.,* 2018, **8**, 5298-5305.

426. B. Eren, D. Torres, O. Karsioglu, Z. Liu, C. H. Wu, D. Stacchiola, H. Bluhm, G. A. Somorjai and M. Salmeron. Structure of copper–cobalt surface alloys in equilibrium with carbon monoxide gas. *J. Am. Chem. Soc.,* 2018, **140**, 6575-6581.

427. X. Nie, H. Wang, M. J. Janik, Y. Chen, X. Guo and C. Song. Mechanistic insight into C−C coupling over Fe−Cu bimetallic catalysts in $CO_2$ hydrogenation. *J. Phys. Chem. C*, 2017, **121**, 13164-13174.

428. J. Shan, J. Liu, M. Li, S. Lustig, S. Lee and M. Flytzani-Stephanopoulos. NiCu single atom alloys catalyze the C-H bond activation in the selective non-oxidative ethanol dehydrogenation reaction. *Appl. Catal. B: Environ.,* 2018, **226**, 534-543.

429. C. Angelici, F. Meirer, A.M.J. Eerden, H. L. Schaink, A. Goryachev, J. P. Hofmann, E. J. M. Hensen, B. M. Weckhuysen and P. C. A. Bruijnincx. Ex situ and operando studies on the role of copper in Cu-promoted $SiO_2$-MgO catalysts for the Lebedev ethanol-to-butadiene process. *ACS Catal*., 2015, **5,** 6005-6015.

430. M. V. Twigg and M. S. Spencer. Deactivation of copper metal catalysts for methanol decomposition, methanol steam-reforming and methanol synthesis. *Top. Catal*., 2003, **22**, 191-203.

431. E. D. Goodman, J. A. Schwalbe and M. Cargnello. Mechanistic understanding and the rational design of sinter-resistant heterogeneous catalysts. *ACS Catal*., 2017, **7**, 7156-7173.

432. H. O. Otor, J. B. Steiner, C. Garcia-Sancho and A. C. Alba-Rubio. Encapsulation methods for control of catalyst deactivation: A review. *ACS Catal*., 2020, **10**, 7630-7656.

433. J. Huo, J.-P. Tessonier and B. H. Shanks. Improving hydrothermal stability of supported metal catalysts for biomass conversions: A review. *ACS Catal.*, 2021, **11**, 5248-5270.

434. L.-C. Chen, H. Cheng, C.-W. Chiang, and S. D. Lin. Sustainable hydrogen production by ethanol steam reforming using a partially reduced copper–nickel oxide catalyst. *ChemSusChem*., 2015, **8**, 1787-1793.

435. A. Kumar, A. Cross, K. Manukyan, R. R. Bhosale, L. J. P. van den Broeke, J. T. Miller, A. S. Mukasyan and E. E. Wolf. Combustion synthesis of copper-nickel catalysts for hydrogen production from ethanol. *Chem. Eng. J.*, 2015, **278**, 46-54.

436. N. K. Das, A. K. Dalai and R. Ranganathan. Hydrogen yield from low temperature steam reforming of ethanol. *Can. J. Chem. Eng*., 2007, 85, 92-100.

437. A. Casanovas, N. J. Divins, A. Rejas, R. Bosch and J. Llorca. Finding a suitable catalyst for on-board ethanol reforming using exhaust heat from an internal combustion engine. *Int. J. Hydrogen Energy,* 2017**, 42,** 13681-13690.

438. S. De, J. Zhang, R. Luque and N. Yan. Ni-based bimetallic heterogeneous catalysts for energy and environmental applications. *Energy Environ. Sci.,* 2016, **9**, 3314-3347.

439. S. Li and J. Gong. Strategies for improving the performance and stability of Ni-based catalysts for reforming reactions. *Chem. Soc. Rev.*, 2014, **43**, 7245-7256.

440. C. Montero, A. Remiro, B. Valle, L. Oar-Arteta, J. Bilbao and A. G. Gayubo. Origin and nature of coke in ethanol steam reforming and its role in deactivation of $Ni/La_2O_3$-$\alpha$-$Al_2O_3$ catalyst. *Ind. Eng. Chem. Res*., 2019, **58**, 14736-14751.

441. M. Radlik, M. Adamowska-Teyssier, A. Krzton, K. Kozieł, W. Krajewski, W. Turek and P. Da Costa. Dry reforming of methane over $Ni/Ce_{0.62}Zr_{0.38}O_2$ catalysts: Effect of Ni loading on the catalytic activity and on $H_2$/CO production. *C. R. Chimie*, 2015, **18**, 1242-1249.

442. G. Wei, M. Shen, H. Li, H. Wang and J. Wang. Hydrothermal stability of $CeO_2$–$Al_2O_3$ composites, a structural study and oxygen storage capacities. *RSC Adv*., 2015, **5**, 80933-80938.

443. Y. Mueanngern, C.-H. Li, M. Spelic, J. Graham, N. Pimental, Y. Khalifa, J. R. Jinschek and L. R. Baker. Deactivation-free ethanol steam reforming at nickel-tipped carbon filaments. *Phys. Chem. Chem. Phys.*, 2021, **23**, 11764-11773.

444. J. A. Rodriguez, D. C. Grinter, Z. Liu, R. M. Palomino and S. D. Senanayake. Ceria-based model catalysts: Fundamental studies on the importance of the metal–ceria interface in CO oxidation, the water–gas shift, $CO_2$ hydrogenation, and methane and alcohol reforming. *Chem. Soc. Rev.*, 2017, **46**, 1824-1841.

445. Z. Liu, T. Duchon, H. Wang, D. C. Grinter, I. Waluyo, J. Zhou, Q. Liu, B. Jeong, E. J. Crumlin, V. Matolın, D. J. Stacchiola, J. A. Rodriguez and S. D. Senanayake. Ambient pressure XPS and IRRAS investigation of ethanol steam reforming on Ni–$CeO_2$(111) catalysts: An in- situ study of C–C and O–H bond scission. *Phys. Chem. Chem. Phys.*, 2016, **18**, 16621-16628.

446. X. Garcia, L. Soler, N. J. Divins, X. Vendrell, I. Serrano, I. Lucentini, J. Prat, E. Solano, M. Tallarida, C. Escudero and J. Llorca. Ceria-based catalysts studied by near ambient pressure X-ray photoelectron spectroscopy: A review. *Catalysts*, 2020, **10**, 286 (48 pages).

447. C. Zhang, S. Li, M. Li, S. Wang, X. Ma, and J. Gong. Enhanced oxygen mobility and reactivity for ethanol steam reforming. *AIChE*, 2012, **58**, 516-525.

448. S. Chen, C. Pei and J. Gong. Insights into interface engineering in steam reforming reactions for hydrogen production. *Energy Environ. Sci.*, 2019, **12**, 3473-3495.

449. I. Coronado, M. Stekrova, M. Reinikainen, P. Simell, L. Lefferts and J. Lehtonen. A review of catalytic aqueous-phase reforming of oxygenated hydrocarbons derived from biorefinery water fractions. *Int. J. Hydrogen Energy*, 2016, **41**, 11003-11032.

450. I. Coronado, M. Pitínová, R. Karinen, M. Reinikainen, R. L. Puurunen and J. Lehtonen. Aqueous-phase reforming of Fischer-Tropsch alcohols over nickel-based catalysts to produce hydrogen: Product distribution and reaction pathways. *Appl. Catal. A, Gen.*, 2018, **567**, 112–121.

451. G. Zoppi, G. Pipitone, H. Gruber, G. Weber, A. Reichhold, R. Pirone and S. Bensaid. Aqueous phase reforming of pilot-scale Fischer-Tropsch water effluent for sustainable hydrogen production. *Catal. Today*, 2021, **367**, 239–247.

452. B. Roy and C. A. Leclerc. Study of preparation method and oxidization/reduction effect on the performance of nickel-cerium oxide catalysts for aqueous-phase reforming of ethanol. *J. Power Sources*, 2015, **299**, 114-124.

453. T. Nozawa, A. Yoshida, S. Hikichi and S. Naito. Effects of Re addition upon aqueous phase reforming of ethanol over $TiO_2$ supported Rh and Ir catalysts. *Int. J. Hydrogen Energy*, 2015, **40**, 4129-4140.

454. Z. Zhao, L. Zhang, Q. Tan, F. Yang, J. Faria and D. Resasco. Synergistic bimetallic Ru–Pt catalysts for the low-temperature aqueous phase reforming of ethanol. *AIChE*, 2019, **65**, 151-160.

455. L. Ferreira-Pinto, M.P.S. Parizi, P.C.C. de Araujo, A. F. Zanette and L. Cardozo-Filho. Experimental basic factors in the production of $H_2$ via supercritical water gasification. *Int. J. Hydrogen Energy*, 2019, **44**, 25365-25383.

456. S. Nanda, R. Rana, Y. Zheng, J. A. Kozinski and A. K. Dalai. Insights on pathways for hydrogen generation from ethanol. *Sust. Energy Fuels*, 2017, **1**, 1232-1245.

457. S. Therdthianwong, N. Srisiriwat, A. Therdthianwong and E. Croiset. Reforming of bioethanol over $Ni/Al_2O_3$ and $Ni/CeZrO_2/Al_2O_3$ catalysts in supercritical water for hydrogen production. *Int. J. Hydrogen Energy*, 2011, **36**, 2877-2886.

458. Z. H. N. Al-Azri, M. AlOufi, A. Chan, G. I. N. Waterhouse and H. Idriss. Metal particle size effects on the photocatalytic hydrogen ion reduction. *ACS Catal*., 2019, **9**, 3946-3958.

459. C. Ampelli, R. Passalacqua, C. Genovese, S. Perathoner, G. Centi, T. Montini, V. Gombac, J. J. D. Jaen and P. Fornasiero. $H_2$ production by selective photo-dehydrogenation of ethanol in gas and liquid phase on $CuO_x/TiO_2$ nanocomposites. *RSC Adv.*, 2013, **3**, 21776-21788.

460. B. L. Tran, S. I. Johnson, K. P. Brooks and S. T. Autry. Ethanol as a liquid organic hydrogen carrier for seasonal microgrid application: Catalysis, theory, and engineering feasibility. *ACS Sust. Chem. Eng.,* 2021, **9**, 7130-7138.

461. K. Katsiev, G. Harrison, Y. Al-Salik, G. Thornton and H. Idriss. Gold cluster coverage effect on $H_2$ production over rutile $TiO_2$(110). *ACS Catal.,* 2019, **9**, 8294-8305.

462. W. H. Leng, P. R. F. Barnes, M. Juozapavicius, B. C. O'Regan and J. R. Durrant. Electron diffusion length in mesoporous nanocrystalline $TiO_2$ photoelectrodes during water oxidation. *J. Phys. Chem. Lett.*, 2010, **1**, 967-972.

463. C. Xing, Y.Zhang, Y. Liu, X. Wang, J. Li, P. R. Martínez-Alanis, M. C. Spadaro, P. Guardia, J. Arbiol, J. Llorca and A. Cabot. Photodehydrogenation of ethanol over $Cu_2O/TiO_2$ heterostructures. *Nanomaterials*, 2021, **11**, 1399 (15 pages)

464. S. Luo, H. Song, D. Philo, M. Oshikiri, T. Kako and J. Ye. Solar-driven production of hydrogen and acetaldehyde from ethanol on Ni-Cu bimetallic catalysts with solar-to-fuels conversion efficiency up to 3.8 %. *Appl. Catal. B: Environ*., 2020, **272**, 118965 (9 pages).

465. Z. Lin J. Li, L. Li, L.Yu, W. Li and G. Yang. Manipulating the hydrogen evolution pathway on composition-tunable CuNi nanoalloys. *J. Mater. Chem. A*, 2017, **5**, 773-781.

466. Y. Zhou, W. Chen, P. Cui, J. Zeng, Z. Lin, E. Kaxiras and Z. Zhang. Enhancing the hydrogen activation reactivity of nonprecious metal substrates via confined catalysis underneath graphene. *Nano Lett*., 2016, **16**, 6058-6063.

467. C. Wei, Y. Sun, G. G. Scherer, A. C. Fisher, M. Sherburne, J. W. Ager and Z. J. Xu. Surface composition dependent ligand effect in tuning the activity of nickel-copper bimetallic electrocatalysts toward hydrogen evolution in alkaline. *J. Am. Chem. Soc.*, 2020, 142, 7765-7775.

468. D. Spanu, S. Recchia, S. Mohajernia, O. Tomanec, S. Kment, R. Zboril, P. Schmuki and M. Altomare. Templated dewetting-alloying of NiCu bilayers on $TiO_2$ nanotubes enables efficient noble-metal-free photocatalytic $H_2$ evolution. *ACS Catal.,* 2018, **8**, 5298-5305.

469. D. Spanu, A. Minguzzi, S. Recchia, F. Shahvardanfard, O. Tomanec, R. Zboril, P. Schmuki, P. Ghigna, and M. Altomare. An operando X-ray absorption spectroscopy study of a NiCu $TiO_2$ photocatalyst for $H_2$ evolution. *ACS Catal*., 2020, **10**, 8293-8302.

470. J. W. Shabaker and J. A. Dumesic. Kinetics of aqueous-phase reforming of oxygenated hydrocarbons: $Pt/Al_2O_3$ and Sn-modified Ni catalysts. *Ind. Eng. Chem. Res.,* 2004**, 43**, 3105-3112.

471. S. Kandoi, J. Greeley, D. Simonetti, J. Shabaker, J. A. Dumesic and M. Mavrikakis. Reaction kinetics of ethylene glycol reforming over platinum in the vapor versus aqueous phases. *J. Phys. Chem. C,* 2011, **115***,* 961-971.

472. M. Faheem, M. Saleheen, J. Lu and A. Heyden. Ethylene glycol reforming on Pt (111): First-principles microkinetic modeling in vapor and aqueous phases. *Catal. Sci. Technol.*, 2016, **6**, 8242-8256.

473. D. Mei, V. L. Dagle, R. Xing, K. O. Albrecht and R. A. Dagle. Steam reforming of ethylene glycol over $MgAl_2O_4$ supported Rh, Ni, and Co Catalysts. *ACS Catal*., 2016, **6**, 315-325.

474. A. Larimi and F. Khorasheh. Renewable hydrogen production by ethylene glycol steam reforming over $Al_2O_3$ supported Ni-Pt bimetallic nano-catalysts. *Renew. Energy*, 2018, **128**, 188.

475. D. J. M. de Vlieger, A.G. Chakinala, L. Lefferts, S. R. A. Kersten, K. Seshan and D. W. F. Brilman. Hydrogen from ethylene glycol by supercritical water reforming using noble and base metal catalysts. *Appl. Catal. B: Environ*., 2012, **111-112**, 536-544.

476. J. W. Shabaker, R. R. Davda, G. W.Huber, R. D. Cortright and J. A. Dumesic. Aqueous-phase reforming of methanol and ethylene glycol over alumina-supported platinum catalysts. *J. Catal*., 2003, **215**, 344-352.

477. G. W. Huber, J. W. Shabaker, S. T. Evans and J. A. Dumesic. Aqueous-phase reforming of ethylene glycol over supported Pt and Pd bimetallic catalysts. *Appl. Catal. B: Environ*., 2006, **62**, 226-235.

478. J. Tao, L. Hou, B. Yan, G. Chen, W. Li, H. Chen, Z. Cheng and F. Lin. Hydrogen production via aqueous-phase reforming of ethylene glycol over a nickel□iron alloy catalyst: Effect of cobalt addition. *Energy Fuels*, 2020, **34**, 1153-1161.

479. Z. Li, B. D. Kay and Z. Dohnalek. Dehydration and dehydrogenation of ethylene glycol on rutile $TiO_2$(110). *Phys. Chem. Chem. Phys*., 2013, **15**, 12180-12186.

480. F. Xu, X. Chen, W. Yang, X. Wang, X. Yang, and Q. Guo. Coverage-dependent ethylene glycol photochemistry on rutile-$TiO_2$ (110). *J. Phys. Chem. C*, 2020, **124**, 14632-14639.

481. L. Chen, Z. Li, R. S. Smith, B. D. Kay and Z. Dohnalek. Molecular hydrogen formation from proximal glycol pairs on $TiO_2$(110). *J. Am. Chem. Soc.,* 2014, **136**, 5559-5562.

482. T. F. Berto, K. E. Sanwald, W. Eisenreich, O. Y. Gutiérrez and J. A. Lercher. Photoreforming of ethylene glycol over $Rh/TiO_2$ and Rh/GaN:ZnO, *J. Catal.,* 2016, **338**, 68-81.

483. W.-T. Chen, Y. Dong, P. Yadava, R. D. Aughterson, D. Sun-Waterhouse and G. I. N. Waterhouse. Effect of alcohol sacrificial agent on the performance of $Cu/TiO_2$ photocatalysts for UV-driven hydrogen production. *Appl. Catal. A, Gen.*, 2020, **602**, 117703 (17 pages).

484. M. Jung, J. N. Hart, J. Scotta, Y.-H Ng, Y. Jiang and R. Amal. Exploring Cu oxidation state on $TiO_2$ and its transformation during photocatalytic hydrogen evolution. *Appl. Catal. A: Gen.,* 2016, **521**, 190-201.

485. D. Praveen Kumar, N. Lakshmana Reddy, B. Srinivas, V. Durgakumari, V. Roddatis, O. Bondarchuk, M. Karthik, Y. Ikuma, and M.V. Shankar, Stable and active $Cu_xO/TiO_2$ nanostructured catalyst for proficient hydrogen production under solar light irradiation, *Solar Energy Materials and Solar Cells*, 2016, **146**, 63-71.

486. M. A. Nadeem, M. Al-Oufi, A. K. Wahab, D. Anjum and H. Idriss. Hydrogen production on $Ag\text{-}Pd/TiO_2$ bimetallic catalysts: Is there a combined effect of surface plasmon resonance with Schottky mechanism on the photo-catalytic activity? *ChemistrySelect,* 2017, **2**, 2754-2762.

487. M. Bowker, C. Morton, J. Kennedy, H. Bahruji, J. Greves, W. Jones, P. R. Davies, C. Brookes, P. P. Wells and N. Dimitratos. Hydrogen production by photoreforming of biofuels using Au, Pd and $Au–Pd/TiO_2$ photocatalysts. *J. Catal*., 2014, **310**, 10-15.

488. N. G. Saeidabad, Y. S. Noh, A. A. Eslami, H.T. Song, H. D. Kim, A. Fazeli and D. J. Moon. A review on catalysts development for steam reforming of biodiesel derived glycerol; Promoters and supports. *Catalysts,* 2020, **10**, 910.

489. B. Liu and F. Gao. Navigating glycerol conversion roadmap and heterogeneous catalyst selection aided by density functional theory: A review. *Catalysts*, 2018, **8**, 44.

490. A. Ismaila, X. Chen, X. Gao and X. Fan. Thermodynamic analysis of steam reforming of glycerol for hydrogen production at atmospheric pressure. *Front. Chem. Sci. Eng.*, 2021, **15**, 60-71.

491. M. Checa, S. Nogales-Delgado, V. Montes and J. M. Encinar. Recent advances in glycerol catalytic valorization: A review. *Catalysts*, 2020, **10**, 1279 (41 pages).

492. B. Liu and J. Greeley. A density functional theory analysis of trends in glycerol decomposition on close-packed transition metal surfaces. *Phys. Chem. Chem. Phys.,* 2013, **15**, 6475-6485.

493. M. Valter, E. Campos dos Santos, L. G. M. Pettersson, and A. Hellman. Selectivity of the first two glycerol dehydrogenation steps determined using scaling relationships. *ACS Catal*., 2021, **11**, 3487-3497.

494. J. P. S. Q. Menezes, R. L. Manfro and M. V. M. Souza. Hydrogen production from glycerol steam reforming over nickel catalysts supported on alumina and niobia: Deactivation process, effect of reaction conditions and kinetic modeling. *Int. J. Hydrogen Energy*, 2018, **43**, 15064.

495. Y. Wang, M. Chen, Z. Yang, T. Liang, S. Liu, Z. Zhou and X. Li. Bimetallic Ni-M (M=Co, Cu and Zn) supported on attapulgite as catalysts for hydrogen production from glycerol steam reforming. *Appl. Catal. A: Gen*., 2018, **550**, 214-227.

496. N. D. Charisiou, V. Sebastian, S. J. Hinder, M. A. Baker, K. Polychronopoulou and M. A. Goula. Ni catalysts based on attapulgite for hydrogen production through the glycerol steam reforming reaction. Catalysts, 2019, **9**, 650.

497. H. D. Demsash, K. V. K. Kondamudi, S. Upadhyayula and R. Mohan. Ruthenium doped nickel-alumina-ceria catalyst in glycerol steam-reforming. *Fuel Process. Technol*., 2018, **169**, 150-156.

498. O. A. Sahraei, F. Larachi, N. Abatzoglou and M. C. Iliuta. Hydrogen production by glycerol steam reforming catalyzed by Ni-promoted Fe/Mg-bearing metallurgical wastes. *Appl. Catal. B: Environ.,* 2017, **219**, 183-193.

499. O. A. Sahraei, A. Desgagnés, F. Larachi and M. C. Iliuta. A comparative study on the performance of M (Rh, Ru, Ni)-promoted metallurgical waste driven catalysts for $H_2$ production by glycerol steam reforming. *Int. J. Hydrogen Energy*, 2021, **46(63)**, 32017-32035.

500. Q. Yang, G. Liu and Y. Liu. Perovskite-type oxides as the catalyst precursors for preparing supported metallic nanocatalysts: A review. *Ind. Eng. Chem. Res.,* 2018, **57**, 1-17.

501. S. Ramesh and N. J. Venkatesha. Template-free synthesis of Ni-perovskite: An efficient catalyst for steam reforming of bioglycerol. *ACS Sustainable Chem. Eng.,* 2017, **5**, 1339-1346.

502. F. Conte, S. Esposito, V. Dal Santo, A. Di Michele, G. Ramis and I. Rossetti. Flame pyrolysis synthesis of mixed oxides for glycerol steam reforming. *Materials*, 2021, **14**, 652.

503. K. Kousi, N. Chourdakis, H. Matralis, D. Kontarides, C. Papadopoulou and X. Verykios. Glycerol steam reforming over modified Ni-based catalysts. *Appl. Catal. A: Gen.,* 2016, **518**, 129.

504. N. D. Charisiou, G. Siakavelas, K. N. Papageridis, A. Baklavaridis, L. Tzounis, K. Polychronopoulou and M. A. Goula. Hydrogen production via the glycerol steam

reforming reaction over nickel supported on alumina and lanthana-alumina catalysts. *Int. J. Hydrogen Energy*, 2017, **42**, 13039-13060.

505. R. R. Soares, D. A. Simonetti and J. A. Dumesic. Glycerol as a source for fuels and chemicals by low-temperature catalytic processing. *Angew. Chem. Int. Ed.,* 2006, **45**, 3982-3985.

506. S. Liu, Z. Yan, Y. Zhang, R. Wang, S.-Z. Luo, F. Jing and W. Chu. Carnon nanotubes supported nickel as the highly efficient catalyst for hydrogen production through glycerol reforming. *ACS Sustainable Chem. Eng*., 2018, **6**, 14403-14413.

507. P. Ebrahimi, A. Kumar and M. Khraisheh. A review of recent advances in water-gas shift catalysis for hydrogen production. *Emergent Materials*, 2020, **3**, 881-917.

508. S. A. Miners, G. A. Rance and A. N. Khlobystov. Chemical reactions confined within carbon nanotubes. *Chem. Soc. Rev*., 2016, **45**, 4727-4746.

509. R. Wang, S. Liu, S. Liu, X. Li, Y. Zhang, C. Xie, S. Zhou, Y. Qiu, S. Luo, F. Jing and W. Chu. Glycerol steam reforming for hydrogen production over bimetallic MNi/CNTs (M = Co, Cu and Fe) catalysts. *Catal. Today*, 2020, **355**, 128-138.

510. H. Zhou, S. Liu, F. Jing, S. Luo, J. Shen, Y. Pang, and W. Chu. Synergetic bimetallic NiCo/ CNT Catalyst for hydrogen production by glycerol steam reforming: Effects of metal species distribution. *Ind. Eng. Chem. Res*., 2020, **59**, 17259-17268.

511. L. Pastor-Pérez and A. Sepúlveda-Escribano. Multicomponent $NiSnCeO_2$/C catalysts for the low-temperature glycerol steam reforming. *Appl. Catal. A: Gen.,* 2017, **529**, 118-126.

512. C. K. Cheng, S. Y. Foo and A. A. Adesina. Glycerol steam reforming over bimetallic Co-Ni/$Al_2O_3$. *Ind. Eng. Chem. Res.,* 2010**, 49***,* 10804-10817.

513. J. Zaffran, C. Michel, F. Auneau, F. Delbe and P. Sautet. Linear energy relations as predictive tools for polyalcohol catalytic reactivity. *ACS Catal*., 2014, **4**, 464-468.

514. F. J. Gutiérrez Ortiz, F. J. Campanario, P. G. Aguilera and P. Ollero. Hydrogen production from supercritical water reforming of glycerol over Ni/$Al_2O_3$□$SiO_2$ catalyst. *Energy*, 2015, **84**, 634.

515. F. J. Gutiérrez Ortiz, F. J. Campanario, P. G. Aguilera and P. Ollero. Supercritical water reforming of glycerol: Performance of Ru and Ni catalysts on $Al_2O_3$ support. *Energy,* 2016, **96** 561-568.

516. F. J. Gutiérrez Ortiz, F. J. Campanario and P. Ollero. Turnover rates for the supercritical water reforming of glycerol on supported Ni and Ru catalysts. *Fuel*, 2016, **180**, 417-423.

517. T. Pairojpiriyakul, E. Croiset, K. Kiatkittipong, W. Kiatkittipong, A. Arpornwichanop and S. Assabumrungrat. Catalytic reforming of glycerol in supercritical water with nickel-based catalysts. *Int. J. Hydrogen Energy,* 2014, **39**, 14739-14750.

518. S. Li, P. E. Savage and L. Guo. Stability and activity maintenance of $Al_2O_3$- and carbon nanotube-supported Ni catalysts during continuous gasification of glycerol in supercritical water. *J. Supercrit. Fluids*, 2018, **135**, 188-197.

519. S. Li, P. E. Savage and L. Guo. Stability and activity maintenance of sol-gel Ni-$M_xO_y$ (M=Ti, Zr, Ta) catalysts during continuous gasification of glycerol in supercritical water. *J. Super-crit. Fluids*, 2019, **148**, 137-147.

520. I.-D. Dumbrava, C.-C. Cormos, A. Imre-Lucaci and A.-M. Cormos. CFD modelling of supercritical water reforming of glycerol for hydrogen production. *Int. J. Hydrogen Energy,* 2022, **47(24)**, 12147-12158.

521. W. Yu, M. D. Porosoff and J. G. Chen. Review of Pt-based bimetallic catalysis: From model surfaces to supported catalysts. *Chem. Rev.,* 2012, **112**, 5780-5817.

522. O. Skoplyak, M. A. Barteau and J. G. Chen. Enhancing $H_2$ and CO production from glycerol using bimetallic surfaces. *ChemSusChem.,* 2008, **1**, 524-526.

523. M. El Doukkali, A. Iriondo and I. Gandarias. Enhanced catalytic upgrading of glycerol into high value-added $H_2$ and propanediols: Recent developments and future perspectives. *Mol. Catal.,* 2020, **490**, 110928 (29 pages).

524. A. Iriondo, V. L. Barrio, J. F. Cambra, P. L. Arias, M. B. Gümez, R. M. Navarro, M. C. Sanchez-Sanchez and J. L. G. Fierro. Hydrogen production from glycerol over nickel catalysts supported on $Al_2O_3$ modified by Mg, Zr, Ce or La. *Top. Catal.*, 2008, **49**, 46-58

525. A. Iriondo, J. F. Cambra, V. L. Barrio, M. B. Guemez, P. L. Arias, M. C. Sanchez-Sanchez, R. M. Navarro and J. L. G. Fierro Glycerol liquid phase conversion over monometallic and bimetallic catalysts: Effect of metal, support type and reaction temperatures. *Appl. Catal. B: Environ.,* 2011, **106**, 83-93.

526. M. El Doukkali, A. Iriondo, P. L. Arias, J. Requies, I. Gandarías, L. Jalowiecki-Duhamel and F. Dumeignil. A comparison of sol–gel and impregnated Pt or/and Ni based -alumina catalysts for bioglycerol aqueous phase reforming. *Appl. Catal. B: Environ*., 2012, **125**, 516-529.

527. M. El Doukkali, A. Iriondo, J. F. Cambra, L. Jalowiecki-Duhamel, A.S. Mamede, F. Dumeignil and P. L. Arias. Pt monometallic and bimetallic catalysts prepared by acid sol–gel method for liquid phase reforming of bioglycerol. *J. Mol. Catal. A: Chem.,* 2013, **368-369**, 125-136.

528. M. El Doukkali, A. Iriondo, J. F. Cambra, I. Gandarias, L. Jalowiecki-Duhamel, F.Dumeignil, and P .L. Arias. Deactivation study of Pt and/or Ni-based □□-$Al_2O_3$ catalysts used in the aqueous phase reforming of glycerol for $H_2$ production. *Appl. Catal. A: Gen*., 2014, **472**, 80-91.

529. M. El Doukkali, A. Iriondo, N. Miletic, J. F. Cambra and P. L. Arias. Hydrothermal stability improvement of NiPt-containing □□-$Al_2O_3$ catalysts tested in aqueous phase

reforming of glycerol/water mixture for $H_2$ production. *Int. J. Hydrogen Energy*, 2017, **42**, 23617-23630.

530. A. Fasolini, D. Cespi, T. Tabanelli, R. Cucciniello and F. Cavani. Hydrogen from renewables: A case study of glycerol reforming. *Catalysts*, 2019, **9**, 722 (21 pages).

531. M. M. Rahman, T. L. Church, M. F. Variava, A. T. Harris and A. I. Minett. Bimetallic Pt-Ni composites on ceria-doped alumina supports as catalysts in the aqueous-phase reforming of glycerol. *RSC Adv*., 2014, **4**, 18951-18960.

532. M. M. Rahman, T. L. Church, A. I. Minett and A. T. Harris. Effect of $CeO_2$ addition to $Al_2O_3$ supports for Pt catalysts on the aqueous-phase reforming of glycerol. *ChemSusChem.,* 2013, **6**, 1006-1013.

533. T. Wang, G. Mpourmpakis, W. W. Lonergan, D. G. Vlachos and J. G. Chen. Effect of oxide supports in stabilizing desirable Pt–Ni bimetallic structures for hydrogenation and reforming reactions. *Phys. Chem. Chem. Phys.,* 2013, **15**, 12156-12164.

534. S. A. Tupy, A. M. Karim, C. Bagia, W. Deng, Y. Huang, D. G. Vlachos and J. G. Chen. Correlating ethylene glycol reforming activity with *in situ* EXAFS detection of Ni segregation in supported NiPt bimetallic catalysts. *ACS Catal.,* 2012, **2**, 2290-2296.

535. J. W. Shabaker, G. W. Huber, R. R. Davda, R. D. Cortright and J. A. Dumesic. Aqueous-phase reforming of ethylene glycol over supported platinum catalysts. *Catal. Lett.,* 2003, **88**, 1-8.

536. M. M. Rahman. Aqueous-phase reforming of glycerol over carbon-nanotube-supported catalysts. *Catal. Lett*., 2020, **150**, 2674-2687.

537. S. Li and J. Gong. Strategies for improving the performance and stability of Ni-based catalysts for reforming reactions. *Chem. Soc. Rev.*, 2014, **43**, 7245-7256.

538. T. van Haasterecht, C. C. I. Ludding, K. P. de Jong and J. H. Bitter. Toward stable nickel catalysts for aqueous phase reforming of biomass-derived feedstock under reducing and alkaline conditions. *J. Catal.,* 2014, **319**, 27-35.

539. A. Morales-Marína, J. L. Ayastuya, U. Iriarte-Velasco and M. A. Gutiérrez-Ortiz. Nickel aluminate spinel-derived catalysts for the aqueous phase reforming of glycerol: Effect of reduction temperature. *Appl. Catal. B: Environ.,* 2019, **244**, 931-945.

540. R. L. Manfro, T. P. M. D. Pires, N. F. P. Ribeiro and M. M. V. M. Souza. Aqueous-phase reforming of glycerol using Ni–Cu catalysts prepared from hydrotalcite-like precursors. *Catal. Sci. Technol.,* 2013, **3**, 1278-1287.

541. D. A. Boga, R. Oord, A. M. Beale, Y.-M. Chung, P. C. A. Bruijnincx and B. M. Weckhuysen. Highly selective bimetallic Pt-Cu/Mg(Al)O catalysts for the aqueous-phase reforming of glycerol. *ChemCatChem*., 2013, **5**, 529-537.

542. D. A. Boga, F. Liu, P. C. A. Bruijnincx and B. M. Weckhuysen. Aqueous-phase reforming of crude glycerol: Effect of impurities on hydrogen production. *Catal. Sci. Technol.,* 2016, **6**, 134.

543. A. Seretis and P. Tsiakaras. Crude bio-glycerol aqueous phase reforming and hydrogenolysis over commercial $SiO_2$-$Al_2O_3$ nickel catalyst. *Renew. Energy*, 2016, **97**, 373-379.

544. B. Liu and J. Greeley. A density functional theory analysis of trends in glycerol decomposition on close-packed transition metal surfaces. *Phys. Chem. Chem. Phys.*, 2013, **15**, 6475-6485.

545. J. Zaffran, C. Michel, F. Auneau, F. Delbecq and P. Sautet. Trade-off between accuracy and universality in linear energy relations for alcohol dehydrogenation on transition metals. *J. Phys. Chem. C*, 2015, **119**, 12988-12998.

546. J. Zaffran, C. Michel, F. Auneau, F. Delbecq and P. Sautet. Towards more accurate prediction of activation energies for polyalcohol dehydrogenation on transition metal catalysts in water. *Catal. Sci. Technol.,* 2016, **6**, 6615-6624.

547. T. Xie, C. J. Bodenschatz and R. B. Getman. Insights into the roles of water on the aqueous phase reforming of glycerol. *React. Chem. Eng.*, 2019, **4**, 383-392.

548. N. Shan and B. Liu. Elucidating molecular interactions in glycerol adsorption at the metal-water interface with Density Functional Theory. *Langmuir*, 2019, **35**, 4791-4805.

549. L. Liu, S. Mao, Q. Li, X. Wang, M. Yang and L. Li. Confinement of hydrogen and hydroxyl radicals in water cages: a density functional theory study. *RSC Adv.,* 2017, **7,** 14537-14543.

550. D. Marx. Proton transfer 200 Years after von Grotthuss: Insights from ab initio simulations. *ChemPhysChem.*, 2006, **7,** 1848–1870.

551. M. Valter, E. Campos dos Santos, L. G. M. Pettersson and A. Hellman. Partial electrooxidation of glycerol on close-packed transition metal surfaces: Insights from first-principles calculations. *J. Phys. Chem. C*, 2020, **124**, 17907-17915.

552. V. L. Oliveira, C. Morais, K. Servat, T. W. Napporn, G. Tremiliosi-Filho and K.B. Kokoh. Glycerol oxidation on nickel based nanocatalysts in alkaline medium – Identification of the reaction products. *J. Electroanal. Chem.,* 2013, **703**, 56-62.

553. M. R. Karimi Estahbanati, M. Feilizadeh, F. Attar and M. C. Iliuta. Current developments and future trends in photocatalytic glycerol valorization: Photocatalyst development. *Ind. Eng. Chem. Res.,* 2020, **59**, 22330-22352.

554. H. Luo, J. Barrio, N. Sunny, A. Li, L. Steier, N. Shah, I. E. L. Stephens and M.-M. Titirici. Progress and perspectives in photo- and electrochemical- oxidation of biomass for sustainable chemicals and hydrogen production. *Adv. Energy Mater.*, 2021, 2101180 (51 pages).

555. G. Dodekatos, S. Schünemann and H. Tüysüz. Recent advances in thermo-, photo-, and electro-catalytic glycerol oxidation. *ACS Catal.,* 2018, **8**, 6301−6333

556. C.-H. Zhou, J. N. Beltramini, Y.-X. Fan and G. Q. Lu. Chemoselective catalytic conversion of glycerol as a biorenewable source to valuable commodity chemicals. *Chem. Soc. Rev*., 2008, **37**, 527-549.

557. M. Simões, S. Baranton and C. Coutanceau. Electrochemical valorisation of glycerol. *ChemSusChem*., 2012, **5**, 2106-2124.

558. M. S. E. Houache, K. Hughes and E. A. Baranova. Study on catalyst selection for electro-chemical valorization of glycerol. *Sustainable Energy Fuels*, 2019, **3**, 1892-1915.

559. K. Wu, B. Dou, H. Zhang, D. Liu, H. Chen and Y. Xu. Effect of impurities of $CH_3OH$, $CH_3COOH$, and KOH on aqueous-phase reforming of glycerol over mesoporous Ni-Cu/$CeO_2$ catalyst. *J. Energy Institute,* 2021, **99**, 198-208.

560. B. L. Kee, W.-J. Wang, O. Akpolat, P. Littlewood, J. P. Seaba, L. Scudiero and S. Ha. Caustic aqueous phase electrochemical reforming (CAPER) of ethanol for process intensified compressed hydrogen production. *Appl. Catal. A: Gen.,* 2022, **641**, 118647.

561. D. Lv, Y. Lei, D. Zhang, X. Song, Y.-W. Li, J. W. H. Niemantsverdriet, W. Hao, Y. Deng and R. Su. Effect of Pd and Au on hydrogen abstraction and C−C cleavage in photoconversion of glycerol: Beyond charge separation. *J. Phys. Chem. C*, 2020, **124**, 20320-20327.

562. P. Panagiotopoulou, E. E. Karamerou and D. I. Kondarides. Kinetics and mechanism of glycerol photo-oxidation and photo-reforming reactions in aqueous $TiO_2$ and Pt/$TiO_2$ suspensions. *Catal. Today,* 2013, **209**, 91-98.

563. C. Minero, A. Bedini and V. Maurino. Glycerol as a probe molecule to uncover oxidation mechanism in photocatalysis. *Appl. Catal. B: Environ.,* 2012, **128**, 135-143.

564. A. Beeby, D. B. H. Mohammed and J. R. Sodeau, Photochemistry and photophysics of glycolaldehyde in solution. *J. Am. Chem. Soc*., 1987, **109**, 857-861.

565. S. Xie, Z. Shen, J. Deng, P. Guo, Q. Zhang, H. Zhang, C. Ma, Z. Jiang, J. Cheng, D. Deng and Y. Wang. Visible light-driven C−H activation and C–C coupling of methanol into ethylene glycol. *Nature Commun., 2018,* **9**, 1181 (7 pages).

566. L. R. Smith, M. A. Sainna, M. Douthwaite, T. E. Davies, N. F. Dummer, D. J. Willock, D. W. Knight, C. R. A. Catlow, S. H. Taylor, and G. J. Hutchings. Gas phase glycerol valorization over ceria nanostructures with well-defined morphologies. *ACS Catal*., 2021, 11, 4893-4907.

567. I. A. Shkrob and M. C. Sauer. Hole scavenging and photo-stimulated recombination of electron-hole pairs in aqueous $TiO_2$ nanoparticles. *J. Phys. Chem. B,* 2004, **108***,* 12497-12511.

568. J. Kennedy, H. Bahruji, M. Bowker, P. R. Davies, E. Bouleghlimat and S. Issarapanacheewin. Hydrogen generation by photocatalytic reforming of potential biofuels: Polyols, cyclic alcohols, and saccharides. *J. Photochem. Photobiol. A: Chem.,* 2018, **356**, 451-456.

569. P. Ribao, M. A. Esteves, V. R. Fernandes, M. J. Rivero, C. M. Rangel and I. Ortiz. Challenges arising from the use of $TiO_2$/rGO/Pt photocatalysts to produce hydrogen from crude glycerol compared to synthetic glycerol. *Int. J. Hydrogen Energy,* 2019, **44**, 28494-28506.

570. T.W.P. Seadira, G. Sadanandam, T. Ntho, C. M. Masuku and M. S. Scurrell. Preparation and characterization of metals supported on nanostructured $TiO_2$ hollow spheres for production of hydrogen via photocatalytic reforming of glycerol. *Appl. Catal. B: Environ.,* 2018, **222**, 133-145.

571. I. Majeed, M. A. Nadeem, E. Hussain, G. I. N. Waterhouse, A. Badshah, A. Iqbal, M. A. Nadeem and H. Idriss. On the synergism between Cu and Ni for photocatalytic hydrogen production and their potential as substitutes of noble metals. *ChemCatChem*., 2016, **8**, 1-11.

572. M. T. Uddin, Y. Nicolas, C. Olivier, W. Jaegermann, N. Rockstroh, H. Junge and T. Toupance. Band alignment investigations of heterostructure $NiO/TiO_2$ nanomaterials used as efficient heterojunction earth-abundant metal oxide photocatalysts for hydrogen production. *Phys. Chem, Chem. Phys.,* 2017, **19,** 19279-19288.

573. A. J. Bard, R. Parsons and J. Jordan. *Standard potentials in aqueous solution.* CRC Press, 1st ed., 1985, Taylor & Francis (ISBN 9780824772918).

574. A. Petala, E. Ioannidou, A. Georgaka, K. Bourikas and D. I. Kondarides. Hysteresis phenomena and rate fluctuations under conditions of glycerol photo-reforming reaction over $CuO_x/ TiO_2$ catalysts. *Appl. Catal. B: Environ.,* 2015, **178**, 201-209.

575. T. W. P. Seadira, C. M. Masuku and M. S. Scurrell. Solar photocatalytic glycerol reforming for hydrogen production over ternary Cu/THS/graphene photocatalyst: Effect of Cu and graphene loading. *Renewable Energy,* 2020, **156**, 84-97.

576. S. G. Babu, R. Vinoth, D. P. Kumar, M. V. Shankar, H.-L. Chou, K. Vinodgopal and B. Neppolian. Influence of electron storing, transferring and shuttling assets of reduced graphene oxide at the interfacial copper doped $TiO_2$ p-n heterojunction for the increased hydrogen production. *Nanoscale*, 2015, **7**, 7849-7857.

577. T. N.Q. Trang, L.T. N. Tu, T. V. Man, M. Mathesh, N. D. Nam and V. T. H. Thu. A high-efficiency photoelectrochemistry of $Cu_2O/TiO_2$ nanotubes based composite for hydrogen evolution under sunlight. *Composites Part B: Eng*., 2019, **174**, 106969 (9 pages).

578. S. Fujita, H. Kawamori, D. Honda, H. Yoshida and M.Arai. Photocatalytic hydrogen production from aqueous glycerol solution using $NiO/TiO_2$ catalysts: Effects of preparation and reaction conditions. *Appl. Catal. B: Environ.,* 2016, **181**, 818-824.

579. N. L. Reddy, K. K. Cheralathan, V. D. Kumari, B. Neppolian, and S. M. Venkatakrishnan. Photocatalytic reforming of biomass derived crude glycerol in water: A sustainable approach for improved hydrogen generation using $Ni(OH)_2$-decorated $TiO_2$ nanotubes under solar light irradiation. *ACS Sustainable Chem. Eng*., 2018, **6**, 3754-3764.

580. M. Gao, P. K. N. Connor and G. W. Ho. Plasmonic photothermic directed broadband sunlight harnessing for seawater catalysis and desalination. *Energy Environ. Sci.,* 2016, **9**, 3151-3160.

581. D. Mohan, C. U. Pittman Jr. and P. H. Steele. Pyrolysis of wood/biomass for bio-oil: A critical review. *Energy & Fuels,* 2006**, 20**, 848-889.

582. P. Fu, A. Zhang, S. Luo, W. Yi and Y. Zhang. Comparative study on the catalytic steam reforming of biomass pyrolysis oil and its derivatives for hydrogen production. *RSC Adv*., 2020, **10**, 12721-12729.

583. E. Ch. Vagia and A. A. Lemonidou. Thermodynamic analysis of hydrogen production via steam reforming of selected components of aqueous bio-oil fraction. *Int. J. Hydrogen Energy,* 2007, **32**, 212-223.

584. G. Pace and S. W. Sheehan, Scaling $CO_2$ capture with downstream flow $CO_2$ conversion to ethanol. *Front. Clim*., 2021, **3**, 656108 (9 pages).

585. R. Martinez, M. C. Huff and M. A. Barteau. Ketonization of acetic acid on titania-functionalized silica monoliths. *J. Catal.,* 2004, **222**, 404-409.

586. B. D. Montejo-Valencia, Y. J. Pagán-Torres, M. M. Martínez-Iñesta and M. C. Curet-Arana. DFT study to unravel the catalytic properties of M-exchanged MFI, (M = Be, Co,

Cu, Mg, Mn, Zn) for the conversion of methane and carbon dioxide to acetic acid. *ACS Catal.,* 2017, **7**, 6719-6728.

587. F. Bossola, S. Recchia and V. D Santo. Catalytic steam reforming of acetic acid: Latest advances in catalysts development and mechanism elucidation. *Current Catalysis,* 2018, **7***,* 89-98.

588. Y. Huang, X. Dong, Y. Yu and M. Zhang. Comparative kinetic Monte Carlo study of acetic acid decomposition to surface carbon species and undesirable byproducts on Pd(100) and Pd/Au(100) from Density Functional Theory-based calculations. *J. Phys. Chem. C,* 2017, **121**, 26733-26741.

589. G. Chen, J. Tao, C. Liu, B. Yan, W. Li and X. Li. Hydrogen production via acetic acid steam reforming: A critical review on catalysts. *Renew. Sustain. Energy Rev.,* 2017, **79**,1091-1098.

590. Z. Zhao, Y. A. Situmorang, P. An, N. Chaihad, J. Wang, X. Hao, G. Xu, A. Abudula and G. Guan. Hydrogen production from catalytic steam reforming of bio-oils: A critical review. *Chem. Eng. Technol.,* 2020, **43**, 625-640.

591. S. Luo, P. Fu, F. Sun, B. Wang, A. Zhang, J. Wang, and Q. Sun. Catalytic steam reforming of bio-oil-derived acetic acid over $CeO_2$-ZnO supported Ni nanoparticle catalysts. *ACS Omega*, 2020, **5**, 19727-19736.

592. X. Hu, L. Zhang and G. Lu. Steam reforming of acetic acid over Cu-Zn-Co catalysts for hydrogen generation: Synergistic effects of the metal species. *Int. J. Hydrogen Energy,* 2016, **41**, 13960-13969.

593. Z. Wang, L. Sun, L. Chen, S. Yang, X. Xie, M. Gao, T. Li, B. Zhao, H. Si and D. Hua. Steam reforming of acetic acid for hydrogen production over Ni/$Ca_xFe_yO$ catalysts. *Int. J. Hydrogen Energy,* 2021, **46**, 33132-33142

594. J. F. Goncalves and M. M.V.M. Souza. Effect of doping niobia over $Ni/Al_2O_3$ catalysts for methane steam reforming. *Catal. Lett.,* 2018**, 148**, 1478-1489.

595. C. H. Mejia, J. E. S. v.de Hoeven, P. E. de Jongh and K. P. de Jong. Cobalt-nickel nanoparticles supported on reducible oxides as Fischer-Tropsch catalysts. *ACS Catal.*, 2020, **10**, 7343-7354.

596. J. P. S. Q. Menezes, A. P. S. Dias, M. A. P. da Silva and M. M.V. M. Souza. Stability of Ni catalysts promoted with niobia for butanol steam reforming. *Biomass & Bioenergy*, 2020, **143,** 105882 (7 pages).

597. X.-Y. Ran, Z.-Y. Du, Y.-P. Guo, J. Feng, and W.-Y. Li. Density functional theory study of acetic acid steam reforming on Ni(111). *Appl. Surf. Sci.,* 2017, **400**, 97-109.

598. X. B. Li, S. R. Wang, Y. Y. Zhu, G. H. Yang and P.J. Zheng. DFT study of bio-oil decomposition mechanism on a Co stepped surface: acetic acid as a model compound. *Int. J. Hydrogen Energy*, 2015, **40**, 330-3399.

599. X. B. Li, L. J. Xue, Y. Y. Zhu, G. Chen, G. H. Yang and S. Wang. Mechanistic study of bio-oil catalytic steam reforming for hydrogen production: Acetic acid decomposition. *Int. J. Hydrogen Energy*, 2018, **43**, 13212-13224.

600. Q. Gao and J. C. Hemminger. Chemisorption and thermal decomposition of acetic acid on Pt(lll). *J. Electron* Spectrosc. *Related Phenom.,* 1990, **54/55**, 667-676.

601. Z.-Y. Du, Y.-X. Ran, Y.-P. Guo, J. Feng and W.-Y. Li. A theoretical study on the role of water and its derivatives in acetic acid steam reforming on Ni(111). *Appl. Surf. Sci.,* 2017, **419***,* 114-125.

602. B. D. Montejo-Valencia, Y. J. Pagan-Torres, M. M. Martinez-Inesta and M. C. Curet-Arana. Density functional theory (DFT) study to unravel the catalytic properties of M-exchanged MFI (M = Be, Co, Cu, Mg, Mn, Zn) for the conversion of methane and carbon dioxide to acetic acid. *ACS. Catal.,* 2017, **7**, 6719-6728.

603. A. Ochoa, J. Bilbao, A. G. Gayubo and P. Castano. Coke formation and deactivation during catalytic reforming of biomass and waste pyrolysis products: A review. *Renew. Sustain. Energy Rev.,* 2020, **119**, 109600 (29 pages).

604. A. Ochoa, B. Aramburu, B. Valle, D. E. Resasco, J. Bilbao, A. G. Gayubo and P. Castano. Role of oxygenates and effect of operating conditions in the deactivation of a Ni supported catalyst during the steam reforming of bio-oil. *Green Chem.*, 2017, *19*, 4315-4333.

605. B. Valle, A. Remiro, A. T. Aguayo, J. Bilbao and A. G. Gayubo. Catalysts of Ni/□-$Al_2O_3$ and Ni/$La_2O_3$-□-$Al_2O_3$ for hydrogen production by steam reforming of bio-oil aqueous fraction with pyrolytic lignin retention. *Int. J. Hydrogen Energy,* 2013, **38**, 1307-1318.

606. A. G. Gayubo, B. Valle, A. T. Aguayo, M. Olazarand and J. Bilbao. Pyrolytic lignin removal for the valorization of biomass pyrolysis crude bio-oil by catalytic transformation. *J. Chem. Technol. Biotechnol.*, 2010, **85**, 132-144.

607. D. J. M. de Vlieger, B. L. Mojet, L. Lefferts and K. Seshan. Aqueous phase reforming of ethylene glycol - Role of intermediates in catalytic performance. *J. Catal.,* 2012, **292**, 239-245.

608. A. Arandia, I. Coronado, A. Remiro, A. G. Gayubo and M. Reinikainen. Aqueous-phase reforming of bio-oil aqueous fraction over nickel-based catalysts. *Int. J. Hydrogen Energy*, 2019, **44**, 13157-13168.

609. P. Lozano, A. I. Simón, L. García, J. Ruiz, M. Oliva and J. Arauzo. Influence of the Ni-Co/Al-Mg catalyst loading in the continuous aqueous phase reforming of the bio-oil aqueous fraction. *Processes* 2021, **9**, 81. (17 pages)

610. D. J. M. de Vlieger, L. Lefferts and K. Seshan. Ru decorated carbon nanotubes – a promising catalyst for reforming bio-based acetic acid in the aqueous phase. *Green Chem.*, 2014, **16**, 864-874.

611. B. Kraeutler and A. J. Bard. Heterogeneous photocatalytic synthesis of methane from acetic acid – new Kolbe reaction pathway. *J. Am. Chem. Soc.,* 1978, **100**, 2239-2240.

612. S. Hamid, R. Dillert and D. W. Bahnemann. Photocatalytic reforming of aqueous acetic acid into molecular hydrogen and hydrocarbons over Co-catalyst-loaded $TiO_2$: Shifting the product distribution. *J. Phys. Chem C*, 2018, **122**, 12792-12809.

613. S. Hamid, R. Dillert, J. Schneider and D. W. Bahnemann. Spectroscopic analysis of proton exchange during the photocatalytic decomposition of aqueous acetic acid: an isotopic study on the product distribution and reaction rate. *Catal. Sci. Technol.,* 2018, **8**, 5886-5899.

614. B. Kraeutler, C. D. Yeager and A. J. Bard. Direct observation of radical intermediates in the photo-Kolbe reaction – heterogeneous photocatalytic radical formation by electron spin resonance. *J. Am. Chem. Soc.,* 1978, **100**, 4903-4905.

615. S. Hamid, I. Ivanova, T. H. Jeon, R. Dillert, W. Choi and D. W. Bahnemann. Photocatalytic conversion of acetate into molecular hydrogen and hydrocarbons over $Pt/TiO_2$: pH dependent formation of Kolbe and Hofer-Moest products. *J. Catal.,* 2017, **349**, 128-135.

616. K. C. Chukwu and L. Árnadóttir. Density functional theory study of decarboxylation and decarbonylation of acetic acid on Pd(111). *J. Phys. Chem. C,* 2020, **124**, 13082-13093.

617. M. Imizcoz and A.V. Puga. Optimising hydrogen production via solar acetic acid photoreforming on $Cu/TiO_2$. *Catal. Sci. Technol*., 2019, **9**, 1098-1102.

618. K. Klier, Methanol synthesis. *Adv. Catal.*, 1982, **31**, 243-313.

619. J. B. Hansen and P. E. H. Nielsen. Methanol synthesis. *Handbook of Catalysis: Online.* 2008 Wiley-VCH Verlag Chap.13 Part 13.

620. X. Cui, R. Huang and D. Deng. Catalytic conversion of C1 molecules under mild conditions. *EnergyChem.,* 2020*,* **3**, 100050 (33 pages).

621. M. S. S. Shah, C. Oh, H. Park, Y. J. Hwang, M. Ma and J. H. Park. Catalytic oxidation of methane to oxygenated products: Recent advancements and prospects for electrocatalytic and photocatalytic conversion at low temperatures. *Adv. Sci.,* 2020, **7**, 2001946 (24 pages).

622. N. Onishi, M. Iguchi, X. Yang, R. Kanega, H. Kawanami, Q. Xu and Y. Himeda. Development of effective catalysts for hydrogen storage technology using formic acid. *Adv. Energy Mater.,* 2019, **9,** 1801275 (14 pages).

623. K. Stangeland, H. Li and Z. Yu. Thermodynamic analysis of chemical and phase equilibria in $CO_2$ hydrogenation to methanol, dimethyl ether, and higher alcohols. *Ind. Eng. Chem. Res.,* 2018, **57**, 4081-4094.

624. X. Cui, R. Huang and D. Deng. Catalytic conversion of $C_1$ molecules under mild conditions. *EnergyChem.,* **3,** 2021**,** 100050 (33 pages).

625. R. Schlögl. Chemical Batteries with $CO_2$. *Angew. Chem. Int. Ed.,* 2022, **61**, e202007397 (23 pages).

626. X. Jiang, X. Nie, X. Guo, C. Song and J. G. Chen. Recent advances in carbon dioxide hydrogenation to methanol via heterogeneous catalysis. *Chem. Rev.,* 2020, **120**, 7984-8034.

627. S. Saeidi, S. Najari, V. Hessel, K. Wilson, F. J. Keil, P. Concepción, S. L. Suib and A. E. Rodrigues. Recent advances in $CO_2$ hydrogenation to value-added products — Current challenges and future directions. *Prog. Energy Combust. Sci*., 2021, **85**, 100905 (64 pages)

628. A. V. Tarasov, F. Seitz, R. Schlögl and E. Frei. In situ quantification of reaction adsorbates in low-temperature methanol synthesis on a high-performance Cu/ZnO:Al Catalyst. *ACS Catal.,* 2019, **9**, 5537-5544.

629. M. Zabilskiy, V. L. Sushkevich, D. Palagin, M. A. Newton, F. Krumeich and J. A. van Bokhoven. The unique interplay between copper and zinc during catalytic carbon dioxide hydrogenation to methanol. *Nat Comm*., 2020, 11, 2409.

630. M. Bowker and K. C. Waugh. From surface science to catalysis: The importance of methoxy and formate species on Cu single crystals and industrial catalysts. *Surf. Sci.,* 2016, **650**, 93-102.

631. Y. Yang, D. Mei, C. H. F. Peden, C. T. Campbell and C. A. Mims. Surface-bound intermediates in low-temperature methanol synthesis on copper: Participants and spectators. *ACS Catal.*, 2015, **5**, 7328-7337.

632. E. L. Kunkes, F. Studt, F. Abild-Pedersen, R. Schlögl and M. Behrens. Hydrogenation of $CO_2$ to methanol and CO on $Cu/ZnO/Al_2O_3$: Is there a common intermediate or not? *J. Catal*., 2015, **328**, 43-48.

633. S. Kattel, P. J. Ramirez, J. G. Chen, J. A. Rodriguez and P. Liu. Active sites for $CO_2$ to methanol on Cu/ZnO catalysts. *Science,* 2017, **355**, 1296-1299.

634. D. B. Clarke, D.-K. Lee, M. J. Sandoval and A. T. Bell. Infrared studies of the mechanism of methanol decomposition on $Cu/SiO_2$. *J. Catal.,* 1994, **150**, 81-93.

635. H. Idriss, K. S. Kim and M. A. Barteau. Surface-dependent pathways for formaldehyde oxidation and reduction on $TiO_2(001)$. *Surface Sci.,* 199, **262**, 113-127.

636. L. C. Grabow and M. Mavrikakis. Mechanism of methanol synthesis on Cu through $CO_2$ and CO hydrogenation. *ACS Catal.,* 2011, **1**, 365–384.

637. F. Studt, M. Behrens, E. L. Kunkes, N. Thomas, S. Zander, A. Tarasov, J. Schumann, E. Frei, J. B. Varley, F. Abild-Pedersen, J. K. Norskov and R. Schlögl. The mechanism of CO and $CO_2$ hydrogenation to methanol over Cu-based catalysts. *ChemCatChem.,* 2015, 7, 1105-1111.

638. H.-T. Luk, C. Mondelli, D. C. Ferré, J. A. Stewart and J. Pérez-Ramírez. Status and prospects in higher alcohols synthesis from syngas. *Chem. Soc. Rev.,* 2017, **46**, 1358-1426.

639. M. Ao, G.-H. Pham, J. Sunarso, M. O. Tade and S. Liu. Active Centers of Catalysts for Higher Alcohol Synthesis from Syngas: A Review. *ACS Catal.*, 2018, **8**, 7025-7050.

640. Z. Li, Y. Deng, N. Dewangan, J. Hu, Z. Wang, X. Tan, S. Liu and S. Kawi. High temperature water permeable membrane reactors for $CO_2$ utilization. *Chem. Eng. J.*, 2021, **420**, 129834.

641. M. T. Xu, M. J. L. Gines, A. M. Hilmen, B. L. Stephens and E. Iglesia. Isobutanol and methanol synthesis on copper catalysts supported on modified magnesium oxide. *J. Catal.,* 1997, **171**, 130-147.

642. G. Prieto, S. Beijer, M. L. Smith, M. He, Y. Au, Z. Wang, D. A. Bruce, K. P. De Jong, J. J. Spivey and P. E. De Jongh. Design and synthesis of copper-cobalt catalysts for the selective conversion of synthesis gas to ethanol and higher alcohols. *Angew. Chem. Int. Ed.*, 2014, **53**, 6397-6401.

643. R.-P. Ye, J. Ding, W. Gong, M. D. Argyle, Q. Zhong, Y. Wang, C. K. Russell, Z. Xu, A. G. Russell, Q. Li, M. Fan and Y.-G. Yao. $CO_2$ hydrogenation to high-value products via heterogen-eous catalysis. *Nat. Commun*., 2019, **10**, 5698 (15 pages).

644. G. Bonura, S. Todaro, L. Frusteri, I. Majchrzak-Kucęba, D. Wawrzyńczak, Z. Pászti, E. Tálas, A. Tompos, L. Ferenc, H. Solt, C. Cannilla and F. Frusteri. Inside the reaction mechanism of direct $CO_2$ conversion to DME over zeolite-based hybrid catalysts. *Appl. Catal. B: Environ.*, 2021, **294**, 120255 (10 pages).

645. H. Zhou, W. Zhu, L. Shi, H. Liu, S. Liu,Y. Ni, Y. Liu, Y. He S. Xu, L. Li and Z. Liu. In situ DRIFT study of dimethyl ether carbonylation to methyl acetate on H-mordenite. *J. Mol. Catal. A: Chem.,* 2016, 417, 1-9.

646. R. Poreddy, S. Mossin, A. D. Jensen and A. Riisager. Promoting effect of copper loading and mesoporosity on Cu-MOR in the carbonylation of dimethyl ether to methyl acetate. *Catalysts*, 2021, **11**, 696 (17 pages)

647. Z. Ren, M. N. Younis, C. Li, Z. Li, X. Yang and G. Wang. Highly active Ce, Y, La-modified Cu/$SiO_2$ catalysts for hydrogenation of methyl acetate to ethanol. *RSC Adv.*, 2020, **10**, 5590-5603. 743.

648. Y. Zhao, B. Shan, Y. Wang, J. Zhou, S. Wang and X. Ma. An effective CuZn-$SiO_2$ bimetallic catalyst prepared by hydrolysis precipitation method for the hydrogenation of methyl acetate to ethanol. *Ind. Eng. Chem. Res.*, 2018, **57**, 4526-4534.

649. X. Gao, B. Xu, G. Yang, X. Feng, Y. Yoneyama, U. Taka and N. Tsubaki. Designing a novel dual-bed reactor to realize efficient ethanol synthesis from dimethyl ether and syngas. *Catal. Sci. Technol.*, 2018, **8**, 2087-2097.

650. V. Subramani and S. K. Gangwal. A review of recent literature to search for an efficient catalytic process for the conversion of syngas to ethanol. *Energy & Fuels*, 2008, **22,** 814-839.

651. S. Michailos, D. Parker and·C. Webb. Design, sustainability analysis and multiobjective optimisation of ethanol production via syngas fermentation. *Waste & Biomass Valorization*, 2019, **10**, 865-876.

652. P. Gao, L. Zhang, S. Li, Z. Zhou and Y. Sun. Novel heterogeneous catalysts for $CO_2$ hydrogenation to liquid fuels. *ACS Cent. Sci.,* 2020, **6,** 1657-1670.

653. D. Xu, Y. Wang, M. Ding, X. Hong, G. Liu and S. C. E. Tsang. Advances in higher alcohol synthesis from $CO_2$ hydrogenation. *Chem.,* 2021, **7**, 849-881.

654. Y. Han, Y. Wang, T. Ma, W. Li, J. Zhang and M. Zhang. Mechanistic understanding of Cu-based bimetallic catalysts. *Front. Chem. Sci. Eng.*, 2020, **14**, 689-748.

655. J. Schumann, A. J. Medford, J. S. Yoo, Z.-J. Zhao, P. Bothra, A. Cao, F. Studt, F. Abild-Pedersen and J. K. Nørskov. Selectivity of synthesis gas conversion to $C_{2+}$ oxygenates on fcc(111) transition-metal surfaces. *ACS Catal.*, 2018, **8**, 3447-3453.

656. L. Wang, L. Wang, J. Zhang, X. Liu, H. Wang, W. Zhang, Q. Yang, J. Ma, X. Dong, J.-G. Kim, X. Meng and F.-S. Xiao. Selective hydrogenation of $CO_2$ into ethanol over cobalt catalysts. *Angew. Chem. Int. Ed.*, 2018, **57**, 6104-6108.

657. L. Wang, S. He, L. Wang, Y. Lei, X. Meng and F.-S. Xiao. Cobalt-nickel catalysts for selective hydrogenation of carbon dioxide into ethanol. *ACS Catal.*, 2019, **9**, 11335-11340.

658. S. Zhang, X. Liu, Z. Shao, H. Wang and Y. Sun. Direct $CO_2$ hydrogenation to ethanol over supported $Co_2C$ catalysts: Studies on support effects and mechanism. *J. Catal.*, 2020, **382**, 86-96.

659. L. Ding, T. Shi, J. Gu, Y. Cui1 Z. Zhang, C.Yang, T. Chen, M. Lin, P. Wang, N. Xue, L. Peng, X. Guo, Y. Zhu, Z. Chen and W. Ding. $CO_2$ hydrogenation to ethanol over Cu@Na-Beta. *Chem*., 2020, **6**, 2673-2689.

660. A. J. Medford, A. C. Lausche, F. Abild-Pedersen, B. Temel N. C. Schjødt, J. K. Nørskov and F. Studt. Activity and selectivity trends in synthesis gas conversion to higher alcohols. *Top. Catal.*, 2014, **57,** 135-142.

661. L. Wang, S. He, L. Wang, Y. Lei, X. Meng and F. Xiao. Cobalt-nickel catalysts for selective hydrogenation of carbon dioxide into ethanol. *ACS Catal.*, 2019, **9**, 11335-11340.

662. X. Wang, P. J. Ramírez, W. Liao, J. A. Rodriguez and P. Liu. Cesium-induced active sites for C−C coupling and ethanol synthesis from $CO_2$ hydrogenation on Cu/ZnO(0001) surfaces. *J. Am. Chem. Soc.*, 2021, **143**, 13103-13112.

663. G. Prieto, S. Beijer, M. L. Smith, M. He, Y. Au, Z. Wang, D. A. Bruce, K. P. de Jong, J. J. Spivey and P. E. de Jongh. Design and synthesis of copper-cobalt catalysts for the selective conversion of synthesis gas to ethanol and higher alcohols. *Angew. Chem. Int. Ed*., 2014, **53**, 6397-6401.

664. S. Liu, Z.-J. Zhao, C. Yang, S. Zha, K. M. Neyman, F. Studt and J. Gong. Adsorption preference determines segregation direction: A shortcut to more realistic surface models of alloy catalysts. *ACS Catal*., 2019, **9**, 5011-5018.

665. S. Liu, C. Yang, S. Zha, D. Sharapa, F. Studt, Z.-J. Zhao and J. Gong. Moderate surface segregation promotes selective ethanol production in $CO_2$ hydrogenation reaction over CoCu catalysts. *Angew. Chem. Int. Ed*., 2022, **61**, e202109027 (6 pages).

666. L. Xiao, H. Zhang, H.Han and W. Wu. Highly selective synthesis of ethanol via $CO_2$ hydrogenation over $CoMoC_x$ catalysts. *ChemCatChem*., 2021, **13**, 3333-3339.